

**A Measurement
of the Gluon Distribution in the Proton
and of
the Strong Coupling Constant α_s
from Inclusive Deep-Inelastic Scattering**

Dissertation

zur

Erlangung der naturwissenschaftlichen Doktorwürde
(Dr. sc. nat.)

vorgelegt der

Mathematisch-naturwissenschaftlichen Fakultät
der

Universität Zürich

von

Rainer Wallny

aus

Deutschland

Begutachtet von

Prof. Dr. Ulrich Straumann

Dr. habil. Max Klein

Zürich 2001

Die vorliegende Arbeit wurde von der Mathematisch-naturwissenschaftlichen Fakultät der Universität Zürich auf Antrag von Prof. Dr. Ulrich Straumann und Prof. Dr. Peter Truöl als Dissertation angenommen.

To the memory of my father

Abstract

A precise measurement of the inclusive deep-inelastic e^+p scattering cross section is discussed in the kinematic range $1.5 \leq Q^2 \leq 150 \text{ GeV}^2$ and $3 \cdot 10^{-5} \leq x \leq 0.2$. The data were recorded with the H1 detector at HERA in 1996 and 1997, and correspond to an integrated luminosity of 20 pb^{-1} . The double differential cross section was measured with typically 1% statistical and 3% systematic uncertainties. The cross section data are combined with published H1 measurements at high Q^2 for a next-to-leading order DGLAP QCD analysis. The H1 data determine the gluon momentum distribution in the range $3 \cdot 10^{-4} \leq x \leq 0.1$ to within an experimental accuracy of about 3% for $Q^2 = 20 \text{ GeV}^2$. A fit of the H1 measurements and the μp data of the BCDMS collaboration allows the strong coupling constant α_s and the gluon distribution to be simultaneously determined. A value of $\alpha_s(M_Z^2) = 0.1150 \pm 0.0017(\text{exp})_{-0.0005}^{+0.0009}(\text{model})$ is obtained in NLO, with an additional theoretical uncertainty of about ± 0.005 , mainly due to the uncertainty of the renormalisation scale.

Zusammenfassung

In dieser Arbeit wird eine Präzisionsmessung des inklusiven tief-inelastischen e^+p Streuquerschnitts im kinematischen Bereich $1.5 \leq Q^2 \leq 150 \text{ GeV}^2$ und $3 \cdot 10^{-5} \leq x \leq 0.2$ diskutiert. Die Daten wurden mit dem H1 Detektor am Elektron-Proton-Speicherring HERA mit einer Luminosität von 20 pb^{-1} in den Jahren 1996 und 1997 aufgezeichnet. Der differentielle Wirkungsquerschnitt wurde mit 1% statistischer und 3% systematischer Unsicherheit bestimmt und zusammen mit bereits von der H1 Kollaboration publizierten Daten im kinematischen Bereich hoher Q^2 einer NLO DGLAP Analyse unterworfen. Dabei wurde die Gluonenimpulsdichte im Bereich $3 \cdot 10^{-4} \leq x \leq 0.1$ mit einer Präzision von 3% bei $Q^2 = 20 \text{ GeV}^2$ bestimmt. In einem kombinierten Fit von H1 e^+p Daten und μp Daten der BCDMS Kollaboration konnte die Kopplungskonstante der starken Wechselwirkung α_s zusammen mit der Gluonenimpulsdichte extrahiert werden. In NLO QCD wurde ein Wert von $\alpha_s(M_Z^2) = 0.1150 \pm 0.0017(\text{exp})_{-0.0005}^{+0.0009}(\text{model})$ bestimmt. Zusätzliche theoretische Unsicherheiten in der Grössenordnung von ± 0.005 ergeben sich hauptsächlich aus der Unbestimmtheit der Renormierungsskala.

Contents

1	Perturbative QCD and Deep Inelastic Scattering	4
1.1	Deep Inelastic Scattering	4
1.2	Bjorken Scaling	5
1.3	Quark Parton Model	6
1.4	Quantum Chromodynamics	8
1.4.1	The Running Coupling Constant	8
1.4.2	Factorisation	12
1.4.3	F_2 and F_L in next-to-leading order QCD	13
1.5	DGLAP Evolution and $(\partial F_2 / \partial \ln Q^2)_x$	14
2	An Accurate Cross Section Measurement at Low x	19
2.1	Extraction of the Cross Section	19
2.2	Kinematic Reconstruction	20
2.3	Data Analysis with the H1 Detector	22
2.3.1	Datasets	22
2.3.2	Event Selection Strategy	24
2.3.3	Electromagnetic Energy Calibration	26
2.3.4	Photoproduction Background	26
2.3.5	Hadronic Energy Scale	26
2.4	Systematic Errors	28

3	QCD Analysis Procedure	31
3.1	Analysis Procedure	31
3.1.1	Singlet and Non-Singlet Evolution of F_2	31
3.2	Flavour Decomposition	34
3.2.1	Simplified Ansatz	34
3.2.2	Generalisation	35
3.3	Parameterisation	36
3.3.1	Ansatz	36
3.3.2	Choice of Parameterisations	38
3.3.3	Input Scale Dependence and χ^2 Saturation	42
3.3.4	Gluon Momentum Fraction	50
3.4	Definition of Minimization Procedure	54
3.4.1	Definition of χ^2	54
3.4.2	Correlated Systematic Error Treatment	54
3.4.3	Error Propagation	55
4	Extraction of the Gluon Distribution	57
4.1	Quality of the Fits	57
4.1.1	Comparison with the Data	57
4.1.2	Pull Distributions	62
4.1.3	QCD Model Parameters	62
4.1.4	Dataset Normalisation	66
4.1.5	Correlated Systematic Errors	66
4.2	Effect of the Q_{min}^2 Cut	69
4.3	Results	73
4.4	Comparison to Heavy Quark Production Results	80
4.4.1	Results for F_2^{cc} in the NLO DGLAP Fits	80
4.4.2	Heavy Quark Treatment and Scheme Dependence	85
4.5	QCD Prediction for $F_L(x, Q^2)$ and its Uncertainties	86

5	Determination of $\alpha_s(M_Z^2)$	93
5.1	$\alpha_s(M_Z^2)$ from a Fit to H1 and BCDMS Data	93
5.2	Systematic Effects in the BCDMS data	96
5.3	Fit to BCDMS data alone	98
5.4	Effect of the Systematic Error Treatment on $\alpha_s(M_Z^2)$	103
5.5	$\alpha_s(M_Z^2)$ from a Fit to H1 and NMC data	106
5.6	Model Uncertainties	108
5.7	Results	108
5.8	Theoretical Scale Uncertainty	113
5.9	Further Cross Checks	113
5.10	$\alpha_s(M_Z^2)$ and the Gluon Distribution at High x	119
	Summary	128

Introduction

High Energy Physics is concerned with basically two tasks: the identification of the elementary constituents of matter and the subsequent study of their properties, and with studying the mechanisms by which these constituents interact with each other.

Experiments to pursue these objectives are nowadays performed by using high energy particle accelerators, which accelerate particle beams to high energies and collide them with particles in stationary “fixed” targets, or with particles in another beam. Around the intersection zones large detectors are installed. These detect particle interactions by means of the energy deposition and the tracks left by secondary particles scattered into the detector. The architecture of these detectors takes into account the type of accelerator they belong to; correspondingly one distinguishes fixed target experiments from colliding beam experiments, the latter covering almost the full solid angle 4π around the interaction zone.

In these high energy physics experiments, particle scattering cross sections, σ , are measured and compared to theoretical predictions. These predictions are calculated as products of matrix elements squared containing the dynamics of the process under study and the lorentz-invariant phase space determined from the kinematics, i.e. energy and momentum conservation. The matrix elements in the language of quantum field theory are depicted as Feynman diagrams where the fundamental constituent fermions exchange virtual bosons which mediate their interaction. The correct theories describing these interactions are constructed using gauge invariance against symmetry transformations and are therefore also called gauge theories.

Constituent fermions are grouped in three families of quarks and three families of leptons. Together with the gauge bosons mediating the interactions, they form the ingredients of the so called Standard Model of particle physics which since the 1970s is the accepted theoretical framework of high energy particle interaction phenomena.

The three forces known to dominate subatomic interactions¹ are mediated by the massless photon for the electromagnetic force, the three intermediate massive vector bosons Z^0 , W^+ and W^- for the weak and eight massless gluons for the strong force. The electromagnetic interaction has very successfully been described by Quantum Electrodynamics (QED). Its generalisation to include weak effects leads to the electroweak gauge field theory. The strong force is described by Quantum Chromodynamics (QCD), essentially a carbon copy of QED with important differences concerning the coupling of the gauge bosons. For each interaction, a coupling constant α enters the theory as a parameter which has to be determined by experiment.

¹The fourth interaction, gravitation, is too feeble to play a role in subatomic physics and is not easily incorporated into the formalism of quantum field theory.

There are two scattering process types distinguished in high energy physics, spacelike and timelike scattering, see Figure 1. Timelike, or s-channel scattering is characterised by the center of mass energy squared, $s > 0$. High center of mass energy can be converted to new and possibly exotic particles found at higher mass scales. Timelike processes are the standard processes used by particle factories. A typical timelike process is electron positron annihilation.

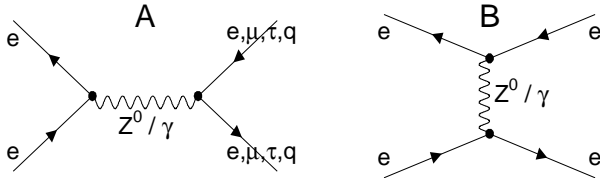


Figure 1: Feynman-Diagrams for production of fermion pairs in e^+e^- collisions. A: timelike (s-channel). B: spacelike (t-channel).

Spacelike scattering is characterised by the four momentum squared $t = q^2 < 0$ which is transferred from one incident particle to the other. The exchanged virtual gauge boson serves as a probe to survey the structure of the other particle. By virtue of the Heisenberg uncertainty relation the negative four momentum squared $Q^2 = -q^2 > 0$, can be related to the resolution λ attained by such a probe, $\lambda = 1/\sqrt{Q^2}$. Thus spacelike processes

serve as microscopes. At HERA², the electron proton collider at DESY, Hamburg, Germany, spatial dimensions of the order of 10^{-18} m can be resolved.

A classic spacelike process is deep inelastic scattering (DIS). In deep inelastic scattering, the structure of nucleons can be studied by measuring the cross section of leptons scattering off nucleons, the building blocks of the atomic nucleus. Nucleons are found to consist of quarks which are bound together by gluons. It is the structure of the proton, the most abundant nucleon, and the interpretation of this structure in the framework of Quantum Chromodynamics, to which this thesis is devoted.

This work was performed with the H1 experiment installed in the North Hall of the HERA electron-proton collider at DESY. In HERA, electrons or positrons with an energy of 27.5 GeV are brought to collisions with 820 GeV protons³ at a center of mass energy of about $\sqrt{s} \approx 300$ GeV at the H1 interaction region and also at the South Hall housing another collider experiment, ZEUS. In Hall West and East, two fixed target experiments are installed, the HERA-B experiment dedicated to the study of CP-violation, and the HERMES experiment which is devoted to the spin structure of the proton.

In this thesis, a measurement of the deep-inelastic electron proton scattering cross section at low momentum transfers Q^2 and low Bjorken x with the H1 detector at HERA is presented and its interpretation performed in terms of Quantum Chromodynamics. After an introduction to the theoretical framework in chapter 1, the data analysis is briefly presented in chapter 2 concentrating on the precision achieved due to the high luminosity of almost 20 pb^{-1} collected during data taking in 1996 and 1997.

The measured deep inelastic scattering cross section is then confronted with the prediction of Quantum Chromodynamics. The analysis uses a new decomposition of the structure functions into parton distributions which avoids the use of deuteron data. This is described in chapter 3.

²Hadron Elektron Ring Anlage

³the proton energy was raised to 920 GeV since the 1998 running period of HERA

The H1 data extend with high precision into a region where quarks and gluons carry very little fractions of proton momentum, or Bjorken x . This is demonstrated to accurately determine the gluon momentum distribution. Results of this analysis are presented in chapter 4.

In a further step, accurate data at large Bjorken x from the muon proton scattering experiment BCDMS are combined with the H1 data and the strong coupling constant α_s is extracted in next-to-leading order perturbation theory, chapter 5. Since the datasets are largely dominated by systematic errors, a careful analysis of systematic uncertainties is performed.

The thesis is concluded with a short summary.

Chapter 1

Perturbative QCD and Deep Inelastic Scattering

1.1 Deep Inelastic Scattering

Deep inelastic electron proton scattering $ep \rightarrow eX$ is characterised by spacelike virtual gauge boson exchange, with the virtuality of the exchanged gauge boson being larger than the proton mass squared, $Q^2 \gg M_p^2$. At four-momentum transfers $Q^2 \ll M_Z^2$, the Born cross section is dominated by one-photon exchange, since the competing weak interaction is suppressed by the mass squared M_Z^2 of the intermediate vector boson Z^0 entering the gauge boson propagator.

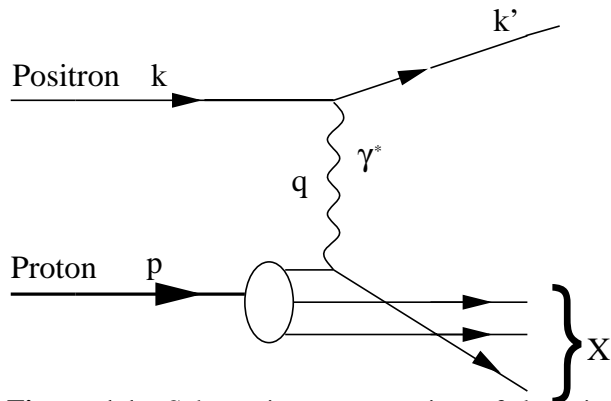


Figure 1.1: Schematic representation of deep inelastic scattering.

The process is described by two independent Lorentz invariant quantities. Let k (p) denote the incoming electron (proton) four momentum and k' the four momentum of the scattered electron, see figure 1.1. Then,

$$Q^2 = -(k - k')^2. \quad (1.1)$$

A further Lorentz invariant kinematic variable is the inelasticity y

$$y = \frac{p(k - k')}{pk}. \quad (1.2)$$

It is dimensionless, bounded to $0 < y < 1$ and corresponds in the rest frame of the proton to the fraction of the incoming lepton energy carried by the exchanged boson.

A third variable, called Bjorken x , is defined as the ratio of the four momentum and the energy transfer in the proton rest frame

$$x = \frac{Q^2}{2p(k - k')} \quad (1.3)$$

which is also dimensionless, bounded to $0 < x < 1$ and related to y and Q^2 and the center of mass energy squared, $s = (k + p)^2$ via the approximate relation

$$Q^2 = xys \quad (1.4)$$

neglecting the proton and the electron masses. In the Quark Parton Model, see below, the variable x corresponds to the fraction of proton momentum carried by the parton which is struck by the exchanged gauge boson.

The computation of the cross section $ep \rightarrow eX$

$$\sigma \sim L_{\alpha\beta} W^{\alpha\beta} \quad (1.5)$$

comprises the leptonic tensor $L_{\alpha\beta}$ describing the lepton-gauge boson vertex which can be completely calculated in QED, and a hadronic tensor $W^{\alpha\beta}$ corresponding to the boson proton vertex, which is unknown. However, using Lorentz invariance and current conservation, the unknown structure of the hadronic initial state can be parameterised by two structure functions $F_2(x, Q^2)$ and $F_L(x, Q^2)$ which enter the double differential cross section as a function of x and Q^2

$$\frac{d^2\sigma}{dx dQ^2} = \kappa \left[F_2(x, Q^2) - \frac{y^2}{Y_+} F_L(x, Q^2) \right], \quad Y_+ = 2(1-y) + y^2, \quad \kappa = \frac{2\pi\alpha^2}{Q^4 x} Y_+. \quad (1.6)$$

The longitudinal structure function F_L is directly proportional to the absorption cross section of longitudinally polarized virtual photons, whereas in F_2 both transverse and longitudinal polarization states enter. κ is related to the well known Rutherford scattering formula, $\frac{4\pi\alpha^2}{Q^4}$, describing the elastic scattering of two pointlike electric charges.

The double differential cross section scaled by the kinematical factor $1/\kappa$ is called the reduced cross section, σ_r

$$\frac{1}{\kappa} \cdot \frac{d^2\sigma}{dx dQ^2} = \sigma_r. \quad (1.7)$$

In most of the kinematic range σ_r is given by $F_2(x, Q^2)$.

1.2 Bjorken Scaling

A surprising outcome of measurements of the deep inelastic scattering cross section performed by a SLAC-MIT collaboration [1] was the observation that the structure function $F_2(x, Q^2)$ showed very little dependence on Q^2 and only seemed to depend on x , see figure 1.2. This behaviour was termed scale invariance or *scaling*. Based on theoretical arguments from current algebra, it was predicted by Bjorken to hold in the limit $Q^2 \rightarrow \infty$, and $\nu \rightarrow \infty$ with $x = \frac{Q^2}{2M_p\nu}$

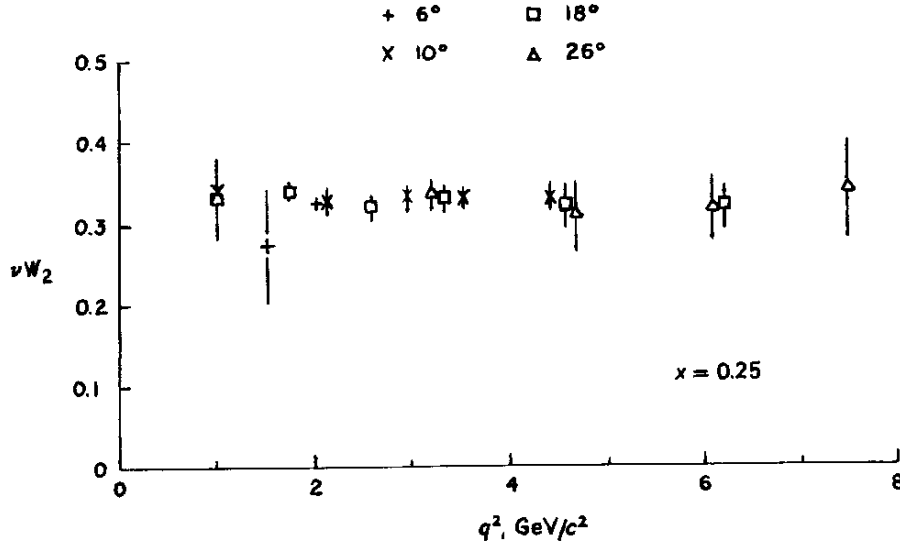


Figure 1.2: Observation of scaling: Independence of the structure function $\nu W_2 = F_2$ of $q^2 = -Q^2$. The Bjorken variable x is kept fixed, $x = 0.25$.

kept fixed, where ν is the energy loss of the incoming lepton, $\nu = E - E'$, and M_p the rest mass of the proton.

Scaling, the Q^2 independence of the structure function F_2 , suggested the existence of pointlike scattering centers in the proton. That the proton itself was not a pointlike Dirac particle was already known since the 1930s from the measurements of the anomalous magnetic moment of the proton [2], and later in the 1950s substantiated by the elastic electron proton scattering experiments by Hofstadter et al. [3].

The fact that the scattering target particle was not pointlike manifested itself in a suppression of the elastic electron proton scattering cross section, parameterised by a form factor, or structure function. This suppression is due to the destructive interference of partial waves scattered off surface of an extended object, provided that the wavelength λ of the incoming particle stream is of the order of the spatial extension of the object.

1.3 Quark Parton Model

Feynman proposed a constituent model of the proton to consist of pointlike particles, called partons [4], which were readily identified with the quarks of the static quark model [5, 6]. In this model, called the Quark Parton Model, the cross section of deep inelastic ep scattering is expressed as the incoherent sum of elementary elastic electron-parton scattering processes.

The incoherence of these elastic scattering processes, i.e. neglecting the parton-parton interactions and treating them as quasi-free, is justified if the calculations are carried out in a frame where the proton moves with infinite momentum. In this infinite momentum frame, the electron parton scattering process can be shown to take place on a much shorter time scale as the parton-parton interactions.

The partons carry a certain fraction of the proton's momentum which is identified with the Bjorken scaling variable x . The number of partons dn of a certain flavour i encountered between an interval x and $x + dx$ is parameterised by a parton distribution function $f_i(x)$, $dn = f(x)dx$. The momentum fraction dp of the protons momentum carried by these partons is then given by $dp = xf_i(x)dx$.

The deep inelastic scattering cross section $\sigma_{ep \rightarrow eX}$, is thus given by convoluting the parton distribution function with the (calculable) elastic electron parton cross sections $\sigma_{eq_i \rightarrow eq_i}$ weighted by the electric charge e_i of the parton and summed over all charged parton flavours i , denoted here as q_i :

$$\left(\frac{d\sigma}{dx dQ^2} \right)_{ep \rightarrow eX} = \sum_i \int dx e_i^2 q_i(x) \left(\frac{d\sigma}{dx dQ^2} \right)_{eq_i \rightarrow eq_i}. \quad (1.8)$$

By equating formula 1.8 with 1.6, the Quark-Parton Master equation is obtained:

$$F_2(x) = \sum_i e_i^2 x [q_i(x) + \bar{q}_i(x)]. \quad (1.9)$$

The structure function F_2 is thus seen to be independent of Q^2 and related to the parton distribution functions of the proton.

The longitudinal structure function F_L of equation 1.6 is related to the absorption cross section σ_L of longitudinally polarised virtual photons whereas F_2 receives a transverse contribution σ_T as well:

$$F_2(x, Q^2) = \frac{Q^2}{4\pi^2\alpha} (\sigma_T(x, Q^2) + \sigma_L(x, Q^2)) \quad (1.10)$$

$$F_L(x, Q^2) = \frac{Q^2}{4\pi^2\alpha} \sigma_L(x, Q^2). \quad (1.11)$$

F_2 and F_L are related according to:

$$F_L(x) = 2xF_1(x) - F_2(x) \quad (1.12)$$

where $F_1(x)$ is a structure function similarly related purely to the absorption of transversely polarized virtual photons.

Due to helicity and angular momentum conservation, and in the absence of intrinsic transverse momentum of the partons in the proton, longitudinally polarized virtual photons cannot be absorbed by spin 1/2 partons, and thus, for spin 1/2 partons F_L is predicted to be zero [7]. For spin 0 partons, F_1 would have been found to be zero. Experiments at SLAC confirmed the spin 1/2 hypothesis [7].

1.4 Quantum Chromodynamics

Soon after the SLAC experiment, violations of scaling were observed in muon nucleon scattering [8] and later confirmed by neutrino nucleon scattering experiments [9]. The relation of F_2^ν to $F_2^{\mu,e}$ confirmed the hypothesis of fractional quark charges. F_2 was found to logarithmically depend on Q^2 , see figure 1.3 for an overview. It shows the proton structure function F_2 versus Q^2 offset by a suitable constant for graphical representation. Scaling is seen to be violated at low values of x , see figure 4.2, as well as high values of x , see figure 4.3. It is a fortunate coincidence that the SLAC measurements which established the Quark Parton Model were performed in the kinematic region of $x \simeq 0.2$ where scaling happens to be exact.

The ‘naive’ application of the Quark Parton Model was compromised not only by scaling violations, but also by the fact that the quarks were found to carry only about 50% of the total momentum of the proton. These two observations were crucial in establishing QCD as the correct field theory of strong quark-gluon interactions.

1.4.1 The Running Coupling Constant

In gauge field theory, the strong interaction is mediated by mediator particles which could, as uncharged partons, account for the observed missing momentum in the proton. However, the field theoretical description of deep inelastic scattering was long troubled by the fact that the Quark Parton Model assumption of quasi-free partons in the proton implied that the coupling strength of the interaction be weak in the short-distance, high momentum transfer regime. Since no free quarks have been observed, however, the coupling strength on the other hand must be rather large in the long distance, low momentum transfer regime, which leads to the confinement of quarks in hadrons. To account for these changes, the coupling strength seems to be varying (‘running’) with the momentum transfer.



Figure 1.4: loop diagrams.

A running coupling constant is expected in quantum field theories. The Q^2 dependence arises from the fact that in higher orders of the theory, infinities arise for example due to fermion loop diagrams in the boson propaga-

tor as depicted in figure 1.4, left. These infinities are called ultraviolet divergencies since the momenta of the fermions in the loops are not fixed by energy conservation. These infinities are removed by a renormalisation procedure which introduces a renormalisation scale μ_r^2 at which the ultraviolet loop divergencies are subtracted off. This leads to a dependence of the renormalised coupling constant α on the renormalisation scale μ_r^2 .

However, physical observables $R(Q^2/\mu_r^2, \alpha_s)$ when computed up to all orders of perturbation theory should not depend on the arbitrary renormalisation scale. Any explicit dependence of R on μ_r^2 should therefore be cancelled by the dependence of α_s on μ_r^2 . This is mathematically expressed by the following equation:

$$\mu_r^2 \frac{\partial R}{\partial \mu_r^2} + \mu_r^2 \frac{\partial \alpha_s}{\partial \mu_r^2} \frac{\partial R}{\partial \alpha_s} = 0. \quad (1.13)$$

This is called the renormalisation group equation. If physical quantities are computed to fixed order, residual dependences of the observables will remain due to missing higher order diagrams. This residual scale dependence must be estimated as part of the theoretical uncertainty on the quantity. However, it is not clear in which range scale uncertainties are best assessed. It has, quite arbitrarily, become customary to vary scales between $1/4\mu^2 \dots 4\mu^2$.

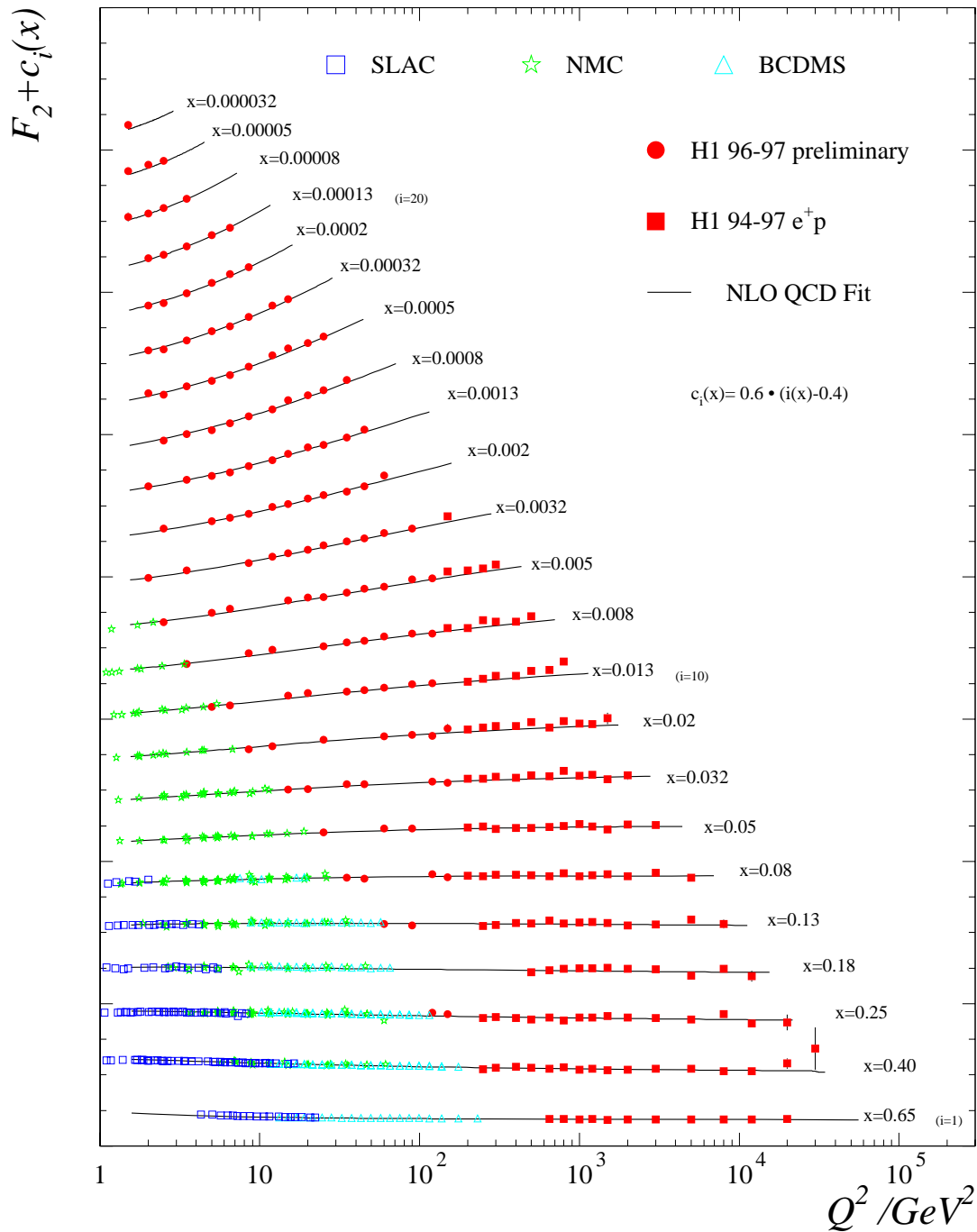


Figure 1.3: Scaling violations measured in lepton proton scattering experiments.

In the case of QED, the loop diagrams effectively lead to vacuum polarisation due to virtual e^+e^- pairs which screen the bare charge e_0 of a particle. At large distances or low momentum transfer, the charge e seen by a probe is smaller than at short distances, or high momentum transfer. Thus the coupling increases with increasing momentum transfer, a behaviour exactly opposite to the behaviour observed in the case of the strong interaction.

The solution of this problem was found by observing that the correct gauge theory of strong interaction is non-Abelian. In QCD, the degree of freedom connected to the interaction is the colour charge which is carried by quarks and by the mediator particles, the gluons, alike. Thus, the gluons can couple to each other in contrast to the electrically neutral photons. This introduces additional loop diagrams depicted in figure 1.4, (right), which lead to an anti-screening effect.

The dependence of the strong coupling constant α_s on the renormalisation scale can be computed by observing that the partial derivative $\partial\alpha_s/\partial\mu_r^2$ of equation 1.13 can itself be expressed in a power series of $\alpha_s(\mu_r^2)$ and so-called β functions which are calculable in QCD:

$$\mu_r^2 \frac{\partial\alpha_s}{\partial\mu_r^2} = \alpha_s\beta(\alpha_s) = -\beta_0 \frac{\alpha_s^2}{4\pi} - \beta_1 \frac{\alpha_s^3}{16\pi^2} + \dots \quad (1.14)$$

$$\beta_0 = (33 - 2n_f)/3$$

$$\beta_1 = 102 - \frac{38}{3}n_f$$

where β_0, β_1 are the first coefficients occurring in the expansion and n_f denoting the number of active flavours, i.e. the quark flavours with masses smaller than μ_r .

In the one-loop approximation, i.e. regarding only the term with β_0 , the coupling constant α_s can be written in terms of the renormalization scale as

$$\alpha_s(\mu_r^2) = \frac{\alpha_s(\mu_0^2)}{1 + b \cdot \alpha_s(\mu_0^2) \ln(\mu_r^2/\mu_0^2)} \quad (1.15)$$

where $b = \beta_0/4\pi = (33 - 2n_f)/12\pi$ and μ_0^2 being a suitably chosen reference scale. The presence of this scale μ_r is at the origin of scaling violations, as will be seen below.

The term $-2n_f/12\pi$ is due to the fermion loops and leads to screening effects similar as in QED. The term $33/12\pi$ gives rise to the antiscreening due to the gluon self-coupling: For less than 17 quark flavours, this is the dominating contribution and the coupling is seen to be falling with increasing μ_r , see figure 1.5. QCD is asymptotically free for $Q^2 \rightarrow \infty$, which is the reason why partons confined in the proton can be regarded as quasi-free as postulated in the Quark Parton Model. This property is unique to non-Abelian gauge theories. For $Q^2 \rightarrow 0$, the coupling is seen to diverge. This can be viewed as a reason for the confinement of quarks and gluons inside hadrons. However, confinement is not really yet understood since the increase of the coupling constant prohibits the use of perturbation theory of the region of Q^2 below a few GeV^2 .

Alternatively, the running of α_s is often expressed as

$$\alpha_s(\mu_r^2) = \frac{1}{b \cdot \ln(\mu_r^2/\Lambda_{QCD}^2)}, \quad (1.16)$$

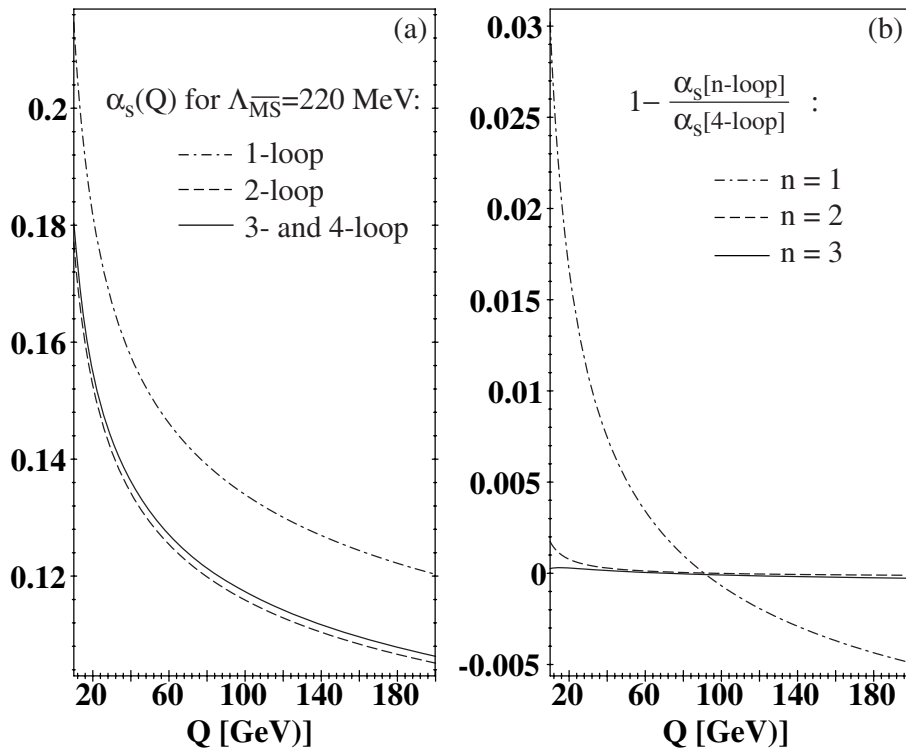


Figure 1.5: The running of α_s [10]: shown are the differences in the Q^2 dependence of the strong coupling constant due to higher orders in perturbation theory, see text.

introducing as a constant of integration a parameter Λ_{QCD} which is of the order of 100 – 300 MeV. Both equation 1.15 and 1.16 are equivalent, differing only in the specification of the boundary condition when solving the differential equation 1.15.

However, Λ is not unambiguously defined beyond leading order and it depends on the number of active flavours n_f , $\Lambda = \Lambda^{n_f}$. Figure 1.5 shows the running of α_s when equation 1.13 is solved to higher orders and Λ kept fixed; from 1 loop to 2 loops a decrease of almost 15% is observed. Therefore, it has become customary to specify instead as fundamental parameter the value of α_s at the reference scale of the Z^0 mass, $\alpha_s(M_Z^2)$ in the so-called \overline{MS} renormalisation and factorisation scheme, see below.

At next-to-leading order, including contributions up to β_1 in equation 1.13, the renormalisation group equation can be solved exactly such that the result is stable with respect to yet higher order contributions. This is in contrast to using the approximate $\log \log$ solution

$$\alpha_s(\mu_r^2) = \frac{1}{b \cdot \ln(\mu_r^2/\Lambda_{QCD}^2)} \left[1 - \frac{b' \ln \ln(\mu_r^2/\Lambda_{QCD}^2)}{b \ln(\mu_r^2/\Lambda_{QCD}^2)} \right] \quad (1.17)$$

with $b' = \beta_1/4\pi\beta_0$. This approximation is sufficiently accurate for $Q^2 > m_c^2$ and used as a convention adopted by [11]. In this analysis, the exact solution is employed and the difference to α_s obtained with the *log log* formula is quoted.

1.4.2 Factorisation

In Quantum Chromodynamics, additional infinities arise connected to peculiar behaviour of the strong coupling constant α_s which are absent in Quantum Electrodynamics. These are the so-called infrared divergencies which arise from gluon radiation off quark lines when the gluon is almost collinear with the quark. These diagrams give rise to large divergent logarithms in the perturbation series.

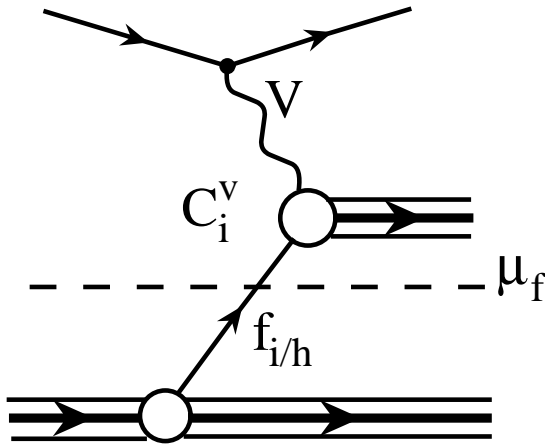


Figure 1.6: Factorisation of hard and soft contributions to the deep inelastic cross section. The contribution to the electron proton cross section $Q^2 < \mu_f^2$ is absorbed in the parton distribution function $f_{i/h}$. The contribution $Q^2 > \mu_f^2$ belongs to the hard scattering process characterised by a coefficient function C^{Vi} , see below.

These divergencies are connected to the 'soft', i.e. long range or low momentum regime of QCD and are thus not perturbatively tractable. They are renormalized in analogy to the ultraviolet divergencies described above, introducing an additional factorisation scale μ_f^2 into the theory. For momentum transfers $Q^2 > \mu_f^2$, α_s is taken to be small and perturbation theory is applicable; this is the regime of short range, high momentum transfer ('hard') interactions. Processes belonging to the 'soft' regime, $Q^2 < \mu_f^2$ are absorbed in the renormalised parton distribution functions which now depend on the factorisation scale, $f(x) \rightarrow f(x, \mu_f^2)$. The separation of 'hard' and 'soft' scale processes is called *factorisation*. This is depicted in figure 1.6, for the example of deep inelastic scattering.

For the Drell Yan process, the massive di-lepton production in hadron hadron collisions, the total cross section $\sigma_{AB \rightarrow l+l^-}$ can be obtained by

$$\sigma_{AB \rightarrow l+l^-} = \int dx_q dx_{\bar{q}} f_{q/A} f_{\bar{q}/B} \cdot \hat{\sigma}_{q\bar{q} \rightarrow l+l^-} \quad (1.18)$$

It turns out that the collinear logarithmic divergencies connected to real and virtual gluon emission which arise in Drell Yan di-lepton production are the *same* as in deep inelastic scattering. In fact it was proven by the factorisation theorems that this was a general feature of hard scattering processes in QCD [12]. As a consequence, the renormalised parton distribution functions are *universal* and depend only on the hadron they belong to. Note that this corresponds to the assumptions made in the Quark Parton Model.

The differential cross sections for a reaction involving hadrons in the initial state can thus be obtained by convoluting the parton distribution functions $f_{i/h}$ of the respective hadron with the hard scattering cross section $\hat{\sigma}$ on the parton level.

1.4.3 F_2 and F_L in next-to-leading order QCD

For the process of deep inelastic scattering, the Quark Parton Model master equation 1.9 must be modified by a factorisation scale dependent quark distribution functions. The scale μ_f^2 to which hard and soft processes are compared to is usually taken to be Q^2 but can also be provided by e.g. the transverse momentum p_t^2 or energy E_t^2 or by a heavy quark mass m_{HQ}^2 .

With $q_i(x) \rightarrow q_i(x, \mu_f^2 = Q^2)$ one thus obtains

$$F_2(x, Q^2) = \sum_i e_i^2 x [q_i(x, Q^2) + \bar{q}_i(x, Q^2)], \quad (1.19)$$

i.e. F_2 is now seen to be Q^2 dependent and scale invariance is violated, albeit only logarithmically as will be seen in the next sections.

Equation 1.19 is valid in the so-called leading log approximation, or in the DIS renormalisation and factorisation scheme to all orders, see below. At higher order, equation 1.19 is modified. Let us define for convenience

$$\bar{F}_2 = \sum_{i=1}^{n_f} e_i^2 \{q_i + \bar{q}_i\},$$

then F_2 is computed in the next-to-leading order of the theory [13] as

$$\frac{F_2}{x} = \left(1 + \frac{\alpha_s}{2\pi} C_q^2\right) \otimes \bar{F}_2(n_f = 3) + \frac{\alpha_s}{2\pi} C_g^2 \otimes \left(\sum_{f=1}^3 e_f^2\right) g + \frac{F_2^{cc}}{x} \quad (1.20)$$

F_2^{cc} denotes the contribution of charm quarks which needs a separate treatment due to effects of the heavy charm mass, see chapter 4.3. C_q and C_g denote the Wilson coefficients for quarks and gluons respectively which are known in perturbation theory to leading and next-to-leading order. Both F_2 and F_2^{cc} are computed to order $\mathcal{O}(\alpha_s^2)$ and the symbol \otimes stands for the convolution:

$$f \otimes g = \int_x^1 \frac{dz}{z} f(z) g(x/z).$$

The coefficient functions in next-to-leading order are dependent on the factorisation and renormalisation scheme due to the fact that there is freedom to choose how non-logarithmic long range and short range contributions are absorbed in parton distributions and coefficient functions. In the DIS scheme, the coefficient functions are chosen such that equation 1.19 is valid order by order. Another conventional scheme is the $\overline{\text{MS}}$ [14] which follows from the idea of dimensional regularisation [15]. In both schemes, μ_f^2 and μ_r^2 are often taken to be equal and fixed to Q^2 .

The proton structure function F_2 in QCD can thus be expressed as a convolution of coefficient functions $C_2^{V,i}$ which describe the perturbatively calculable interaction of the incoming lepton with a parton of flavour i mediated by a gauge boson V and distributions of partons $f_{i/h}$ in the hadron h which have to be taken from experiment.

Similar expressions can be found for the longitudinal structure function F_L . Note that there is a theoretical ambiguity as to which order $\mathcal{O}(\alpha_s)$ F_2 and F_L are consistently calculated since in the leading order of the theory $F_L=0$, reproducing the Callan-Gross relation, equation 1.12.

The first non-vanishing order for F_L is $\mathcal{O}(\alpha_s)$ [16, 17]

$$\frac{F_L}{x} = \frac{\alpha_s}{2\pi} C_q^L \otimes \bar{F}_2 + \frac{\alpha_s}{2\pi} C_g^L \otimes \left(\sum_f e_f^2 \right) g \quad (1.21)$$

However, $\mathcal{O}(\alpha_s^2)$ corrections on F_L are sizable and this analysis employs consequently the $\mathcal{O}(\alpha_s^2)$ equations

$$\begin{aligned} \frac{F_L}{x} = & \left(\frac{\alpha_s}{2\pi} C_q^L + \frac{\alpha_s^2}{(2\pi)^2} C_{2,NS}^L \right) \otimes \bar{F}_2^{NS} \\ & + \left(\frac{\alpha_s}{2\pi} C_q^L + \frac{\alpha_s^2}{(2\pi)^2} C_{2,S}^L \right) \otimes \bar{F}_2^S \\ & + \left(\frac{\alpha_s}{2\pi} C_g^L + \frac{\alpha_s^2}{(2\pi)^2} C_{2,g}^L \right) \otimes \left(\sum_f e_f^2 \right) g \end{aligned} \quad (1.22)$$

\bar{F}_2^{NS} and \bar{F}_2^S are functions of so-called non-singlet and singlet quark distribution functions, respectively, which will be discussed in the next section.

1.5 DGLAP Evolution and $(\partial F_2 / \partial \ln Q^2)_x$

Both F_2 and F_L are measurable quantities and thus should not depend on the choice of factorisation scale μ_f . This requirement yields evolution equations for the parton distribution functions $f_i(x, \mu_f^2)$ in which the structure functions decompose:

$$\frac{df_i(x, \mu_f^2)}{d \ln \mu_f^2} = \frac{\alpha_s(\mu_f^2)}{2\pi} \int_x^1 \frac{dy}{y} f_i(y, \mu_f^2) P_{ij}(x/y) \quad (1.23)$$

This equation, known as the Dokshitzer, Gribov, Lipatov, Altarelli and Parisi (DGLAP [18]) equation, is the analogue of the differential equation 1.15 describing the evolution of α_s with μ_r^2 . In the following, μ_f^2 is taken to be equal to Q^2 for simplicity.

The functions $P_{ij}(x/y)$ are splitting functions calculable in perturbative QCD as a power series of $\alpha_s(Q^2)$:

$$P_{ij}(z, \alpha_s(Q^2)) = \delta_{ij}P_{ij}^{(0)}(z) + \frac{\alpha_s}{2\pi}P_{ij}^{(1)}(z) + \dots \quad (1.24)$$

They are known up to next-to-leading order, $P^{(1)}$. Calculations in next-to-NLO are underway [19].

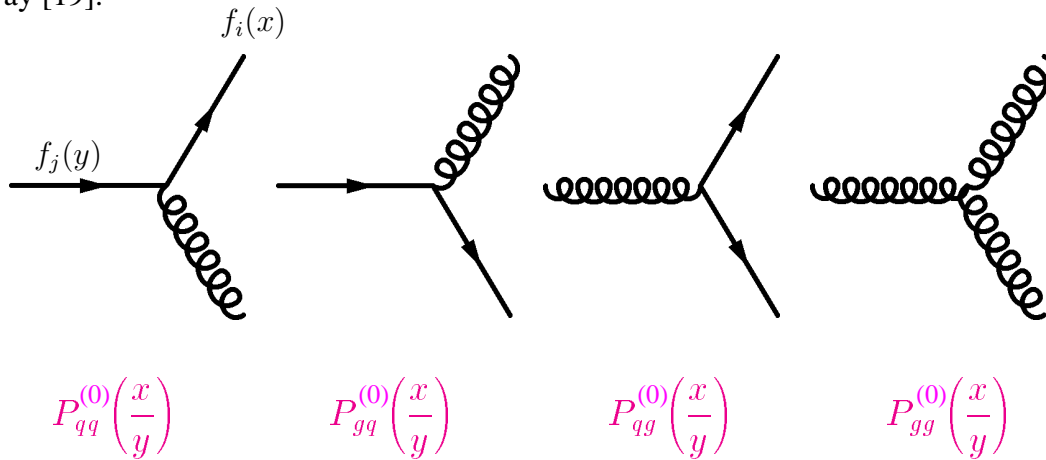


Figure 1.7: Leading order splitting functions. $P_{ij}^{(0)}(\frac{x}{y})$ denotes the probability for parton j with momentum fraction y to split into a parton i with momentum fraction x .

The leading order splitting functions $P_{ij}^{(0)}$ provide an appealing interpretation as the probability for finding a parton of type i with momentum fraction x originating from a parton j with momentum fraction $y > x$, see figure 1.7. The interpretation as probabilities implies that the splitting functions are positive definite for $x < 1$, and satisfy sum rules

$$\begin{aligned} \int_0^1 dx P_{qq}^{(0)}(x) &= 0 \\ \int_0^1 dx x \left[P_{qq}^{(0)}(x) + P_{gq}^{(0)}(x) \right] &= 0 \\ \int_0^1 dx x \left[2n_f P_{qg}^{(0)}(x) + P_{gg}^{(0)}(x) \right] &= 0 \end{aligned} \quad (1.25)$$

which correspond to quark number and momentum conservation in the splitting of quarks and gluons, respectively. Thus, the DGLAP equation 1.23 with the leading order splitting functions provide an intuitive picture as to the origin of the scaling violations of F_2 .

Consider the process of quark gluon bremsstrahlung described by the splitting function P_{qq} . If the resolving power of a photon given by its virtuality $Q^2 = Q_0^2$ is small, any virtual gluon emission and subsequent absorption process may not be resolved by the photon probe and the quark gluon pair will be ‘seen’ as a whole object. If the resolution increases, $Q^2 > Q_0^2$, the photon can couple to a quark which has radiated off a gluon and thus has lost some momentum which was carried away by the gluon.

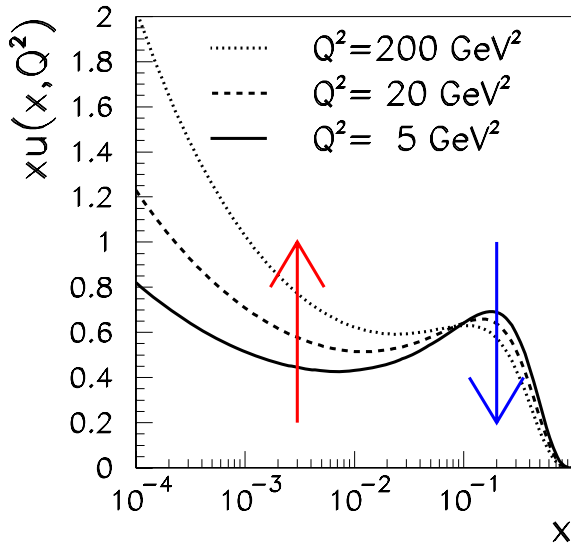


Figure 1.8: U quark momentum distribution with increasing Q^2 .

As a consequence, fewer quarks will be found at high momentum fraction x if Q^2 is increased. This is indicated in figure 1.8 which shows the momentum distribution of u quarks in the proton. At high x , the quark number distribution is seen to decrease with increasing Q^2 . On the other hand, gluons can fluctuate into quark antiquark pairs as controlled by the splitting function P_{qq} . These so-called sea quarks are preferably produced at low x and, provided the resolving power of the virtual photon is large enough, it can couple to the sea quarks as well, leading to an increase of quarks seen with increasing Q^2 at low x . Since the structure function F_2 is given essentially by the charge weighted quark distributions, the resolution dependence of the quark distributions are reflected in the scaling violations of F_2 .

For the following discussion it turns out to be beneficial to consider linear combinations of quark distribution functions according to their net flavour content. Quark distribution functions with net flavour quantum numbers are defined by

$$\Delta_{ij}(x, Q^2) = q_i(x, Q^2) - q_j(x, Q^2) \quad (1.26)$$

$$\bar{\Delta}_{ij}(x, Q^2) = \bar{q}_i(x, Q^2) - \bar{q}_j(x, Q^2) \quad (1.27)$$

as well as by linear combinations thereof.

Since the gluon distribution does not carry any flavour quantum numbers, it is a flavour singlet. A quark flavour singlet parton momentum distribution function Σ can be defined by

$$\Sigma(x, Q^2) = \sum_q [q(x, Q^2) + \bar{q}(x, Q^2)]. \quad (1.28)$$

Writing down the DGLAP evolution equations for the gluon, the quark singlet and the quark non-singlet distributions one arrives at a set of $2n_f - 1$ scalar evolution equations for the non-singlet

$$\frac{d\Delta_{ij}(x, Q^2)}{d \ln Q^2} = \frac{\alpha_s(Q^2)}{2\pi} \int_x^1 \frac{dy}{y} \Delta_{ij}(y, Q^2) P_{qq}(x/y) \quad (1.29)$$

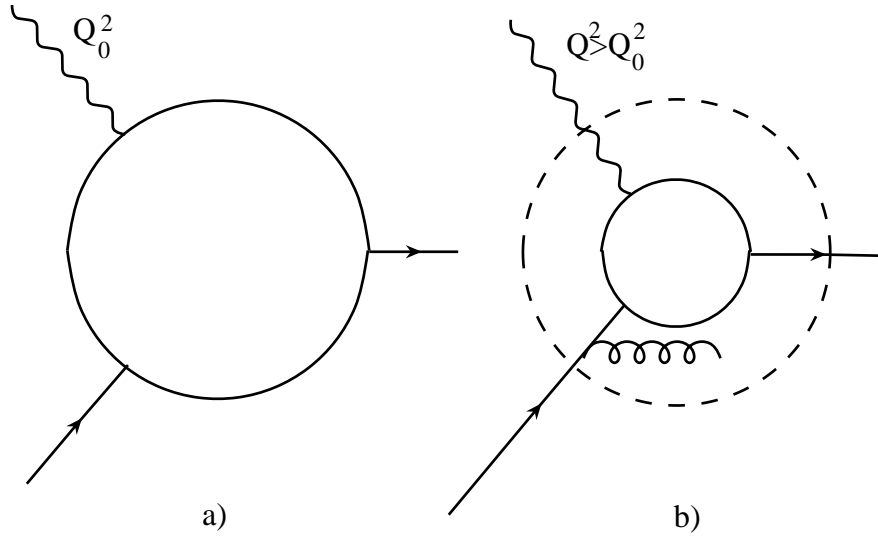


Figure 1.9: Resolution effects explaining the Q^2 dependence of quark distribution functions. At low resolution a) quarks and gluons radiated off are seen as one entity; at higher resolution scales b), quark and radiated gluon can be resolved. Since the gluon takes away some fraction of the quark's momentum, fewer quarks at high momentum fractions are detected if the resolution is increased.

and a system of 2×2 coupled equations

$$\begin{aligned} \frac{d\Sigma(x, Q^2)}{d \ln Q^2} &= \frac{\alpha_s(Q^2)}{2\pi} \int_x^1 \frac{dy}{y} [\Sigma(y, Q^2) P_{qq}(x/y) + g(y, Q^2) P_{qg}(x/y)], \\ \frac{dg(x, Q^2)}{d \ln Q^2} &= \frac{\alpha_s(Q^2)}{2\pi} \int_x^1 \frac{dy}{y} [\Sigma(y, Q^2) P_{gq}(x/y) + g(y, Q^2) P_{gg}(x/y)], \end{aligned} \quad (1.30)$$

for the quark flavour singlets $\Sigma(x, Q^2)$ and $xg(x, Q^2)$. These $2n_f + 1$ coupled integro-differential equations can be solved when boundary conditions $\Sigma(x, Q_0^2)$, $xg(x, Q_0^2)$ and $\Delta(x, Q_0^2)$ are specified which have to be taken from the data. Once these boundary conditions are specified, the evolution with Q^2 of the parton distribution functions, and as a consequence F_2 and F_L , are completely predicted.

Combining the result of the DGLAP equations with equation 1.20, a prediction for the dependence of $F_2(x, Q^2)$ on Q^2 is found to be

$$\frac{dF_2(x, Q^2)}{d \ln Q^2} = \frac{\alpha_s(Q^2)}{2\pi} \left[\int_x^1 \frac{dy}{y} \frac{x}{y} P_{qq}(x/y) F_2(y, Q^2) + \sum_q e_q^2 \int_x^1 \frac{dy}{y} \frac{x}{y} P_{qg}(x/y) yg(y, Q^2) \right] \quad (1.31)$$

thus explaining the logarithmic scaling violations of $F_2(x, Q^2)$ observed in figure 1.3 in the framework of QCD. The reason for the logarithmic dependence of the structure function on Q^2 is the running of the coupling constant α_s .

Note that the DGLAP equations do not give any x dependence of the parton distribution functions. The x dependence has to be entirely specified by the boundary conditions, taken from outside the theory. This is a consequence of the fact that the DGLAP evolution sums up the leading contribution which is coming from large logarithms $\ln Q^2$. In principle, an expansion has to be performed in powers of

$$\alpha_s^p (\ln Q^2)^q \ln(1/x)^r$$

In the leading order DGLAP theory, where $\ln Q^2$ is considered as the dominant contribution, $p = q \geq r \geq 0$. At NLO, terms for which $p = q + 1 \geq r \geq 0$ are summed as well. At HERA, x is sufficiently small that the terms proportional to $\ln(1/x)$ should become important and DGLAP be bound to fail; however, no such effect has so far been established. A search for such effects beyond DGLAP in inclusive scattering has been systematically performed in this analysis.

An important feature of the DGLAP evolution equations is the fact that the convolution integrals run from x up to 1 rather than from 0 to 1. Thus, the theory provides predictions for the parton densities at higher momentum fraction $y > x$, independently of the knowledge of the parton distributions at momentum fractions smaller than x .

This allows the application of the QCD fit technique: parton distributions are parameterised at some input scale Q_0^2 , then they are evolved to higher values of Q^2 and the theoretical prediction based on the DGLAP evolution is tested against the data.

Chapter 2

An Accurate Cross Section Measurement at Low x

2.1 Extraction of the Cross Section

The deep inelastic cross section (equation 1.6) is measured double differentially in the Lorentz invariant kinematic variables x and Q^2 . Measuring the cross section requires to basically count the number of events N originating from DIS occurring in a bin, a certain region of x and Q^2 , \square , and dividing this number by the luminosity \mathcal{L} provided by the particle accelerator,

$$\sigma^{\square} = N/\mathcal{L}. \quad (2.1)$$

Of course, events from competing non-DIS processes give rise to a background contribution N^{BG} in the bin which has to be identified and subtracted, $N \rightarrow N^{rec} - N^{BG}$.

High energy physics experiments basically measure energy depositions in calorimeters and tracks in the detector's tracking devices left by secondary particles produced in the hard interaction. Thus, the Lorentz invariant variables must be reconstructed from the laboratory frame measurements of particle energies and scattering angles.

In practice, these measurements suffer from imperfections of the detector: particles can escape detection through acceptance holes such as cracks in the calorimeters, the geometry of the detector or the beam pipe hole, due to detector inefficiencies (ϵ) and the like. Furthermore, the reconstructed variables x_{rec} and Q_{rec}^2 are not to arbitrary precision identical to the true variables of the hard interaction x and Q^2 due to the finite resolution achieved by the detector in measuring angles and energies (smearing acceptance Acc). Also, radiative corrections (δ^{rad}) can lead to systematic deviations of the measured from the 'true' kinematic variables of the interaction at Born level [20].

These effects lead to event migrations, $N \neq N^{rec}$, which have to be accounted for in the extraction of the cross section (unfolding). Also, the effect of determining the cross section differentially in $dx dQ^2$ by finite-sized bins $\square = \Delta x \Delta Q^2$ adapted to the detector resolution has to be accounted for (bin-center-correction Δ^{bc}).

Thus, equation 2.1 has to be modified:

$$\sigma^{\square} = \frac{N^{rec} - N^{BG}}{\mathcal{L}} \frac{\Delta^{bc}}{\epsilon_{Acc}} \frac{1}{1 + \delta^{rad}}$$

It is obvious that the precision of the deep inelastic cross section measurement can be maximised if these effects and their corresponding uncertainties can be well controlled. In particular, high precision relies on good angular and energy resolution, accurate alignment and precise calibration of the energy response.

2.2 Kinematic Reconstruction

The H1 detector is a collider experiment which is optimized to measure hard interactions in electron proton collisions. The interaction region is surrounded by a central tracking system and a liquid argon calorimeter (LAr) with hadronic and electromagnetic sections. In the backward region, a lead-scintillator fibre calorimeter SPACAL is installed, complemented by a backward drift chamber BDC and a backward silicon tracker BST. Figure 2.1 shows a side view of the detector with the main components relevant to this analysis marked. The H1 detector has nearly 4π coverage of the solid angle in calorimetry. This allows a redundant reconstruction of the scattering kinematics from energy and scattering angle measurements. The details of the detector setup are described elsewhere [21].

As such are available the energy E'_e and scattering angle θ_e of the final state electron. The coordinate system of H1 is defined such that the positive z axis is in the direction of the incident proton beam. Polar angles θ are defined with respect to the proton beam direction.

In practice, Q^2 and y are experimentally determined and x is computed using equation 1.4. Using these variables from the scattered electron alone,

$$y_e = 1 - \frac{E'_e}{E_e} \sin^2(\theta_e/2), \quad Q_e^2 = \frac{E_e'^2 \sin^2 \theta_e}{1 - y_e}. \quad (2.2)$$

are obtained. This is the so-called “electron method”. This was the only kinematic reconstruction method available to the deep inelastic fixed target experiments at SLAC and CERN.

The reconstruction accuracy in Q^2 , x and y depends on the energy and the angle precisions as [22]¹:

$$\frac{\delta Q^2}{Q^2} = \frac{\delta E_e}{E_e} \oplus \tan\left(\frac{\theta}{2}\right) \cdot \delta\theta, \quad (2.3)$$

$$\frac{\delta x}{x} = \frac{1}{y} \cdot \frac{\delta E_e}{E_e} \oplus \left[\tan\left(\frac{\theta}{2}\right) + \left(\frac{1}{y} - 1\right) \cdot \cot\left(\frac{\theta}{2}\right) \right] \cdot \delta\theta, \quad (2.4)$$

$$\frac{\delta y}{y} = \left(1 - \frac{1}{y}\right) \cdot \frac{\delta E_e}{E_e} \oplus \left(\frac{1}{y} - 1\right) \cdot \cot\left(\frac{\theta}{2}\right) \cdot \delta\theta, \quad (2.5)$$

¹dropping indices e on x, y, Q^2 and $'$ on E_e for simplicity

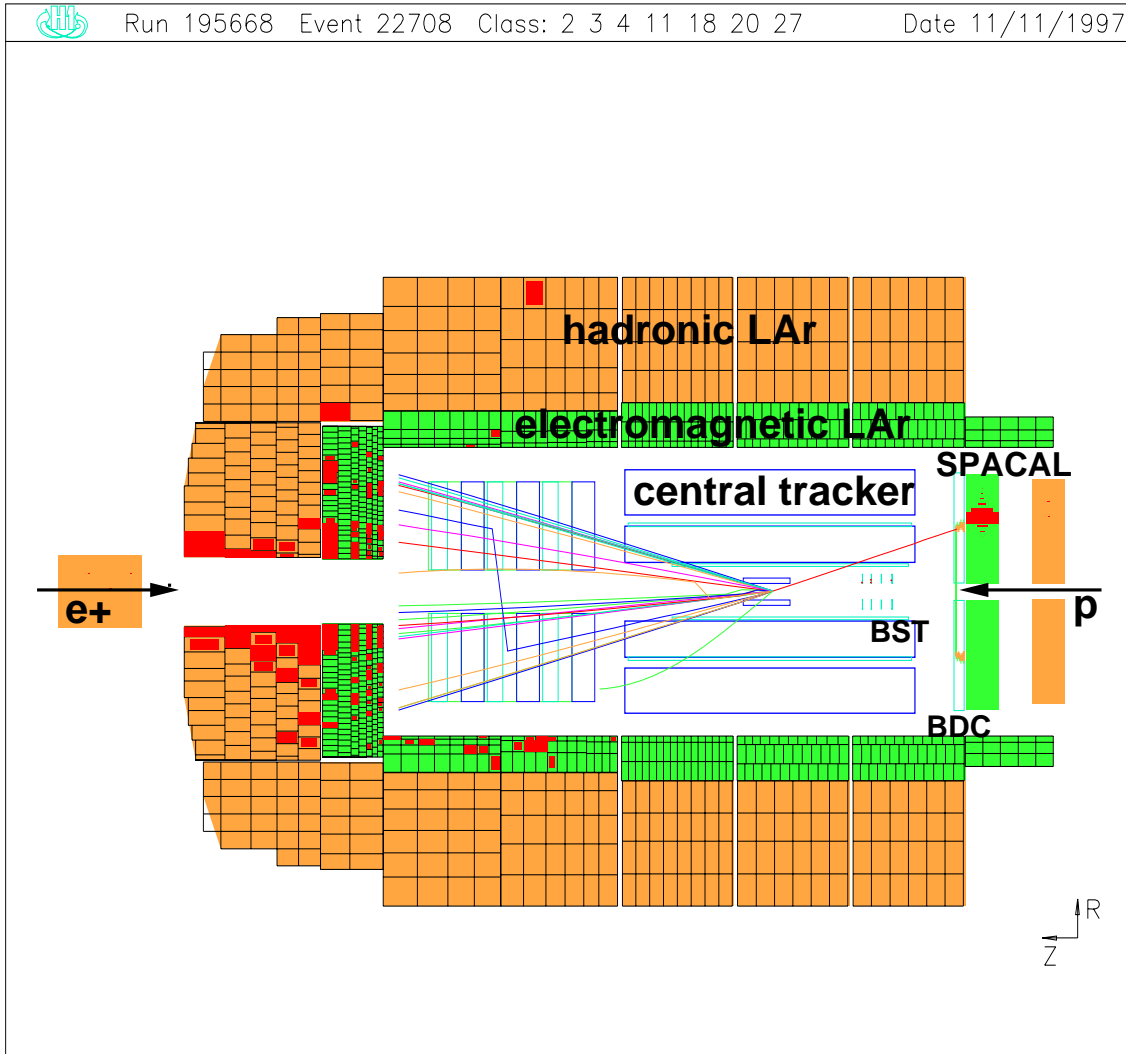


Figure 2.1: Side view of the H1 detector. Positrons of $E_e = 27.5$ GeV are colliding with $E_p = 820$ GeV protons. The main components are a liquid argon calorimeter with electromagnetic and hadronic sections (LAR), a lead scintillating fibre calorimeter in the backward region SPACAL, a backward drift chamber (BDC) and a backward silicon tracker (BST). A low Q^2 DIS event is shown, with the scattered positron entering the SPACAL.

where \oplus denotes the quadratic summation of the terms. While the electron method is accurate at large y , corresponding to low E'_e , the resolution $\delta y/y$ rapidly degrades with $1/y$ as E'_e approaches the electron beam energy E_e .

The inelasticity y can also be determined from hadronic final state particles with energies E_i and scattering angles θ_i , or, correspondingly, $p_{z,i} = E_i \cdot \cos \theta_i$ (neglecting the particle masses).

$$y_h = \frac{\sum_i (E_i - p_{z,i})}{2E_e} \equiv \frac{\Sigma}{2E_e}, \quad (2.6)$$

where E_i and $p_{z,i}$ are the energy and longitudinal momentum component of a particle i in the hadronic final state. This is the Jacquet-Blondel or ‘‘Hadronic Method’’ [23]. The kinematics

can also be reconstructed with the “ Σ method” using the variables [24]

$$y_\Sigma = \frac{\Sigma}{\Sigma + E'_e(1 - \cos \theta_e)}, \quad Q_\Sigma^2 = \frac{E_e'^2 \sin^2 \theta_e}{1 - y_\Sigma}. \quad (2.7)$$

The hadronic variables y_h and y_Σ are related according to

$$y_\Sigma = \frac{y_h}{1 + y_h - y_e} \quad (2.8)$$

and can be well measured down to low $y \simeq 0.004$.

The variable y_Σ is less sensitive to initial state radiation than y_h since the initial energy E_e in the denominator in equation 2.6 can be calculated using the total energy reconstructed in the detector which leads to equation 2.7. The precision of this method depends on the calorimeter sampling fluctuations which become important at low $P_{t,h}$, where $P_{t,h}$ is the total transverse momentum of the hadronic final state particles. The resolution $\delta y_h/y_h$ degrades $\propto 1/(1 - y)$, limiting the hadron method to low values of y .

Thus, the electron method and the hadronic method complement one another and extend to different regions of phase space. For the data analysis described in the next section, the kinematic reconstruction by means of the electron method is used for values $y > 0.15$, and for lower values the hadronic method is employed.

The redundancy of the kinematic reconstruction allow yet another method to be used based on angle measurements only. From the hadronic final state particles, an effective hadronic scattering angle θ_h can be derived which is defined as

$$\tan \frac{\theta_h}{2} = \frac{\Sigma}{P_{t,h}}, \quad (2.9)$$

In the naive quark parton model, θ_h defines the direction of the struck quark related to θ_e as

$$\tan \frac{\theta_h}{2} = \frac{y}{1 - y} \cdot \tan \frac{\theta_e}{2}. \quad (2.10)$$

This relation, together with the definition of y_e (equation 2.2), determines the scattered electron energy from θ_e and θ_h in the “double angle method” [25]. This method is essential for calibration purposes since the energy response of the detector can be compared to the double angle prediction.

2.3 Data Analysis with the H1 Detector

2.3.1 Datasets

In this work, datasets on the deep inelastic neutral current scattering cross section were analysed taken by the H1 collaboration in 1996 and 1997.

The data were taken in different samples:

- Sample H1 Main - data taken in the years 1996 and 1997 with luminosities of 4.5 pb^{-1} and 13.4 pb^{-1} , respectively. These two data sets are combined to provide the cross section measurement for Q^2 values from 15 GeV^2 to 150 GeV^2 and for $Q^2 = 12 \text{ GeV}^2$ at $y > 0.17$.
- Sample H1 MB - data taken in the autumn of 1997 during a two week period dedicated to the lower Q^2 region. The data from this special run with a luminosity of 1.8 pb^{-1} are used in the Q^2 range from 1.5 GeV^2 to 8.5 GeV^2 and for $Q^2 = 12 \text{ GeV}^2$ at low $y < 0.17$.

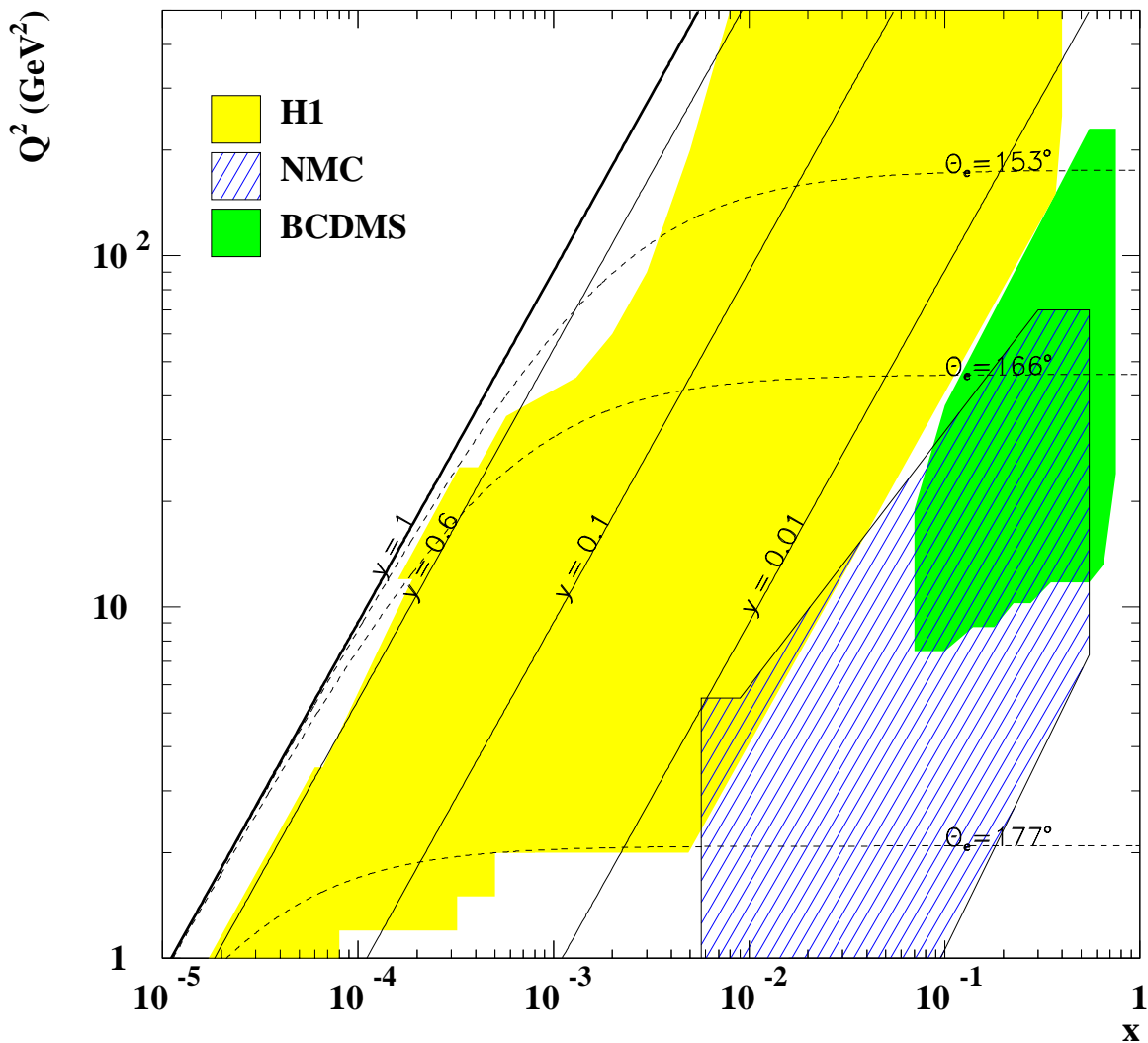


Figure 2.2: Kinematic plane Q^2 versus x covered by the H1 data taken in 1996 and 1997 as well as fixed target experiments. The region of SPACAL acceptance used in the data analysis is marked (dashed lines). The reduced cross section 1.7 is dominated by the structure function F_2 in the region $y < 0.6$ which is by far the largest part of the phase space covered. The region $y > 0.6$ for $Q^2 > 10 \text{ GeV}^2$ is explored with a dedicated trigger.

These datasets cover a region in $1.5 < Q^2 < 150 \text{ GeV}^2$ and $3 \cdot 10^{-5} < x < 0.25$ depicted in figure 2.2. Values of the inelasticity $y > 0.8$ were achieved for $Q^2 > 12 \text{ GeV}^2$ in a separate analysis based on a dedicated trigger sample with luminosities of 2.8 pb^{-1} obtained 1996 and 3.4 pb^{-1} in 1997 [26, 27].

The data analysis of this work was performed on the H1 MAIN and H1 MB data samples in the kinematic region $y < 0.8$. The results on the extracted double differential cross section measurement from the H1 MAIN dataset for $y < 0.15$ (Σ method) and the results from the H1 MB for $y > 0.15$ (electron method), limited to $y < 0.6$ for $Q^2 < 5 \text{ GeV}^2$, were published in [27].

2.3.2 Event Selection Strategy

DIS events at low Q^2 are identified with the final state electrons scattered in the backward calorimeter SPACAL of the H1 detector, covering scattering angles of ($153^\circ < \theta_e < 177^\circ$). According to equation 2.7, this limits the measurement to $Q^2 < 150 \text{ GeV}^2$.

This calorimeter is a lead-fibre spaghetti calorimeter with high energy resolution [28]

$$\frac{\sigma_E}{E} = \frac{7.5\%}{\sqrt{E[\text{GeV}]}} \oplus 1\%$$

and high transverse granularity. This allows an accurate energy measurement of the scattered electron as well as the distinction of electromagnetic from hadronic energy deposits by means of their respective lateral shower profile.

Electromagnetic energy deposits by neutral particles can be removed by requiring a signal in the track detectors in front of the calorimeter. Tracks of charged final state particles are recorded in the central track detector which allows to reconstruct the primary vertex of the interaction. Beam related background can thus be removed [29].

Longitudinal momentum conservation in neutral current DIS events constrains the variable $E - p_z$, summed over the final state particles,

$$E - p_z = \Sigma + E'_e(1 - \cos \theta_e) \quad (2.11)$$

to be approximately equal to $2E_e$. In radiative events a photon may carry a significant fraction of the $E - p_z$ sum. These events can be removed from the data sample by a suitable cut on $E - p_z$.

Figures 2.3 and 2.4 show the distributions for a second analysis [27] of the energy E' and polar angle θ_e of the scattered electron as well as the inelasticity y_h derived from hadronic variables for selected DIS events belonging to the two datasets H1 Main and H1 MB. The data are compared to a Monte Carlo Simulation and found to be well described.

These distributions also demonstrate the high statistical precision of the 1996 and 1997 data. The statistical error is $< 1\%$ in the bulk region of phase space. Thus, the experimental uncertainty on the cross section is dominated by the systematic uncertainties which are briefly discussed in the following.

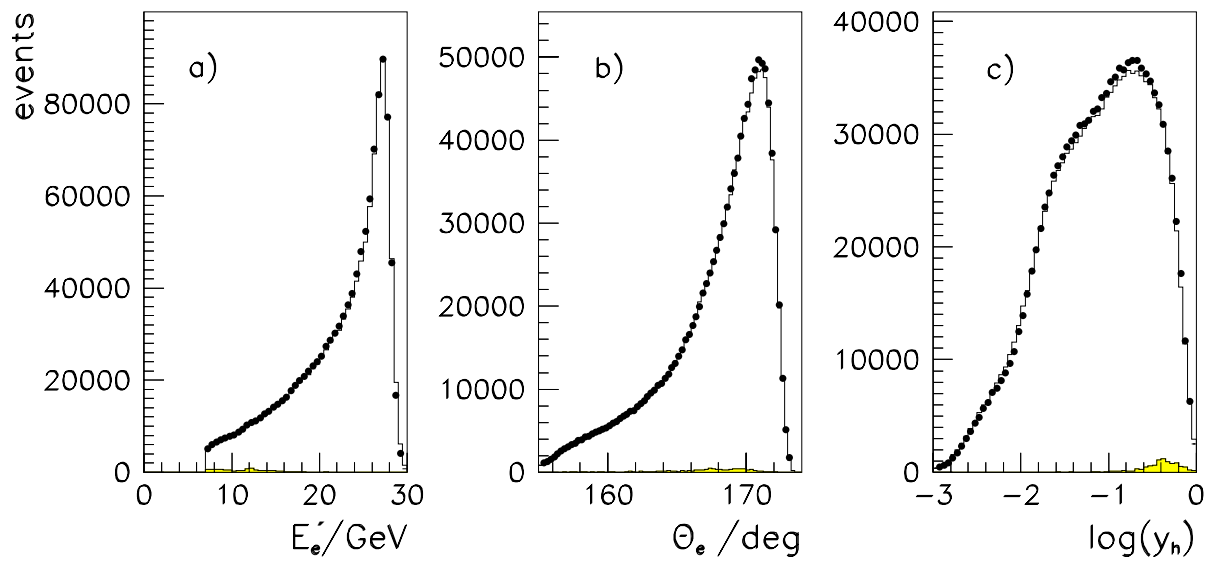


Figure 2.3: Distributions of a) the energy, b) the polar angle of the scattered electron, and c) y_h for the data sample *A* taken in 1996/97 (solid points). The histograms show the simulation of DIS and the small photoproduction background (shaded), normalised to the luminosity of the data.

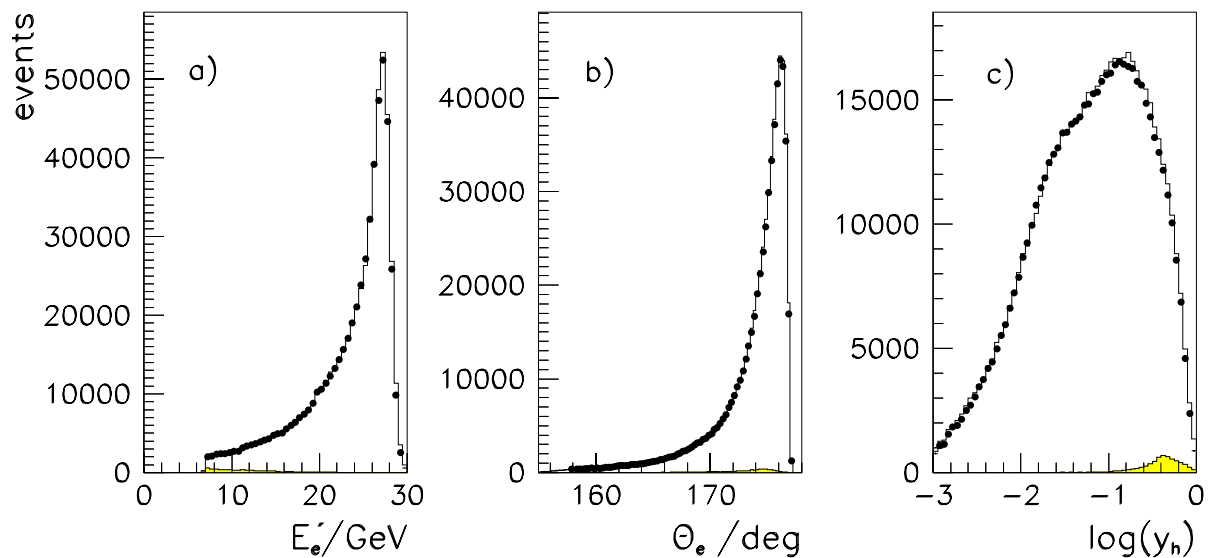


Figure 2.4: Distributions of a) the energy, b) the polar angle of the scattered electron, and c) y_h for the low Q^2 data sample *B* taken in 1997. The histograms represent the simulation of DIS and the small photoproduction background (shaded), normalised to the luminosity of the data.

2.3.3 Electromagnetic Energy Calibration

At low Q^2 the DIS events exhibit an accumulation at E'_e about the electron beam energy which is called the kinematic peak. This kinematic peculiarity serves as a high quality measure of the accuracy of the electromagnetic energy scale [30]. By using the energy reference scale provided by the double angle method, the calibration of the backward detector can be further improved [31] and resolution effects be understood.

The electromagnetic energy scale is accurate up to about 0.5% at high energies $E'_e \sim E_e$ and is known to be less precise $\sim 3\%$ at lower energies. This can be determined with QED Compton events [32, 33, 34].

The calorimeter resolution suffers from energy losses due to showering in the endflanges and electronics of the tracking devices in front of the backward calorimeter, see figure 2.5 for an illustration. The energy loss due to showering in the dead material was measured by the charge deposited in the backward drift chamber in front of the SPACAL and corrected for [34]. However, the impact of a degrading energy resolution on the y_e resolution at lower energies, corresponding to high y , is seen to be damped by a factor $(1 - 1/y)$, see equation 2.5. This allows a rather uniform precise determination of y or x in the range accessible to the electron method.

2.3.4 Photoproduction Background

At small energies electron misidentification becomes possible due to photoproduction background which causes hadrons or showering photons to fake genuine scattered electron signatures in the backward detectors. Apart from the highest y region, where data are used for background subtraction [31, 26] this background is subtracted on a statistical basis using a simulation program [35]. The normalisation of this simulation to a control sample taken from the data is only known to about 20% accuracy, which is the dominant source of uncertainty on the extracted cross section at high y .

2.3.5 Hadronic Energy Scale

The central electromagnetic and hadronic liquid argon calorimeter determines the inelasticity y_h or the $E - p_z$ of the event by reconstructing the hadronic energy and partially the scattering angle of hadrons. If tracks are measured in front of an active calorimeter cell by the central tracker, the calorimeter energy is masked and the momentum measurement of the central tracker is used instead in order to improve the hadronic final state reconstruction.

The calorimeter response is calibrated using the p_t balance between the scattered electron and the hadronic final state particles. The calibration method used is based on a Lagrangian minimisation which determines 128 calibration constants for 8 octants and 8 wheels in the electromagnetic and hadronic calorimeter [36].

At small energies corresponding to low y_h , the calorimeter noise contribution becomes sizeable. The noise is determined from the data and used in the simulation. This limits the measurement to y_h values larger than 0.002. In this region the hadronic final state disappears to an increasing extent in the forward direction.

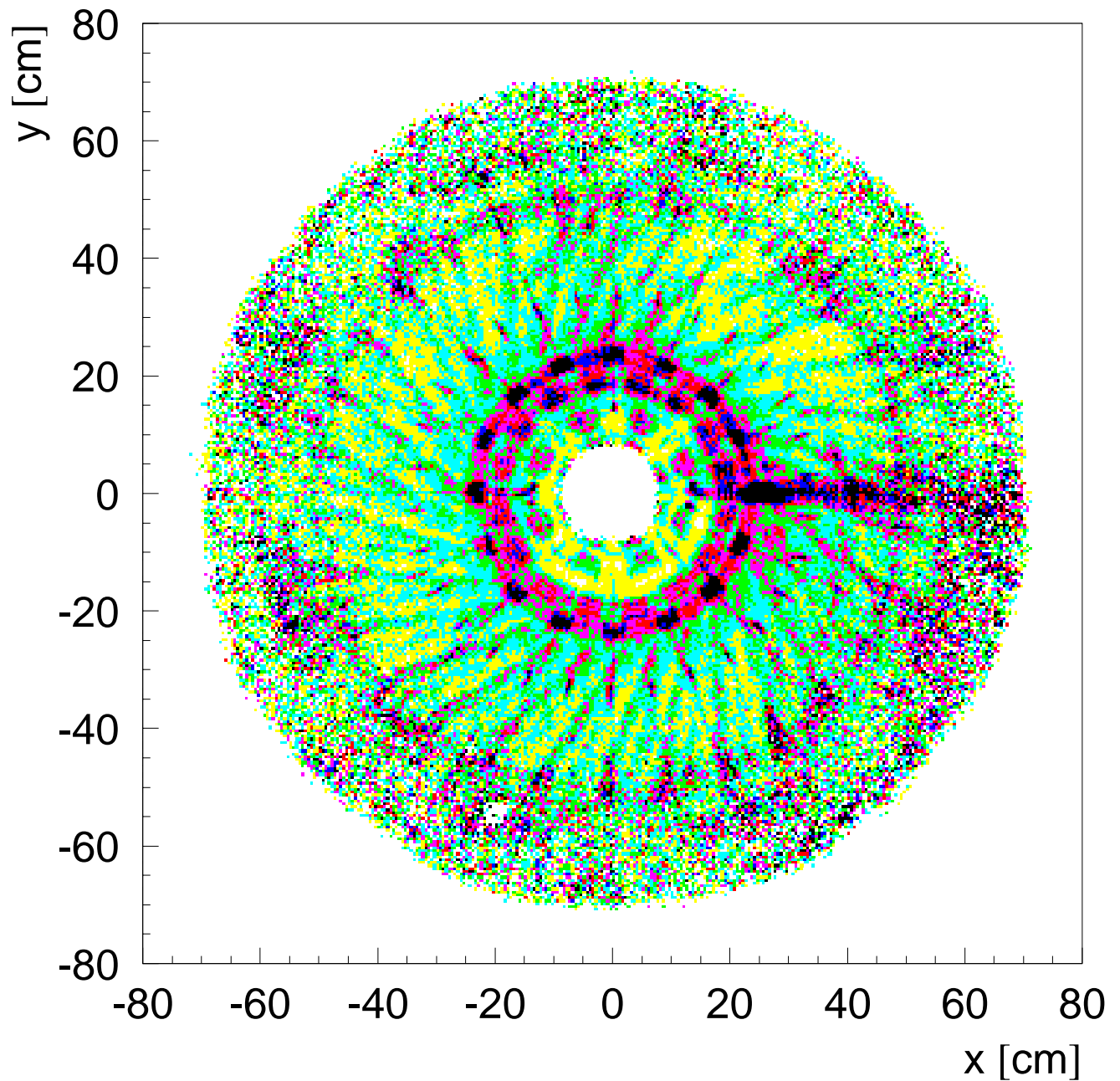


Figure 2.5: Visualisation of the dead material in front of the backward calorimeter SPACAL. Shown is the mean charge measured in the backward chamber in arbitrary units. Darker colours indicate high charge deposits. The most prominent 16 fold structure is due to readout electronics for the central inner proportional chamber CIP which is part of the central tracker of H1.

2.4 Systematic Errors

The uncertainties present in the variables E_e , θ_h , E_h , in the noise and the photoproduction background subtraction introduce point-to-point correlations between many data points. The impact of these correlated systematic error sources on the cross section measurement can be studied and estimated using a Monte-Carlo simulation.

The effect of the electromagnetic and hadronic energy scale uncertainties can be controlled by using the overconstrained kinematic reconstruction methods. Figure 2.6 shows an extraction of F_2 with the Σ and the electron method extended in the region where the resolutions of both methods are known to degrade. However, both extractions are seen to agree even in kinematic regions where one method is precise and the other degraded by resolution effects, respectively. This demonstrates that the energy scales are well understood.

Table 2.1 summarizes the correlated error sources and their impact on the measured cross section as determined by the Monte Carlo simulation. The uncorrelated errors are listed in [27]

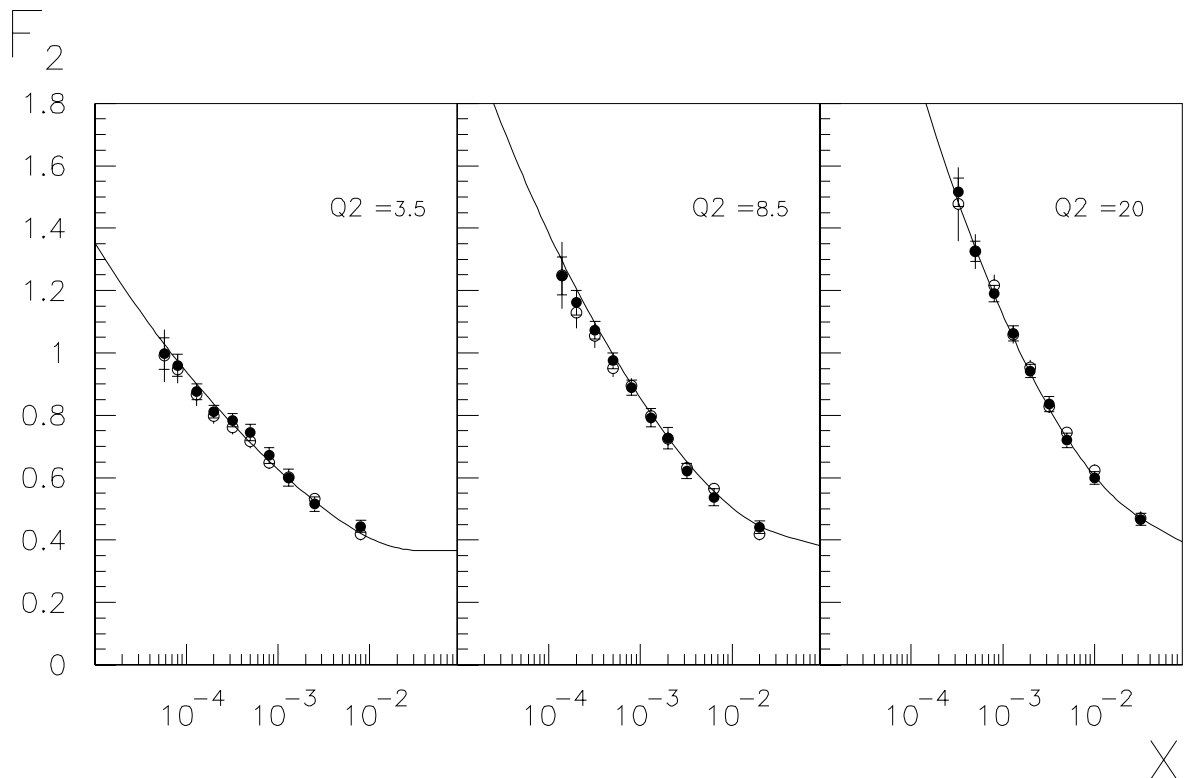


Figure 2.6: Comparison of the dependence of the structure function F_2 on x extracted with the electron (solid points) and the Σ method (open points) for different bins of Q^2 . Both methods have been extended in the region where their resolutions are known to degrade and miscalibrations would become visible.

source	size of uncertainty	typical cross section error [%]
scattered positron energy scale	0.3% at $E'_e \simeq 27.5$ GeV	1
	2.7% at $E'_e = 3$ GeV	2
scattered positron angle	0.3 mrad	0.5
hadronic energy scale in LAr	2%	2
LAr noise	25% of noise	max of 5 at lowest y
photoproduction background	20% of background	3 at large y

Table 2.1: Sources of correlated systematic errors and their typical effect on the cross section measurement accuracy.

Summarising this brief account, the cross section has been measured to within an accuracy of about 3% which represents an improvement of about 3 times over the 94 data. It is particularly gratifying to see that this data and the previous data agree well, see figure 2.7, because the backward apparatus of the H1 detector was completely exchanged in 1995. This vigorous upgrade program leads to an extension of the y range and to much improved precision in the kinematic reconstruction. The steady increase of the luminosity of HERA could thus be utilised to produce high precision datasets on the deep inelastic scattering cross section. The physics information contained in these data sets is explored in the following chapters.

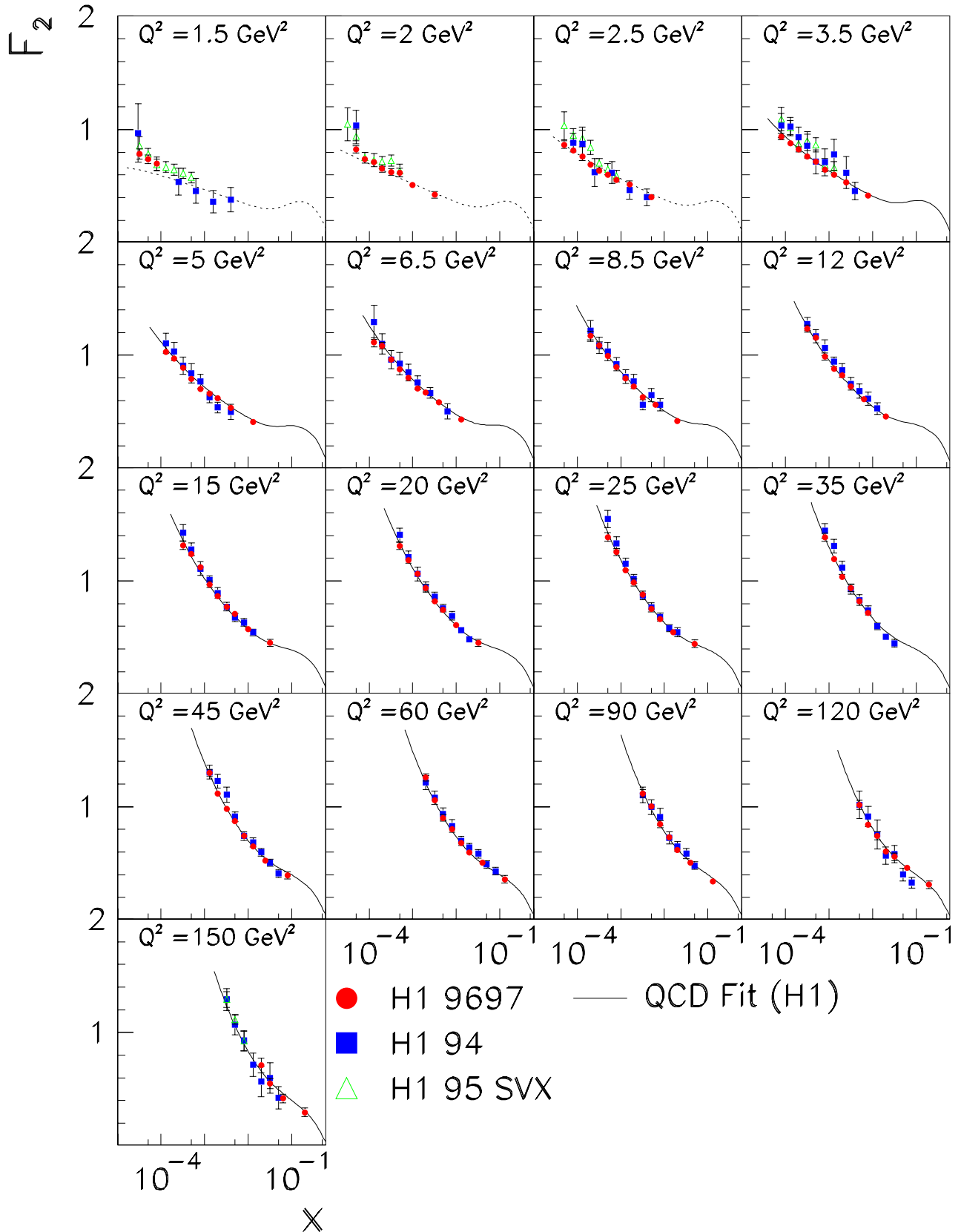


Figure 2.7: Measurement of the proton structure function F_2 for different datasets recorded by the H1 collaboration. Shown is the dependence of F_2 on x for different bins of Q^2 . The dataset discussed in this work is labeled H1 9697, the combination of the H1 MB and H1 Main datasets, see text.

Chapter 3

QCD Analysis Procedure

The accuracy of the inclusive cross section measurement at low x and Q^2 reached by the H1 experiment has allowed to perform a first simultaneous determination of the strong coupling constant α_s and of the gluon momentum distribution xg at low x . This requires an extremely careful QCD analysis to be performed which is the main goal of this work.

The predictions of the QCD evolution equations 1.29 and 1.30 are confronted with the reduced differential cross section measurements of the H1 low Q^2 data, discussed in the previous chapter, as well as with recent H1 data at high $Q^2 \geq 150 \text{ GeV}^2$ [37] from the same data taking period.

The guiding principles of the analysis are a use of a minimal number of datasets and fit parameters alongside a maximal exploitation of experimental knowledge on the uncertainties of the data with full error propagation to the determined values of α_s and xg . They therefore are complementary to the procedure applied in global fits [38, 39, 40] which aim for an almost complete determination of all parton momentum distribution functions in the nucleon using a maximum amount of available data. Global analyses have to address questions on the consistency of the various datasets [41] and have to deal with quite challenging error propagation problems [42, 43].

3.1 Analysis Procedure

3.1.1 Singlet and Non-Singlet Evolution of F_2

The gluon xg and quark flavour singlet Σ distributions are dynamically coupled via the DGLAP equations 1.30 whereas quark flavour non-singlets evolve independently of xg [44]. Solving the evolution equations thus requires to specify the gluon, singlet and non-singlet parton momentum distribution functions as boundary conditions at an input scale Q_0^2 .

It is instructive to identify the singlet and non-singlet contributions to F_2 in the leading order QCD formalism with Q^2 dependent quark distribution functions. In the quark-parton model, the proton structure function F_2 is given by a sum of quark and anti-quark momentum distribution

functions, see equation 1.19. The flavour singlet parton momentum distribution function Σ is given as

$$\Sigma(x, Q^2) = \sum_q [q(x, Q^2) + \bar{q}(x, Q^2)]. \quad (3.1)$$

Flavour non-singlet parton momentum distribution functions can be defined as

$$\Delta_{ij}(x, Q^2) = q_i(x, Q^2) - q_j(x, Q^2) \quad (3.2)$$

$$\bar{\Delta}_{ij}(x, Q^2) = \bar{q}_i(x, Q^2) - \bar{q}_j(x, Q^2) \quad (3.3)$$

as well as linear combinations thereof.

For simplicity, consider a four quark flavour model with massless (u, d, s, c) quarks, and let $U = u + \bar{u} + c + \bar{c}$ and $D = d + \bar{d} + s + \bar{s}$, where the functional dependence on (x, Q^2) is implied but suppressed for clarity in the following. Then, the quark flavour singlet function is given as $\Sigma = U + D$, while $\Delta = U - D$ defines a flavour non-singlet quark distribution function, yielding the decompositions

$$F_2 = \frac{4}{9}xU + \frac{1}{9}xD \quad (3.4)$$

$$F_2 = \frac{5}{18}x\Sigma + \frac{1}{6}x\Delta \quad (3.5)$$

for the proton structure function F_2 . Thus, F_2 is determined by two independent combinations of quark distribution functions which define the singlet and non-singlet sector of the DGLAP equations.

Traditionally, QCD analyses based on the DGLAP equations make use of both lepton-proton and lepton-deuteron data [45, 46, 47, 48, 49] in order to separate the non-singlet and singlet evolution, and also to determine the parton distributions of up and down quarks simultaneously. This can be illustrated as follows.

Invoking isospin symmetry, the deuteron structure function F_2^d , disregarding nuclear corrections, is given as

$$F_2^d = \frac{5}{18}x\Sigma + \frac{1}{6}(\Delta - \Delta^+) \quad (3.6)$$

with $\Delta^+ = (u + \bar{u}) - (d + \bar{d})$ defining an additional non-singlet parton momentum distribution function which is sensitive to the up and down quark distribution functions. Assuming an isospin symmetric up and down quark sea, one obtains $\Delta^+ = u_v - d_v$ which represents another constraint on the valence quark distributions. In such fits, the quark counting rules can therefore separately be enforced on the valence up and down quark distributions.

Furthermore, since $\Delta^+ = \Delta - (c + \bar{c}) + (s + \bar{s})$, it can be seen that F_2^d is an almost pure singlet function apart from a small charm and strange quark sea contribution. By adding deuteron and proton structure function data in the fit, the singlet and non-singlet dynamics can thus be separated.

Since precise data over a wide (Q^2, x) range are now available, however, which represent a strong constraint on the evolution of Σ , Δ and xg , a QCD analysis without using deuteron data is attempted here. This will not lead to flavour separated parton distribution, but it will be shown to be adequate to the goal of measuring α_s and xg . A notable advantage of such an approach is its independence of corrections for nuclear binding effects in the deuteron (shadowing, target mass and Fermi motion). These corrections imply an additional uncertainty to the fit results due to the use of nuclear models [50, 51]. Furthermore, the constraint of the present data on the u and d quark distributions is still limited in the valence region, see figure 3.1.

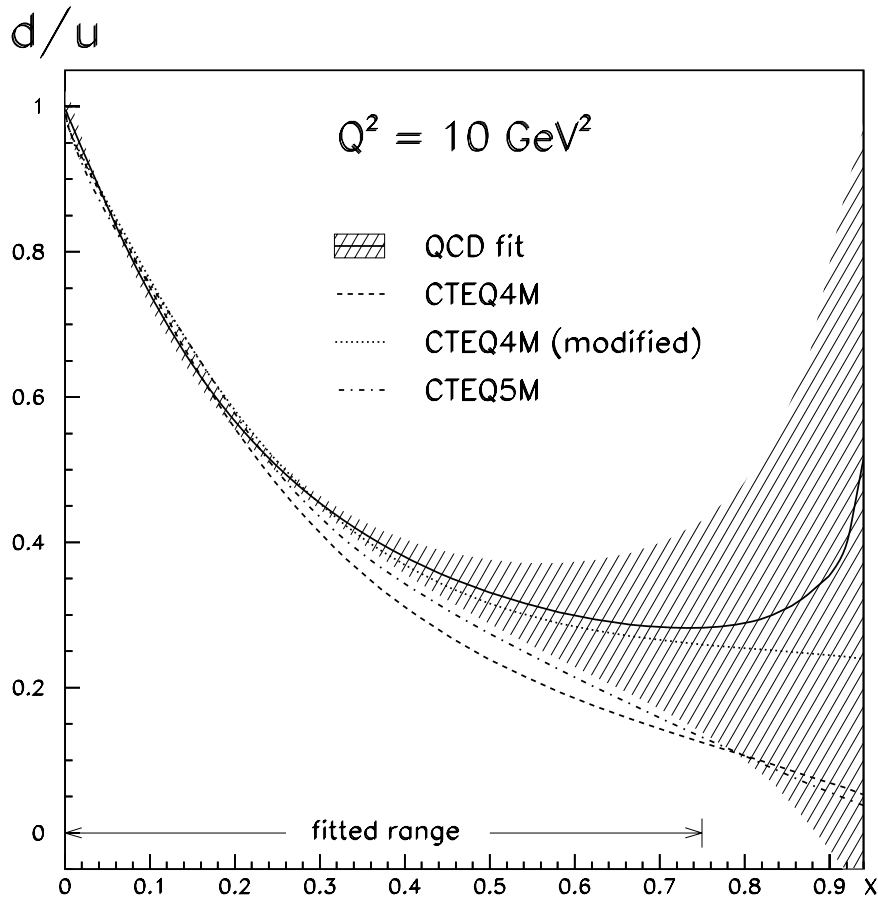


Figure 3.1: The ratio of the up and down quark distribution and its uncertainty. At high x , d/u is essentially still undetermined [47].

3.2 Flavour Decomposition

In this analysis, an attempt is made to use proton target data only. Thus the up and down valence quark distributions cannot be disentangled, but the valence quark counting rules may still be applied to an effective valence quark distribution. This requires a suitably chosen flavour decomposition of F_2 in singlet and non-singlet quark distributions.

3.2.1 Simplified Ansatz

In the present analysis, the sum in equation 1.19 extends only over up, down and strange (u, d, s) quarks. The charm and beauty contributions are treated differently due to heavy quark mass effects, see chapter 4. At low x , about 20% of the inclusive cross section is due to charm production, dominated by the photon-gluon fusion process, whereas the beauty contribution is less than 1%. These heavy flavour contributions are added using NLO QCD calculations [52] in the on-mass shell renormalisation scheme using $m_c = 1.4 \text{ GeV}$ and $m_b = 4.5 \text{ GeV}$.

For the three light flavours, F_2 then decomposes in singlet and non-singlet quark distributions as

$$F_2 = \frac{2}{9} \cdot x\Sigma + \frac{1}{3} \cdot x\Delta \quad (3.7)$$

with $\Delta = (2U - D)/3$ defining a non-singlet distribution.

Now a suitable projection of F_2 into two independent quark distribution functions V and A which allow the use of the valence quark counting rule is found according to

$$F_2 = \frac{1}{3}xV + \frac{11}{9}xA. \quad (3.8)$$

Assuming for simplicity $s + \bar{s} = \frac{1}{2}(\bar{u} + \bar{d})$, the functions V and A are related to the u-type $U = u + \bar{u}$ and d-type $D = d + \bar{d} + s + \bar{s}$ quark distributions as

$$U = \frac{2}{3}V + 2A \quad (3.9)$$

and

$$D = \frac{1}{3}V + 3A. \quad (3.10)$$

The inverse relations defining V and A are

$$V = \frac{3}{4}(3U - 2D) = \frac{9}{4}u_v - \frac{3}{2}d_v + \frac{9}{2}\bar{u} - 3(\bar{d} + \bar{s}) \xrightarrow{\bar{u}=\bar{d}} \frac{3}{4}(3u_v - 2d_v) \quad (3.11)$$

and

$$A = \frac{1}{4}(2D - U) = \bar{d} + \bar{s} - \frac{1}{2}\bar{u} - \frac{1}{4}u_v + \frac{1}{2}d_v \xrightarrow{\bar{u}=\bar{d}} \bar{u} - \frac{1}{4}(u_v - 2d_v). \quad (3.12)$$

Assuming roughly $u_v = 2d_v$ for illustration one finds $V \approx \frac{3}{2}u_v$ and $A \approx \bar{u}$, i.e. V defines a valence type distribution while A is dominated by the sea quarks and determines the low x behaviour of F_2 .

An advantage of this decomposition is that V is constrained by the relation

$$\int_0^1 V dx = 3, \quad (3.13)$$

i.e. although only proton target data are used the quark counting rule can be employed. Another constraint is provided by the momentum sum rule

$$\int_0^1 (xg + \Sigma) dx = 1. \quad (3.14)$$

This ansatz is generalised in the following section to account for the observed small deviations of the strange [53] and antiquark [54] distributions from the conventional assumptions about the sea.

3.2.2 Generalised Flavour Decomposition of F_2

Recent measurements of Drell-Yan muon pair production at the Tevatron [54] have established a difference between the \bar{u} and \bar{d} distributions which was first observed in [55]. Charged current neutrino-nucleon experiments determined the relative amount of strange quarks in the nucleon sea to be

$$s + \bar{s} = \left(\frac{1}{2} + \epsilon\right) \cdot (\bar{u} + \bar{d}), \quad (3.15)$$

with a recent value of $\epsilon = -0.08$ [56]. The evolution of $s + \bar{s}$ in DGLAP QCD is found to yield a linear dependence of ϵ on $\ln Q^2$ which is used to extrapolate the NuTeV result obtained at 16 GeV^2 , to $Q^2 = Q_0^2$. Both results have been accounted for by modifying equation 3.10 according to

$$D = \frac{1}{3}V + kA, \quad (3.16)$$

which, using equation 3.9, results in

$$V = \frac{3}{2} \cdot \frac{1}{k-1} (kU - 2D) \quad (3.17)$$

and $\Sigma = V + A \cdot (2+k)$. Choosing $k = 3 + 2\epsilon$ can be shown to remove the strange contribution to the function V yielding

$$V = \frac{3}{4} \cdot \frac{1}{1+\epsilon} [(3+2\epsilon)u_V - 2d_V + (5+2\epsilon)(\bar{u} - \bar{d})], \quad (3.18)$$

which coincides with equation 3.11 for $\epsilon = 0$ and $\bar{u} = \bar{d}$. Because the integral $\delta = \int(\bar{u} - \bar{d})dx$ is finite¹, this choice of k allows the counting rule constraint (equation 3.13) to be maintained as

$$\int_0^1 V dx = 3 + \delta \cdot \frac{3}{4} \cdot \frac{5 + 2\epsilon}{1 + \epsilon} = v(\epsilon, \delta). \quad (3.19)$$

If this constraint is released in a fit to the H1 data, a value of $\int V dx = 2.24 \pm 0.13(\text{exp})$ is obtained instead of about 2.5 following from equation 3.19. The modified expression for the A function in terms of quark distributions becomes

$$A = \frac{1}{4} \cdot \frac{1}{1 + \epsilon} [4\bar{u} - (u_V - 2d_V) - 5(\bar{u} - \bar{d}) + 2\epsilon(\bar{u} + \bar{d})]. \quad (3.20)$$

For the naive assumptions $\epsilon = 0$ and $\bar{u} = \bar{d}$ this yields the approximate relations on the right side of equations 3.11 and 3.12 and $A \simeq \bar{u}$ at low $x < 0.1$. In the analysis these generalised expressions are used for V , its integral and A .

3.3 Parameterisation

The DGLAP equations do not predict the x -dependence of the parton distribution functions. Therefore, the x -dependence has to be parameterised at a given input scale Q_0^2 with an a priori unknown functional form. On parameterising the parton momentum distribution functions, a compromise has to be found between the flexibility of the parameterisation and the stability of the fit. If too few parameters or a wrong functional dependence are used, the fit result will necessarily be biased. Such a bias will be most pronounced at low Q^2 close to the input scale and will be 'washed out' by the DGLAP evolution at a higher Q^2 . This is demonstrated in figure 3.2.

If too many parameters are given, unconstrained parameters will degenerate and destabilize the fit. Unfortunately, in the absence of unlimited computer power and the mathematical means to explore the full functional space, the ansatz of the parameterisations remains a heuristic, non-rigorous procedure. Our choice is guided by reasonable physics assumptions and it is shown that the number of parameters can be limited by studying the behaviour of the χ^2 function with respect to adding or removing individual parameters.

3.3.1 Parameterisation Ansatz

Arguments from outside the DGLAP formalism [58] suggest that terms like

$$xq = a_q x^{b_q} (1 - x)^{c_q} \quad (3.21)$$

should be present in all parton momentum distribution functions.

¹The most accurate measurement of $\int_0^1 (\bar{u} - \bar{d}) dx$ has been performed by the E866/NuSea Collaboration [54] which obtained a value of -0.118 ± 0.011 at $\langle Q^2 \rangle = 54 \text{ GeV}^2$.

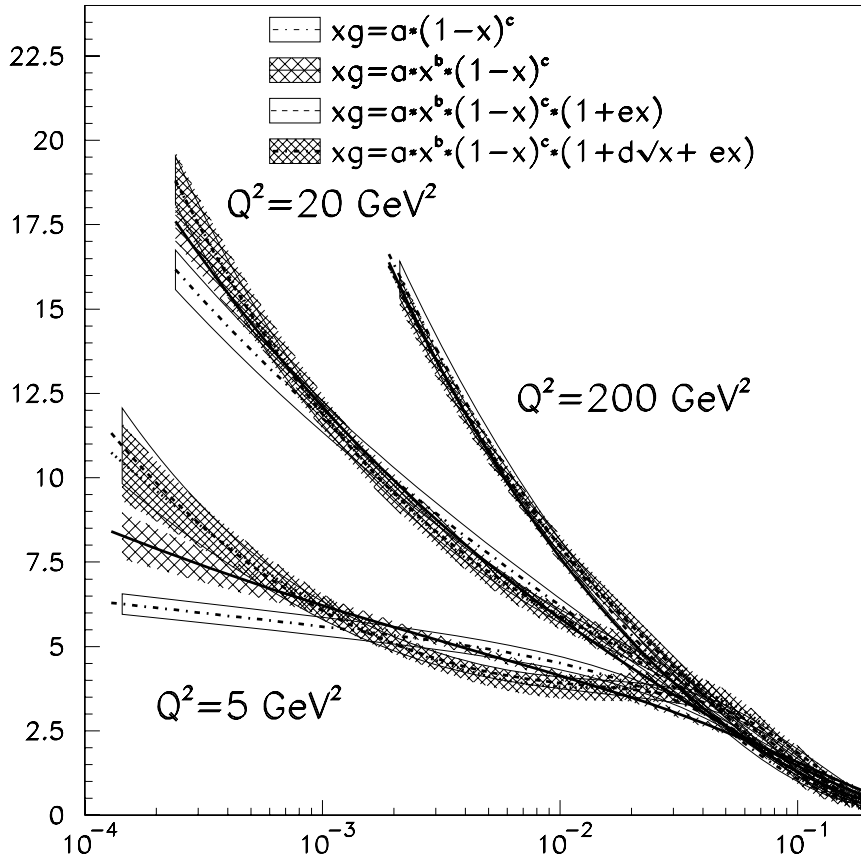


Figure 3.2: gluon distribution shown at different scales Q^2 from QCD fits based on different input parameterisations. Due to evolution effects, the differences between the parameterisations diminish with higher scales.

The a parameter is fixed by the counting rules, the parameters b and c can be guessed from the expected behaviour of the parton distributions in the limits $x \rightarrow 0$ and $x \rightarrow 1$ and are associated with the small- x Regge behaviour and large- x valence counting rules, respectively [57, 58].

With increased precision and coverage of the x -range, it is obvious that this three parameter ansatz needs to be extended to model the observed x -dependence of F_2 .

In this analysis, parameterisations are based on the MRST ansatz² where xq , equation 3.21, is multiplied by a term $(1 + d\sqrt{x} + ex)$. While this ansatz provides enough flexibility for the parton momentum distribution functions themselves, this does not necessarily hold for linear combinations of parton momentum distribution functions like the A and V distribution described above. An extension of the MRST-type parameterisation was therefore suggested and higher powers of

²A similar test described below was performed based on the CTEQ parameterisation ansatz, using a term $1 + dx^e$ to be multiplied on equation 3.21. This ansatz has the benefit of intrinsic positivity of the parton momentum distribution functions but is discounted on the basis of much worse χ^2 for the given datasets in this analysis. It is thus not considered any further.

\sqrt{x} are included. The most general ansatz considered in this analysis is

$$xq = a_q x^{b_q} (1-x)^{c_q} [1 + d_q \sqrt{x} + e_q x + h_q x^{3/2} + f_q x^2] \quad (3.22)$$

Using these parameterisations, a functional space is spanned as input for the DGLAP evolution with the input scale Q_0^2 being an additional parameter. A change in the input scale in general produces a different functional space, i.e. generally affects the solution of the DGLAP evolution.

3.3.2 Choice of Parameterisations

The functions A , V are linear combinations of quark distribution functions. Thus a systematic study including the gluon distribution is performed to identify an optimum parameterisation for A , V and xg . This regards the functional shape and the number of parameters in equation 3.22, but the optimal parameterisation is also dependent on the data sets under study since the degree of precision of data, e.g. in the high x region, determines how detailed the high x shape of F_2 has to be parameterised. Yet, in order to allow for up to .e.g. 7 parameters per input distribution function, 4096 different parameterisation combinations would have to be considered which is computationally prohibitive. Therefore, only parameterisations are considered which are flexible enough to accommodate the global fit results which provide individual parton momentum distribution functions. The CTEQ, MRST and GRV parton momentum distribution function sets are then used to construct the A and V distributions at $Q_0^2 = 4 \text{ GeV}^2$. These distributions are then re-fit with parameterisations of increasing flexibility using an arbitrarily chosen error band. This provides initial information how V and A may be parameterised. The final choice is then derived from fits to data, see below.

V distribution

Fig. 3.3 shows a comparison of different parameterisations with the V distribution based on MRST parton momentum distribution functions. Only parameterisations with more than one high x parameter can successfully describe the V distribution, while adding more than two parameters does not significantly improve the description. Similar results are found using the CTEQ and GRV parton momentum distribution function sets, i.e. a parameterisation

$$xV = a_V x^{b_V} (1-x)^{c_V} [1 + d_V \sqrt{x} + e_V x] \quad (3.23)$$

is chosen for all fits presented in this analysis.

A distribution

Fig. 3.4 displays a similar study for the A distribution. The best description is obtained using two or more high x parameters. With two or less parameters, details of the high x behaviour of A are not correctly described. However, the small negative bump at $x > 0.2$ has its origin in

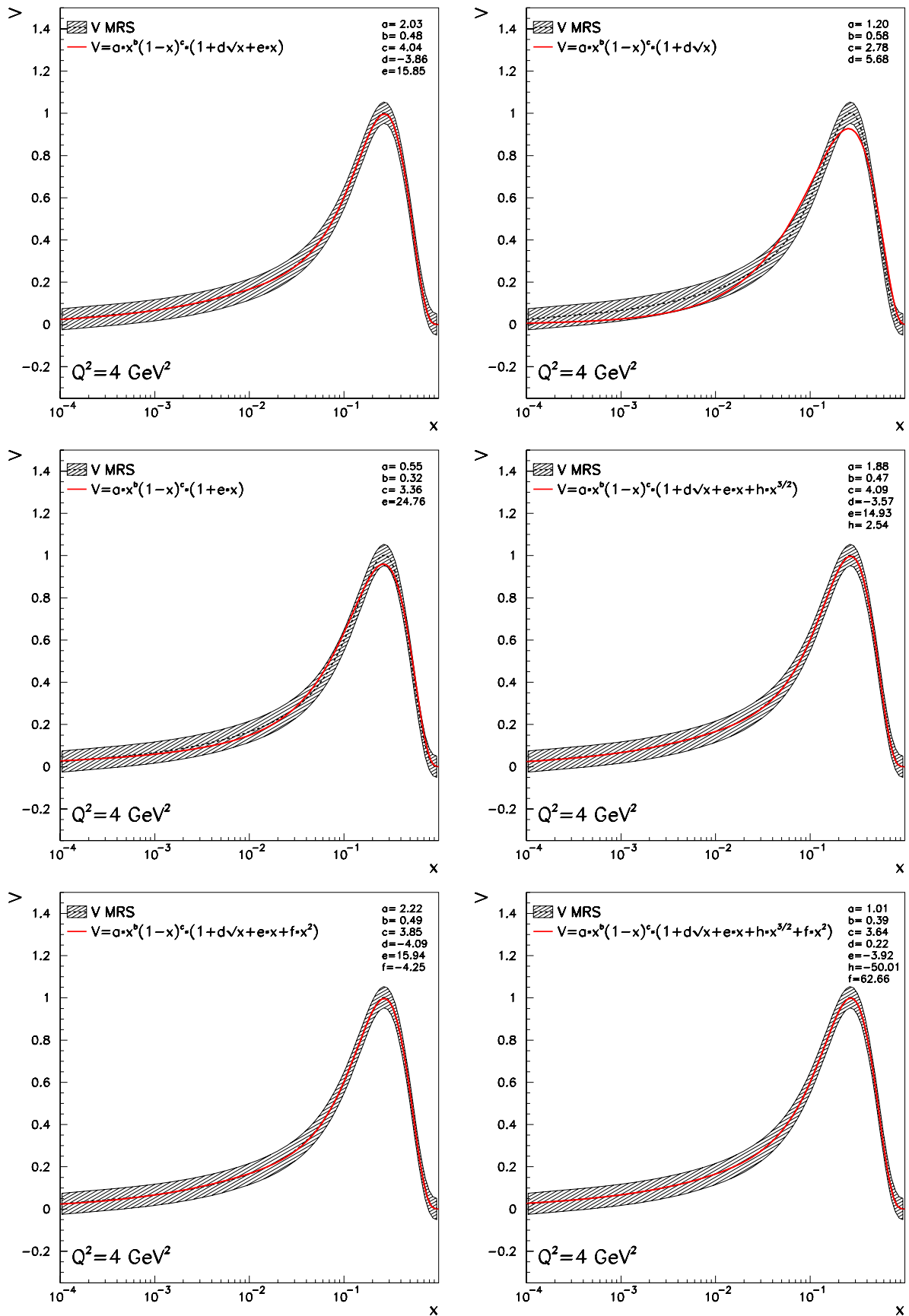


Figure 3.3: Fits of the V distribution calculated with MRST parton distribution functions using different parameterisations.

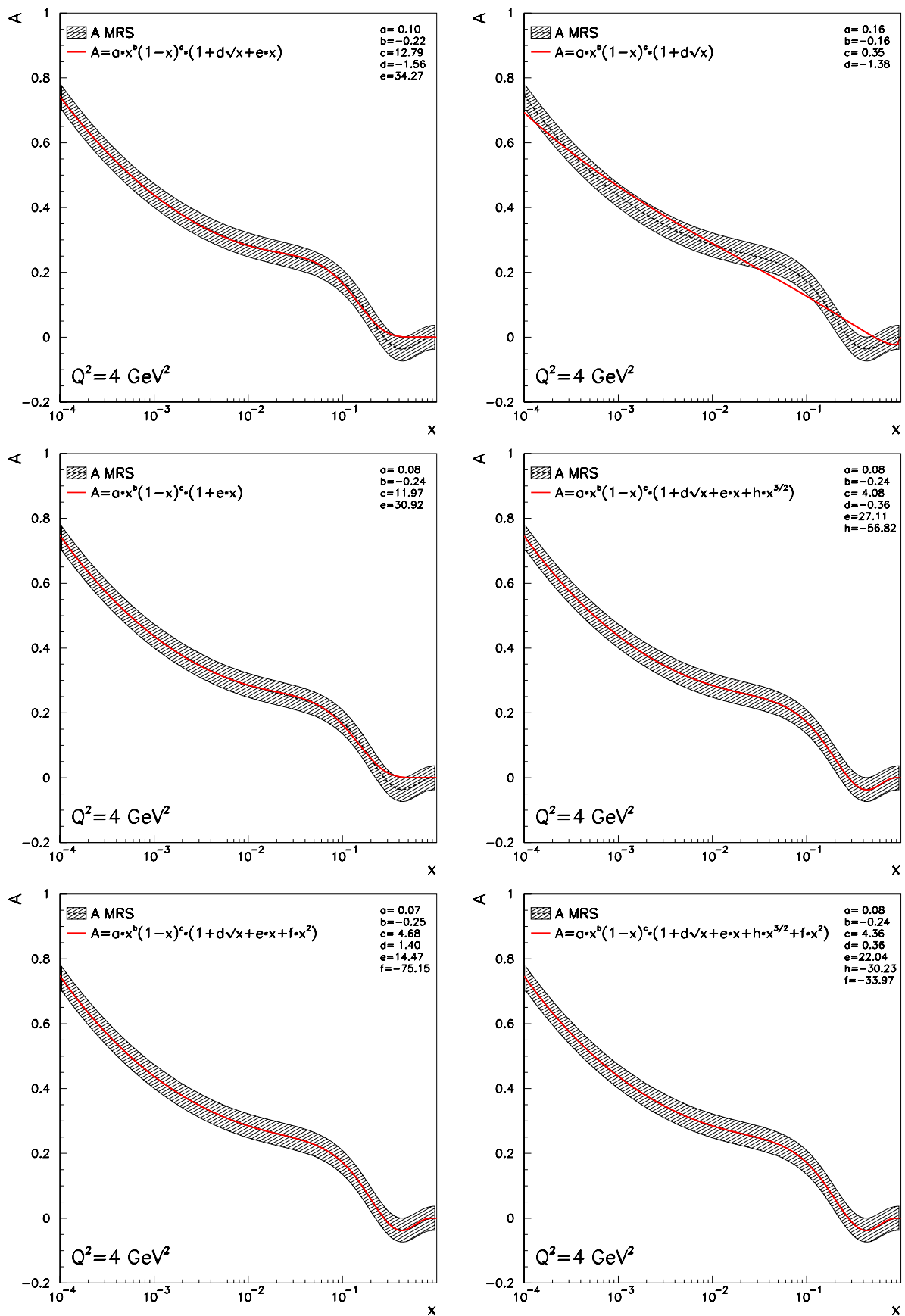


Figure 3.4: Fits of the A distribution calculated with MRST parton distribution functions using different parameterisations.

the difference of the valence quark distributions, see equation 3.12 with $u_v > 2d_v$ at $x \approx 0.3$. Such a behaviour requires the presence of three additional parameters d, e and h or f in order to be reproduced correctly. At the present level of accuracy, the data do not require the presence of more than d and e , see below. So parameterisations with a flat behaviour at $x > 0.2$ have to be taken further into account as well.

xg distribution

The gluon distribution is of particular interest because it dominates particle production cross sections at low x . In NLO QCD the “twist-2” gluon distribution has a valence like shape near $Q^2 \approx 1\text{GeV}^2$ and thus vanishes at low x as is demonstrated in figure 3.5 a). This behaviour of the gluon at low scales has been observed previously [38, 59, 60].

In figure 3.5 b) one finds that the singlet distribution for $Q^2 \simeq 1\text{GeV}^2$ rises. In this Q^2 range in NLO QCD the observed rise of F_2 at low x is not due to xg but rather due to the sea quarks. With rising Q^2 this behaviour changes, i.e. the gluon contribution to the evolution equations dominates over the sea quark contribution.

At low x , the proton structure in the DIS region is thus determined by the QCD vacuum. For $x = 0.07$ the gluon distribution is nearly independent of Q^2 which likely is a reflection of the interplay of the gluon-singlet dynamics in the region of scaling where $(\partial F_2(x, Q^2)/\partial \ln Q^2)_x$ is about zero. For the singlet distribution this is seen at $x = 0.1$.

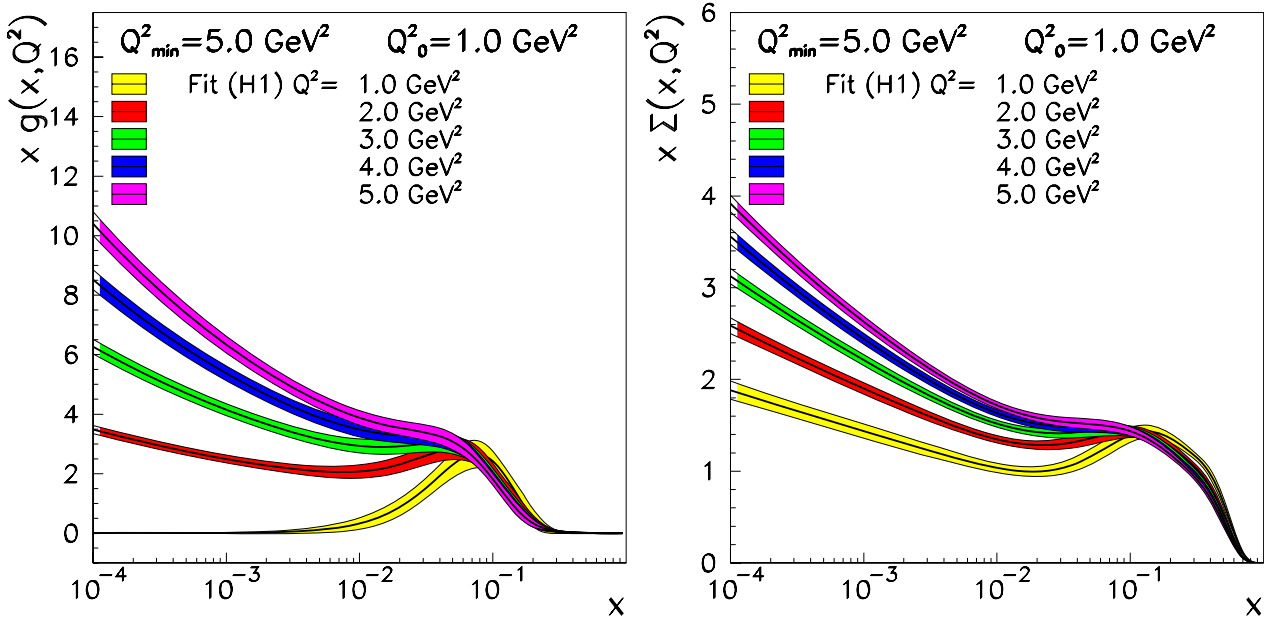


Figure 3.5: Evolution of the (a) gluon distribution xg and the (b) singlet distribution Σ .

The validity of extracting a parton distribution at scales as low as $Q^2 \simeq 1 \text{ GeV}^2$ is however a matter of debate since the perturbative expansion parameter α_s at $Q^2 \sim 1 \text{ GeV}^2$ is about 0.4. Results can be sensitive of whether the evolution is technically performed ‘forward’ ($Q_0^2 < Q_{\min}^2$) or ‘backward’ ($Q_0^2 > Q_{\min}^2$) as described in figure 3.6 and in the latter case xg can even become

negative, clearly in contradiction to the probability distribution interpretation of the parton momentum distribution functions. Because of these problems, fits were extended to data with $Q^2 \simeq 1 \text{ GeV}^2$ for technical applications like the reweighting of simulated events to the experimental cross section, but the physics conclusions were obtained from fits starting at larger $Q^2 \geq 3.5 \text{ GeV}^2$.

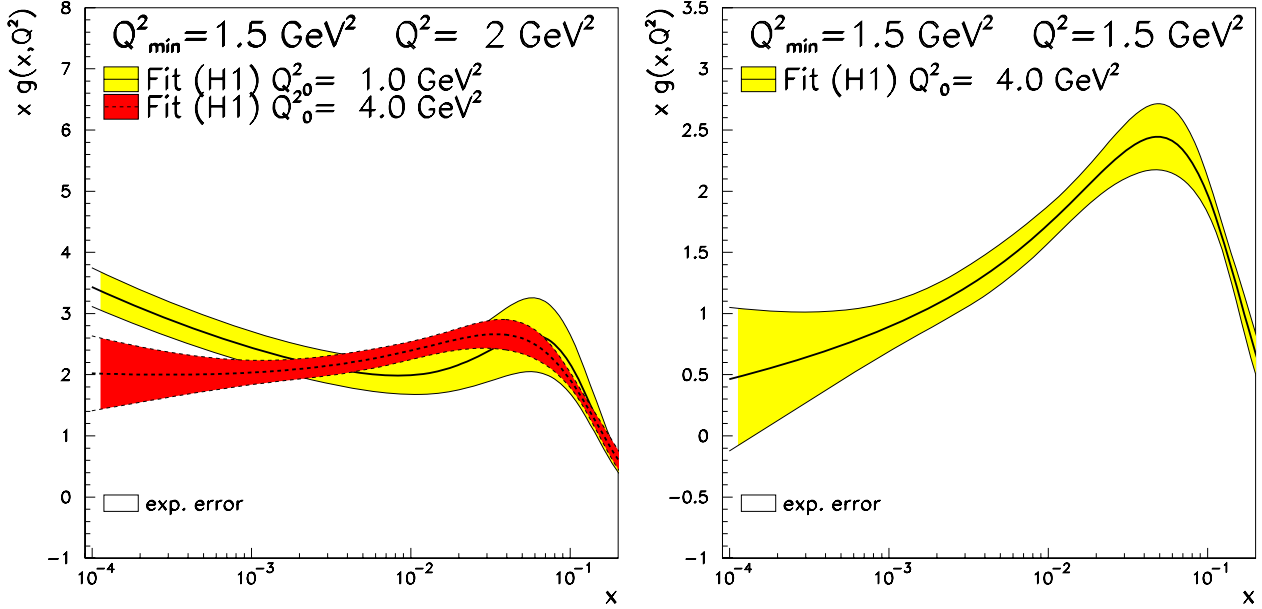


Figure 3.6: a) Gluon Distribution shown at a scale of $Q^2 = 2 \text{ GeV}^2$ for forward (solid) and backward (dashed) evolution. b) At low scales $Q^2 \simeq 1 \text{ GeV}^2$, the gluon behaves valence like and in the case of backward evolution can even become negative.

It is interesting to recall that the dynamical parton procedure suggested in [62] parameterises the input parton distributions at even lower scales of $Q_0^2 \simeq 0.4 \text{ GeV}^2$. Thus the region of applicability of perturbative QCD, $Q^2 > 1 \text{ GeV}^2$ is far away from the chosen starting point of the evolution. This ansatz leads to a rather successful prediction of the rise of F_2 towards low x , prior to the first measurements at HERA.

As perturbative QCD fits are technically successful down to such low scales it is desirable for the xg parameterisation to be flexible enough in order to account for the strong variation from a valence like shape at around $Q^2 \simeq 1 \text{ GeV}^2$ up to a nearly monotonous rising shape around $Q^2 \simeq 4 \text{ GeV}^2$. Figure 3.7 shows that the 3 parameter ansatz of equation 3.21 can accommodate this variation, but as will be shown in the next section, at the expense of a rather strong dependence on the input scale Q_0^2 and an unfavourable χ^2 of the fit.

3.3.3 Input Scale Dependence and χ^2 Saturation

Table 3.1 summarises the eight combinations of parameterisations for the xg and A distributions considered for the following analyses.

The parameterisation for the central fit to the H1 data is selected using the optimum χ^2 of the fit requiring stability of the fit towards a variation of the input scale Q_0^2 and of the lowest Q_{min}^2 of

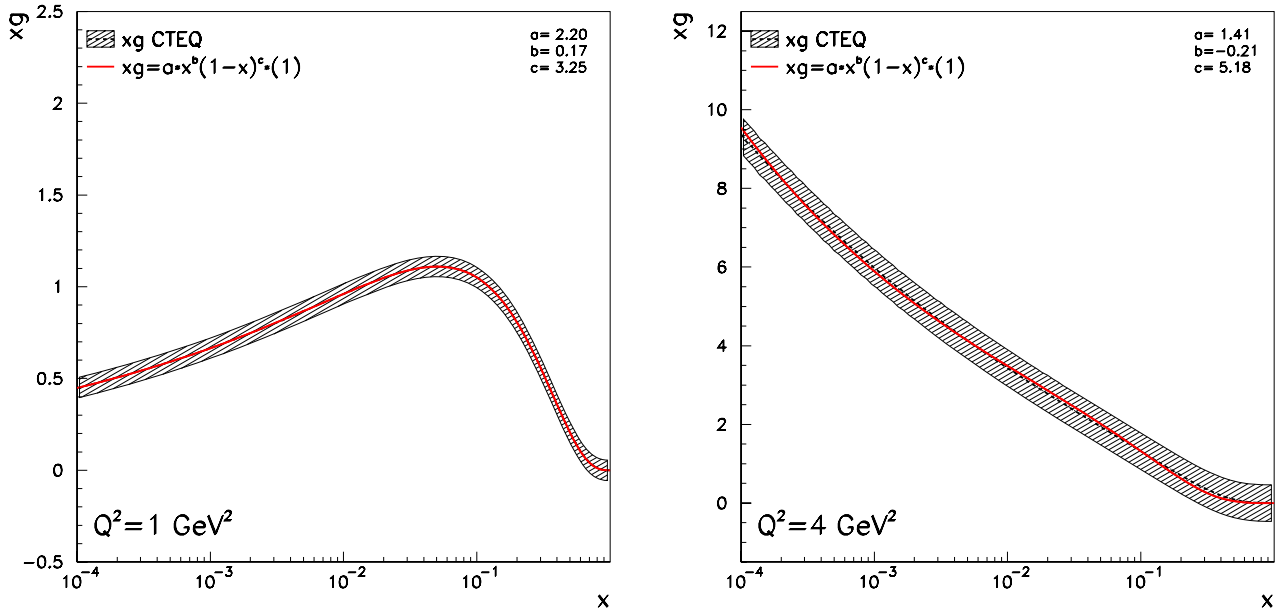


Figure 3.7: Fit of a three parameter ansatz according to equation 3.21 to the gluon distribution xg based on the CTEQ parton momentum distribution function set at (a) $Q^2 = 1 \text{ GeV}^2$ and (b) $Q^2 = 4 \text{ GeV}^2$.

data points entering the fit. In order to achieve this goal parameters are added in the xg and A distribution until addition of a further parameter achieves saturation, i.e. the χ^2 improves by just about one unit when adding an additional degree of freedom. For each parameter set, χ^2 was studied as a function of Q_0^2, Q_{min}^2 and for part of the analysis also of $\alpha_s(M_Z^2)$.

type	gluon	A
CP1	$1 + ex$	$1 + ex$
CP2	$1 + d\sqrt{x} + ex$	$1 + ex$
CP3	$1 + ex$	$1 + d\sqrt{x} + ex$
CP4	$1 + d\sqrt{x} + ex$	$1 + d\sqrt{x} + ex$
CP5	$1 + ex$	$1 + ex + fx^2$
CP6	$1 + d\sqrt{x} + ex$	$1 + ex + fx^2$
CP7	$1 + ex$	$1 + d\sqrt{x} + ex + fx^2$
CP8	$1 + d\sqrt{x} + ex$	$1 + d\sqrt{x} + ex + fx^2$

Table 3.1: Types of parameterisations of the xg and A distributions at the initial scale Q_0^2 . The fit to H1 data only uses the parameterisation CP3, while the fit to H1 and BCDMS data uses CP4, see text.

Figure 3.8 illustrates this procedure. The three parameter fit based on a three parameter gluon distribution (equation 3.21) clearly results in a strong dependence of χ^2 on the input scale. The ‘correct’ value of the input scale is not predicted by theory, but this dependence indicates that the parameterisation is not flexible enough and any non-optimal choice of the input scale will likely cause a bias in the resulting gluon distribution at higher scales.

Figure 3.10 a)-c) illustrates this dependence of the fit result at a scale of $Q^2 = 5 \text{ GeV}^2$ for fits with gluon parameterisations with 3 up to 5 parameters. Figure 3.10 d) compares the gluon

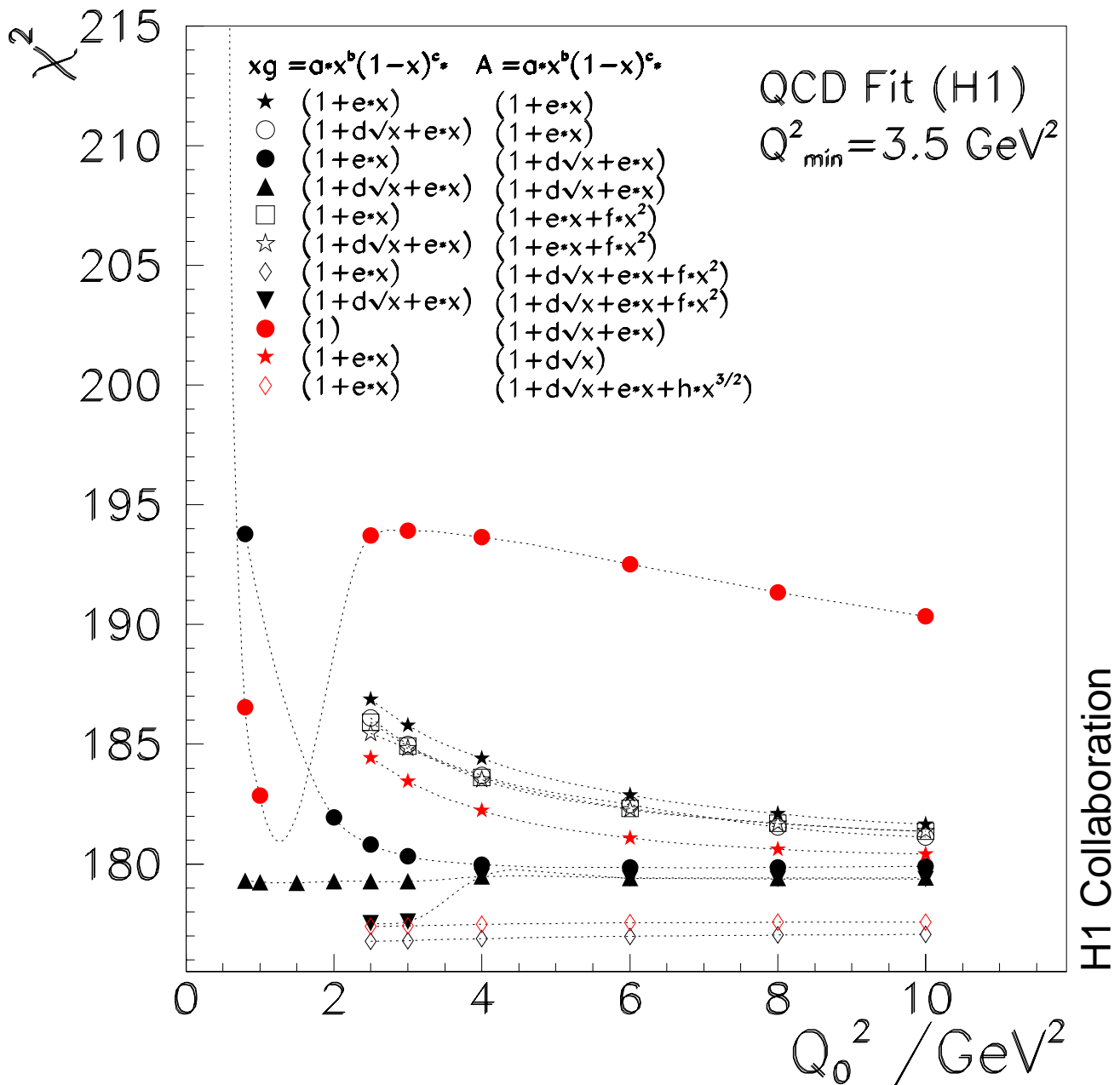


Figure 3.8: Dependence of χ^2 on the input scale Q_0^2 for different parameterisations of the parton distributions xg and A in the NLO QCD fit to the H1 data for $Q_{\min}^2 \geq 3.5 \text{ GeV}^2$. The V parameterisation is given by equation 3.23.

distribution at 20 GeV^2 for 3,4 and 5 parameters determined at Q_0^2 values which lead to the best χ^2 . These distributions agree rather well.

A parameterisation of the gluon distribution with 3 parameters and an input scale $Q_0^2 = 7 \text{ GeV}^2$ as was used in [63] is therefore not appropriate. Instead the three parameter gluon distribution ansatz prefers an input scale $Q_0^2 \sim 1 \text{ GeV}^2$. Recent analyses [64, 92] prefer values around $Q^2 \sim 4 \text{ GeV}^2$, i.e. above the charm quark mass squared. In this analysis stability towards the input fit parameters was required at scales in excess of 2 GeV^2 .

It is instructive to observe that the additional high x parameters d and/or e required by the fits mostly affect the region between 0.01 and 0.1 while the low x behaviour is governed by the parameter b . This is demonstrated for the gluon distribution in figure 3.9. This region in x is particularly important, since gluons in this x region give the major contribution to the proton momentum as is demonstrated in figure 3.11.

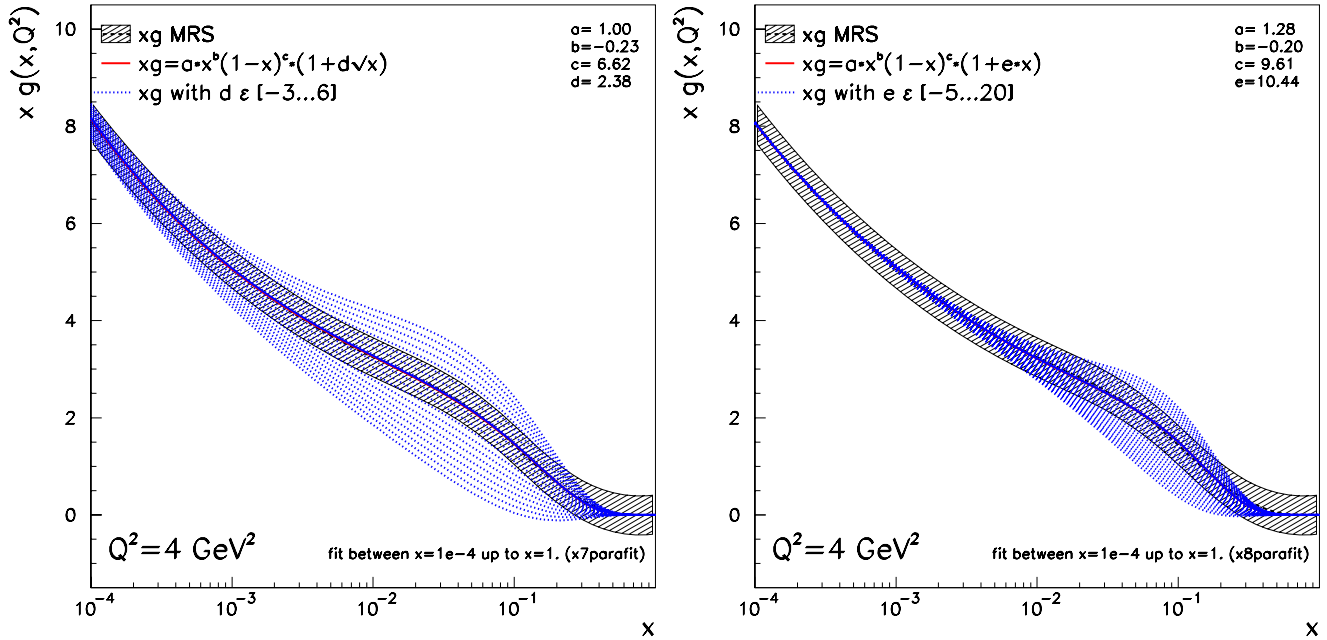


Figure 3.9: Effect of additional high x parameters in the gluon distribution. At a scale of $Q^2 = 4 \text{ GeV}^2$, the gluon taken from the MRST parton momentum distribution functions is re-fit using an additional $(1 + d\sqrt{x})$ (a) or $(1 + ex)$ (b) term multiplied on equation 3.21. The parameters d and e are then arbitrarily varied, keeping the integral of xg fixed. The variation marks the region of largest sensitivity of xg to the values of d (left) and e (right).

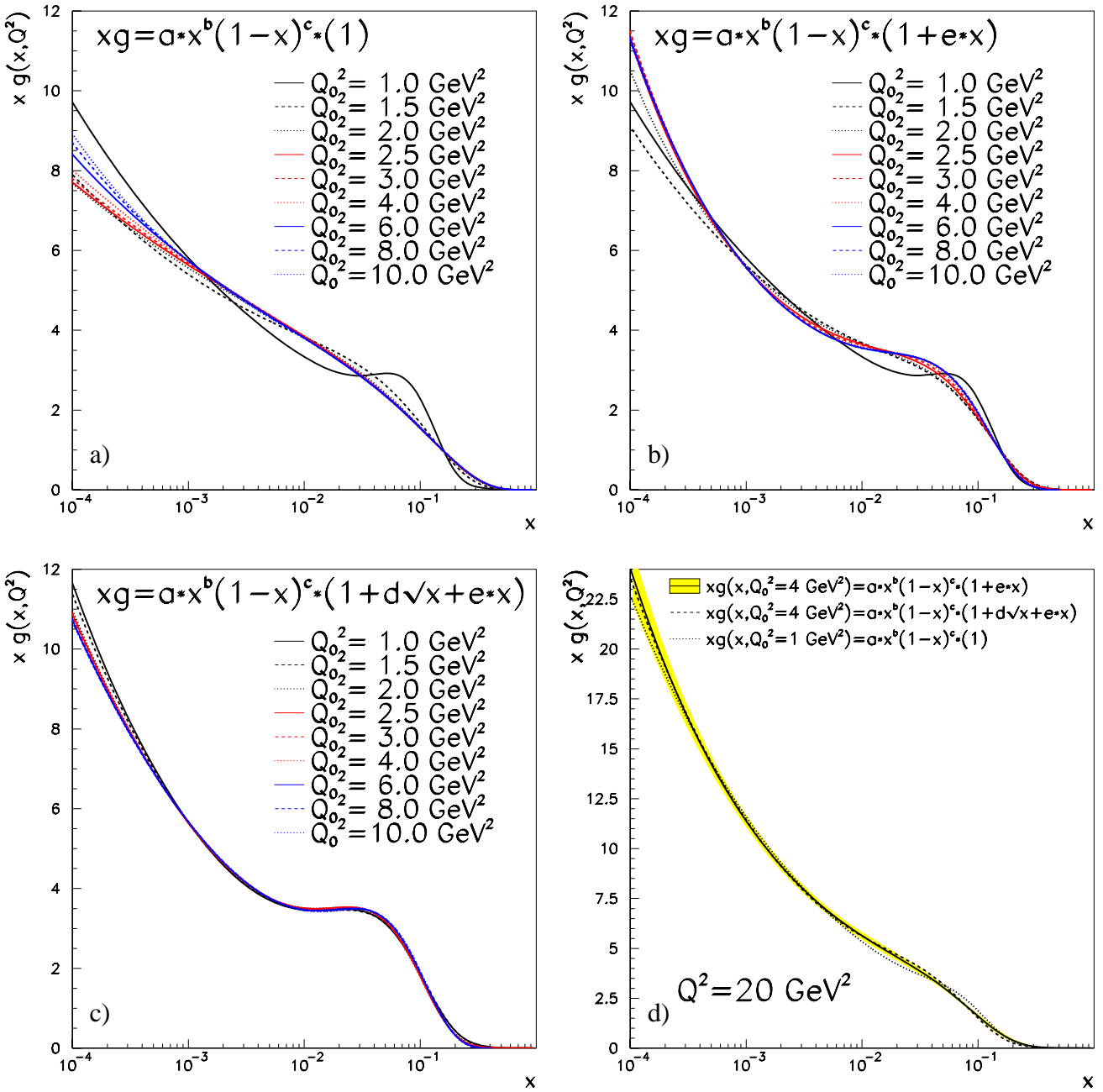


Figure 3.10: a)-c) Stability of the QCD fit to H1 data with respect to the variation of the input scale $1 < Q_0^2 < 10 \text{ GeV}^2$ for different parameterisations. Data points with $Q^2 \geq Q_{min}^2 = 3.5 \text{ GeV}^2$ are included in the fit. The gluon distribution is shown at $Q^2 = 5 \text{ GeV}^2$. d) Gluon distributions shown at a scale of $Q^2 = 20 \text{ GeV}^2$ for different parameterisations from fits with the input scale Q_0^2 which corresponds to the best χ^2 as determined from figure 3.8. Thus for an optimal choice of Q_0^2 , the resulting gluon distributions depend only weakly on the chosen parameterisation for $Q^2 > Q_0^2$. The error band represents the experimental uncertainty of the central fit.

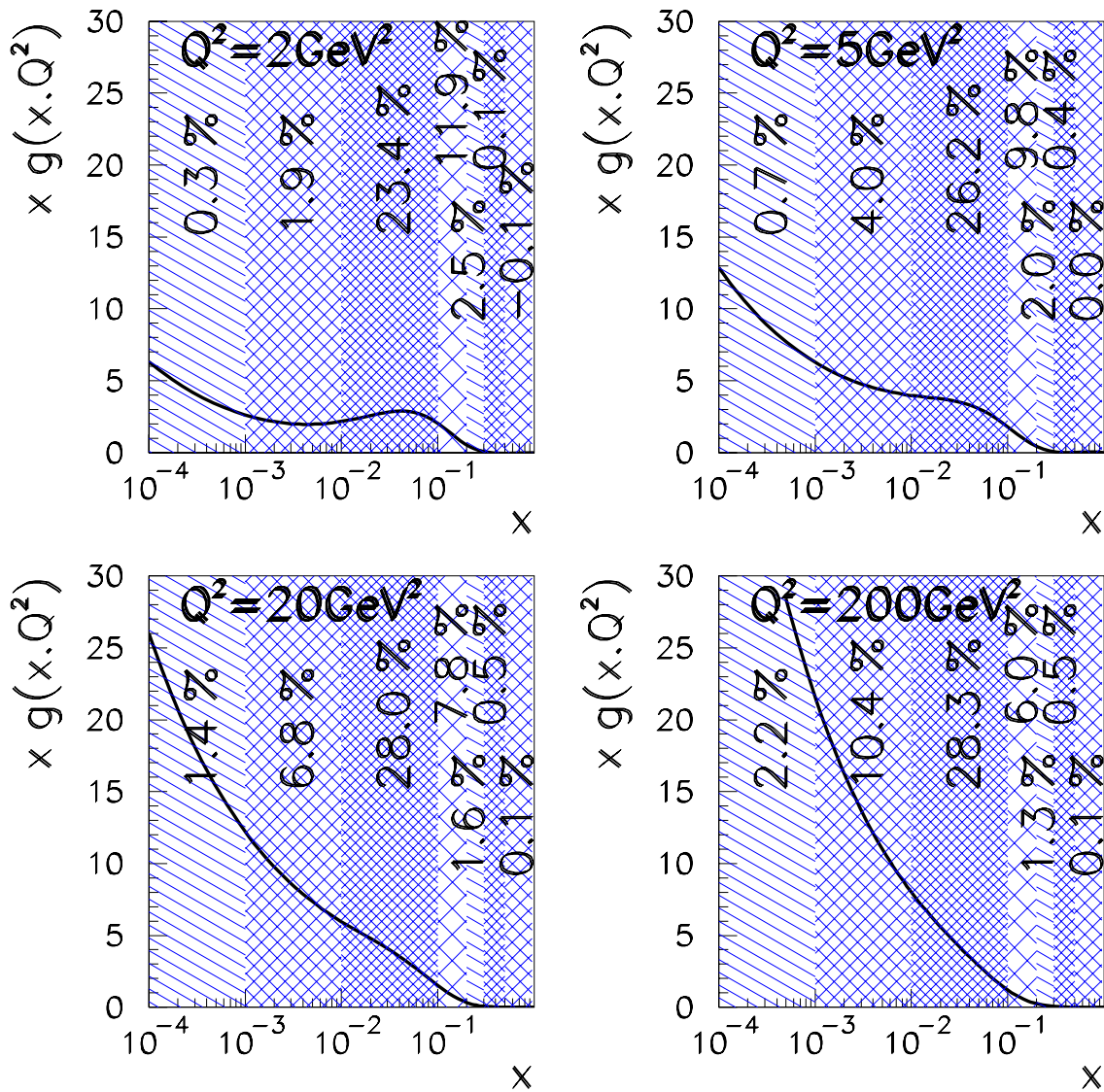


Figure 3.11: Gluon momentum fraction for $Q^2 = 2, 5, 20, 200 \text{ GeV}^2$ in ranges $10^{-4} < x < 10^{-3}$, $10^{-3} < x < 10^{-2}$, $10^{-2} < x < 10^{-1}$, $0.1 < x < 0.2$, $0.2 < x < 0.3$, $0.3 < x < 0.5$, $0.5 < x < 1$.

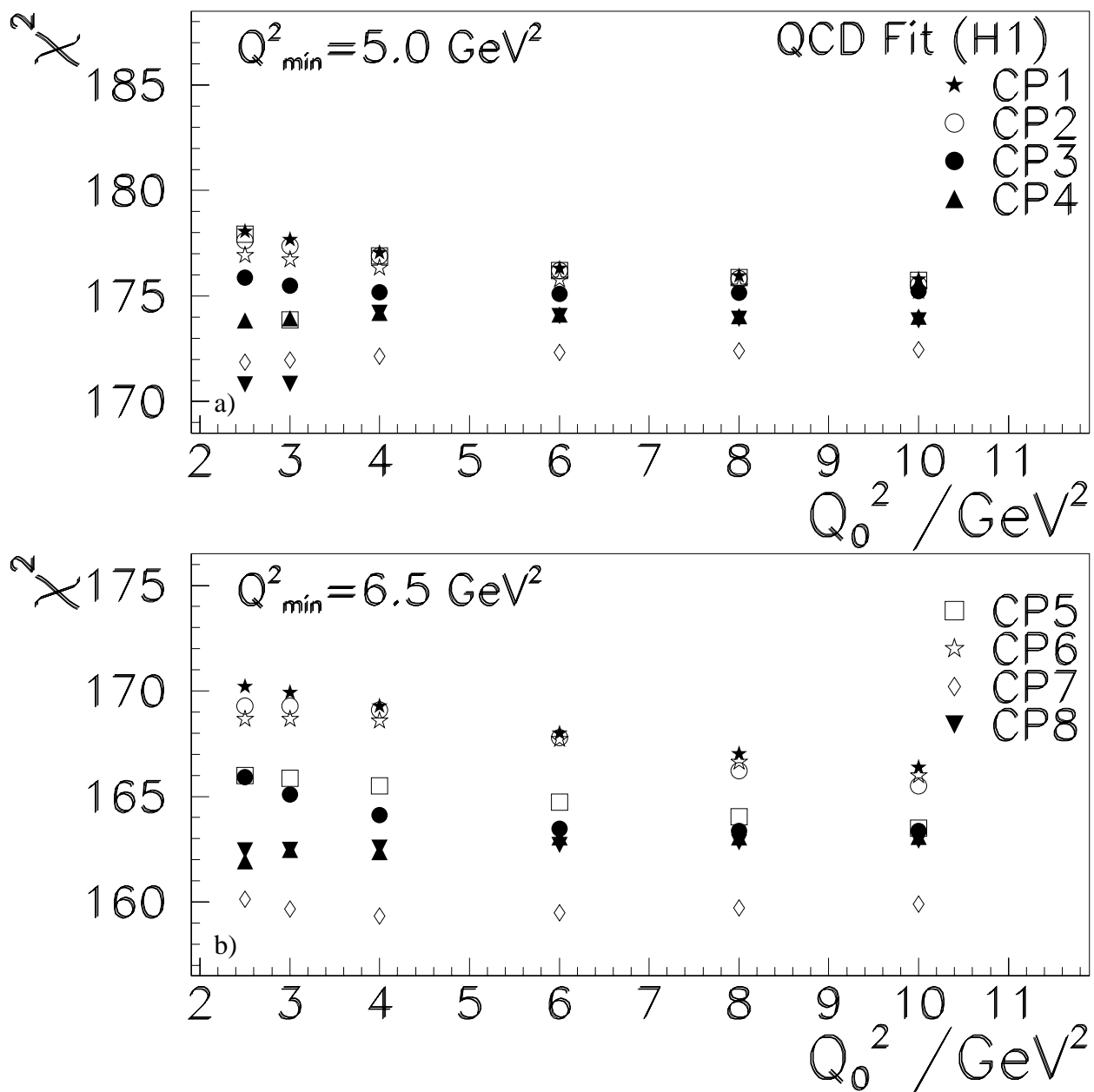


Figure 3.12: Stability of fits to the H1 data for a) $Q_{\min}^2 = 5 \text{ GeV}^2$ and b) $Q_{\min}^2 = 6.5 \text{ GeV}^2$ with respect to varying the input scale Q_0^2 .

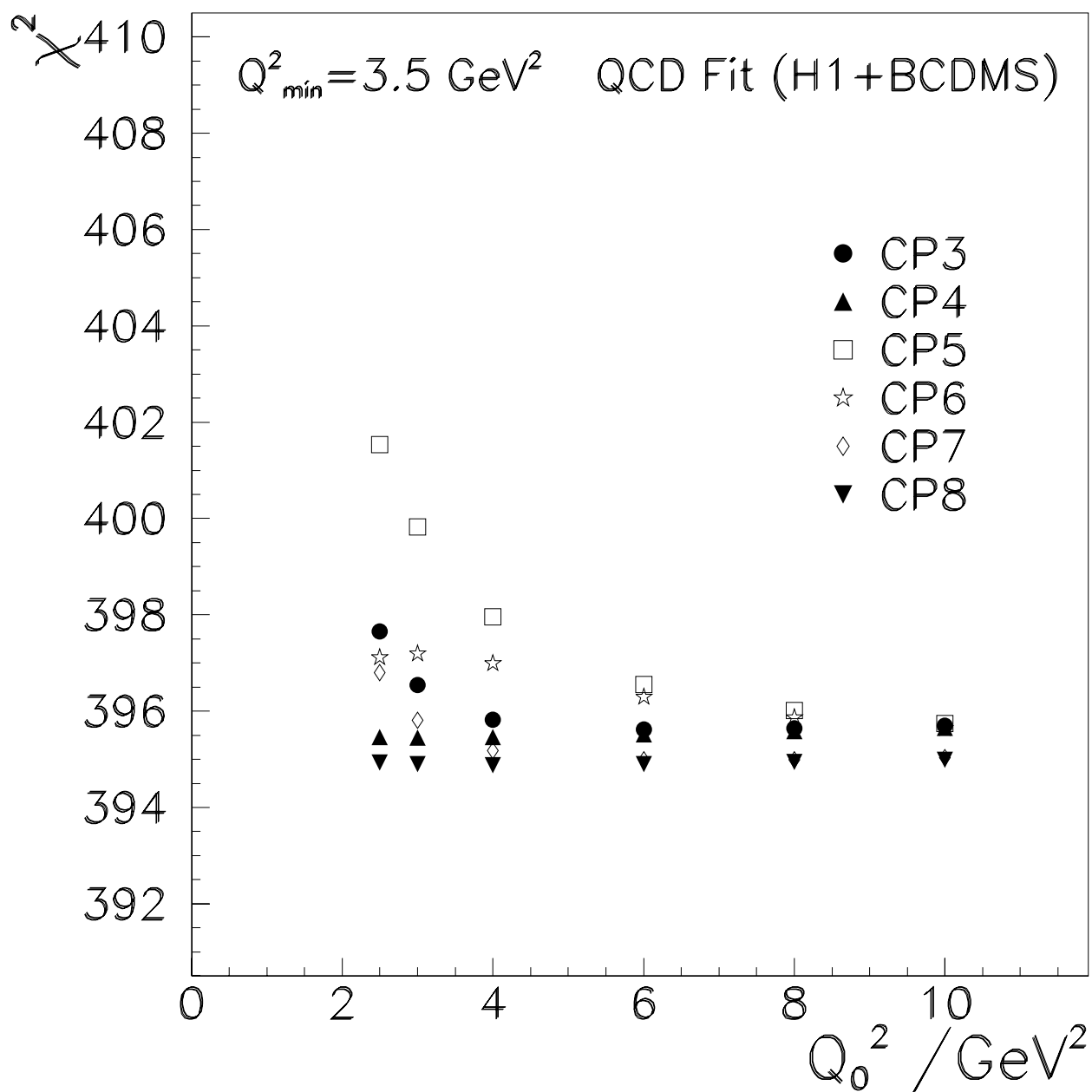


Figure 3.13: Stability of fits to the H1+BCDMS data for $Q_{min}^2 = 3.5 \text{ GeV}^2$ with respect to varying the input scale Q_0^2 .

3.3.4 Gluon Momentum Fraction

Figure 3.8 shows that the χ^2 -saturation criterion selects the fits with an A ansatz with the maximal number of parameters considered. However, the gain in χ^2 is about one unit only, and the V distribution in these fits become distorted and significantly deviate from the majority of fits, see figure 3.14. This behaviour may result from too many unconstrained parameters in the A distribution.

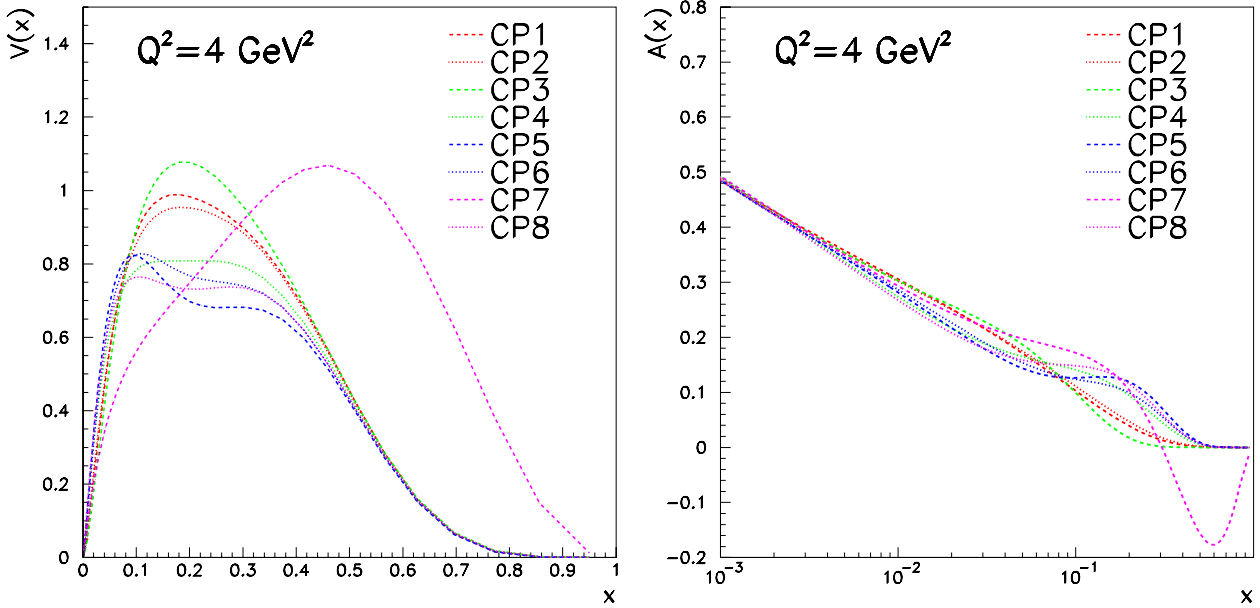


Figure 3.14: Comparison of the V (a) and A (b) distributions for the parameterisations of table 3.1.

A cross check for the stability of the fit was provided by determining the momentum fraction of the proton carried by gluons, see figure 3.15. The deviating fits also determine a gluon momentum fraction which is incompatible with other measurements even at low scales Q^2 . They are therefore excluded from further analysis. The gluon momentum fraction in addition was used to verify the flavour decomposition ansatz in A, V and xg distributions to fit proton target data only as described above. The standard QCD analyses use proton and deuteron data to control the singlet, non-singlet and gluon distributions, allowing the conventional u_v, d_v and xg distributions to be used as described in e.g. [20]. Figure 3.16 demonstrates that the resulting gluon momentum fractions for both the conventional and the proton only ansatz are in very good agreement. The momentum fraction carried by the gluons is determined to be 0.43 ± 0.02 (*exp*) at $Q^2 = 4 \text{ GeV}^2$ where the error is due to the measurement uncertainties. The results also agree with previous determinations at $Q^2 = 7 \text{ GeV}^2$ [45, 65]. The fit to proton only data is also repeated without imposing the constraint given by the momentum sum rule. This fit determines the integral $\int_0^1 x(\Sigma + g)dx$ to be 1.016 ± 0.017 (*exp*), where Σ is the singlet parton distribution function, equation 1.28. This value is found to be nearly independent of the minimum Q^2 value of the data included in the analysis. Thus the momentum sum rule is confirmed with good accuracy. Imposing it fixes one normalisation parameter.

Based on these observations the central fit to the H1 data was performed with the CP3 parameterisation of table 3.1. For the H1+BCDMS analysis the parameterisation CP3 and CP4

were found to be adequate by the same procedure for the central fit of $Q_{min}^2 = 3.5 \text{ GeV}^2$. Since, however, parameterisation CP3 proved slightly more vulnerable to variations of Q_{min}^2 than CP4, parameterisation CP4 was selected for the central H1+BCDMS fit. This allowed for more flexibility at high x as required by the more accurate high x data in the fit.

In all subsequent studies however were also performed with the alternative ansatz CP1-CP2, and CP4-5 and CP8 which yielded the correct momentum fraction to cross check the results. As is demonstrated in figure 3.12, the parameterisation ansatz CP3 also proved adequate under variation of Q_{min}^2 .

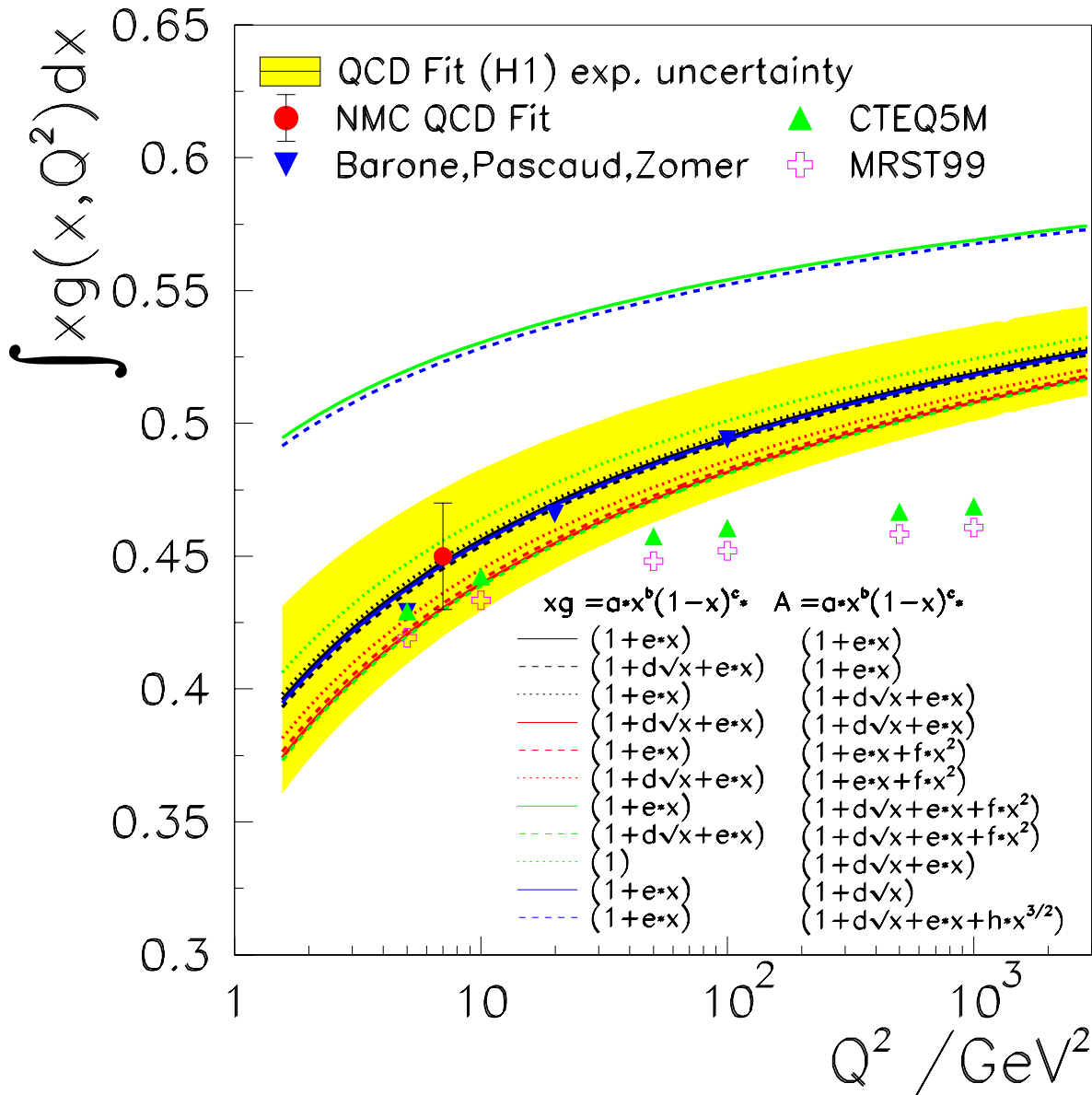


Figure 3.15: The fraction of the proton momentum carried by gluons as a function of Q^2 , obtained in different NLO DGLAP fits. Solid curve: fit to H1 data alone; dashed curve: fit to H1 and BCDMS proton data; dotted curve: fit to H1 ep and BCDMS μp and μd data. The shaded error band represents the experimental uncertainty in the analysis of the H1 data alone. The solid point is due to a QCD analysis by the NMC collaboration [45]. Also shown are results of global analyses [38, 39, 66].

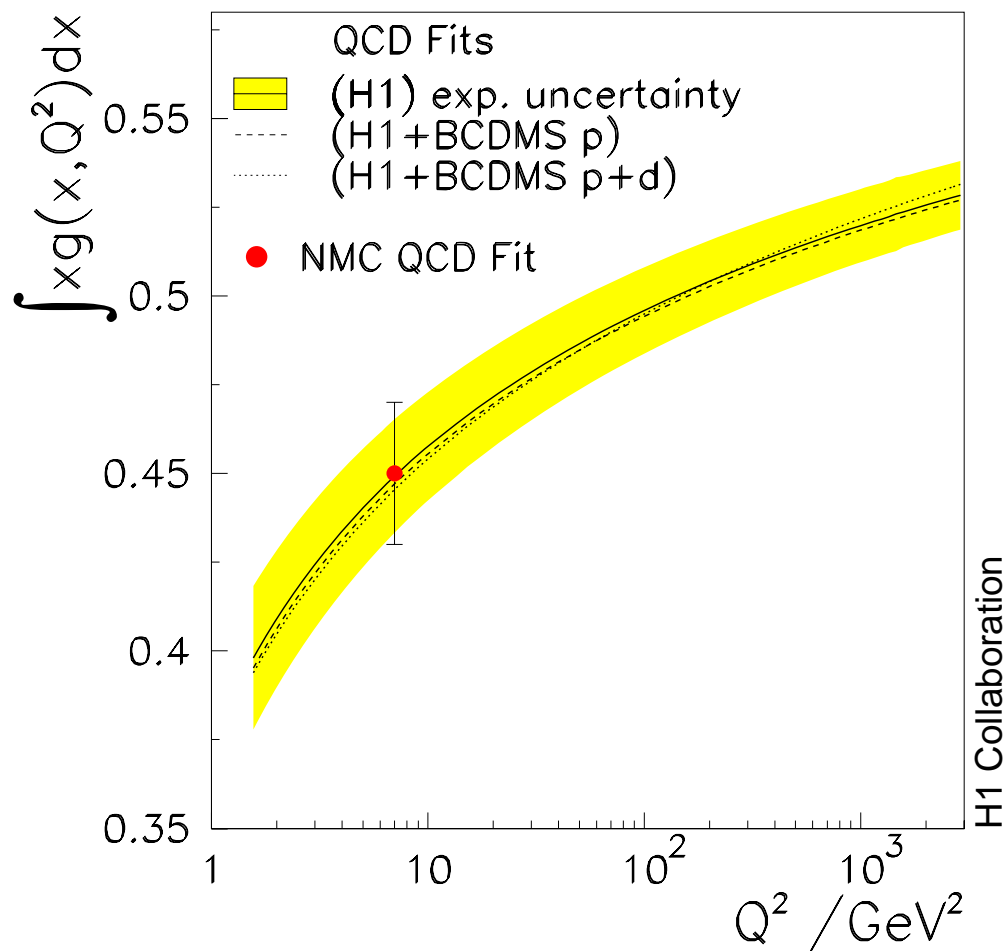


Figure 3.16: The fraction of the proton momentum carried by gluons as a function of Q^2 , obtained in different NLO DGLAP fits. Solid curve: fit to H1 data alone; dashed curve: fit to H1 and BCDMS proton data; dotted curve: fit to H1 ep and BCDMS μp and μd data. The shaded error band represents the experimental uncertainty in the analysis of the H1 data alone. The solid point is due to a QCD analysis by the NMC collaboration [45].

3.4 Definition of Minimization Procedure

3.4.1 Definition of χ^2

The fit parameters are determined by finding the least square deviations between the theoretical prediction of the reduced cross section σ_r^{th} and the measured reduced cross section σ_r^{exp} minimizing

$$\chi^2 \simeq \sum_i \frac{[\sigma_r^{exp}(x_i, Q_i^2) - \sigma_r^{th}(x_i, Q_i^2)]^2}{\delta_{i,unc}^2 + \delta_{i,stat}^2}. \quad (3.24)$$

The sum over i runs over all data points of all datasets involved. The theoretical neutral current double differential cross section is computed in its reduced form using equation 1.7. The structure functions F_2 and F_L are calculated using equations 1.20 and 1.22, respectively.

3.4.2 Correlated Systematic Error Treatment

The experimental systematic errors introduce point-to-point correlations which are not properly taken into account by equation 3.24. Treatment of these correlations is provided following a method proposed by [66].

In principle, the evaluation of correlated systematic errors and their propagation (see below) can be incorporated in a standard Hessian matrix approach, see [67, 42]. However, the many more parameters in the fit in practice require the inversion of matrices of large dimensions which is numerically unstable if the eigenvalues of the Hessian matrix span a large range of values. Therefore, in this analysis a different method is used by which the correlated uncertainties are parameterized by a set of fit parameters s_λ where λ indicates the systematic error source as described in table 2.1. It has been shown [43] that this method is equivalent to the standard Hessian matrix approach.

Therefore, the model prediction $\sigma_{r,i}^{th}(p)$ corresponding to a set of model fit parameters p and systematics parameters s_λ at a given point (x_i, Q_i^2) is modified according to

$$\sigma_{r,i}^{th}(p) \rightarrow \sigma_{r,i}^{th}(p, s) = \sigma_{r,i}^{th}(p) \times \left(1 + \sum_\lambda s_\lambda \delta_{i\lambda}^{syst}\right) \quad (3.25)$$

where $\delta_{i\lambda}^{syst}$ is the relative systematic error of data point i due to source λ . For the further statistically correct treatment of the correlated systematic errors and their propagation it is assumed that the s_λ are uncorrelated and gaussian distributed with zero mean and unit variance³. A value of $s_\lambda = \pm 1$ therefore indicates a deviation of the measurement of one standard deviation away from the central value.

³This also implies averaging the effect of asymmetric error sources. Note that these assumption can be violated with certain error sources, i.e. noise treatment.

Further systematic error sources are the relative normalizations of the data sets which are mainly determined by the luminosity measurements and global trigger and reconstruction efficiencies. Accordingly, further correlated systematic parameters ν_k are introduced which estimate the number of standard deviations of the normalization uncertainty δ_k^{norm} of experimental data set k .

For the parameters s_λ and ν_k related to systematics counter (penalty) terms are introduced into the χ^2 definition to control their variation in $\pm 1\sigma$ limits. The full χ^2 definition therefore reads for a fit to n_{exp} datasets with relative normalization uncertainties δ_k^{norm} , $n_p(k)$ data points and $n_s(k)$ correlated systematic error sources s_λ which give rise to a relative correlated systematic error $\delta_{i\lambda}^{syst}$ on the cross section, as

$$\begin{aligned} \chi^2 &= \sum_k^{n_{exp}} \sum_i^{n_p(k)} \frac{[\sigma_{r,i}^{exp} - \sigma_{r,i}^{th} \times (1 - \nu_k \delta_k^{norm} - \sum_\lambda^{n_s(k)} s_{\lambda,k} \delta_{i\lambda}^{syst})]}{\delta_{i,sta}^2 + \delta_{i,unc}^2} \\ &+ \sum_k \nu_k^2 + \sum_k \sum_\lambda (s_\lambda^{exp})^2. \end{aligned} \quad (3.26)$$

Note that the systematics parameters s_λ are not counted as free parameters since they are constrained by the penalty terms in the χ^2 definition. The QCD fit program used determines the free parameters using the MINUIT minimization program [68] and the systematics are fitted in each MINUIT iteration using a least square minimization procedure exploiting the linear dependence of the χ^2 on the systematics parameters s_λ , saving computer time [69]. Furthermore, the derivatives of the χ^2 with respect to the systematics parameters are determined which is needed for the error propagation.

3.4.3 Error Propagation

In order to propagate the statistical and systematic uncertainties of the cross section on the parton momentum distribution functions, two Hessian matrices \mathbf{M} and \mathbf{C} are computed at the minimum χ_{min}^2

$$M_{\lambda\mu} = \frac{1}{2} \frac{\partial^2 \chi^2}{\partial p_\lambda \partial p_\mu}, \quad C_{\lambda\mu} = \frac{1}{2} \frac{\partial^2 \chi^2}{\partial p_\lambda \partial s_\mu}, \quad (3.27)$$

The statistical and systematic covariance matrices are then given by [66]

$$\mathbf{V}^{stat} = \mathbf{M}^{-1}, \quad \mathbf{V}^{syst} = \mathbf{M}^{-1} \mathbf{C} \mathbf{C}^T \mathbf{M}^{-1}, \quad (3.28)$$

For any function G which depends on the model parameters p , $G = G(p)$. The error ΔG is then obtained using

$$\Delta G^2 = \sum_\lambda \sum_\mu \frac{\partial G}{\partial p_\lambda} V_{\lambda\mu} \frac{\partial G}{\partial p_\mu} \quad (3.29)$$

where the matrix $V_{\lambda\mu}$ corresponds to \mathbf{V}^{stat} , \mathbf{V}^{syst} or both added in quadrature for the statistical, systematic and the total error.

In order to define envelopes for a function $G(p)$ which is minimal for a set of model parameters p_f , the variation of these parameters $p - p_f$ can be found by

$$(p - p_f)_\lambda = \pm \frac{\sum_\mu V_{\lambda\mu} \frac{\partial G}{\partial p_\mu}}{\sqrt{\Delta G^2}} \quad (3.30)$$

These envelopes are the error bands shown in all subsequent figures. They are defining the 68% probability for a given point $G(p)$ (which can be thought of e.g. the gluon distribution at a fixed x and Q^2) to stay in the envelope under variation around the minimum of a fit parameter p by its uncertainty.

Note that this statistical interpretation relies on simplifying assumptions which in practice are often not precisely met, e.g. gaussian fluctuating systematic errors. Furthermore, especially at high x , the estimation can be biased by the parameterisation as well.

Chapter 4

Extraction of the Gluon Distribution

This chapter presents the results for the extraction of the gluon distribution from the inclusive cross section data in NLO QCD. Two central fits are performed, one to H1 data alone, the other with H1 data in combination with BCDMS proton target data. Both central fits employ data above a minimum $Q_{min}^2 \geq 3.5 \text{ GeV}^2$. A cut $Q^2 \leq 3000 \text{ GeV}^2$ is applied to eliminate the region where electroweak interference effects are important, which involve the structure function $x F_3$.

For the fit to H1 data alone, the H1 low x data, presented in chapter 2, are used as well as recent data of the H1 collaboration [37] from the same data taking period, which cover the high x range at high $Q^2 \geq 150 \text{ GeV}^2$. This fit assumes a fixed $\alpha_s(M_Z^2) = 0.115$ and uses the parameterisation CP3 of table 3.1 discussed in the previous chapter.

In the fit to H1 and BCDMS data, α_s is left as a free parameter. For reasons linked to correlated systematic errors, a cut of $y_\mu > 0.3$ is imposed on the BCDMS data as will be justified in the following chapter, where the results on α_s are presented as well. The parameterisation used is CP4 of table 3.1.

4.1 Quality of the Fits

4.1.1 Comparison with the Data

The measured double differential reduced cross section σ_r is compared with the QCD fit to the high and low x H1 data, see figure 4.1. The data are compared to published data of the fixed target muon-proton scattering experiments BCDMS and NMC. These are well described by the fits to H1 (H1+BCDMS) data with a total χ^2 per degree of freedom of 0.8 (0.87), see table 4.1.3. In the high x region, the fit to H1 data is only constrained by the H1 high Q^2 data describing nevertheless the high x data of the fixed target experiments NMC and BCDMS rather well.

At lowest x , the cross section receives significant contributions from the longitudinal structure function F_L , leading to a turnover at the kinematic edge of $y \sim 0.5$. The highest y values in the 97 data analysis were reached for $Q^2 > 12 \text{ GeV}^2$. The turning cross section behaviour is well reproduced by the NLO QCD calculation, as is illustrated in figure 4.26.

The structure function $F_2(x, Q^2)$ is extracted from the reduced cross section data using the prediction of the fit for the longitudinal structure function $F_L(x, Q^2)$. This extraction was limited to $y < 0.6$ since at higher values of y , the uncertainties of F_2 due to uncertainties in F_L become appreciable. The result is shown in figures 4.2 and 4.3.

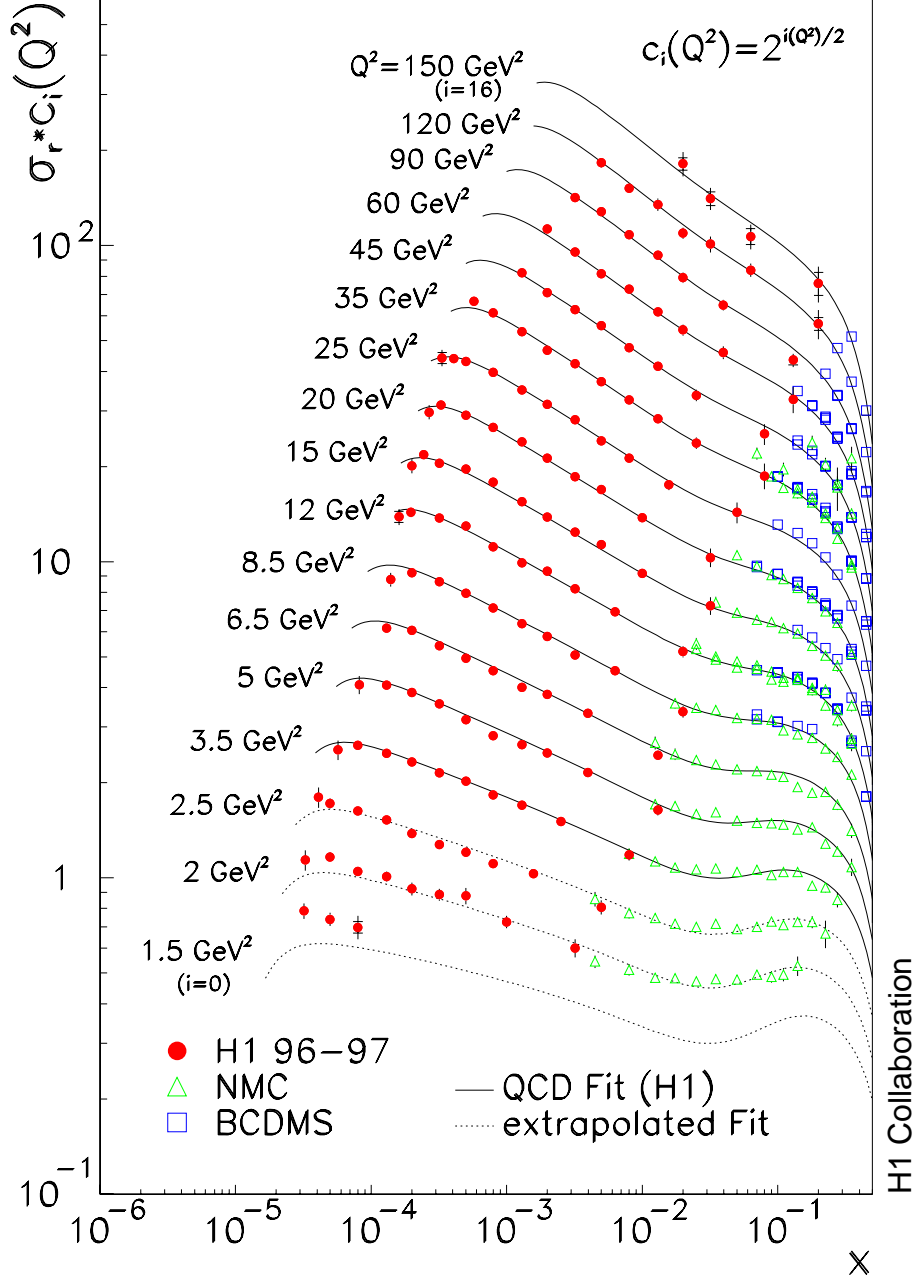


Figure 4.1: Measurement of the reduced DIS scattering cross section (closed points). Triangles (squares) represent data from the NMC (BCDMS) muon-proton scattering experiments. The solid curves illustrate the cross section obtained in the central NLO DGLAP QCD fit to the present data at low x , with $Q_{min}^2 = 3.5 \text{ GeV}^2$, and to the H1 data at high Q^2 . The dotted curves show the extrapolation of this fit towards lower Q^2 . The curves are labelled with the Q^2 value the data points belong to and scale factors are conveniently chosen to separate the measurements.

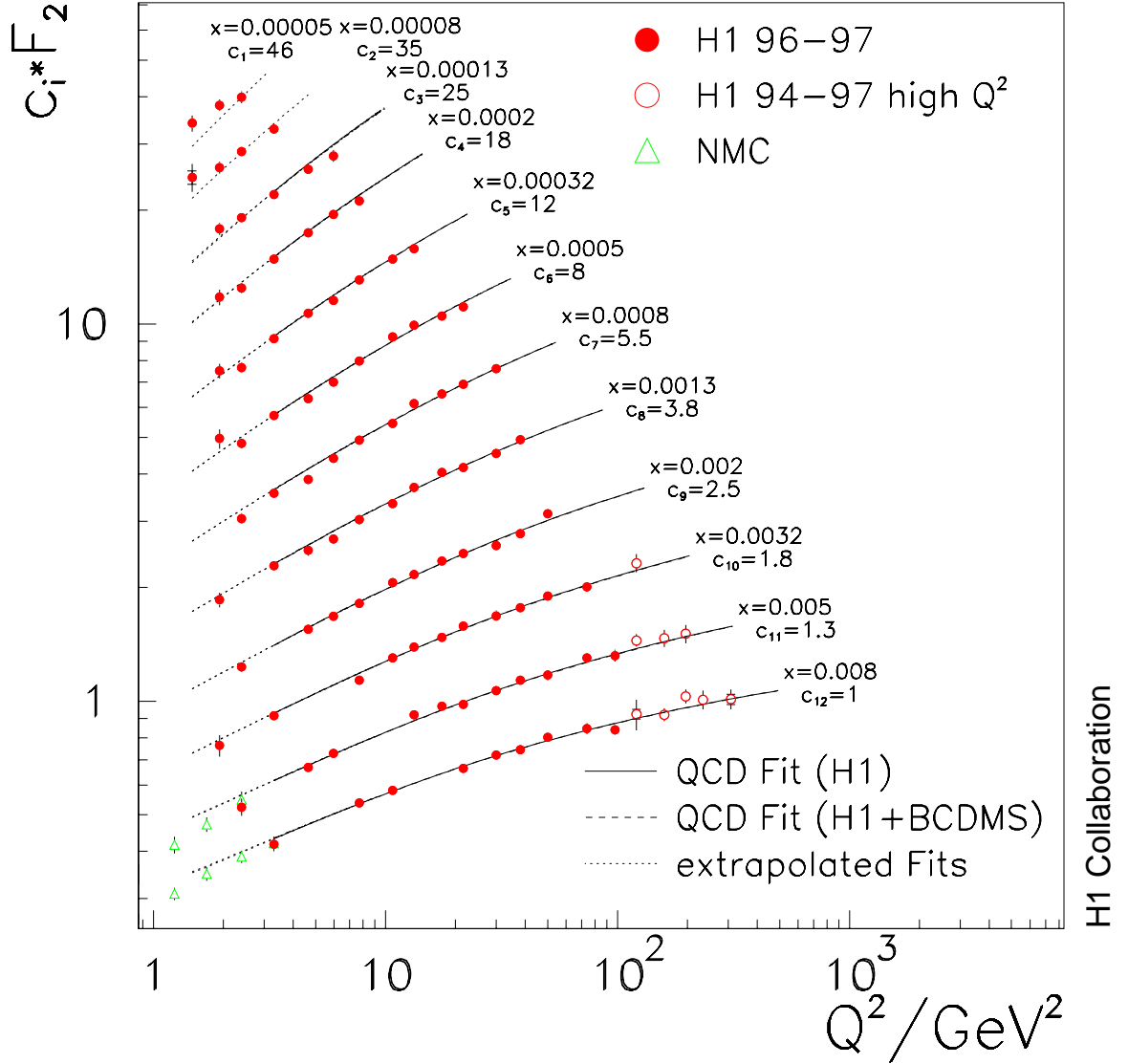


Figure 4.2: Measurements of the proton structure function $F_2(x, Q^2)$ by the H1 and the NMC experiments. Solid curves: NLO DGLAP QCD fit to the H1 cross section data. Overlaid as dashed curves are the results of the QCD fit to the H1 ep and BCDMS μp data, for $y_\mu > 0.3$, which are indistinguishable from those of the pure H1 fit. Dotted curves: fit extrapolations at fixed x into the region below $Q^2 = 3.5 \text{ GeV}^2$.

At low x , F_2 rises with Q^2 . From approximate calculations it can be seen that at low $x < 0.01$ the quark contribution to the derivative $(\partial F_2 / \partial \ln Q^2)_x$ in the DGLAP equations is negligible. Furthermore, the splitting function P_{gg} can be expanded and an approximate relation is obtained in leading order, for $Q^2 > 3 \text{ GeV}^2$ [70]

$$(\partial F_2 / \partial \ln Q^2)_x \simeq \frac{2}{3} \cdot \frac{5\alpha_s(Q^2)}{9\pi} xg(2x, Q^2) \quad (4.1)$$

Thus the observed increase of the rise of F_2 vs $\ln Q^2$, see figure 4.4, with decreasing x implies

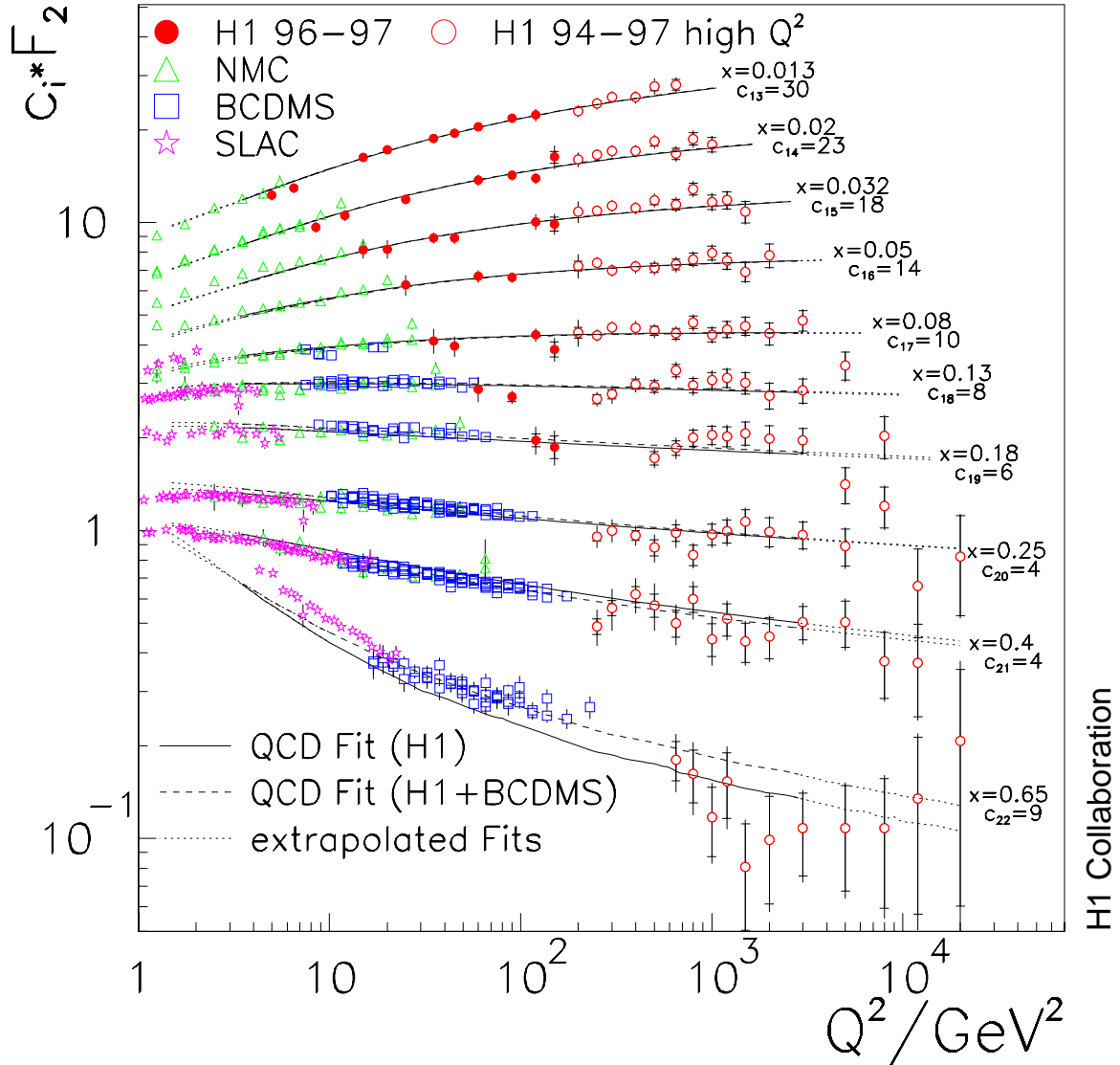


Figure 4.3: Measurements of the proton structure function $F_2(x, Q^2)$ by the H1 experiment and by fixed target muon-proton scattering experiments. The error on the data points is the total measurement uncertainty. The inner error bars represent the statistical error. Solid curves: fit to the H1 cross section data. Dashed curves: fit to the H1 ep and BCDMS μp data, for $y_\mu > 0.3$. Dotted curves: extrapolations to data not used in the fit.

that the gluon distribution xg rises towards low x . This rise at a certain value of x has to be damped since unitarity of the total cross section imposes a limit on the gluon distribution in a given sphere of the proton radius.

In figures 4.2 and 4.3, the solid lines give the result of the QCD fit with $Q_{min}^2 = 3.5 \text{ GeV}^2$ to the H1 data. This fit also describes the fixed target data in the non-overlapping regions rather well, except for the data points at $x = 0.65$ where the fit curve is below the BCDMS data. The H1 data at this value of x [37] have a correlated systematic uncertainty of 12%, due to the energy scale error for the scattered positron, which accommodates the observed difference. Note that a

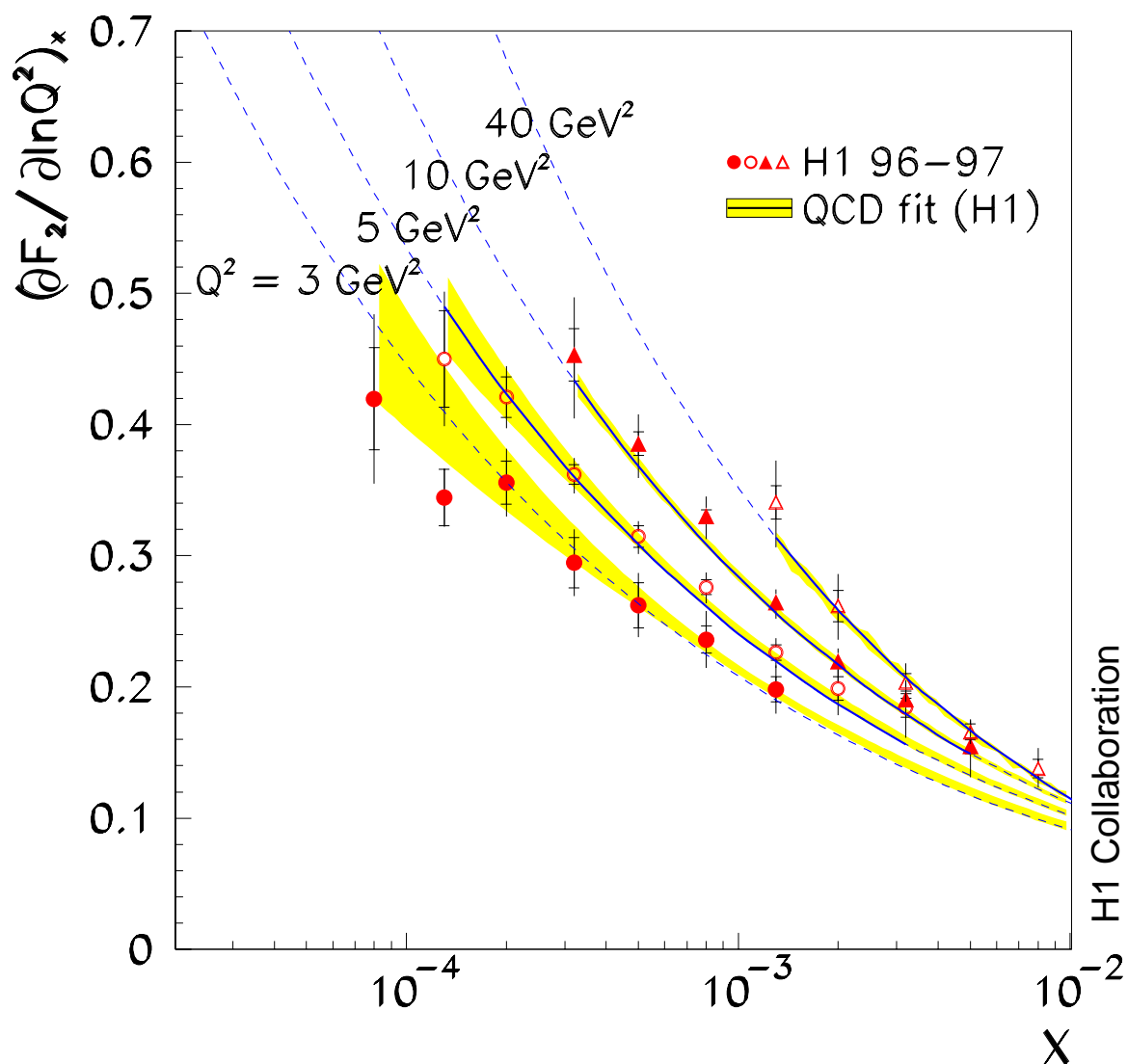


Figure 4.4: Measurement of the partial derivative $(\partial F_2/\partial \ln Q^2)_x$ taken at fixed x and plotted as functions of Q^2 . The error bars represent the quadratic sum of statistical and systematic errors. The straight solid lines are given by the function $b(x) + 2c(x) \ln Q^2$ determined in fits to $F_2(x, Q^2)$ at fixed x . The dashed lines represent the derivatives as calculated with the QCD fit to the H1 data. The error bands are due to the experimental and model uncertainties in the QCD fit which includes data in the QCD fit for $Q^2 \geq 3.5 \text{ GeV}^2$.

new, preliminary H1 measurement [71] of $F_2(x, Q^2)$ at high Q^2 and x results in a consistent but larger F_2 values for $x = 0.65$ which may resolve the difference between the BCDMS and H1 high x data observed here.

4.1.2 Pull Distributions

Table 4.1.3 summarises the fit results for the H1 and H1+BCDMS fits. The χ^2 per degree of freedom is slightly below 1 indicating an overestimation of the uncorrelated errors. Figure 4.5 shows the pull distribution for the individual datasets in the fit to H1 data alone, 4.6 in the fit to H1 and BCDMS data. The pulls are defined as

$$pull = \frac{Data - c_{sys} * Theory}{uncorr.error}$$

where c_{sys} reflects the effect of the correlated error sources.

4.1.3 QCD Model Parameters

Table 4.2 presents the extracted QCD parameters of the fits to the H1 data alone in the full kinematic range and for $y < 0.35$ (see below) and to the H1 and BCDMS data. The result for the parameter c_g comes out to be rather large as compared to the dimensional counting rule expectation [72]. A fit with $d_g = e_g = 0$ to H1 and BCDMS data, however, yields $c_g = 6.5$ for the fit to H1 and BCDMS data, not far from dimensional counting rule expectations [72], yet with a deteriorated χ^2 . Note that the gluon normalisation a_g and the low x parameter b_g are observed to be strongly correlated, explaining the different values obtained from the analysis of H1 data without and with a cut in y . The resulting gluon distributions, however, agree very well, see below.

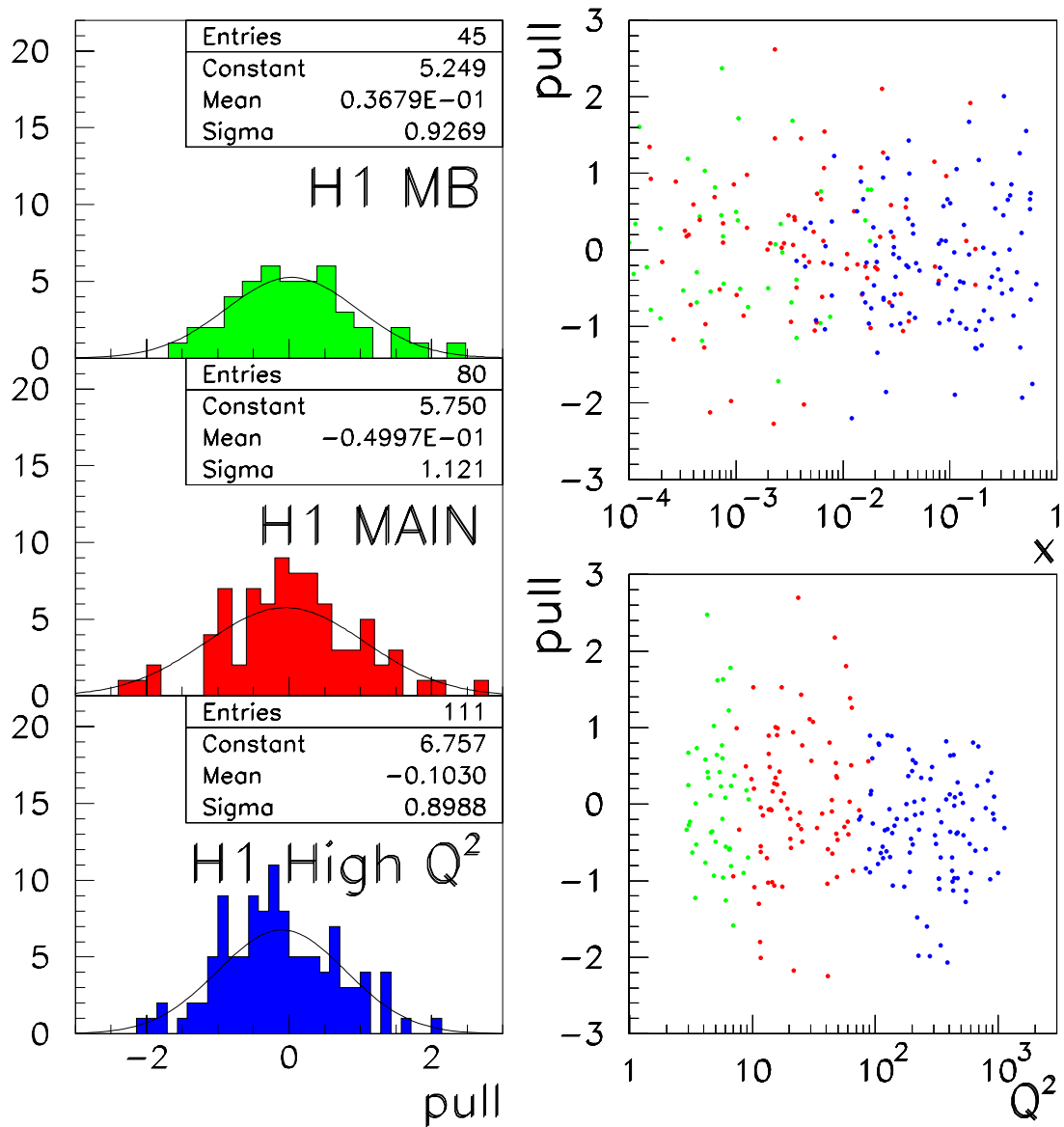


Figure 4.5: left: Pull distribution for the fit to H1 data alone. right: Pulls versus x and Q^2 . No systematic trend is observed in these distributions pointing to a good description of the measurement in the full kinematic range, including the region of lowest x .

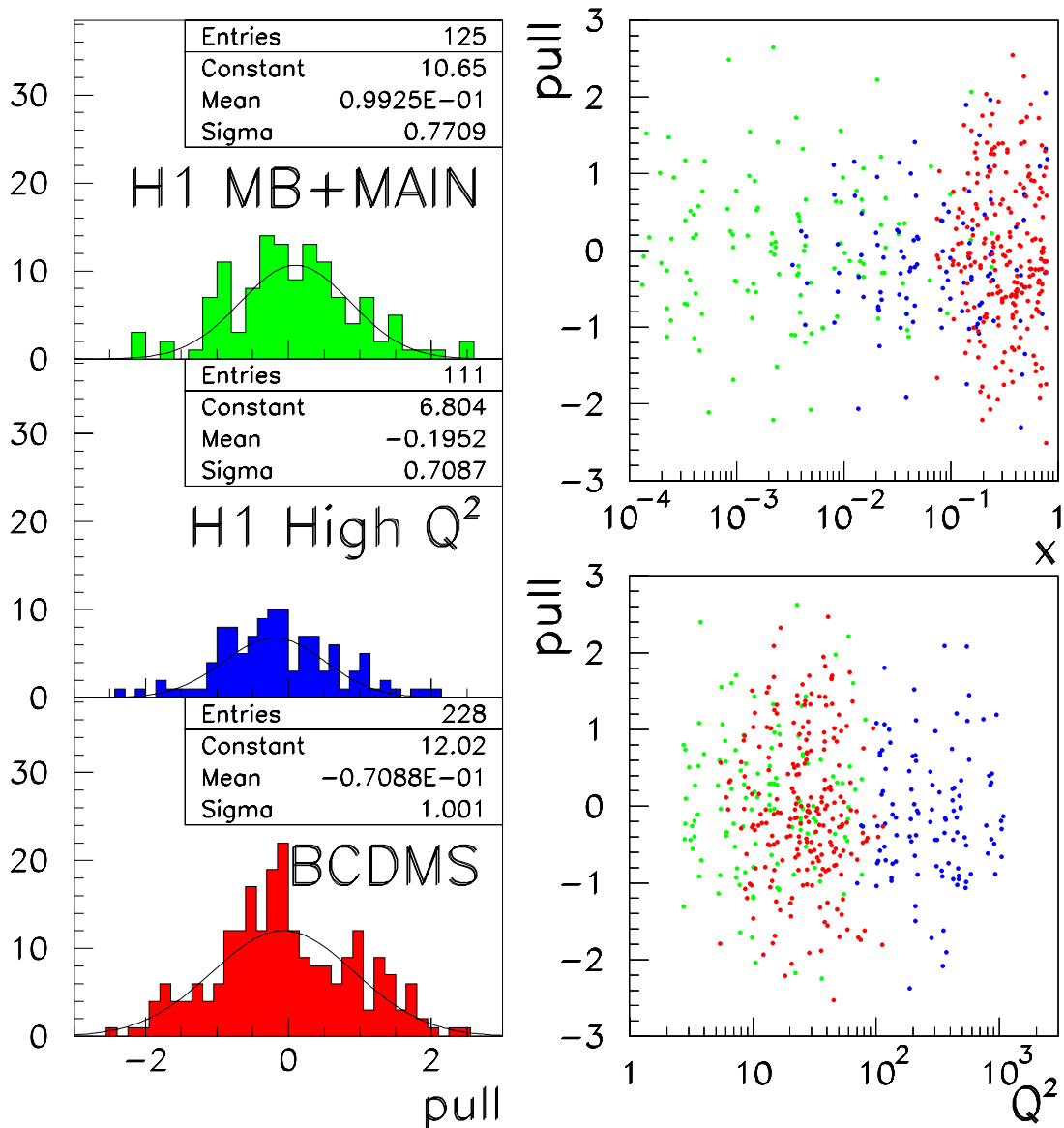


Figure 4.6: left: Pull distribution for the H1+BCDMS fit. right: Pulls versus x and Q^2 . A cut in the BCDMS data for $y > 0.3$ is applied, see chapter 5.

	(a) H1	(b) H1+BCDMS	(c) H1 ($y < 0.35$)
# parameters	12	13 +1 (α_s)	12
total χ^2	180	394	151
partial χ^2	stat/syst/#pts	stat/syst/#pts	stat/syst/#pts
H1 MB	32/2.4/45	32/2.5/45	28/1.1/37
H1 Main	67/2.5/80	68/2.4/80	53/1.3/65
H1 high Q^2	74/2.5/111	78/2.8/111	64/2.6/90
BCDMS-100	-	51/0.5/58	-
BCDMS-120	-	38/0.5/62	-
BCDMS-200	-	64/0.5/56	-
BCDMS-280	-	53/1.0/52	-
χ^2 /d.o.f	0.80	0.87	0.84

Table 4.1: χ^2 characterisation of the central fit results using the H1 alone (a) , the H1+BCDMS data (b) and of a fit to the H1 data with a cut in $y < 0.35$ (c) for the F_L extrapolation method, see section 4.5.

(a) H1		a	b	c	d	e
	gluon	0.477	-0.341	15.7	-	83.0
	V	178.	1.62	5.70	-2.87	2.86
	A	0.193	-0.149	18.2	-2.76	25.8
(b) H1 ($y < 0.35$)		a	b	c	d	e
	gluon	0.277	-0.419	15.5	-	118.0
	V	162.	1.57	5.71	-2.92	3.00
	A	0.167	-0.166	16.1	-1.9	21.2
(c) H1+BCDMS		a	b	c	d	e
	gluon	1.10	-0.247	17.5	-4.83	68.2
	V	86.3	1.47	4.48	-2.12	1.60
	A	0.229	-0.130	19.7	-3.82	29.8

Table 4.2: Parameters of the input distributions $xq(x) = a_q x^{b_q} (1-x)^{c_q} [1 + d_q \sqrt{x} + e_q x]$ for $xg(x, Q^2)$, $V(x, Q^2)$ and $A(x, Q^2)$ at the initial scale $Q_0^2 = 4 \text{ GeV}^2$ for fits to data above $Q^2 \geq 3.5 \text{ GeV}^2$ using H1 data (a), H1 data with a cut on $y < 0.35$ (b) and H1 and BCDMS (c) data with a cut $y_\mu > 0.3$ on the BCDMS data, see chapter 5.

4.1.4 Dataset Normalisation

In the fits, the datasets are allowed to float within their quoted normalisation uncertainties. The normalisations imposed by the fit as well as their quoted uncertainties are listed in table 4.3. In the case of the BCDMS data, the datasets taken at different beam energies share an absolute cross section normalisation uncertainty of 3%, but in addition are allowed to float 1% relative to each other. Fixing all normalisations increases χ^2 by 26 units in the case of the H1+BCDMS fits and about 10 units in the fits to H1 data alone.

	(a) H1 Fit	abs	(b) H1 Fit	abs	(b) H1+	abs	rel	quote
		%	($y < 0.35$)	%	BCDMS Fit	%	%	%
H1 MB		1.36		1.32		1.34		1.7
H1 MAIN		-0.32		-0.32		-0.49		1.7
H1 high Q^2		-1.18		-1.11		-1.25		1.7
BCDMS-all						-1.79		3
H1 MB		0.87		0.91		0.89		1.7
H1 MAIN +high Q^2		-1.1		-1.08		-1.25		1.7
BCDMS-all						-1.91		3
BCDMS-100							+0.5	1
BCDMS-120							+0.4	1
BCDMS-200							-0.4	1
BCDMS-280							-0.8	1

Table 4.3: Normalisation shifts applied to the datasets in the fits to H1 data only (a), H1 data only with a cut in $y < 0.35$ (b) and H1+BCDMS data (c). Absolute normalisations are given in per cent. The H1 MAIN dataset normalisation was fixed to the H1 high Q^2 normalisation since both datasets are largely taken in a common luminosity period. In addition, results are shown if all normalisations are left free. For the BCDMS dataset, the relative normalisations of various datasets taken at different beam energies are also given. These are observed to be unaffected by fixing or not fixing the H1 dataset normalisations. The last column represents the quoted uncertainties for the datasets.

4.1.5 Correlated Systematic Errors

As explained in chapter 3 the fit treats the effect of point-to-point correlations due to systematic uncertainties by introducing scale parameters s_λ and corresponding penalty terms in the χ^2 . Figure 4.7 shows these parameters exhibiting their correlation with α_s . As can be seen, all but two parameters are within their quoted uncertainties.

In the case of the uncertainties introduced by the photoproduction background subtraction γp , a direct correlation of $s_\lambda^{\gamma p}$ to the longitudinal structure function $F_L(x, Q^2)$ exists since both their

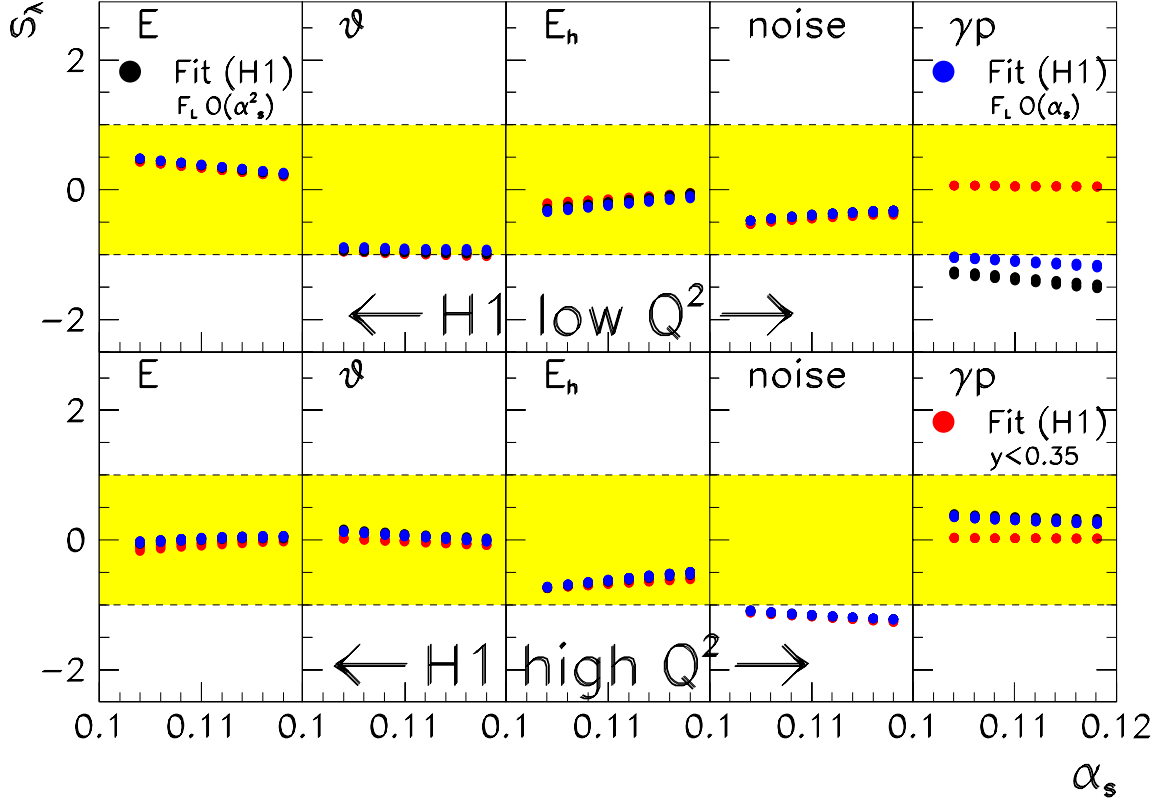


Figure 4.7: Dependence of the correlated error scale parameters s_λ as determined by a fit to H1 data (black points), H1 data with $y < 0.35$ and F_L computed to $\mathcal{O}(\alpha_s^2)$ (red points), compared to a fit to the same data fit F_L computed to $\mathcal{O}(\alpha_s)$ (blue points). The yellow bands indicate the $\pm 1\sigma$ estimated region.

effects become important in the relatively small kinematic region at high y . The large negative scale parameter means that the fit prefers F_L to be somewhat larger than calculated. A larger F_L in QCD could, for example, be calculated if F_L was expressed to $\mathcal{O}(\alpha_s)$: in figure 4.8 the effect of changing the F_L theory from $\mathcal{O}(\alpha_s^2)$ to $\mathcal{O}(\alpha_s)$ is displayed. As a result, F_L becomes bigger and χ^2 improves slightly in the fit, see figure 5.18 in chapter 5.

This correlation of a physics effect with a systematic error source parameter is at first sight a weakness of the approach, since a possible mismatch of data to theory may capture a systematic scale parameter which happens to be correlated with such an effect. However, claiming a data-to-theory mismatch which is still accounted for by a 1σ shift in the correlated systematics is not warranted either. The usage of the scale parameter method allows to track a possible deviation by observing the behaviour of the suspicious scale parameter with respect to other parameters in the fit. In this particular case, the effect on the γp background subtraction can be completely removed by applying a cut $y < 0.35$. Using this cut, the extracted physics quantities α_s and xg can be studied and an almost negligible effect on the result is found, as is described in section 4.5.

Another deviation is seen in the noise treatment of the high Q^2 data set which is the dominant

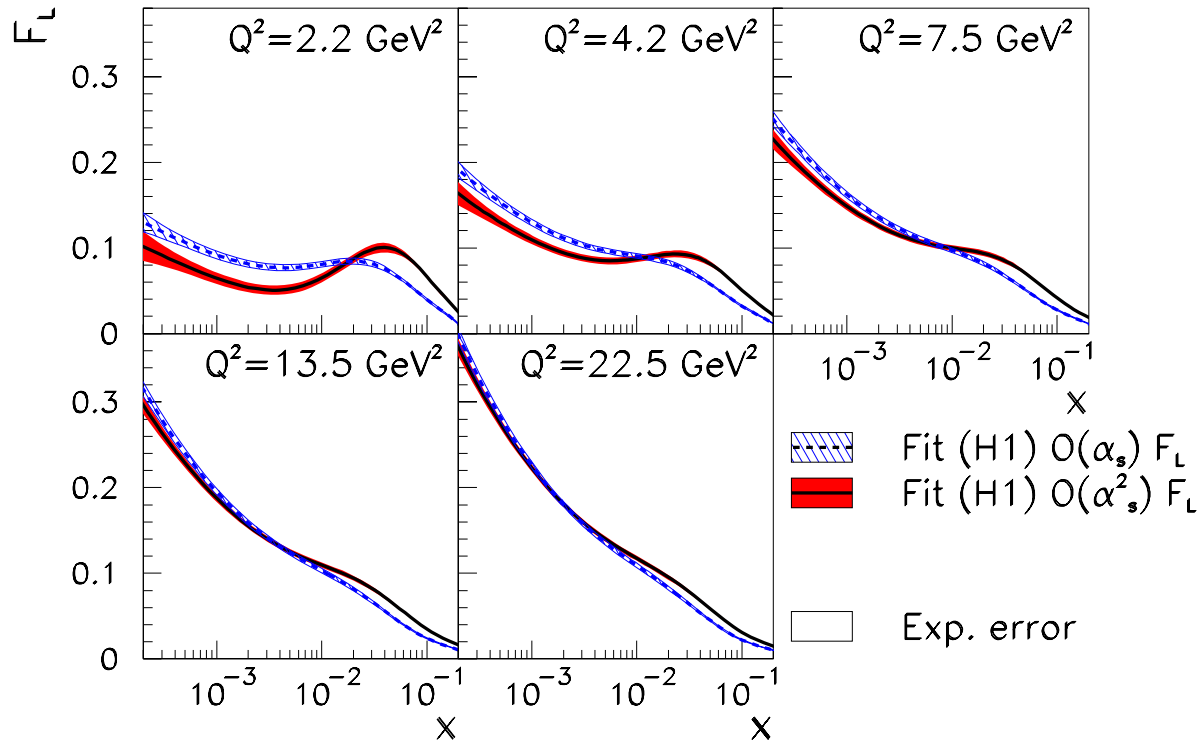


Figure 4.8: Longitudinal structure function F_L versus x in different bins of Q^2 . Shown is the difference between calculating $F_L(x, Q^2)$ to order $\mathcal{O}(\alpha_s)$ (dashed line) and $\mathcal{O}(\alpha_s^2)$ (solid line). F_L calculated to $\mathcal{O}(\alpha_s)$ is seen to be higher at low x as the

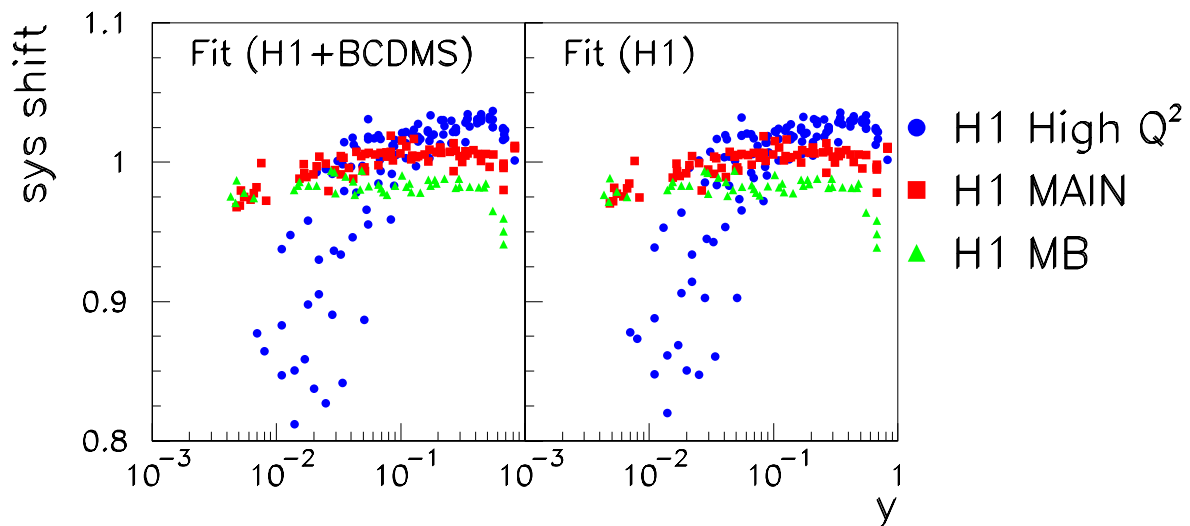


Figure 4.9: Total shift applied to the data points due to the correlated systematic errors in the fit to (a) H1+BCDMS and (b) H1 data. At $y < 0.05$, the points are moved to the edge of their estimated correlated error.

correlated error source at low y . Here, the effect can be traced to 20 points in the high Q^2 data set which are moved to the edge of their estimated systematic uncertainty. Figure 4.9 shows the correlation of the shift to the data with y attributed due to the correlated systematics errors. These points can be removed from the fit by a cut $y > 0.03$ applied to the high Q^2 data. These points have no effect on the extracted gluon distribution and their impact on the extraction of α_s will be covered in the following chapter.

4.2 Effect of the Q_{min}^2 Cut

An extension of the analysis to low values of Q^2 and x is of interest to study possible deviations from NLO DGLAP evolution. The effect of including data at low values of Q^2 is twofold. On the one hand, the DGLAP evolution from the input scale to these points is performed into the region where α_s becomes large and the convergence of the perturbation series thus becomes worse. Also, in the low Q^2 region higher twist effects, especially at higher x , become important proportional to $1 + h(x)/Q^2$ where $h(x)$ is a suitably chosen polynomial parameterising the x dependence.

On the other hand, the measurement of the slope $(\partial F_2 / \partial \ln Q^2)_x$ requires at least two data points with different Q^2 above Q_{min}^2 for fixed x . Thus the minimum value x_{min} at which this slope can be measured depends on Q_{min}^2 . Again, in the region of low x departures from the DGLAP prediction are expected since terms proportional to $\log(1/x)$ become important which are neglected in the DGLAP equations.

Thus the dependence of the fit result on the chosen Q_{min}^2 is studied systematically. Figure 4.10 shows the H1 F_2 data for $x \leq 8 \cdot 10^{-4}$ together with the fit curves for different values of Q_{min}^2 . The fit with $Q_{min}^2 = 1.5 \text{ GeV}^2$ describes all the data very well. If Q_{min}^2 is raised, the fit curves extrapolated below $Q^2 = Q_{min}^2$ tend to undershoot the data excluded from the fit. The gluon distributions at $Q^2 = 5 \text{ GeV}^2$ obtained from these fits are shown in figure 4.11 in the low x range where the gluon distribution is constrained. They are consistent within the estimated uncertainty in the overlapping regions. According to equation 4.1 the derivative $(\partial F_2 / \partial \ln Q^2)_x$ determines the gluon distribution at a value of approximately $2x$. The gluon distributions in figure 4.11 are therefore shown only down to $x \simeq 2x_{min}$.

Figure 4.12 shows the resulting pull distributions on varying Q_{min}^2 . The pulls are centered and no local deviations are observed. Extension of this study into the region of $Q^2 \simeq 1 \text{ GeV}^2$ is of interest. It requires precision data in a large range of x [73]. For such Q^2 values the gluon distribution $xg(x, Q^2)$, in leading twist NLO QCD, is observed to approximately vanish at low x acquiring a valence-like shape. This behaviour may be largely influenced by still higher order corrections [74].

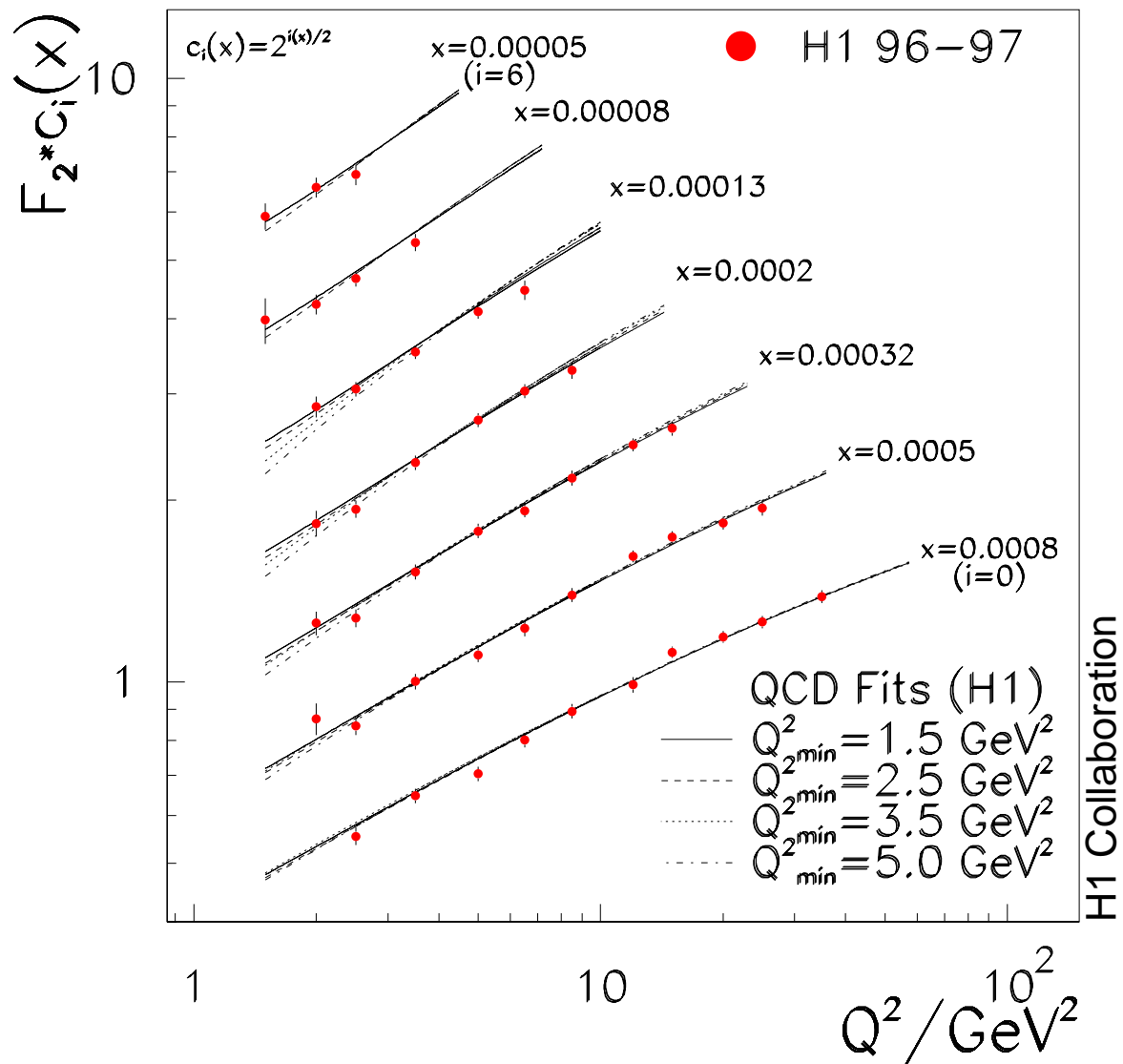


Figure 4.10: Effect of the Q_{\min}^2 cut on the structure function F_2 in the DGLAP QCD fit to the H1 data (points). The curves represent fits with different minimum Q^2 values. The central fit uses $Q_{\min}^2 = 3.5 \text{ GeV}^2$.

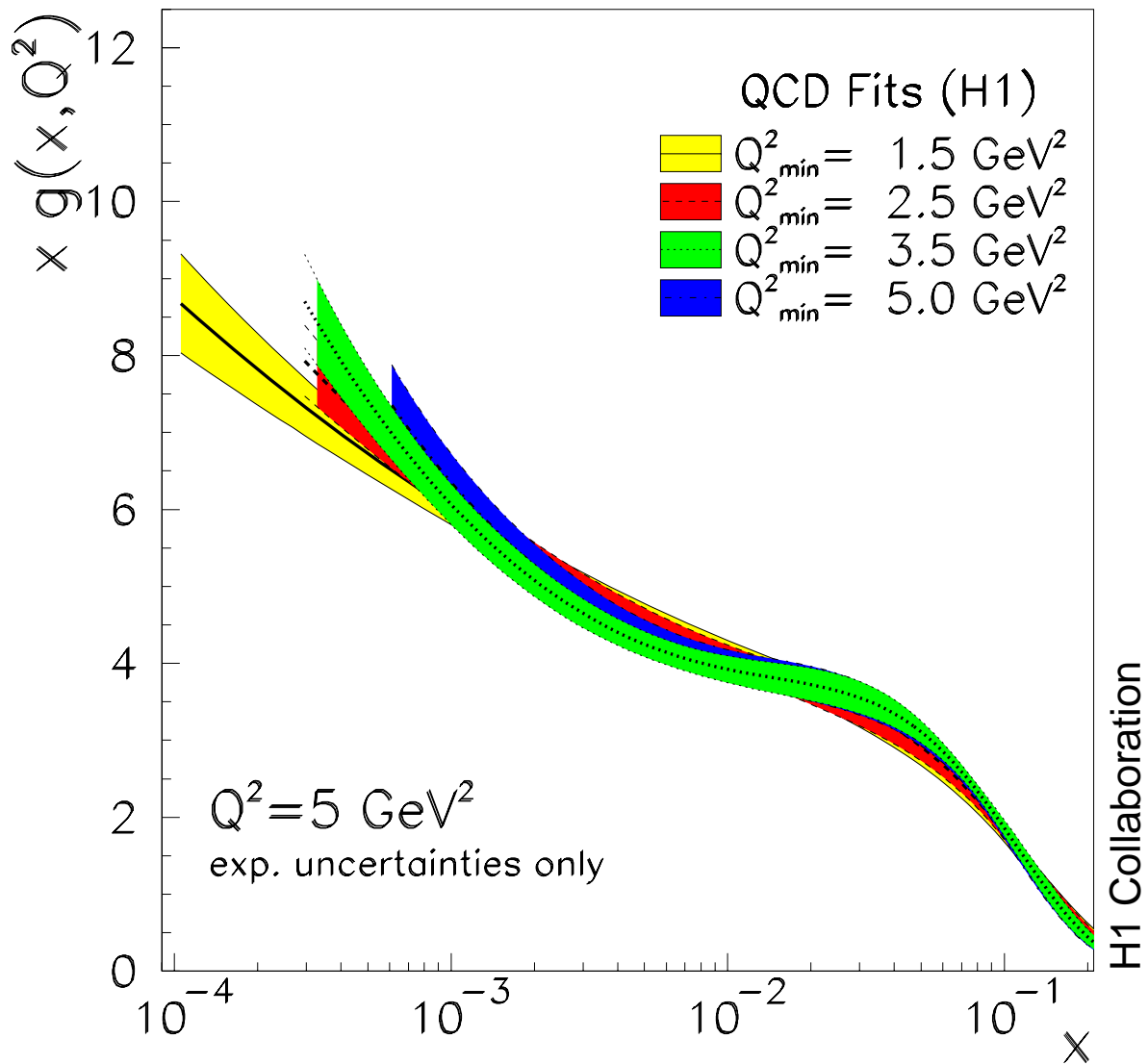


Figure 4.11: Effect of the Q_{min}^2 cut, applied in the DGLAP QCD fit to the H1 data, on the gluon distribution at $Q^2 = 5 \text{ GeV}^2$. The distributions are shown down to x values corresponding to twice the minimum x values of the data which allow a Q^2 slope to be measured.

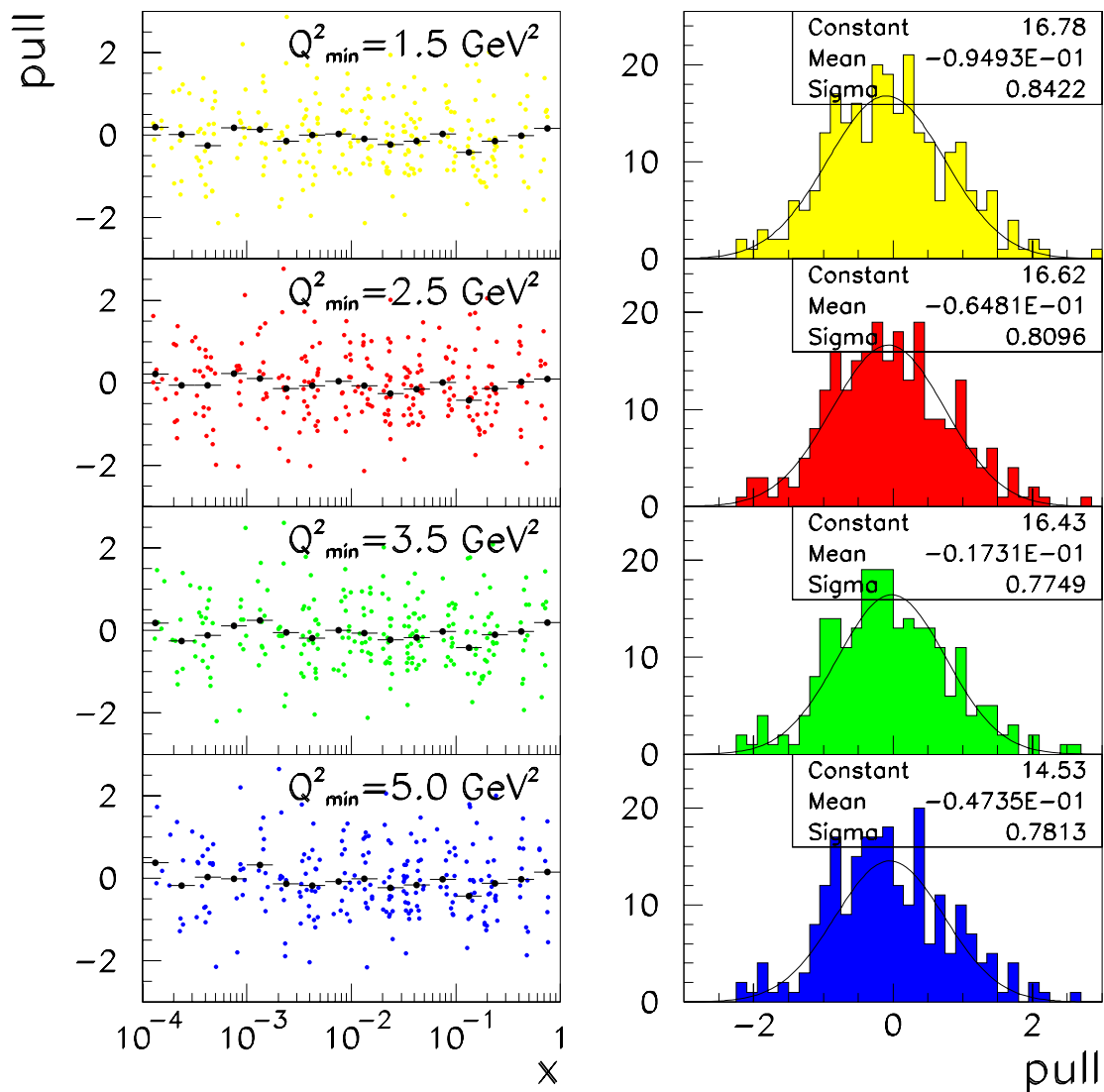


Figure 4.12: Effect of the Q_{min}^2 cut on the pull distributions for fits to H1 data alone. Left: Pulls of the H1 data points versus x . Right: Pull distributions with a gaussian fit. The analysis uses $Q_{min}^2 = 3.5 \text{ GeV}^2$ as default.

4.3 Results

The gluon distribution from the fit to the H1 and the BCDMS proton cross section data is shown in figure 4.15 for $Q^2 = 5, 20$ and 200 GeV^2 with error bands illustrating the uncertainty of the analysis. As qualitatively discussed above, the DGLAP evolution leads to a gluon distribution which rises dramatically towards small x and increasing with Q^2 .

The inner error band represents the experimental uncertainty of the determination of xg for α_s fixed. This fit, however, simultaneously determines $xg(x, Q^2)$ and α_s , with the results for the latter being discussed in the following chapter. The error band for both the experimental as well as the α_s uncertainty is illustrated by the middle error band. Due to partial cancellation of errors in the combined fit, this error band is smaller as compared to the more traditional analysis where α_s is being fixed to its central value, taken for example from the world average, and the lower and upper bounds obtained by repeating such a fit with α_s being fixed to the upper ($\alpha_s + \delta\alpha_s$) and the lower ($\alpha_s - \delta\alpha_s$) value given by the uncertainty $\delta\alpha_s$, see figure 4.13

The full error band includes in addition the same uncertainties connected with the fit ansatz, listed in table 5.3, as for the determination of α_s , described in chapter 5. The main contributions to these model uncertainties are depicted in figure 4.14. For the low x behaviour of xg these are dominated by the choice of Q_{min}^2 , as discussed in section 4.2.

The inner solid line illustrates the behaviour of xg , as determined with the H1 data alone, which is seen to be in very good agreement with the fit to the H1 and BCDMS data. This is expected since the H1 data fix the gluon distribution at low x and the BCDMS data only contribute for $x > 0.07$. Figure 4.16 compares the experimental uncertainties of the gluon distribution for fits to the H1, H1+NMC and the H1+BCDMS proton target data with α_s fixed. At low x , the experimental accuracy is determined entirely by the H1 data, see insert of figure 4.16. The gluon distribution as determined by the fit to the H1+NMC data is found to be somewhat lower at low x , but this behaviour is caused by the NMC data below a $Q^2 < 8 \text{ GeV}^2$ as can be seen in figure 4.17. If these NMC data points are removed, the gluon distributions obtained from H1 and fixed proton target data agree very well with each other and to a gluon distribution extracted from a fit to H1+BCDMS proton and deuteron target data.

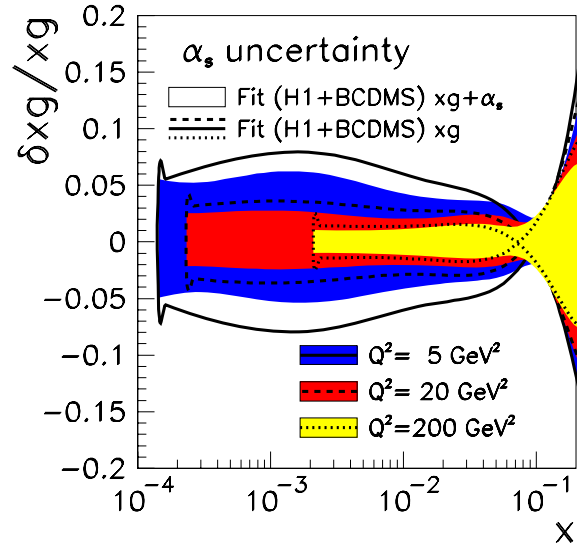


Figure 4.13: Relative error on the gluon distribution at $Q^2 = 5, 20$ and 200 GeV^2 . Compared is the uncertainty due to α_s from the combined fit (boxes) with a fit where α_s is fixed to 0.1150 for the central value, and the upper and lower bounds for the gluon distribution are obtained by fixing α_s to $\alpha_s \pm \delta\alpha_s$ (lines). The upper ($\delta\alpha_s = +0.0019$) and lower ($\delta\alpha_s = -0.0018$) uncertainty as are obtained by the α_s analysis described in chapter 5.

Figure 4.18 shows the gluon distribution determined from H1+BCDMS data by this analysis to a preliminary result by the ZEUS collaboration [63]. In that analysis, a rather global fit using the

most recent ZEUS data, fixed target and neutrino nucleon data from the CCFR collaboration with a standard flavour decomposition is performed. The model assumptions used are very different concerning the parameterisation, the value of α_s , and the correlated systematic error and heavy flavour treatment. If, in a technical study, the same model assumptions are employed forcing α_s to $\alpha_s=0.118$ and adopting a 3 parameter gluon distribution, which is disfavoured by an increase of 20 units in the total χ^2 in this analysis, see figure 5.25, the central values are found to agree very well, see figure 4.19. The treatment of systematic errors is not the same in both analyses to which partly the difference in accuracy has to be attributed.

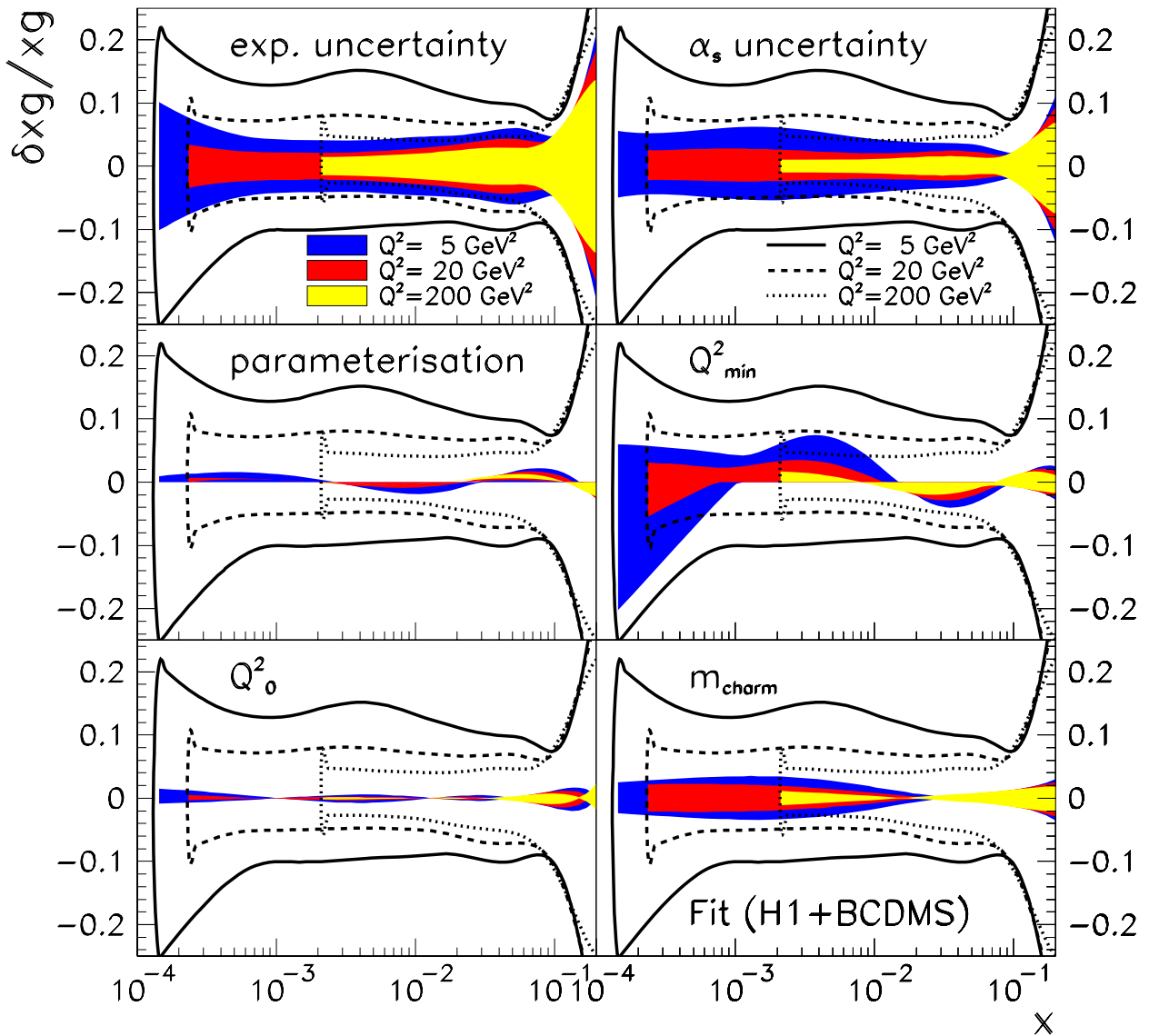


Figure 4.14: Relative uncertainty of the gluon distribution due to the most important error sources as obtained from a fit to H1+BCDMS data. Shown in coloured boxes are the relative errors for the Q^2 values 5, 20, 200 GeV². The corresponding total error is plotted in solid, dashed and dotted lines. For xg , the dominating uncertainty source apart from the experimental error are seen to be α_s and Q^2_{min} .

These analyses determine xg from the scaling violations of F_2 . It is more accurate but consistent with determinations of the gluon distribution by the H1 experiment in open charm [75] production, to be discussed in the next section, and deep-inelastic dijet [76] production, shown in figures 4.22 and 5.21, respectively.

Note that the different ways of measuring gluon related quantities provide an important cross check to the theory. It is conceivable that deviations to the DGLAP formalism are present in the

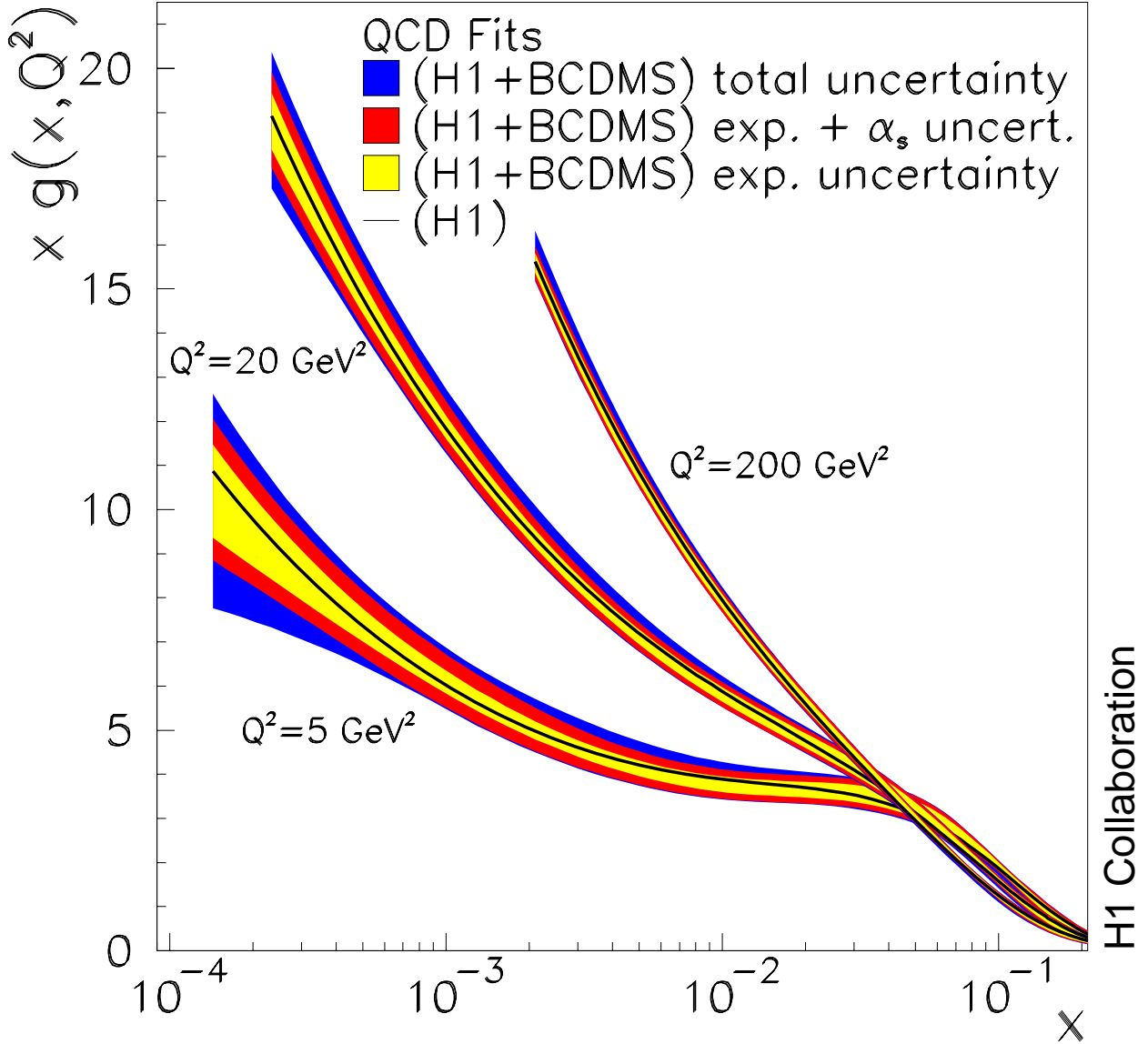


Figure 4.15: Gluon distribution resulting from the NLO DGLAP QCD fit to H1 ep and BCDMS μp cross section data in the massive heavy flavour scheme. The innermost error bands represent the experimental error for fixed $\alpha_s(M_Z^2)=0.1150$. The middle error bands include in addition the contribution due to the simultaneous fit of α_s . The outer error bands also include the uncertainties related to the QCD model and data range. The solid lines inside the error band represent the gluon distribution obtained in the fit to the H1 data alone. This distribution is obtained at $Q_0^2 = 4 \text{ GeV}^2$, and the results at larger Q^2 are obtained by the evolution prescribed by DGLAP QCD.

data but are absorbed by the flexibility provided by the QCD model parameters in the inclusive fits. A possible deviation from the DGLAP formalism may manifest itself in a contradiction to another gluon dependent quantity, measured i.e. in jet or heavy quark production and its prediction based on the inclusive gluon distribution. Such gluon dependent quantities are F_2^{cc} and F_L , discussed in the following sections.

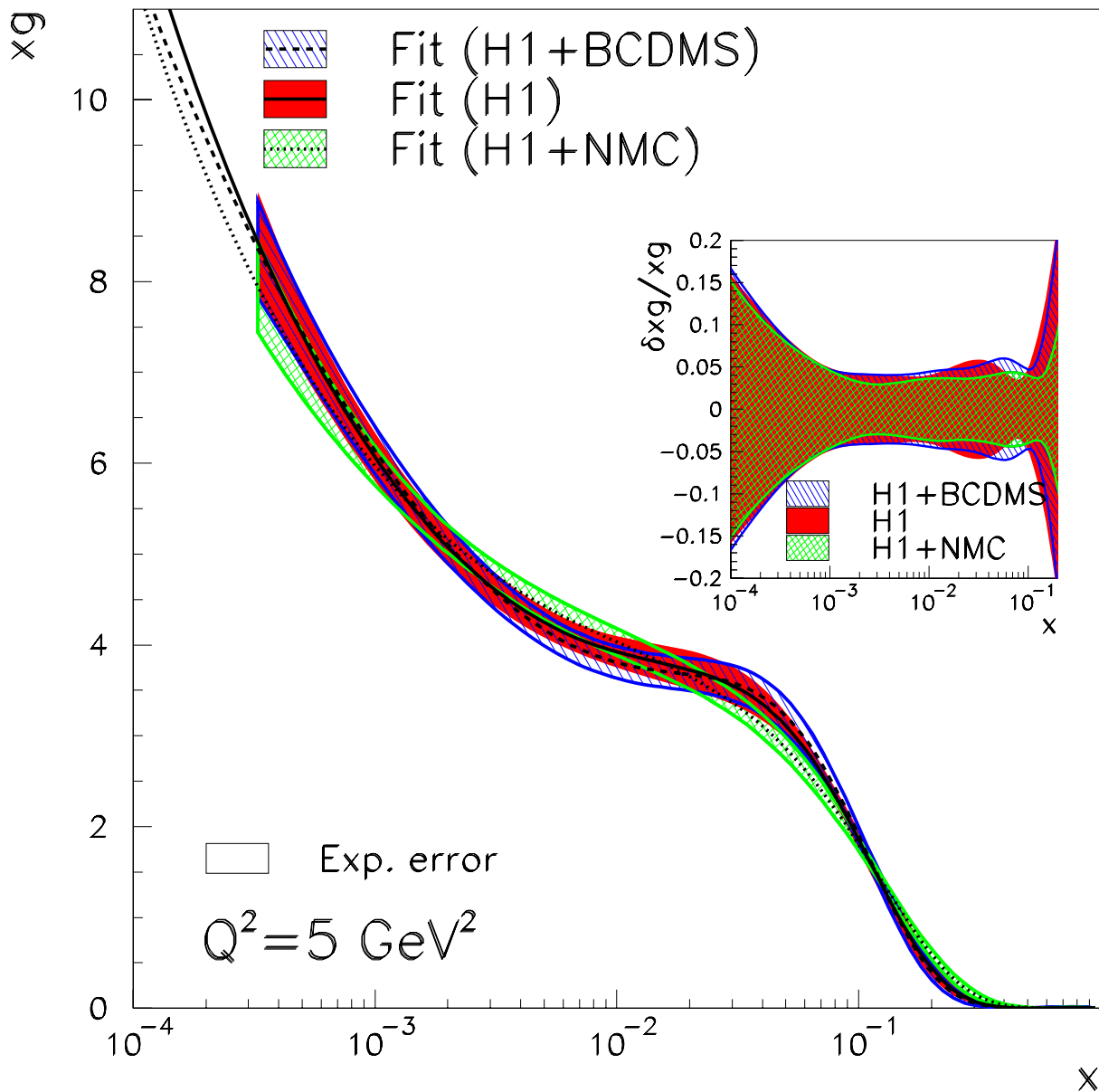


Figure 4.16: Comparisons of the gluon distributions at $Q^2 = 5 \text{ GeV}^2$ obtained in fits to H1, H1+BCDMS and H1+NMC proton target data. The error bands show the experimental uncertainty. In the fits to H1 and H1+BCDMS data, the low x behaviour is dominated by the H1 data since the x range of the BCDMS data is limited to $x \geq 0.07$. The insert shows the relative errors of all the determinations. It is visible that the uncertainty of the gluon distribution at low x is determined by the H1 data alone.

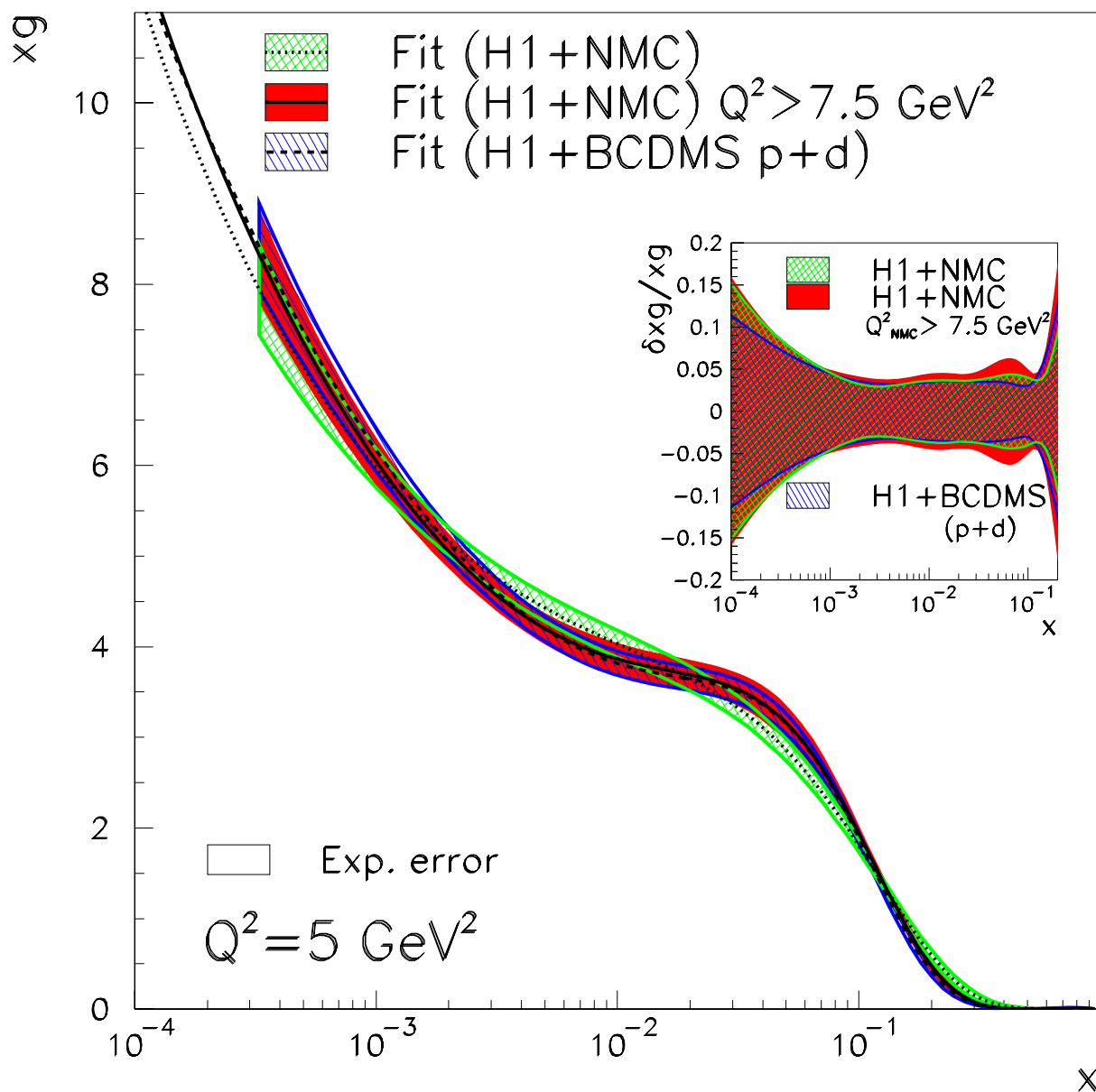


Figure 4.17: Comparisons of the gluon distributions at $Q^2 = 5 \text{ GeV}^2$ obtained in fits to H1+BCDMS proton and deuteron target data, to H1+NMC proton target data and H1+NMC proton target with a cut in $Q^2 > 7.5 \text{ GeV}^2$ in the NMC data. The error bands show the experimental uncertainty. The gluon distribution from fits to H1+BCDMS proton and deuteron target data are seen to agree very well when a cut $Q^2 > 7.5 \text{ GeV}^2$ is applied in the NMC data.

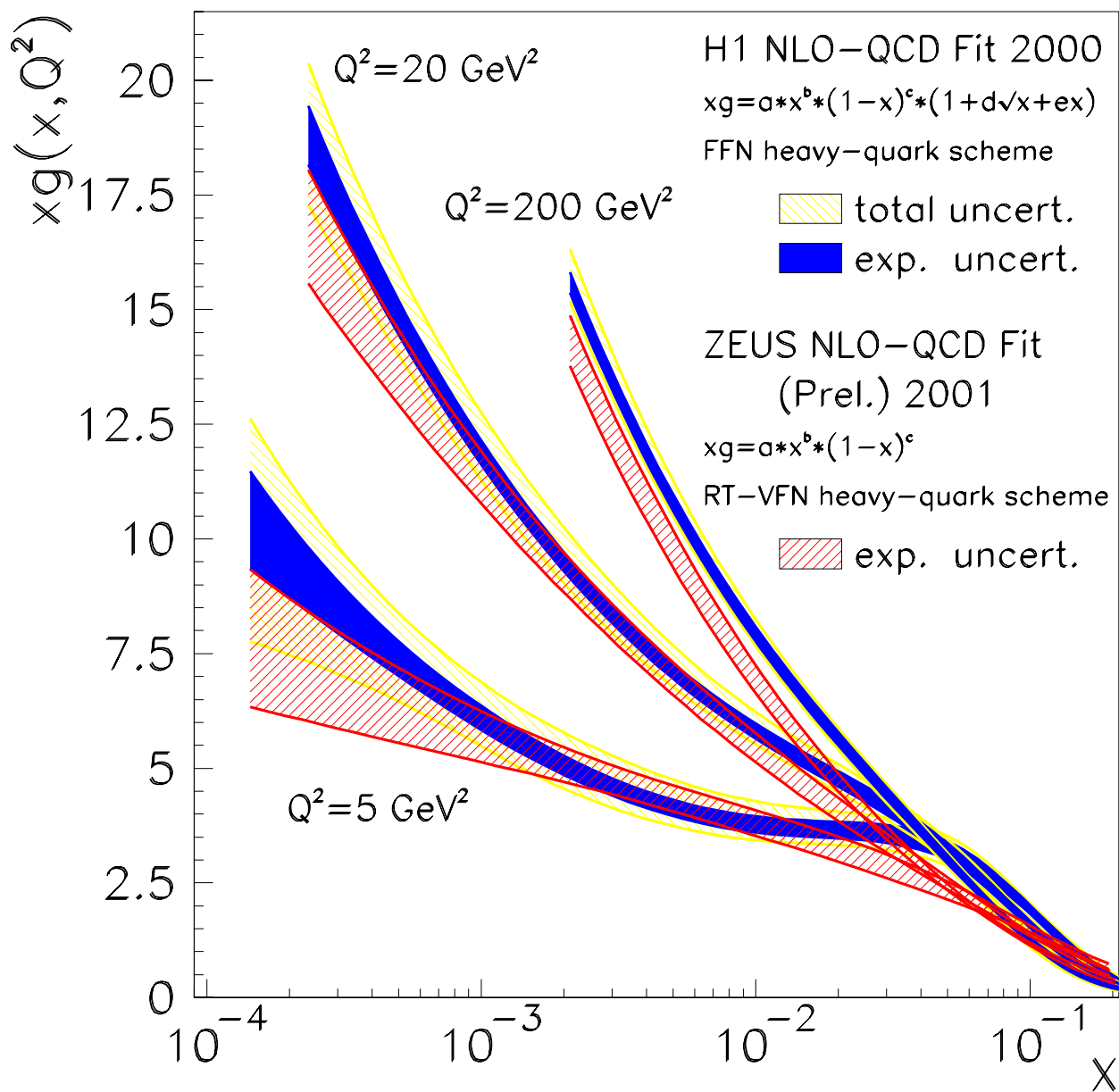


Figure 4.18: Comparison of the gluon distributions at $Q^2 = 5, 20, 200 \text{ GeV}^2$ for the fits by the H1 and ZEUS collaborations. The model assumptions differ, see text.

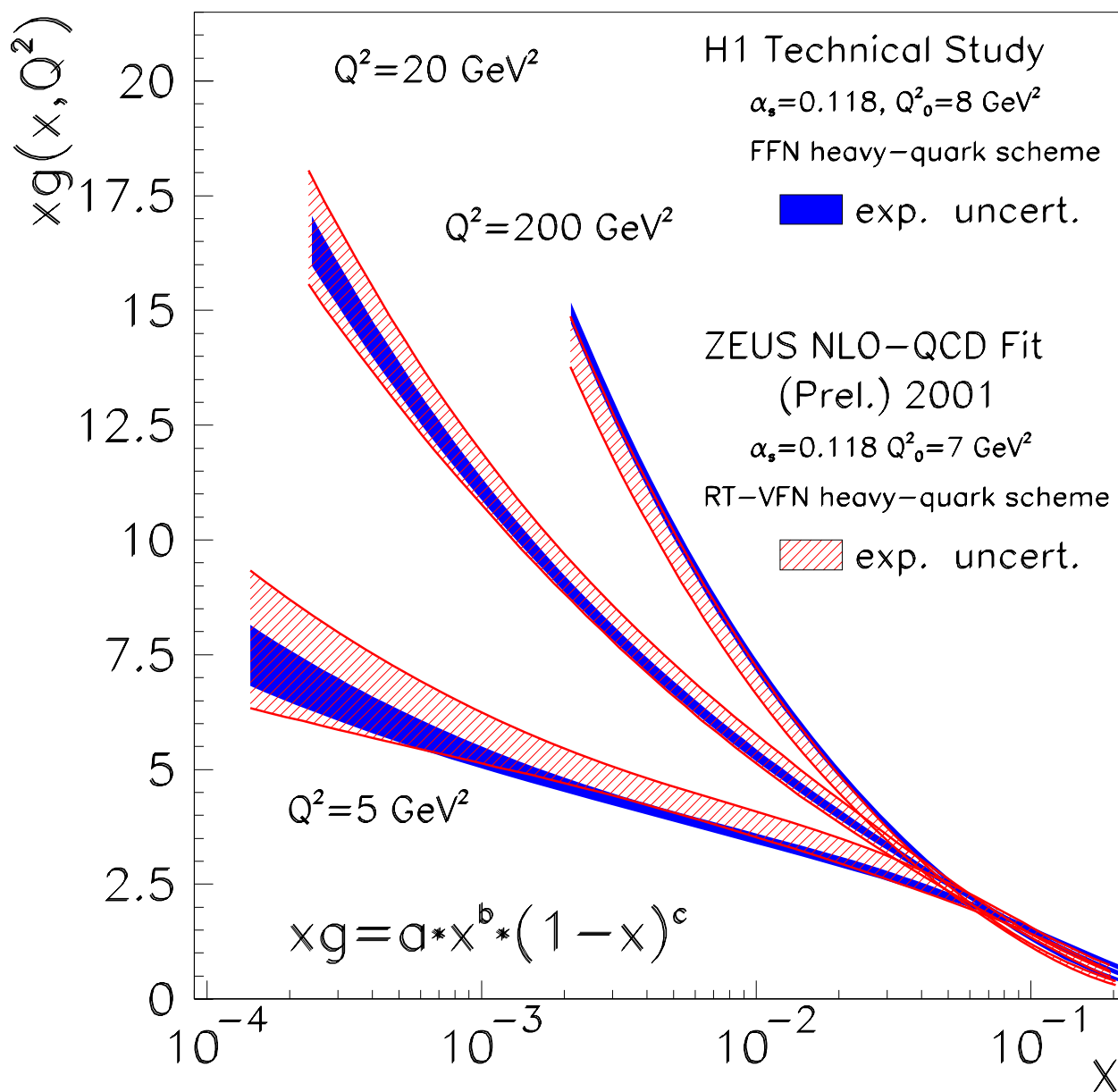


Figure 4.19: Comparison of the gluon distribution results at $Q^2 = 5, 20, 200 \text{ GeV}^2$ for the fits by the H1 and ZEUS collaborations using the same model assumptions. Only experimental errors are shown. The treatment of correlated systematic errors differs, which accounts for part of the observed difference in accuracy. At Q^2 , the impact of the different heavy quark mass treatments is visible. The Roberts-Thorne variable flavour number scheme [77] used in the ZEUS analysis approaches the massless heavy quark scheme at high Q^2 which is systematically lower, compare figure 4.25 and see section 4.4.

4.4 Comparison to Heavy Quark Production Results

In QCD quarks are considered 'heavy' or 'light' depending on the relation of the heavy quark mass to the Λ_{QCD} parameter. Thus c, b, t are heavy quarks as $m_{HQ} \gg \Lambda_{QCD} = 250 \text{ MeV}$.

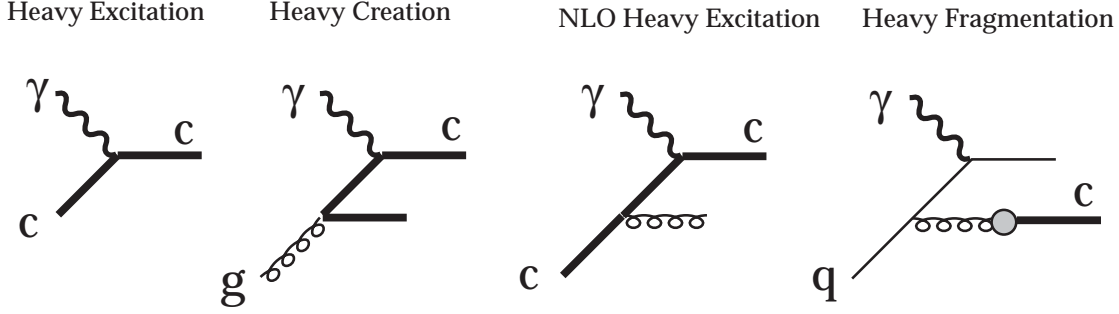


Figure 4.20: Basic processes for DIS heavy quark production.

For momentum transfers $Q^2 \gg m_{HQ}^2$, the heavy quark mass effects can be neglected and heavy quarks can be treated as massless partons. The dominant heavy quark excitation diagram is depicted in figure 4.20 a). For momentum transfers $Q^2 \approx m_{HQ}^2$ however, mass effects suppress the heavy excitation term and the $\mathcal{O}(\alpha_s)$ diagrams (figure 4.20 b-d) become important. Heavy quarks are then predominantly produced via photon-gluon fusion (Figure 4.20 b), a process which has early been considered as an ideal test of non-Abelian gauge field theories [78, 79, 61].

4.4.1 Results for F_2^{cc} in the NLO DGLAP Fits

Within the Photon Gluon Fusion approximation the charm structure function F_2^{cc} is given as the convolution of the heavy quark coefficient function with the gluon density, i.e. $F_2^{cc}(x, Q^2, m^2) = e_c^2 \cdot f_g \otimes H_{2,g}$. Since the gluon density is large and the charge of the charm quark is $2/3$, F_2^{cc} is thus expected to be sizeable at low x .

Measurements by H1 [80] and ZEUS [81] have determined the contribution of F_2^{cc} to about 20%, see figure 4.21. For this analysis it is important to note that the gluon density appears here in a different way than in the DGLAP evolution equations. Therefore charm production is an important process for checking the consistency of the determination of the gluon density in the proton. This can be done either by reconstructing the gluon kinematics from the tagged charmed meson, see figure 4.22, or by measuring F_2^{cc} as the contribution of events with charmed mesons to the total cross section. Figure 4.23 compares a recent measurement of F_2^{cc} [80] with the calculation within the fits to H1+BCDMS data described below. One observes a trend in the data to exceed the calculation, yet there is no discrepancy outside the single or twice the experimental error.

The main model uncertainties of F_2^{cc} determined by the fits to H1+BCDMS data are depicted in 4.24. The overall dominating uncertainty is the dependence of the charm mass which is taken to be $m_c = 1.4 \text{ GeV}$ and varied by $\delta m_c = 0.1 \text{ GeV}$.

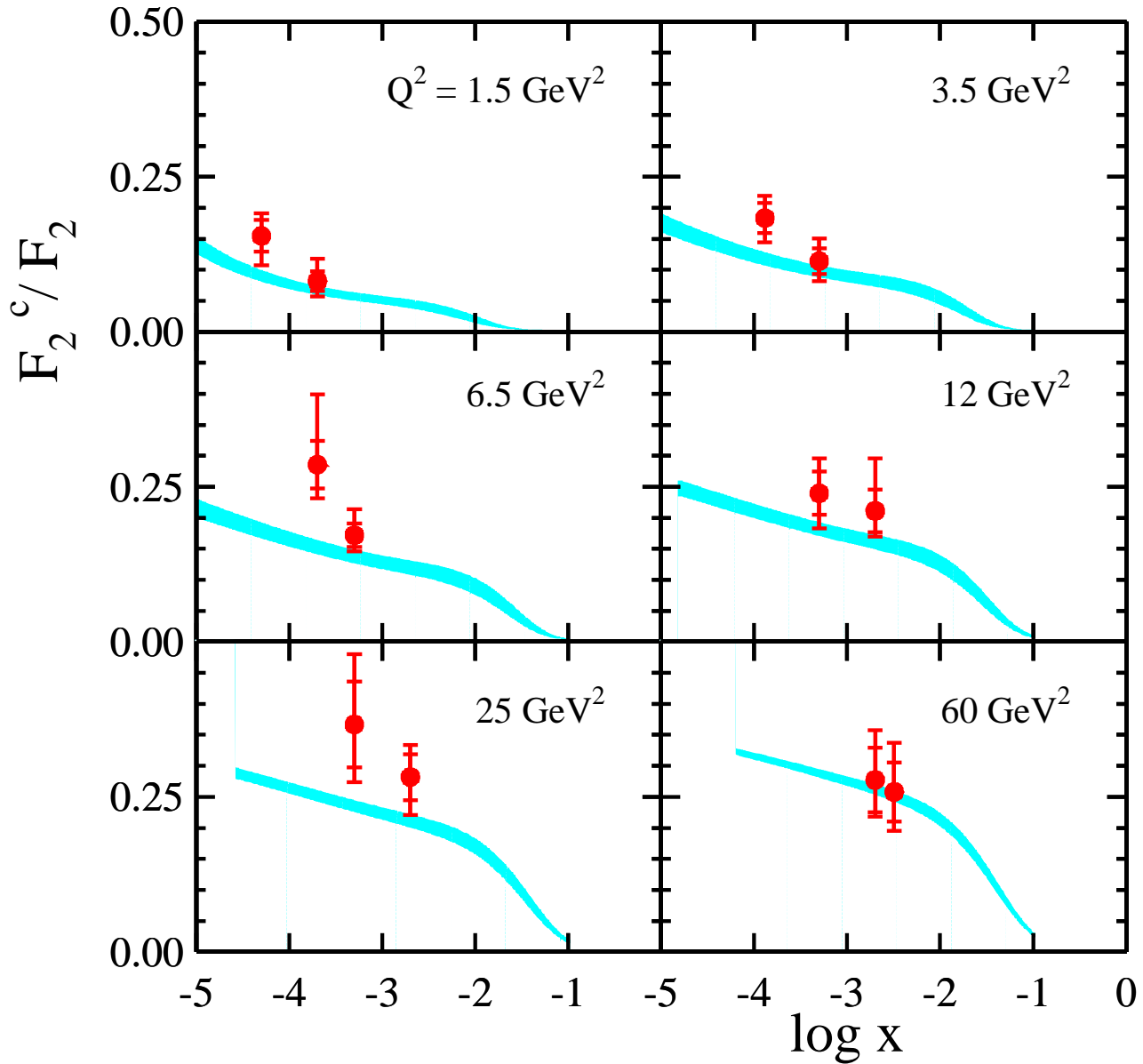


Figure 4.21: The ratio of F_2^{cc} over F_2 as derived from inclusive D^{*+} production as a function of x for different bins in Q^2 . The error bars refer to the statistical (inner) and the total error (outer), respectively. The shaded bands represent the predictions of the NLO DGLAP evolution obtained from this analysis determined by the uncertainty of the charm quark mass of about ± 100 MeV.

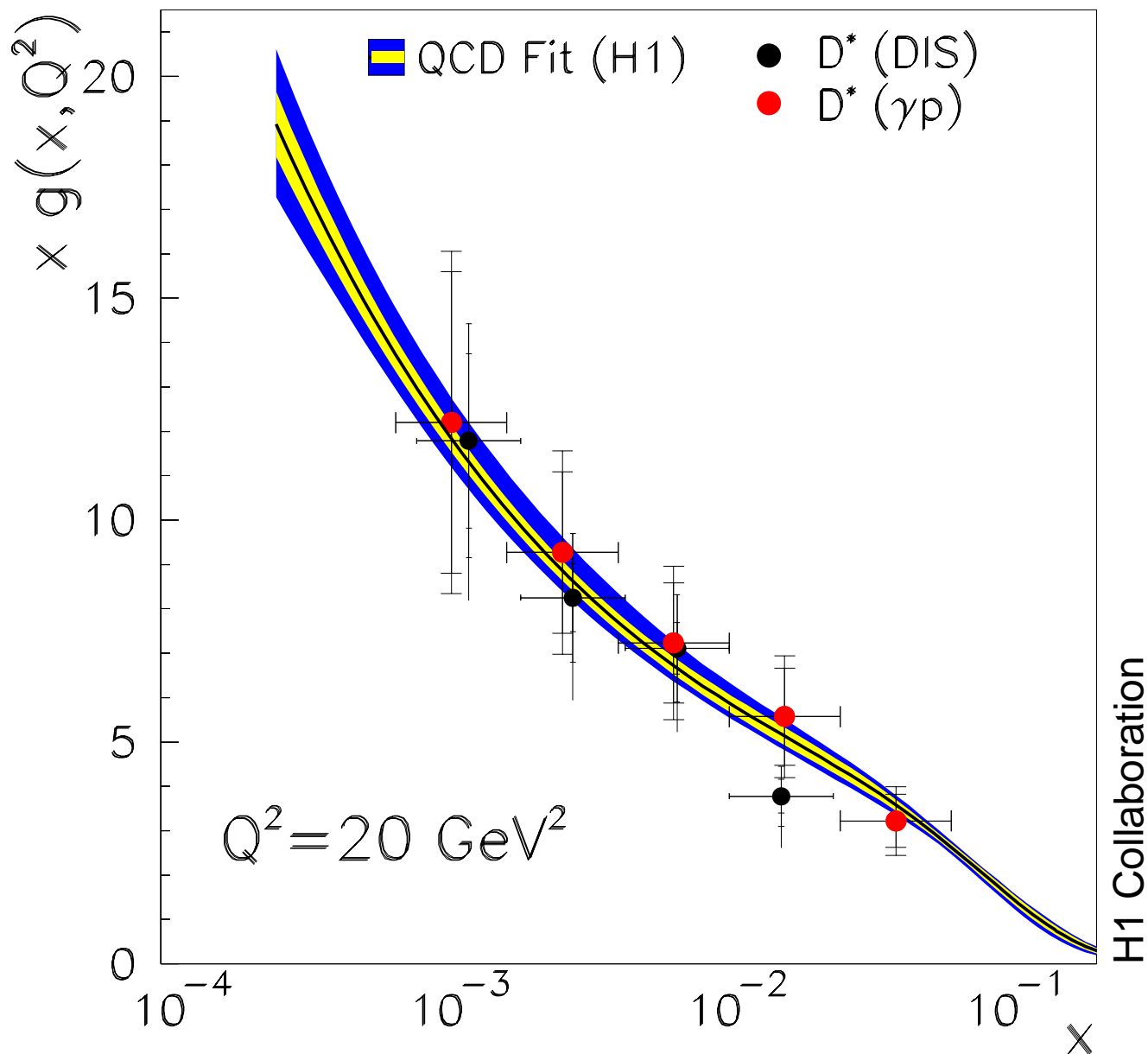


Figure 4.22: Comparison of the gluon distribution from scaling violations at $Q^2 = 20 \text{ GeV}^2$ with results from open charm production in DIS and photoproduction [82, 83, 84]. These analyses were based on 1995 data.

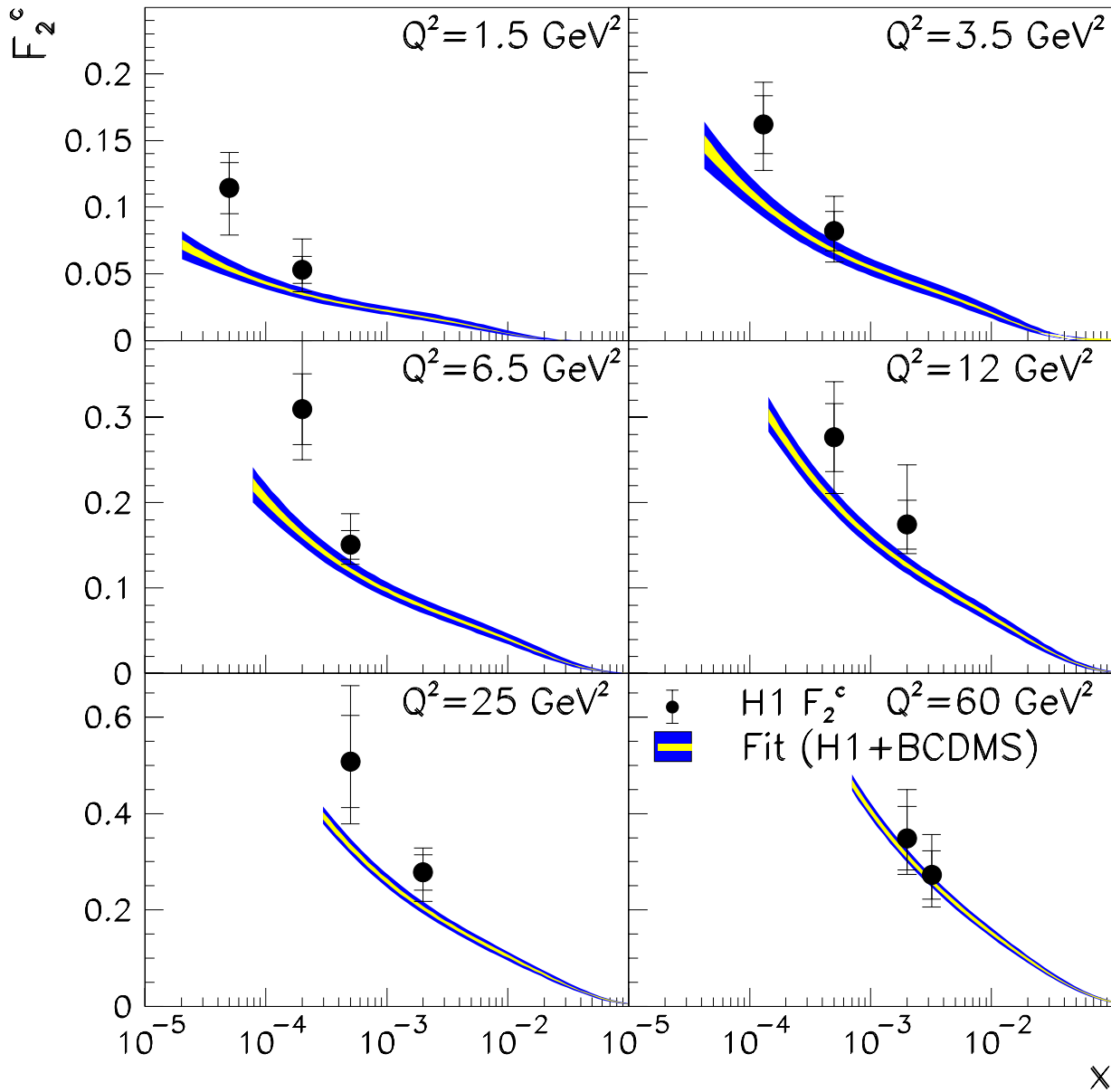


Figure 4.23: The charm contribution F_2^{cc} to the proton structure function F_2 [80]. The error bars refer to the statistical (inner) and the total error (outer). The shaded inner (outer) band reflects the experimental (total) uncertainty on F_2 as determined by the NLO DGLAP fits of this analysis. The total uncertainty is dominated by the charm mass uncertainty, see figure 4.24.

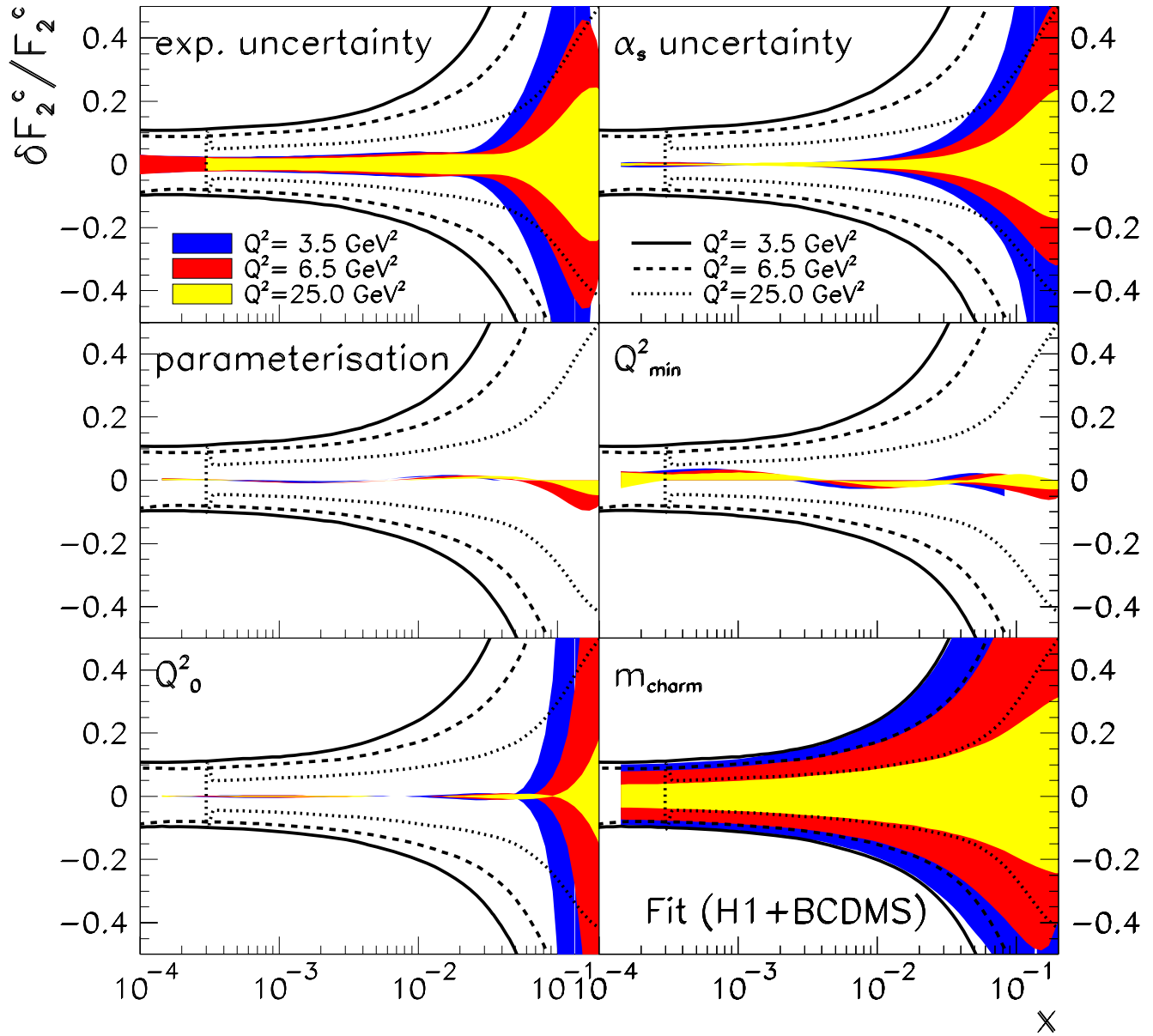


Figure 4.24: Relative errors on F_2^{cc} by different model uncertainties. The sources of uncertainty are the same as given for the gluon distribution uncertainty, see figure 4.14. The uncertainty is dominated by the assumed 100 MeV error of m_c .

4.4.2 Heavy Quark Treatment and Scheme Dependence

Since the charm quark contribution is so large, the photon-gluon fusion process has to be calculated in NLO for a consistent treatment. These calculations were done in [85] and [86]. The H1 fit uses the program of [87]. The higher order corrections are due to virtual corrections, bremsstrahlung and Bethe Heitler scattering ($\gamma^* q \rightarrow c\bar{c}q$) [88]. In NLO there appears a correction to the $H_{2,g}$ function and a part from the convolution of the quark densities with a coefficient function $H_{2,q}$ in NLO. As was shown in [89], the quark contribution is smaller than 5% at low x .

Since F_2^{cc} depends on Q^2 and on the charm quark mass m_c , there are two scales in the calculation. Their relation defines which prescription one may use for the heavy flavour treatment.

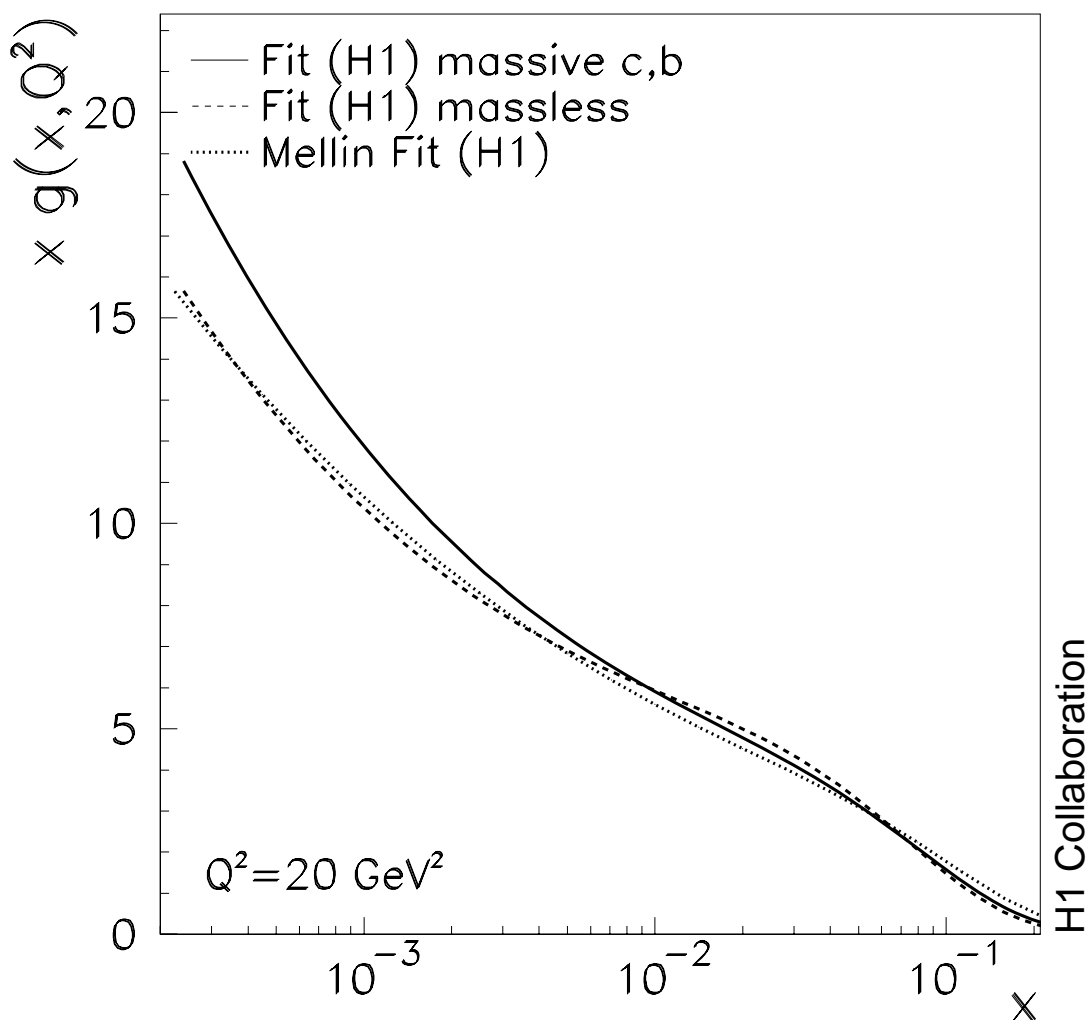


Figure 4.25: Comparison of gluon distributions obtained in NLO DGLAP QCD fits to the H1 data, using different prescriptions: solid curve: standard fit using the massive heavy flavour scheme; dashed curve: fit in the massless scheme; dotted curve: fit in the massless scheme using a Mellin n space program.

Near the charm production threshold, one considers three light flavours, i.e. the proton to consist of three light quarks u, d, s and the gluon, while charm quarks arise not from a proton charm quark distribution but via photon-gluon fusion. This is the massive flavour scheme or three fixed flavour number scheme (3FFNS). Away from the threshold, one considers 4 light quarks with 4 parton densities which defines the four fixed flavour number scheme (4FFNS) which is also called the massless scheme.

In 1997 an attempt was made to define a procedure which interpolates between these fixed flavour number schemes and which are called variable flavour number schemes (VFNS). In leading order this was done by [90] and a higher order generalisation was considered [91]. The MRST group introduced a smoothness derivative criterion which leads to a similar, but distinct solution of this problem [92].

The charm structure function calculated in QCD depends on the treatment of charm, and so does the gluon distribution. These quantities are thus only defined in a theoretical context. The same is true for bottom quarks which, however, contribute only at the per cent level to the inclusive scattering cross section. In this analysis, the 3FFNS scheme is used, treating u, d, s as light quarks and the charm and bottom quarks as heavy in next-to-leading order.

The dependence of the gluon distribution on the heavy quark treatment is depicted in figure 4.25. If the massive quark description for charm and beauty production is replaced by the massless treatment of heavy quarks, the gluon distribution changes as illustrated. The gluon distribution in the massless fit is about 15% lower at small x as compared to the standard result. A consistent cross check of this massless fit result is obtained with a QCD evolution program based on the Mellin n space technique [93]. This technique provides an alternative solution to the DGLAP evolution of massless quarks, solving the convolution integrals by reducing them to simple products via Mellin transformations.

4.5 QCD Prediction for $F_L(x, Q^2)$ and its Uncertainties

Another quantity with complementary information about the gluon distribution is the longitudinal structure function F_L which leads to a damping effect of the reduced double differential cross section σ_r towards low x , as can be seen in figure 4.26. Effects related to F_L become appreciable only at highest $y > 0.6$, since F_L enters the cross section with a kinematical weighting factor proportional to y^2 . This is a tiny fraction of the logarithmic phase space of the H1 data in x and Q^2 as can be seen in figure 2.2.

The QCD fit to the H1 F_2 data allows a prediction to be made for the longitudinal structure function. $F_L(x, Q^2)$ is closely related to the gluon distribution, see equations 1.21 and 1.22. To order $\mathcal{O}(\alpha_s)$, an approximate relation [94] similar to the approximation 4.1 for xg can be obtained for $F_L(x, Q^2)$:

$$xg(x, Q^2) = \frac{3}{5} \cdot \left[\frac{3\pi}{4\alpha_s} F_L(0.4x, Q^2) - \frac{1}{2} \cdot F_2(0.8x, Q^2) \right], \quad (4.2)$$

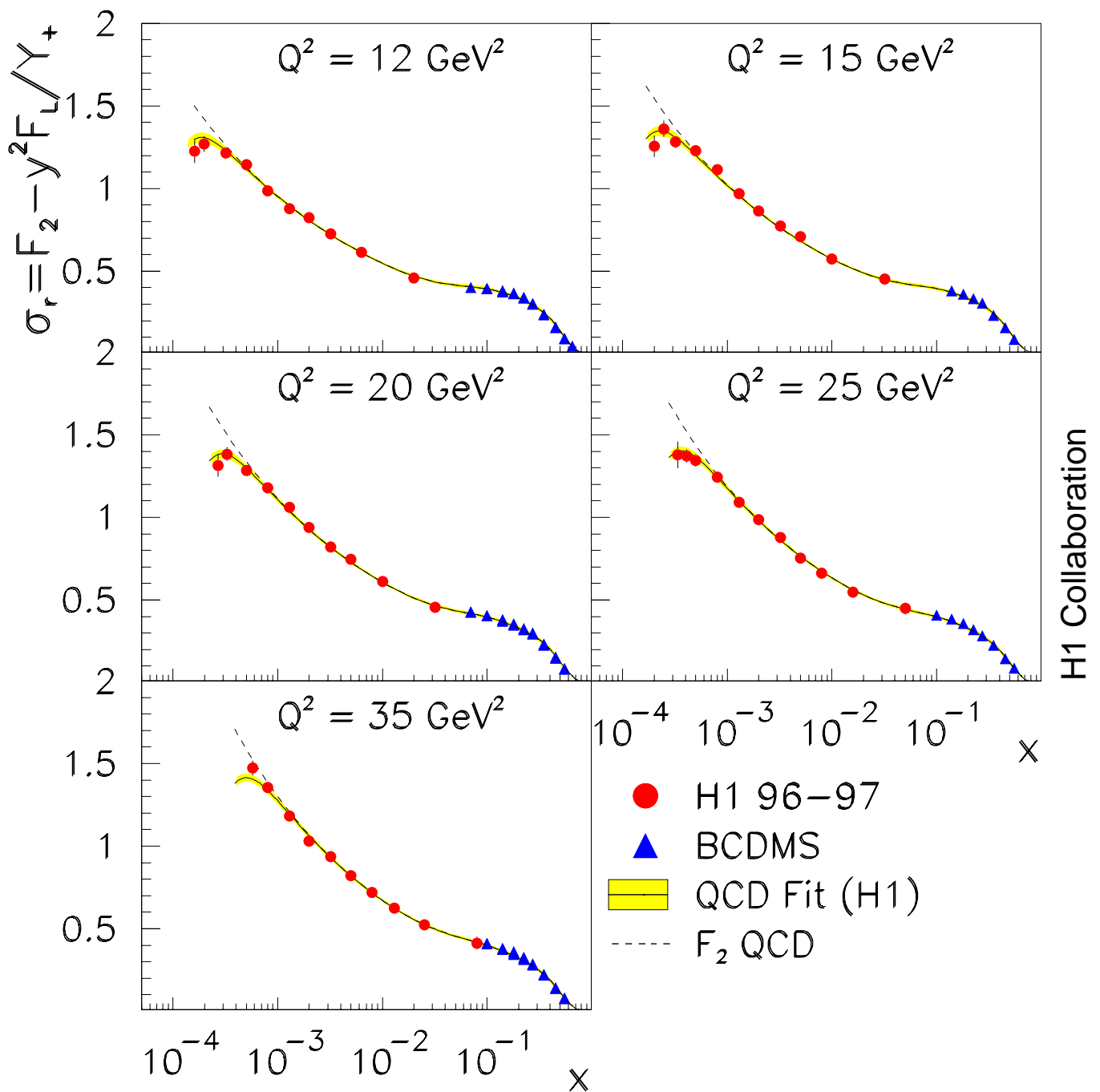


Figure 4.26: Measurement of the reduced DIS scattering cross section (closed points). Triangles represent data from the BCDMS muon-proton scattering experiment. The curves represent a NLO QCD fit to the H1 data alone, using data with $y < 0.35$ and $Q^2 \geq 3.5 \text{ GeV}^2$. The dashed curves show the F_2 structure function as determined with this fit. The error bands represent the experimental and model uncertainty of the QCD fit.

i.e. $F_L(x, Q^2)$ is essentially proportional to $\alpha_s \cdot xg(x, Q^2)$ at low x . From equation 4.1, it is evident that $(\partial F_2 / \partial \ln Q^2)_x$ is proportional to $\alpha_s \cdot xg(x, Q^2)$ as well. Thus, the scaling violations of F_2 provide a prediction for F_L^{QCD} . A potentially strong cross check of the theory is thus obtained by comparing F_L^{QCD} to measured values of F_L^{exp} .

However, a direct measurement of $F_L(x, Q^2)$ can only be performed by lowering the center of mass energy \sqrt{s} of the HERA collider and by comparing the double differential cross sections at fixed x and Q^2 for varying \sqrt{s} . Changing the center of mass energy \sqrt{s} can either be provided by lowering the beam energy of either beam [95] or using radiative events where the incoming lepton loses energy due to initial state radiation before the hard scattering event [96]. The latter technique suffers from statistical limitations and experimental challenges, whereas the former technique is envisaged at a later stage of the HERA collider program.

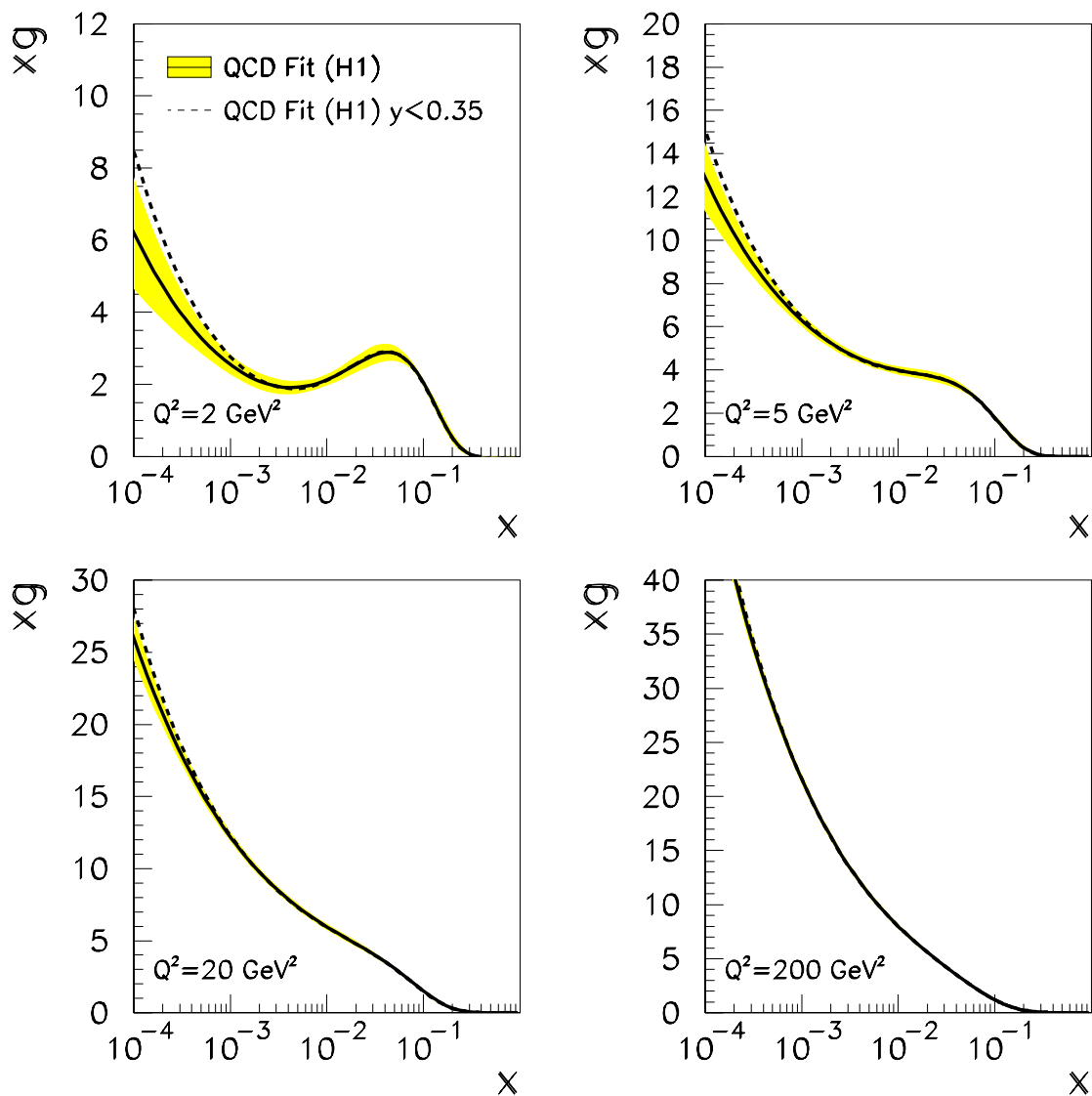


Figure 4.27: Comparison of gluon distributions obtained for the QCD fit to H1 data without (with) a cut in $y < 0.35$.

In the absence of a direct measurement, values of F_L can still be obtained by exploiting the fact that F_2 can be unambiguously extracted in a large kinematic range from the double differential cross section due to the kinematic suppression of F_L . For $y < 0.35$, F_2 extracted from σ_r is free of uncertainty due to F_L and thus can be used to obtain a prediction of F_2^{QCD} at low x based on QCD evolution in Q^2 .

Both the gluon distribution and F_L^{QCD} are seen to be almost independent of the data at high y when the results of QCD fits with and without a cut in $y < 0.35$ are compared, see figures 4.28 and 4.27. Thus both F_L^{QCD} and $xg(x, Q^2)$ are determined by the scaling violations of F_2 .

By analogy of the extraction of $F_2(x, Q^2)$ on a prediction of $F_L(x, Q^2)$, the cross section for-

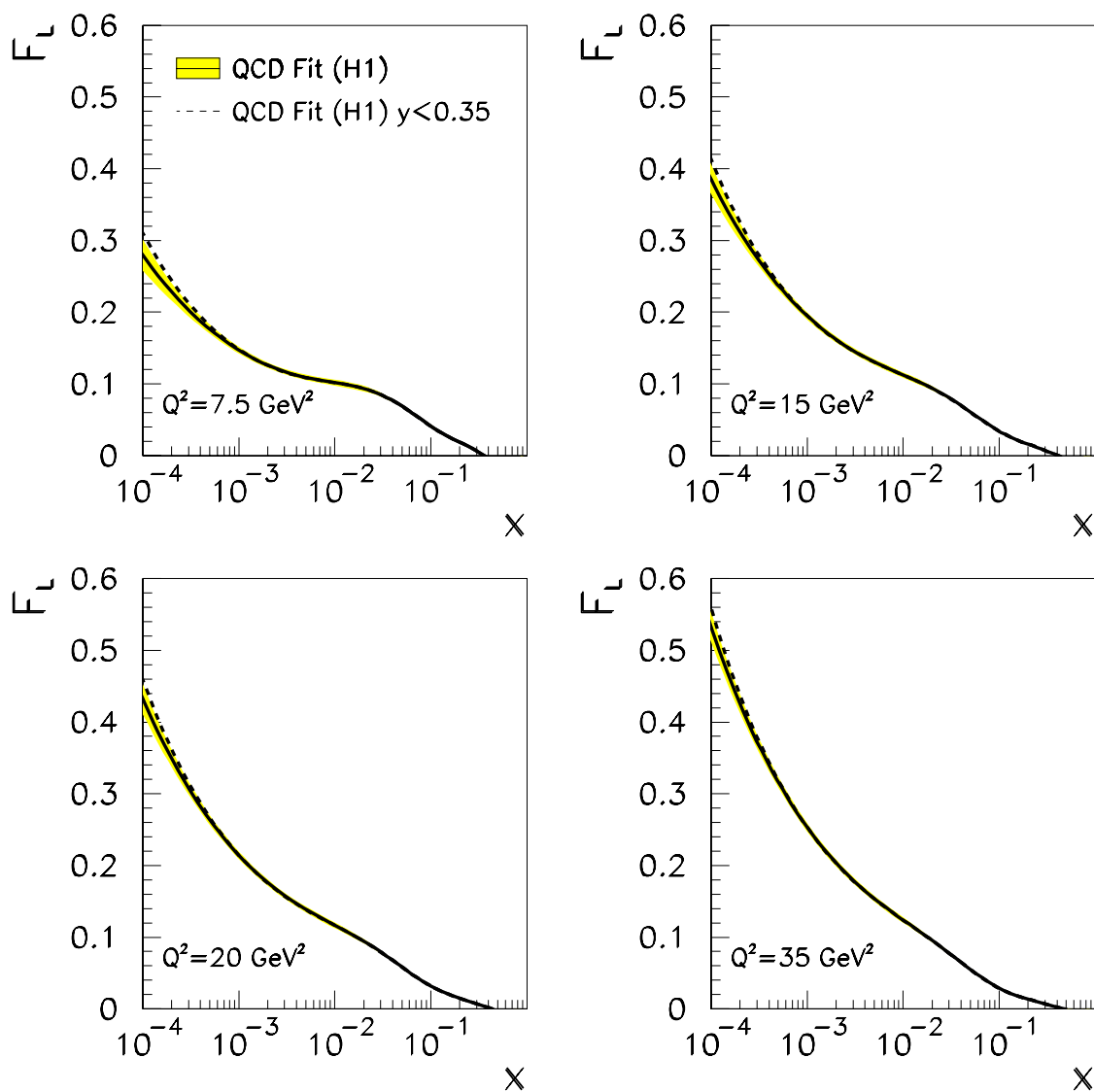


Figure 4.28: Comparison of F_L^{QCD} obtained for the QCD fit to H1 data without (with) a cut in $y < 0.35$.

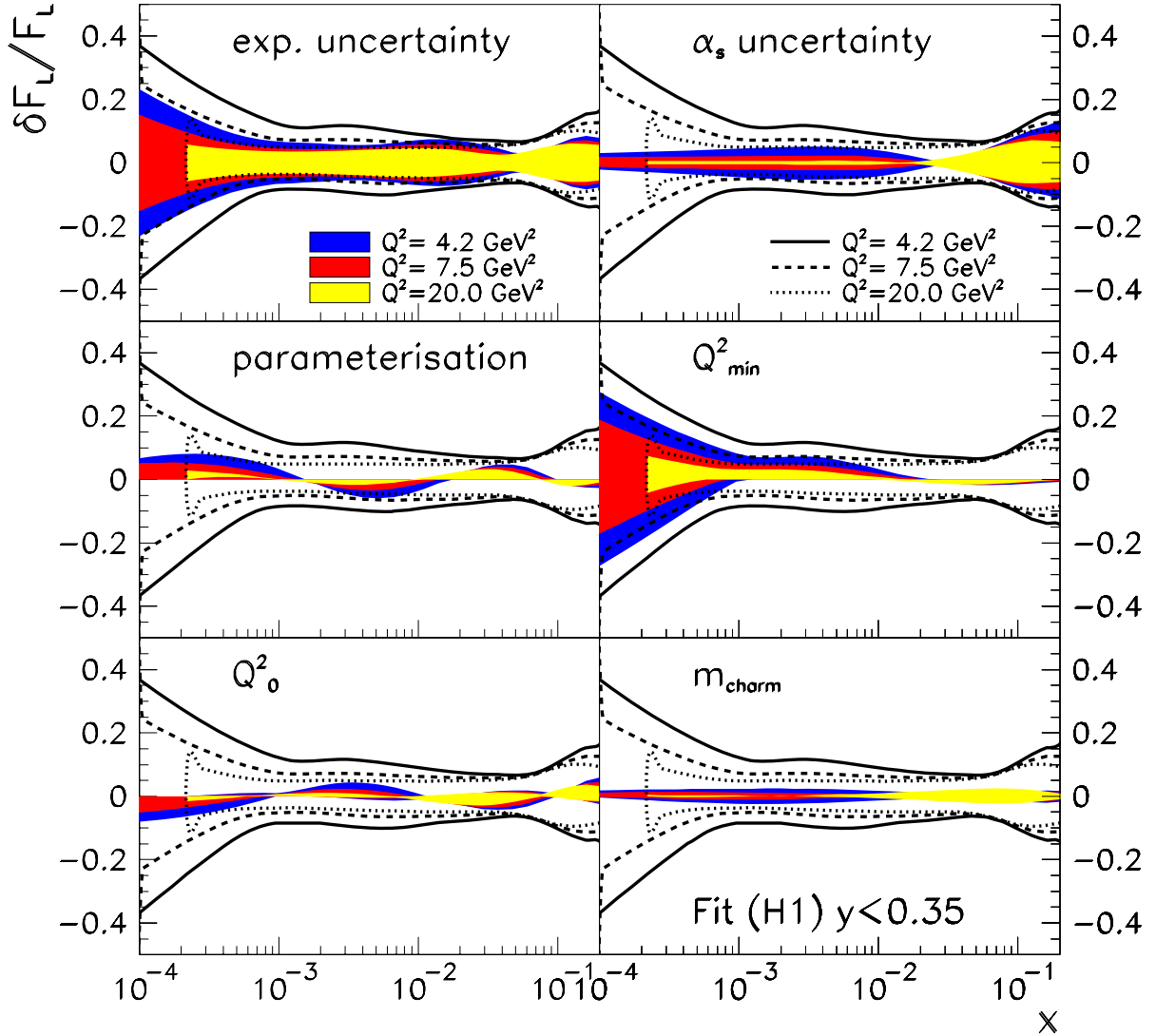


Figure 4.29: Relative errors on $F_L^{\text{QCD}}(x, Q^2)$ by different model uncertainties. The sources of uncertainty are the same as given for the gluon distribution uncertainty, see figure 4.14.

mula 1.7 can be inverted,

$$F_L^{\text{exp}}(x, Q^2) = [F_2(x, Q^2)^{\text{QCD}} - \sigma_r] \cdot \frac{Y_+}{y^2}, \quad (4.3)$$

and an extraction of $F_L^{\text{exp}}(x, Q^2)$ is obtained which can be compared to the QCD prediction $F_L^{\text{QCD}}(x, Q^2)$. At low $Q^2 < 10 \text{ GeV}^2$, the QCD fit representation of F_2 is replaced by a QCD independent method which uses the derivative $\frac{\partial F_2}{\partial \ln x}$. F_L data points obtained with these methods are displayed in figure 4.30 where additional data from fixed target are shown as well. The experimental determination of F_L^{exp} , taking properly into account the correlated systematic errors which partly cancel, is described in [26].

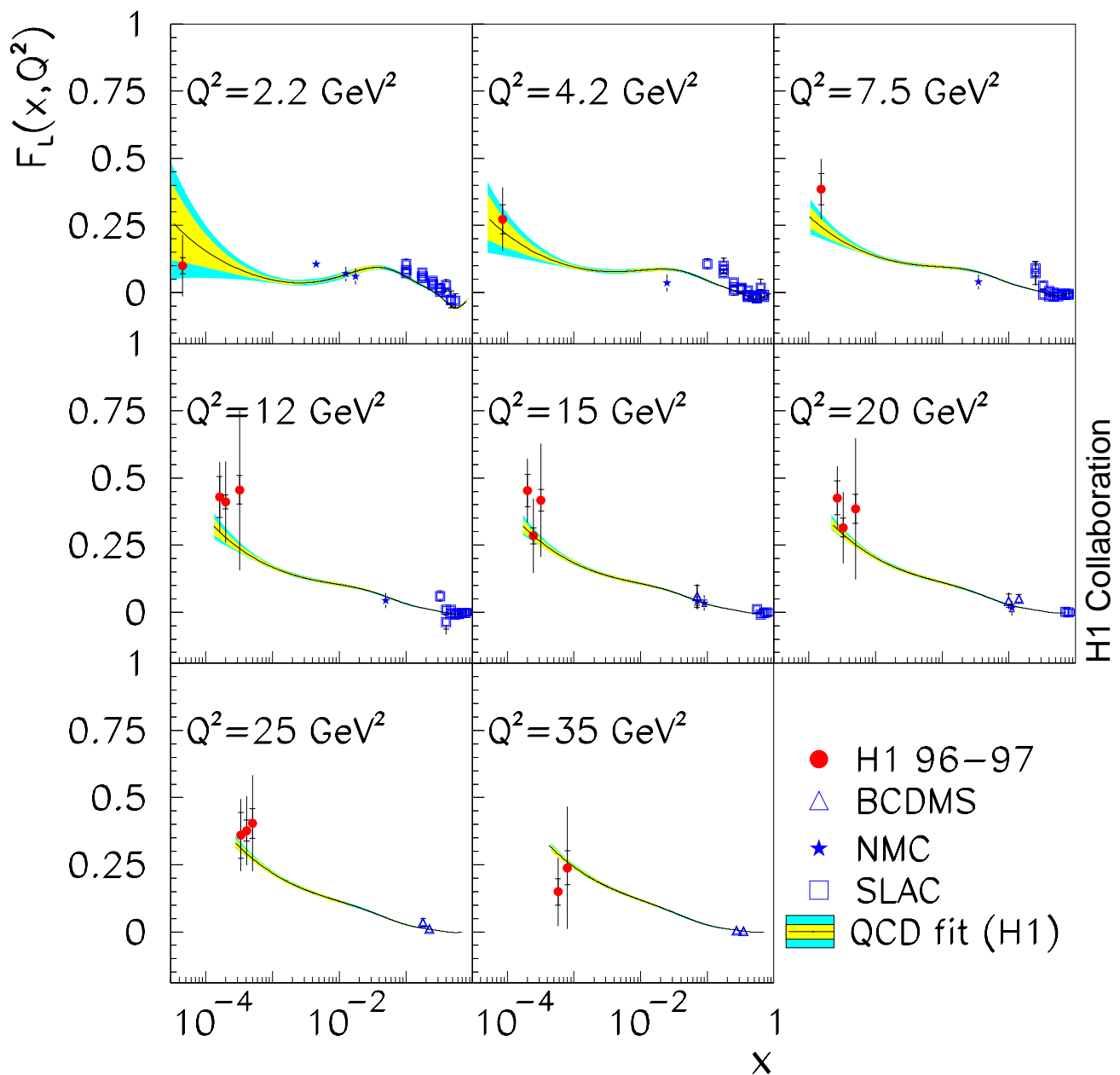


Figure 4.30: The longitudinal structure function $F_L(x, Q^2)$ for different bins of Q^2 as obtained by H1 at low x , and by charged lepton-nucleon fixed target experiments at large x . The measurements for $Q^2 < 10 \text{ GeV}^2$ are determined with the derivative method while the points for larger Q^2 are due to the extrapolation method. The error on the data points is the total uncertainty of the determination of F_L representing the statistical, the systematic and the model errors added in quadrature. The inner error bars show the statistical error. The error bands are due to the experimental (inner) and model (outer) uncertainty of the calculation of F_L using the NLO QCD fit to the H1 data for $y < 0.35$ and $Q^2 \geq 3.5 \text{ GeV}^2$.

The QCD fit, similarly as for xg , allows the longitudinal structure function to be predicted with a certain accuracy limited by the experimental and model uncertainties. The error bands in 4.30 reflect these uncertainties in the QCD analysis to H1 data with a cut in $y < 0.35$. The largest effects are seen to result from the experimental errors and from the adopted minimum value of Q^2 used in the analysis while the uncertainty due to α_s , the charm mass and the parameterisations are small. Figure 4.30 compares the QCD fit prediction with the data points obtained from the H1 data as well as from fixed target experiments. At the present level of accuracy, the data are consistent with the QCD calculation to order $\mathcal{O}(\alpha_s^2)$ obtained from the QCD fit.

The net uncertainties at smallest x are large because the fit is restricted to $y < 0.35$ in order to become independent of F_L . If the fit is extended to the highest y , or smallest x , region, the uncertainty becomes nearly twice smaller at low x . Then, however, the F_L data themselves are potentially influencing the fit and the comparison of the extracted F_L data points [26, 27] with the QCD prediction becomes conceptionally less convincing.

Chapter 5

Determination of $\alpha_s(M_Z^2)$

The strong coupling constant α_s is the only fundamental free parameter of QCD. It is therefore not surprising that it enters the computation of many observables in QCD. However, in practice α_s is correlated with other phenomenological parameters of the theory, which account for the non-perturbative part of the theory, in particular with the x dependence of the parton distributions.

Deep inelastic lepton nucleon scattering has been an ideal testing ground for determining α_s since the theory is probed at high momentum transfers where QCD is asymptotically free and the theory well formulated up to higher orders in perturbation theory. The determination of the strong coupling constant in this analysis uses the DGLAP equations to NLO which govern the scaling violations of $F_2(x, Q^2)$ and also of $F_L(x, Q^2)$.

A potential problem arises from the correlation of α_s with the gluon distribution. This is resolved here by using high precision data at low x and high x . While the scaling violations at low x are proportional to $\alpha_s \cdot xg$, in the valence quark region at high x they are predominantly determined by α_s alone since the non-singlet evolution is independent of xg . Employing the new precision data of H1 at low x and the BCDMS data at high x , both the non-singlet (high x) as well as the singlet (low x) sector of the DGLAP equations are well constrained. This is demonstrated to determine α_s and to disentangle its correlation with xg .

5.1 $\alpha_s(M_Z^2)$ from a Fit to H1 and BCDMS Data

The fit to the H1 data alone determines $\alpha_s(M_Z^2)$ to be 0.115 with an experimental error of ± 0.005 . This is the first measurement of α_s with HERA inclusive cross section data alone. The precision of the large x , high Q^2 H1 data [37] however is not sufficient to enable a competitive determination of $\alpha_s(M_Z^2)$ and of the gluon distribution simultaneously from the H1 data alone. The most precise measurement of the DIS inclusive cross section at large x was obtained by the BCDMS μp scattering experiment [97] (figure 4.3). These data are therefore combined with the H1 measurements.

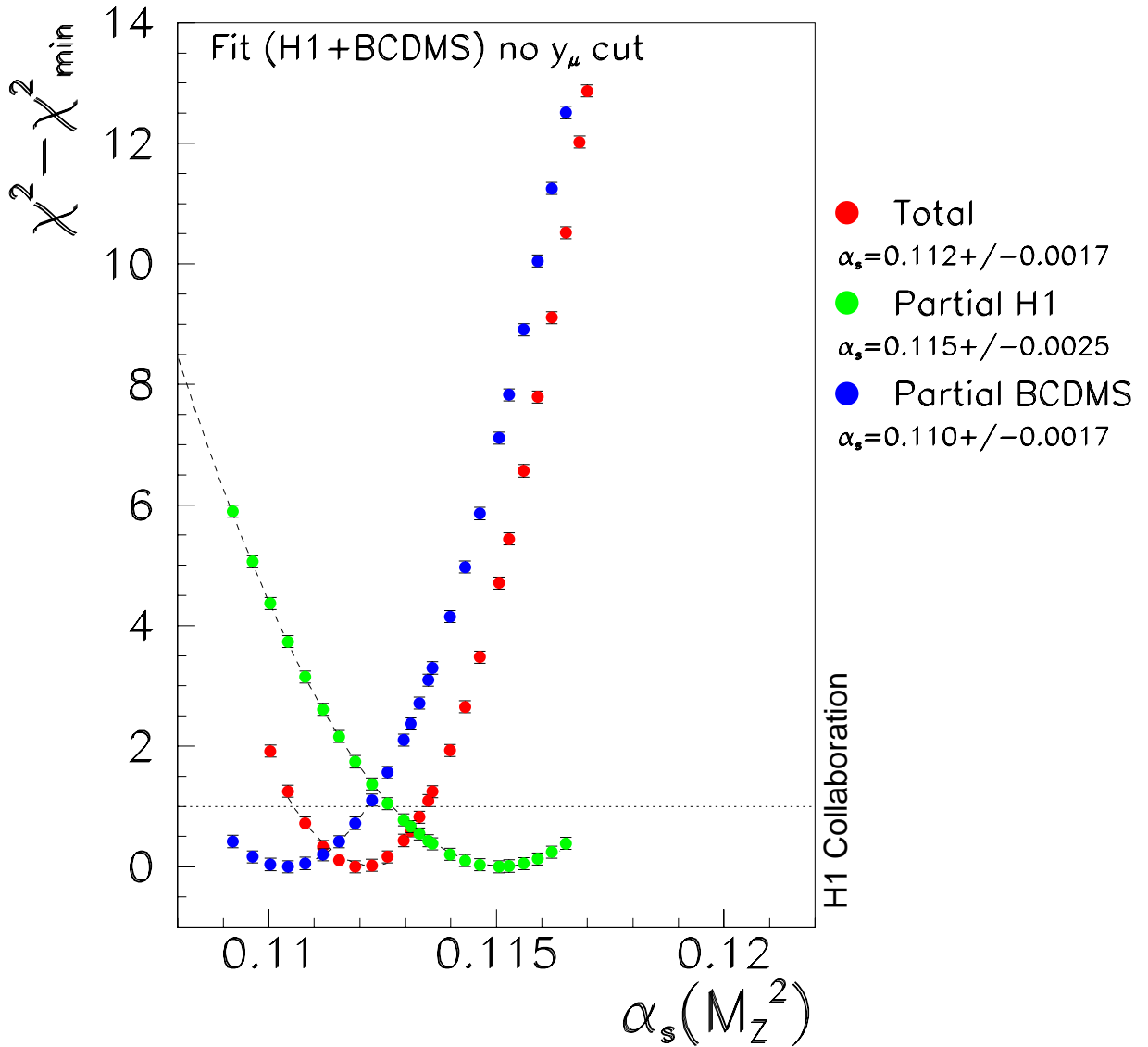


Figure 5.1: χ^2 minimisation curves for a fit to H1 and BCDMS data. The total (*red*) as well as the partial χ^2 contributions of the H1 (*green*) and BCDMS (*blue*) data give precise minima. However, the partial contributions are seen to favour different optimal minima which are on the edge of being compatible with each other.

In a first step, a fit is performed to the complete data sets. A minimum is found at $\alpha_s = 0.112$ with an experimental uncertainty of ± 0.0017 , see figure 5.1. That value is compatible with, but more precise than a determination of $\alpha_s(M_Z^2)$ from BCDMS and SLAC data [46] which yielded $\alpha_s = 0.113 \pm 0.005$, where the quoted total error includes scale uncertainties of the order of 0.004. This value for long represented a puzzle as it seemed that deep inelastic scattering and e^+e^- data, preferring central values around 0.120, would lead to different results which even invited speculations about the existence of light gluinos [98, 99].

However, by looking at the partial contribution of both experiments to the combined fit, one

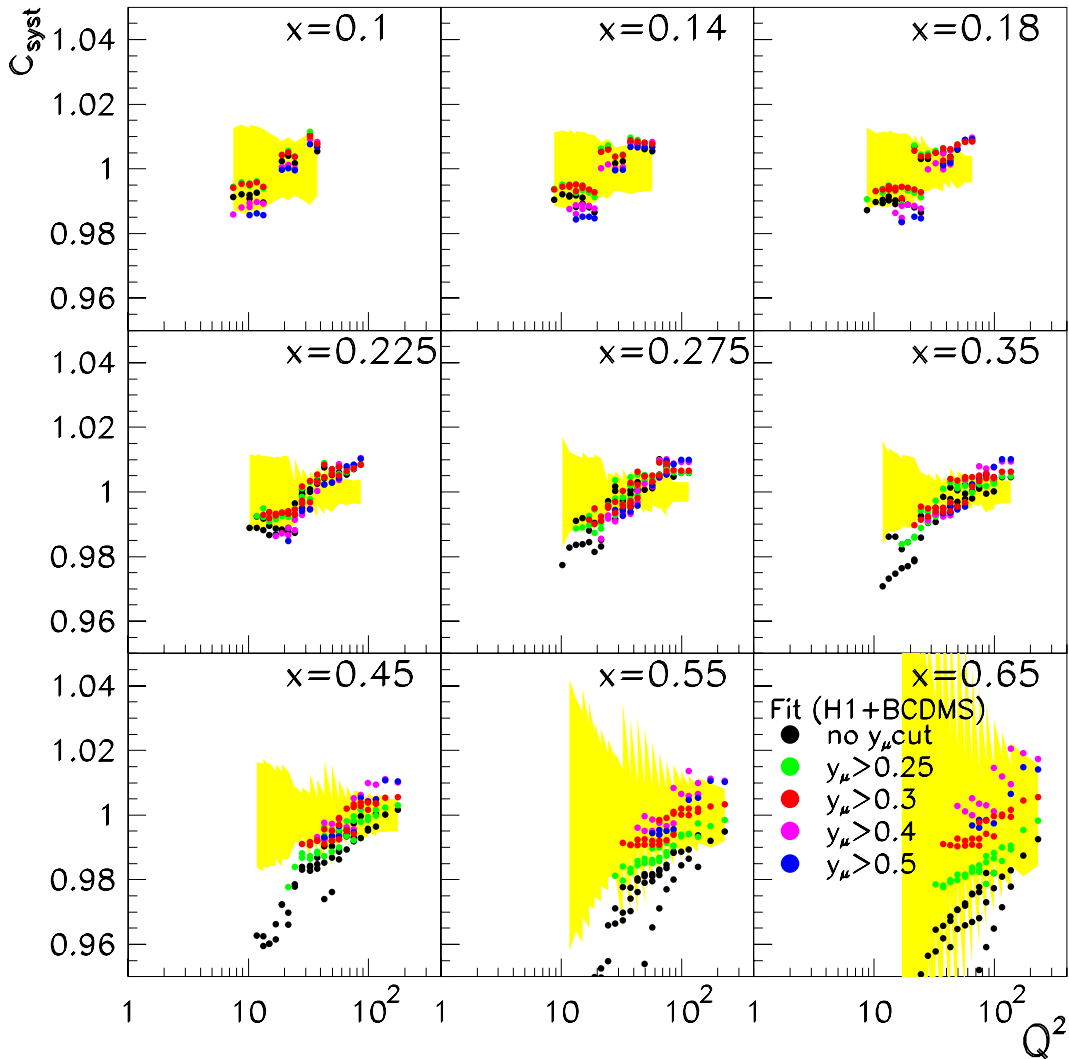


Figure 5.2: Shifts due to correlated systematic error sources applied to the BCDMS data in different bins of x versus Q^2 . The yellow band indicates the estimated correlated error of the points. At low y , corresponding to low Q^2 at fixed x , the data are seen to be moved out of the quoted 1σ error limit. If successive cuts in y are applied, this behaviour is seen to be cured for cuts in $y_\mu > 0.3$.

observes a distinct disagreement between the H1 data and the BCDMS data regarding the preferred value of α_s , see figure 5.1. A similar effect was inherent to the analysis of the BCDMS and SLAC data: By essentially averaging two different results, about 0.110 for BCDMS and 0.120 for SLAC, the joint fit result of 0.113 was obtained reflecting the different accuracy and kinematic range of the two data sets. These observations lead to a reanalysis of the BCDMS data.

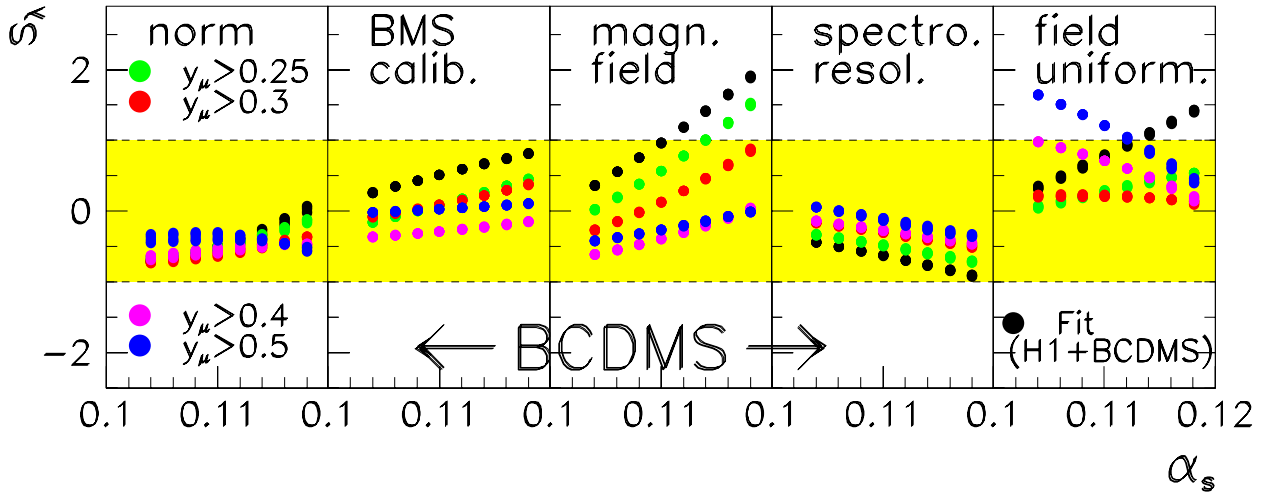


Figure 5.3: Dependence of the BCDMS scale parameters s_λ on α_s for (from left to right) the overall normalisation, the calibration of the incoming muon momentum measurement, the spectrometer magnetic field calibration and resolution as well as the magnetic field uniformity. The yellow bands indicate the estimated 1σ uncertainty.

5.2 Systematic Effects in the BCDMS data

This analysis uses a careful evaluation of the correlated systematic errors by means of scale parameters s_λ which are fitted together with the QCD model parameters. By this method, regions of data are identified in which the fit causes large systematic shifts of the data points. The analysis was based on the original data sets as published by BCDMS [97].

It turns out that the fit tends to influence the data in a Q^2 dependent way. Some shifts of the data are imposed. Most of them stay within the systematic errors quoted by BCDMS apart from data at largest $x > 0.3$, which correspond to low values of y , where the resulting shifts exceed the systematic error limits, see figure 5.2. The low y region in this experiment is particularly strongly affected by the energy scale uncertainty of the scattered muon, see figure 5.3. As is discussed in chapter 2, the measurement of the inclusive cross section at low y based on lepton kinematic reconstruction may become problematic since the errors diverge proportional to $1/y$. While the HERA collider experiments can switch to hadronic reconstruction methods, these are not accessible to the BCDMS experiment since the hadrons were readily absorbed in the iron toroids.

The low y data of the BCDMS F_2 measurements tend to be in conflict with the data from the SLAC ep measurement [100, 38], see figure 4.3. In this region the BCDMS data accuracy is dominated by systematic errors while the SLAC measurement is statistically limited. This also suggests the presence of large systematic effects in the low y region of the BCDMS data which were studied previously [101].

Based on these observations, a systematic study was performed and part of the low y data was finally removed which, as is seen in figure 5.2, restores the data behaviour for $y_\mu > 0.3$. Figure 5.3 displays the sensitivity of the five correlated systematic error sources to cutting the

data in y and their correlation with α_s . Such an increasing cut produces α_s to move to higher values until saturation is reached around $y_\mu \geq 0.3$, see figure 5.4.

At the same time, the scale parameters associated with the systematic error sources approach their allowed 1σ region. If one cuts much beyond $y = 0.3$ the field uniformity is seen to vary strongly, however, and such harsh cuts remove a very large amount of the BCDMS data, see table 5.1. Apart from this source, all other sources are seen not to show any significant departures of the systematic error scale parameters as soon as one removes the smallest y part of the data. Thus, in the following analysis involving BCDMS data a cut of $y_\mu > 0.3$ was used for the final analysis removing a minimum amount of data. The scale parameters of the H1 data sets are observed to be largely unaffected by the cuts in y of the H1 data and can be inspected in figure 5.9.

Fit (H1+BCDMS)	total χ^2_{min}	best α_s	χ^2 @ best α_s H1	χ^2 @ best α_s BCDMS	# points BCDMS
no y cut	513	0.112	188	325	348
$y > 0.25$	439	0.114	186	253	265
$y > 0.3$	395	0.115	185	210	228
$y > 0.4$	321	0.115	184	137	162
$y > 0.5$	257	0.114	184	73	100

Table 5.1: The α_s minimum as determined by fits to H1 and BCDMS data for varying cuts in y_μ . The total as well as partial χ^2 contributions by H1 (a) and BCDMS (b) data are displayed as well as the number of BCDMS data points remaining in the fit. There are 236 H1 points in the fit.

Figure 5.5 shows the effect of the cut in y on the contribution of the BCDMS data to χ^2 (“partial χ^2 ”). As is demonstrated, the low value of α_s from BCDMS is related to the data at low y . As expected, cutting on y in the BCDMS data has no significant effect on the value of α_s preferred by the H1 data which is about 0.115 for all cut values of y_μ . The H1 data, however, gain four units in partial χ^2 without the lowest BCDMS y data in the fit to the joint data set, see figure 5.6 and table 5.1. This effect is even more pronounced if the systematic scale parameters s_λ are fixed to 0.

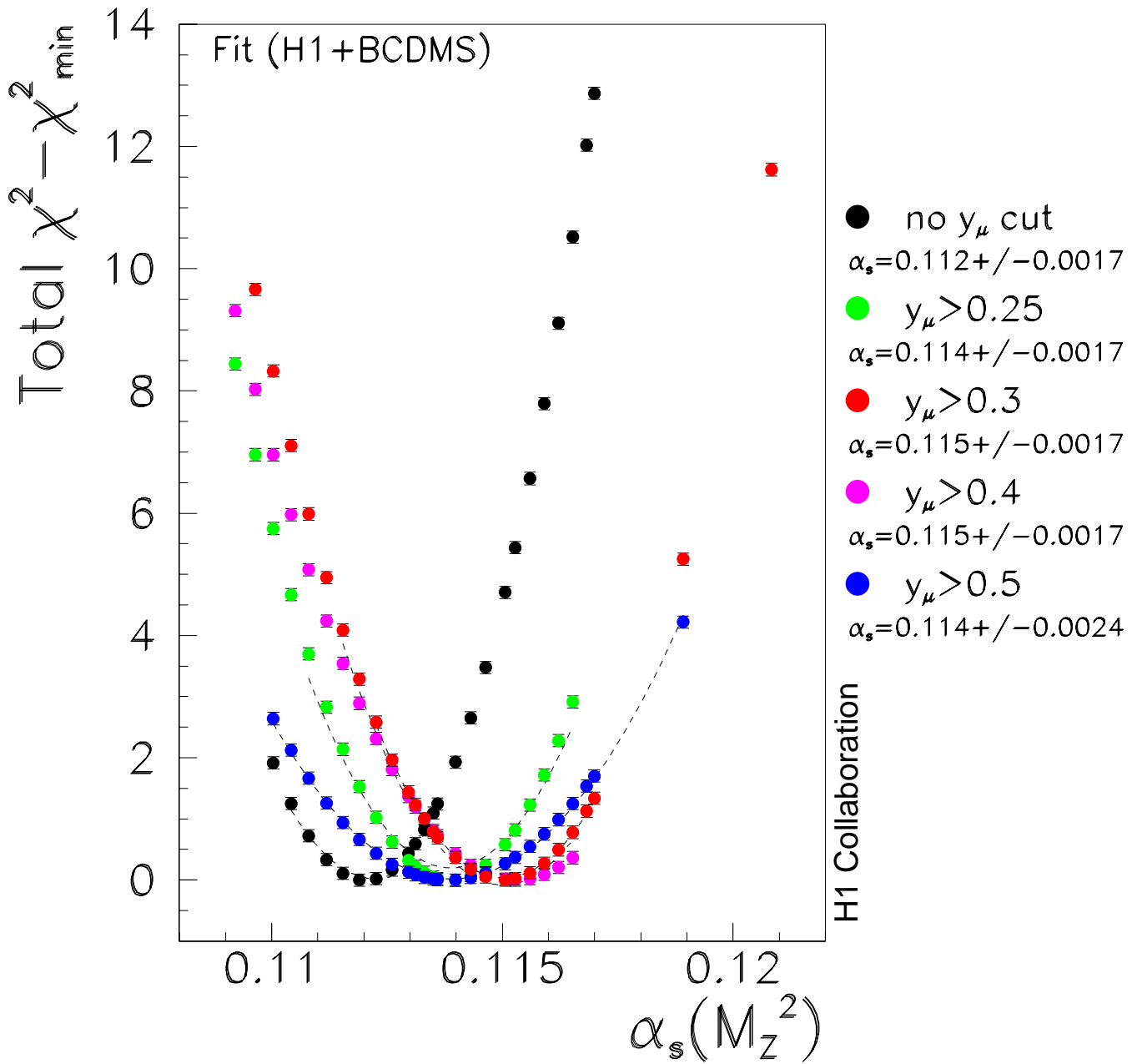


Figure 5.4: χ^2 minimisation curves for fits to H1 and BCDMS data for varying cuts y_μ in the BCDMS data.

5.3 Fit to BCDMS data alone

In the investigation of the BCDMS data, fits are also performed to this data alone. Such a fit, like all fits to the high x fixed target data, determines α_s essentially from the non-singlet DGLAP evolution equation dominated by valence quark contributions. These fits thus inherently neglect the gluon distribution to which the high x data are not much sensitive. Consequently, the fits to BCDMS data alone are rather insensitive to the parameterisation of the low x parton momentum

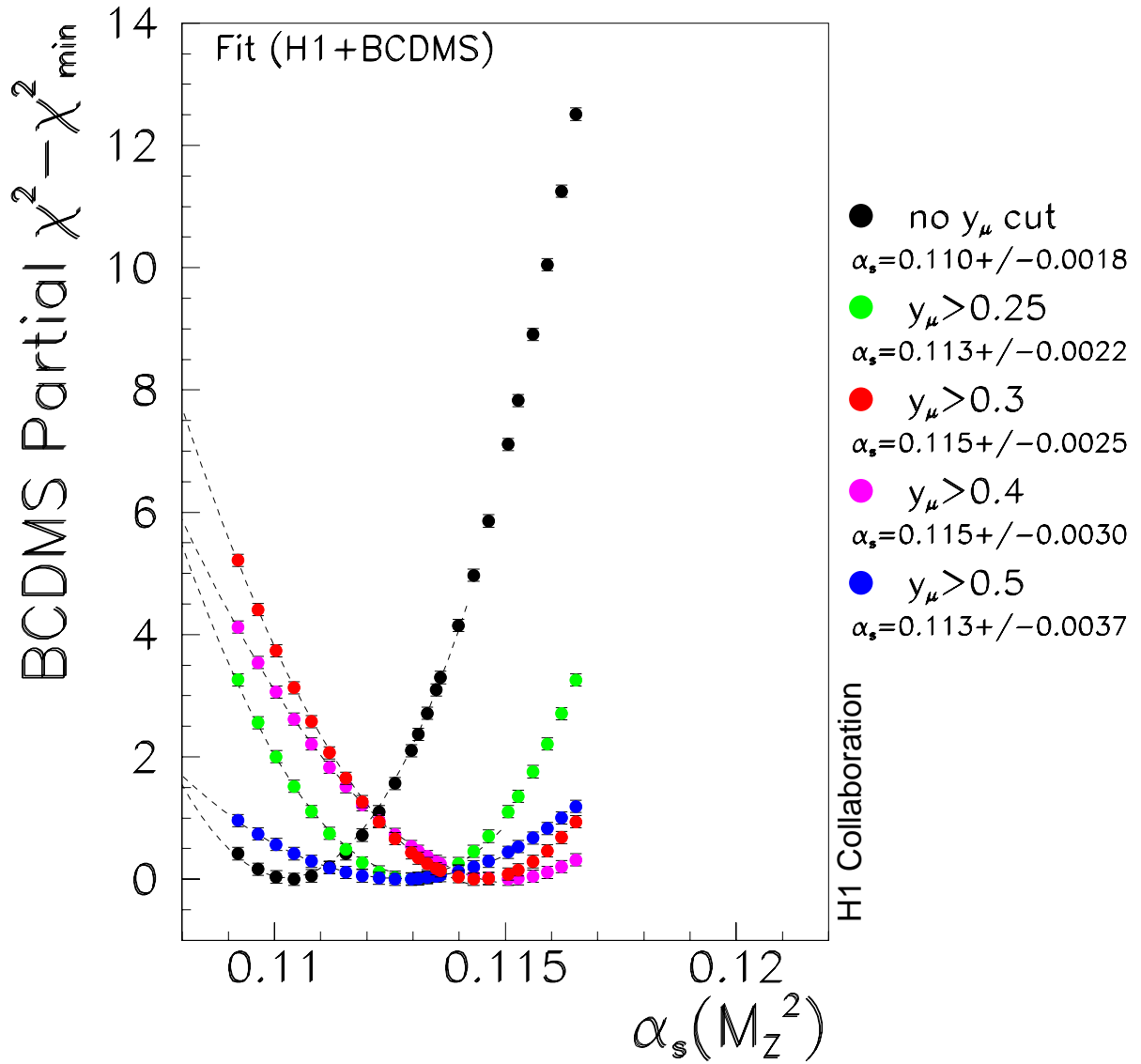


Figure 5.5: Partial χ^2 contribution of the BCDMS data to the fits to H1 and BCDMS data with varying cuts in y_μ .

distribution functions xg and A , see figure 5.7. Following the criterion of χ^2 saturation, the parameterisation CP1 was selected for these fits which has the smallest number of parameters. CP4 has too many parameters to allow for a stable fit, see table 3.1.

The effect of increasing $\alpha_s(M_Z^2)$ with increasing cut in y is also borne out by the fits to BCDMS data alone, see figure 5.8. Within the present analysis it is thus clear that the very low value of α_s in the BCDMS data is connected with the lowest y data region which is problematic as discussed above. Therefore in all subsequent analyses only BCDMS data with $y_\mu > 0.3$ are used to avoid these systematic effects.

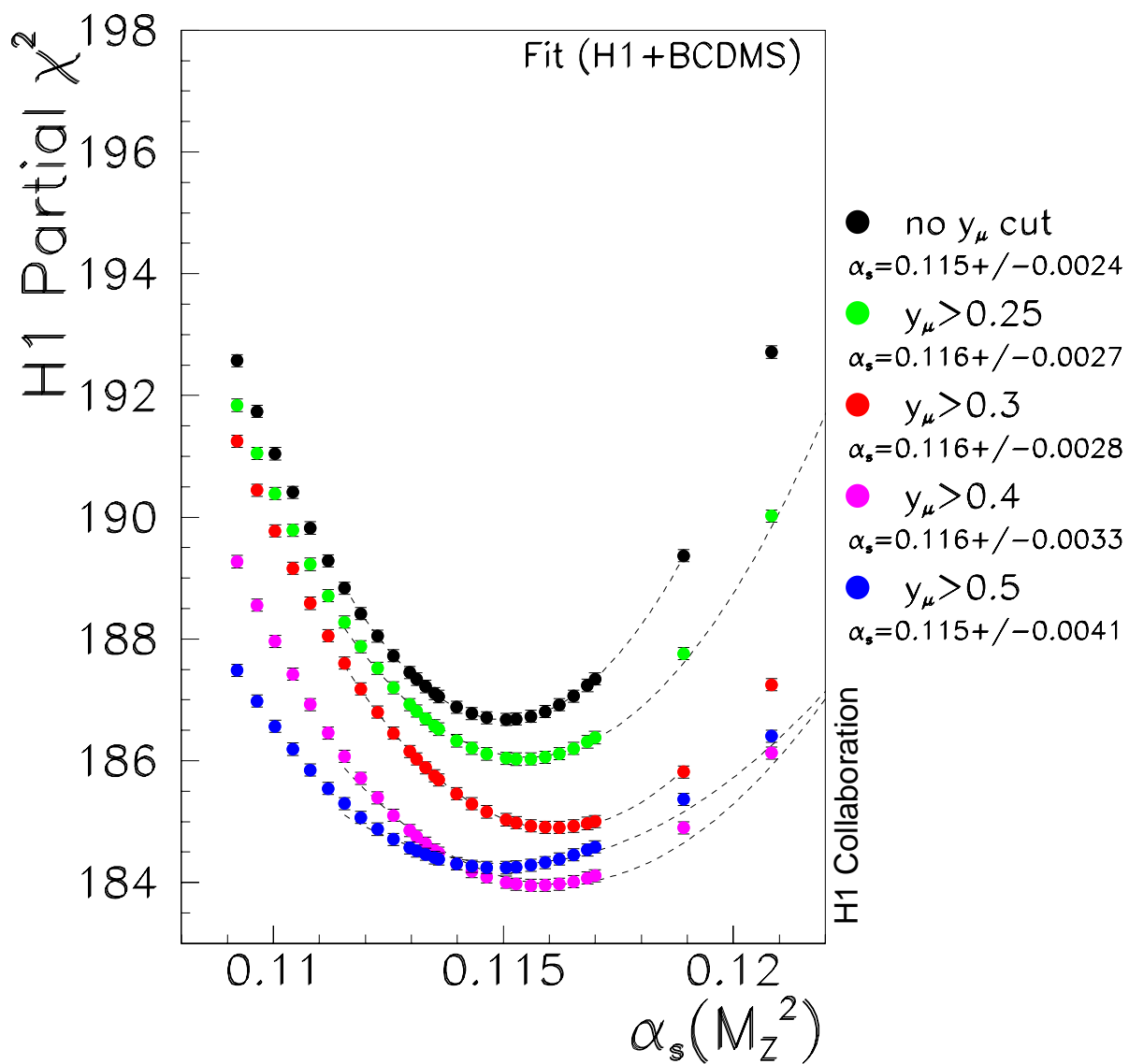


Figure 5.6: Partial χ^2 contribution of the H1 data to the fits to H1 and BCDMS data with varying cuts in y_μ .

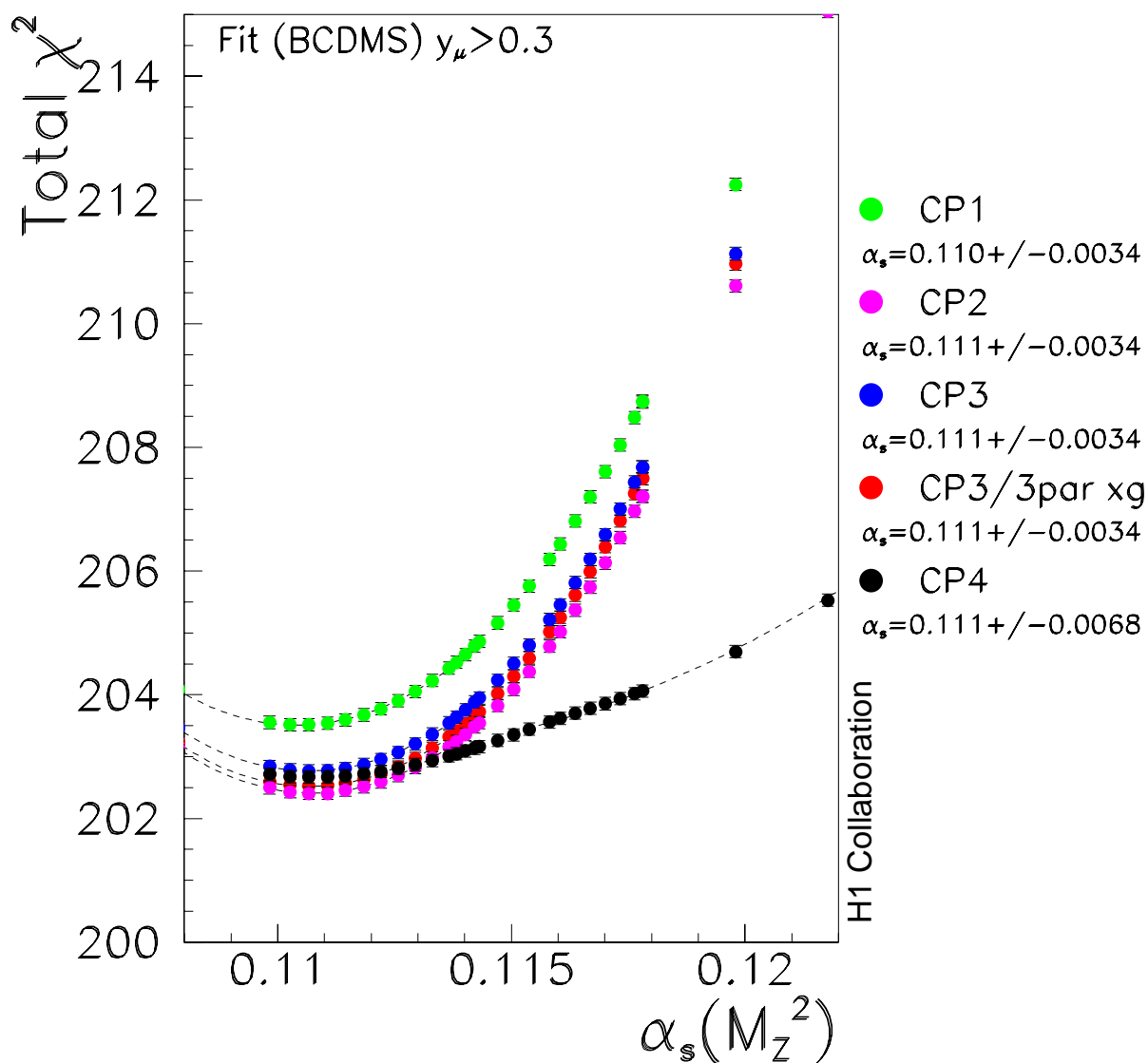


Figure 5.7: χ^2 minimisation curves for fits to BCDMS data alone for various different parameterisations, see table 3.1.

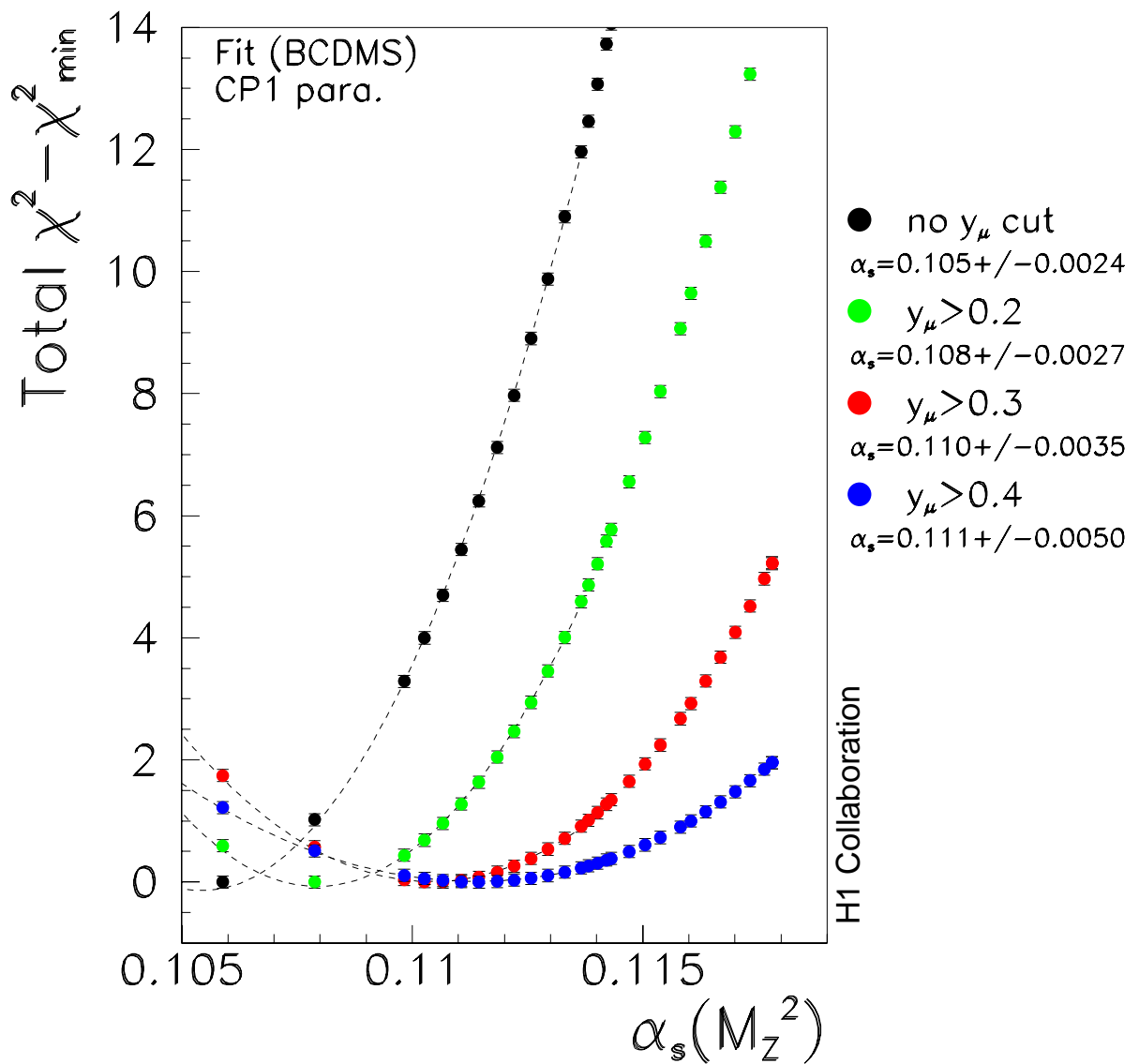


Figure 5.8: Effect of y_μ cuts on the fits to BCDMS data alone.

5.4 Effect of the Systematic Error Treatment on $\alpha_s(M_Z^2)$

In this analysis the treatment of the systematic errors is particularly crucial, because correlations between systematic error scale parameters and extracted physics quantities can occur. In the case of α_s , this can be demonstrated, for example, by considering the normalisations of the datasets. If the datasets which cover different ranges in Q^2 are re-normalised and moved against each other, this introduces slopes in the data, which in turn affect the results extracted from $(\partial F_2/\partial \ln Q^2)_x$, i.e. α_s and $xg(x, Q^2)$. Fixing the normalisations is not a way out of this situation, since certain relative shifts of the datasets against each other are allowed by the experimental measurement accuracies. It is thus considered natural in this analysis to allow for a possible variation of the data within limits set by the errors for each of the correlated error sources like the normalisations.

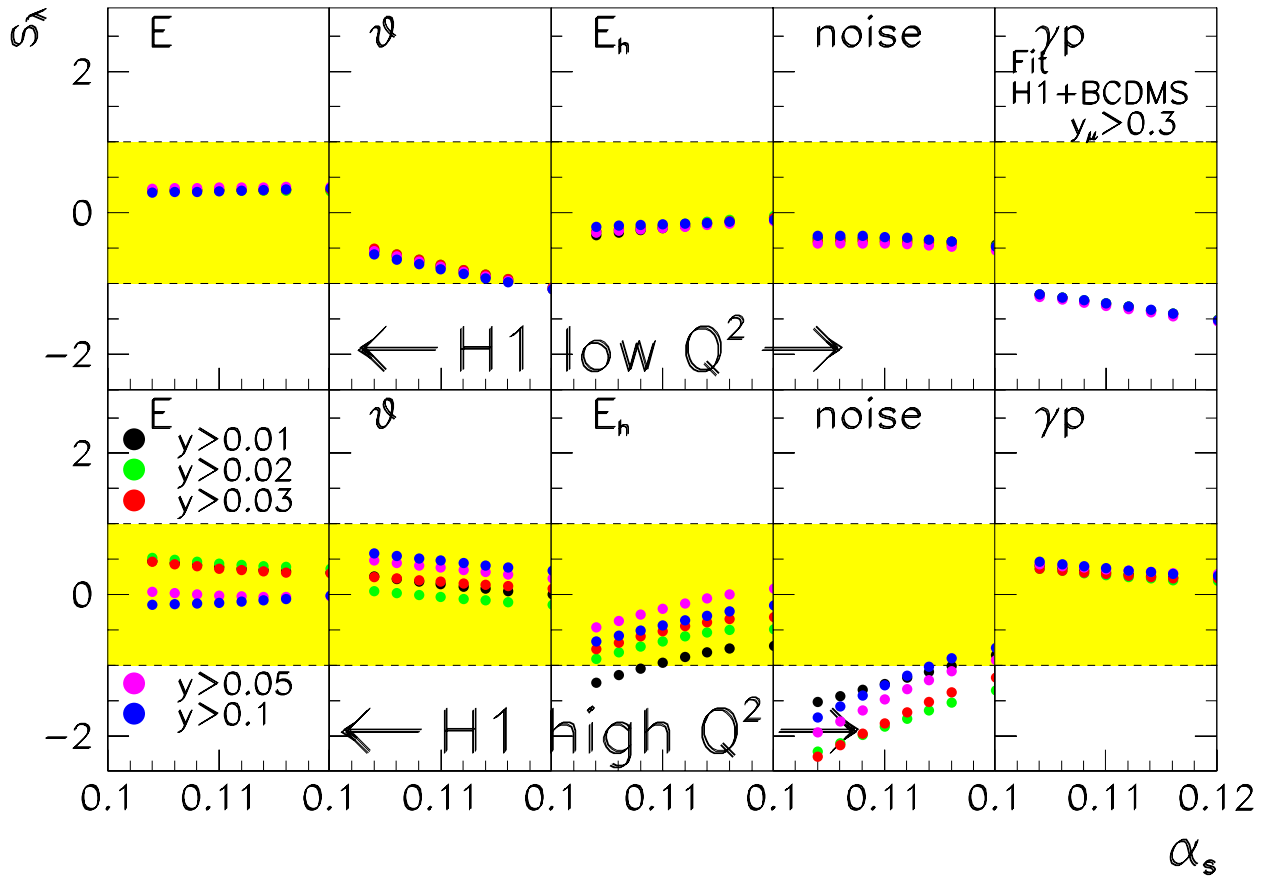


Figure 5.9: Scale parameters for the systematic error sources for the H1 low (top row) and high (bottom row) Q^2 datasets. These are (from left to right) uncertainties due to the electromagnetic energy scale, lepton scattering angle, hadronic energy scale, calorimeter noise and photoproduction background effects. The different colours indicate different cuts in the H1 dataset, see text.

Figure 5.9 shows the systematic error scale parameters for the H1 datasets in a combined fit to H1 and BCDMS data. The potential problems observed when fitting H1 data only are somewhat deteriorated, as regards the hadronic energy scale and noise treatment of the high Q^2 data as

well as the scattering angle uncertainty in the low Q^2 data, see figure 4.7. This indicates a slight consistency problem of the high x datasets which was already discussed in figure 4.3.

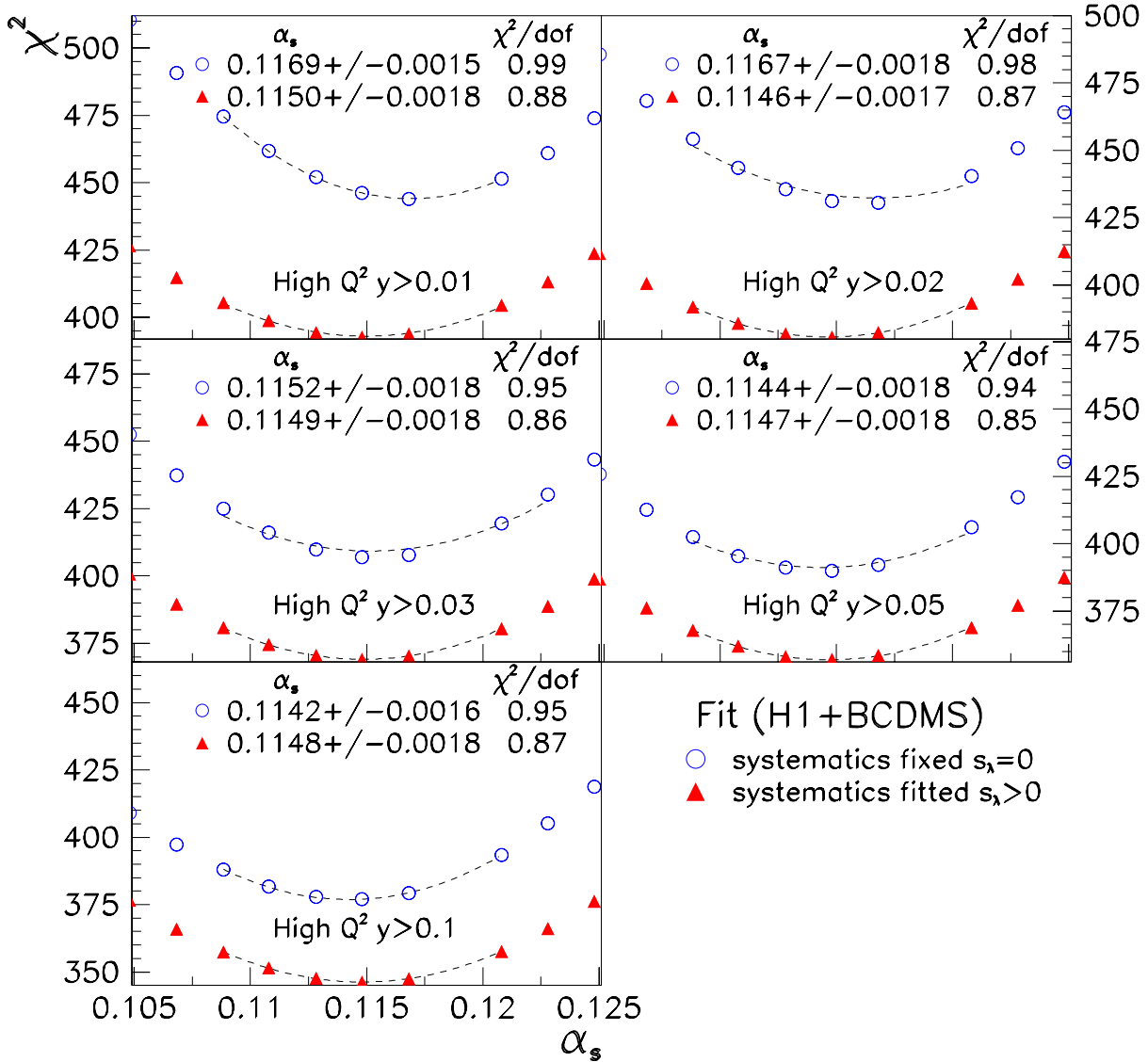


Figure 5.10: The impact of fixing the scale parameters s_λ depending on successive cuts in y in the H1 high Q^2 data.

To assess the extent to which these problems may influence the result on α_s , a special study is performed where all the systematic error scale parameters were fixed to zero. Figure 5.10 shows the resulting α_s minimisation curves for different cuts in the y range of the H1 high Q^2 data. As can be seen, fixing the scale parameters worsens the total χ^2 by about 50 units. Moreover, while there is good stability of α_s observed in all the y -cut conditions when the systematic scale parameters s_λ are part of the minimisation, α_s depends on the y cut when all $s_\lambda = 0$. The observed change of α_s is related to the presence of data points which are already known to be

Fit (H1+BCDMS)	# points	χ^2_{min}					
		s_λ fixed			s_λ free		
		total	H1	BCDMS	total	H1	BCDMS
cut H1 high Q^2	H1 high Q^2						
$y > 0.01$	109	444	229	215	392	183	209
$y > 0.02$	100	430	216	214	380	171	209
$y > 0.03$	91	407	194	213	369	160	209
$y > 0.05$	78	390	177	213	357	148	209
$y > 0.1$	58	376	163	213	346	136	209

Table 5.2: Total and partial χ^2 contributions to fits of H1 and BCDMS data for increasing cuts in y in the H1 high Q^2 data.

moved to the edge of their correlated errors in the H1 only fit, see figures 4.9 and 4.7. By fixing the scale parameters the consistency issues of the H1 high Q^2 and BCDMS data appear to be amplified.

If points are successively removed from the H1 high Q^2 data set, the χ^2 per degree of freedom is observed to saturate above a cut $y > 0.03$ for fits fixing the scale parameters and those with scale parameters released. Such a cut removes 20 H1 high Q^2 points from the fit, see table 5.4. The change in α_s , when fixing the scale parameters, is thus attributed mainly to consistency problems between the H1 high Q^2 data and the BCDMS data and can be traced back to the calorimeter noise effect in the H1 data. These problems can be accounted for by the correlated systematic errors when using released scale parameters in the fit.

When all data at high $Q^2 > 120 \text{ GeV}^2$ are removed, a value of α_s of 0.114 ± 0.002 (exp) is obtained, i.e. the data tend to slightly increase the central value. Because of the still limited accuracy of the high Q^2 data and since the variation of α_s with Q^2 gets logarithmically weaker at high Q^2 , this data set has a small influence on the experimental error only.

5.5 $\alpha_s(M_Z^2)$ from a Fit to H1 and NMC data

In order to cross check the result on $\alpha_s(M_Z^2)$ obtained so far, the BCDMS data are exchanged with the NMC data. Figure 5.11 shows the dependence of α_s on the minimum Q_{min}^2 of data used in the fit to H1+BCDMS and H1+NMC data. The BCDMS data are limited to $Q^2 \geq 7.5 \text{ GeV}^2$. A choice of Q_{min}^2 below this value affects the low x H1 data only in the fit to H1 and BCDMS data. For the value $Q_{min}^2 \geq 7.5 \text{ GeV}^2$ and above, the results of the fits to H1+BCDMS and H1+NMC data are consistent. However, there is also NMC data below such a cut. This introduces a dependence of α_s on Q_{min}^2 for lower Q^2 as is illustrated in figure 5.11. As can be seen in figure 5.12, the minima of the partial χ^2 of the H1 and NMC data are seen not to agree if low Q^2 NMC data are included whereas the minimum preferred by the H1 partial χ^2 contribution stays unaffected by the cut Q_{min}^2 . At the higher Q_{min}^2 value, both partial χ^2 contributions agree.

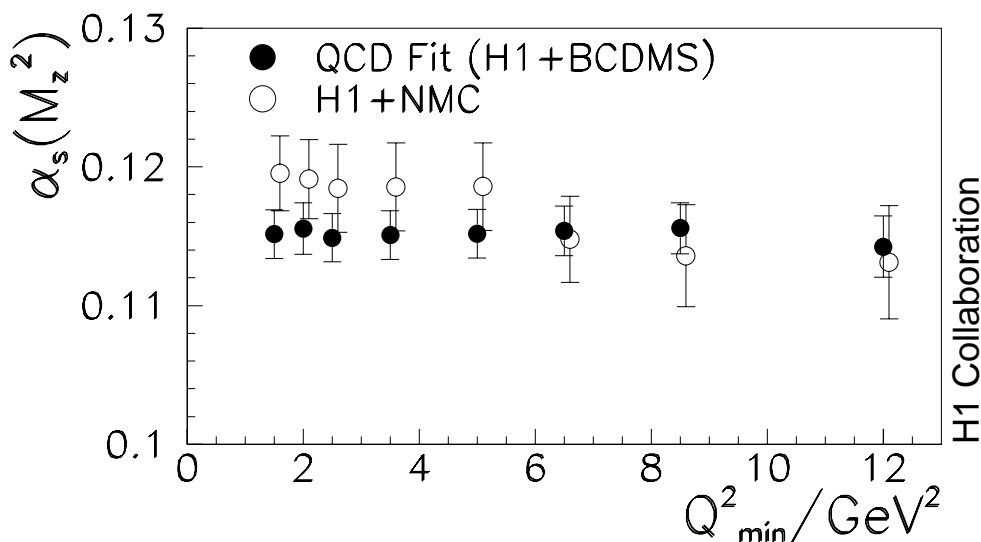


Figure 5.11: Dependence of $\alpha_s(M_Z^2)$ obtained in fits to the H1 and BCDMS data on the minimum Q^2 value used. The error bars denote the experimental uncertainty of $\alpha_s(M_Z^2)$. Note that the BCDMS data have an intrinsic Q_{min}^2 of 7.5 GeV^2 and are limited in this analysis to $y_\mu \geq 0.3$ (see text). An increase of Q_{min}^2 implies that the minimum x rises correspondingly, i.e. from $x = 3.2 \cdot 10^{-5}$ at $Q_{min}^2 = 1.5 \text{ GeV}^2$ to $x = 8 \cdot 10^{-4}$ at $Q_{min}^2 = 12 \text{ GeV}^2$.

In order to cope with this Q_{min}^2 dependence of the NMC data, previous analyses used phenomenological higher twist corrections [47]. Higher twist effects arise due to re-interactions of the quark struck in the hard interaction with the proton remnant which are non-perturbative and related to confinement.

Due to the intrinsic Q^2 cut of the BCDMS data, such higher twist effects need not to be corrected since they vanish at higher Q^2 and are likely to be small when a cut $W^2 > 10 \text{ GeV}^2$ is applied [102], where W is the invariant mass of the hadronic final state. Such a cut is imposed when fixed target data is used. In addition, data from fixed target experiments above $x > 0.76$ are excluded as well.

The results of H1+NMC fits are seen to be significantly less precise than the fits to the H1 and BCDMS data, so the determination of α_s by H1 and fixed target data is suitably performed restricting the analysis to the latter dataset combination.

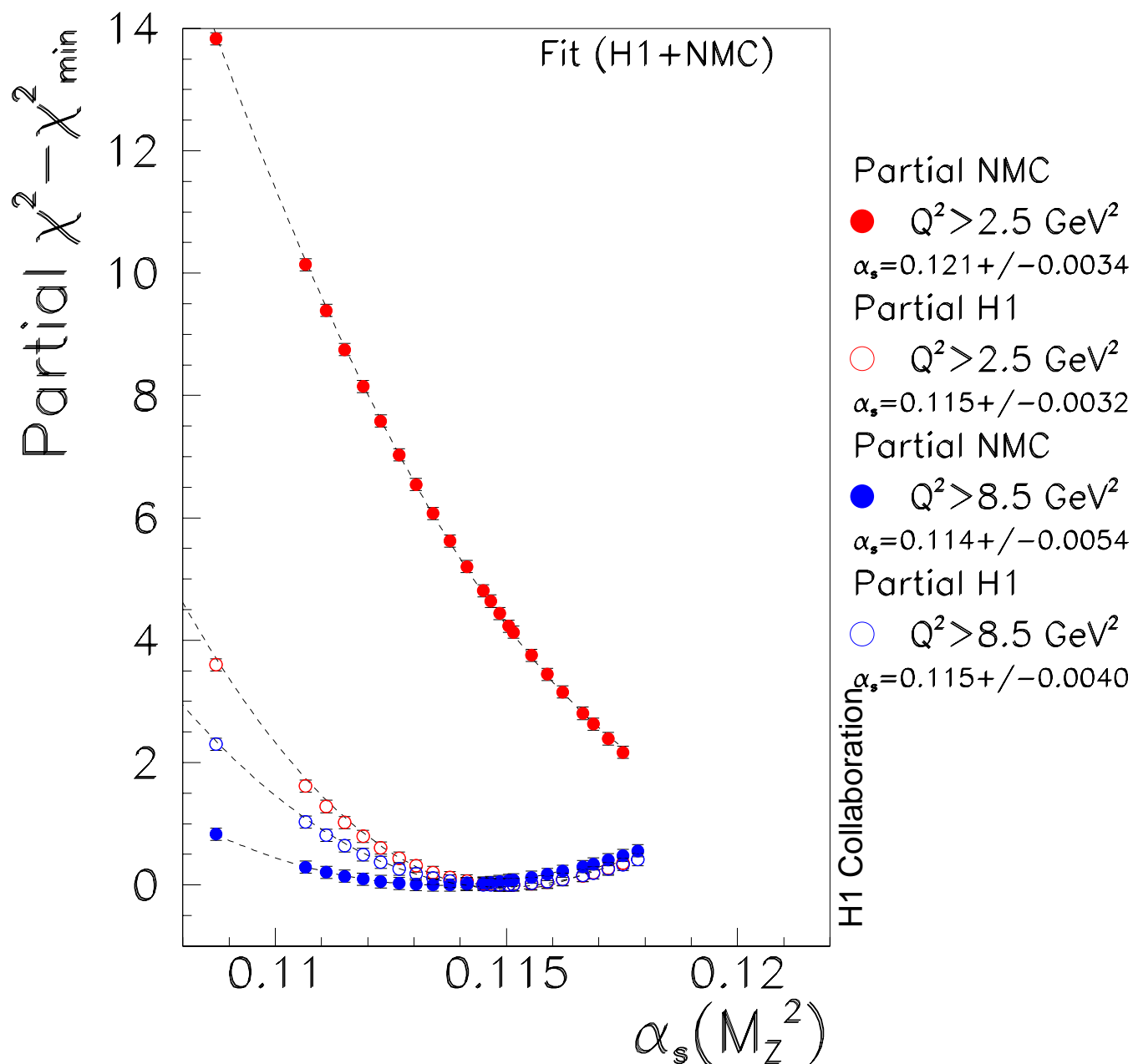


Figure 5.12: Partial χ^2 contribution of NMC (solid points) and H1 (open points) for cuts in the data $Q_{\min}^2 \geq 2.5 \text{ GeV}^2$ (red) and $Q_{\min}^2 \geq 8.5 \text{ GeV}^2$ (blue). The minima of the partial χ^2 contributions agree for the higher value of Q_{\min}^2 . For $Q_{\min}^2 = 2.5 \text{ GeV}^2$, no minimum is observed in the fitted region. The parabola fit to the visible branch is thus only used to guide the eye, and the fit value obtained is unreliable.

5.6 Model Uncertainties

The model assumptions for the DGLAP fits are a source of additional uncertainties. These model uncertainties are listed in table 5.3. The value obtained for $\alpha_s(M_Z^2)$ is nearly independent of Q_0^2 and of the chosen parameterisation for the large set of input distributions considered, see table 3.1. The dominant contributions to the model uncertainties, each of the order of 0.0005, come from the charm mass uncertainty and from a variation of the cut on the lowest x data and on the high x data included in the fit. The overall model uncertainty is much smaller than the experimental uncertainty.

analysis uncertainty	$+\delta \alpha_s$	$-\delta \alpha_s$
$Q_{min}^2 = 2 \text{ GeV}^2$		0.00002
$Q_{min}^2 = 5 \text{ GeV}^2$	0.00016	
parameterisations	0.00011	
$Q_0^2 = 2.5 \text{ GeV}^2$	0.00023	
$Q_0^2 = 6 \text{ GeV}^2$		0.00018
$y_e < 0.35$	0.00013	
$x < 0.6$	0.00033	
$y_\mu > 0.4$	0.00025	
$x > 5 \cdot 10^{-4}$	0.00051	
uncertainty of $\bar{u} - \bar{d}$	0.00005	0.00005
strange quark contribution $\epsilon = 0$	0.00010	
$m_c + 0.1 \text{ GeV}$	0.00047	
$m_c - 0.1 \text{ GeV}$		0.00044
$m_b + 0.2 \text{ GeV}$	0.00007	
$m_b - 0.2 \text{ GeV}$		0.00007
total uncertainty	0.00088	0.00048

Table 5.3: Contributions to the error of $\alpha_s(M_Z^2)$ in the analysis of H1 ep and BCDMS μp data which are due to the selection of data and to the fit assumptions.

5.7 Results

The results of the fits in the preceding sections are summarized in figure 5.13 for the fits to H1 data alone, BCDMS data alone and a fit to both H1+BCDMS data. In the combined fit to H1 and BCDMS data both data sets give a consistent and comparable contribution to the experimental error on α_s . This is illustrated in figure 5.14.

In the fits presented, the experimental uncertainty is determined in the usual way by determining the $\chi^2 + 1$ points at the χ^2 minimisation curve. There is a theoretical debate in global fits as to whether $\chi^2 + 1$ can be rigorously statistically interpreted if the majority of data points are dominated by correlated systematic errors and, furthermore come from different experiments [41].

In the treatment of systematic errors adopted here however the correlations are part of the minimisation. Assuming that the correlated errors are gaussian fluctuating, χ^2 retains its statistical interpretation [103].

The α_s value thus obtained in the NLO analysis of the H1 and BCDMS proton data, applying a cut $y_\mu > 0.3$, is

$$\alpha_s(M_Z^2) = 0.1150 \pm 0.0017 (exp) \pm_{-0.0005}^{+0.0009} (model). \quad (5.1)$$

The value of this analysis of 0.1150, is lower but still consistent with the world average of 0.1184 ± 0.0031 which is based on complete NNLO QCD[10]. In a moment analysis [104] of scaling violations the effect of NNLO corrections was calculated to be

$$\Delta\alpha_s = \alpha_s^{\text{NLO}} - \alpha_s^{\text{NNLO}} = 0.0012,$$

i.e. the value obtained in this analysis in NLO has to be compared to a world average value at NLO of $\alpha_s = 0.1195$.

The combination of low x data with high x data determines the gluon distribution and α_s . A correlation is observed, see figure 5.15, between α_s and the parameter b_g , which governs the shape of the gluon distribution at low x , see equation 3.22. Two lines are drawn which mark the behaviour of the correlation between b_g and α_s when α_s is fixed and b_g determined in the fit, solid lines, or vice versa (dashed line).

In the fit to BCDMS data alone for $y_\mu > 0.3$ and using $xg = ax^b(1-x)^c$, a χ^2 minimum is found at $\alpha_s(M_Z^2) = 0.111 \pm 0.003 (exp)$ and b_g is determined to be positive. A positive value of b_g implies that $xg(x, Q_0^2)$ falls as x decreases. The fit to BCDMS data alone thus leads to a wrong expectation of the behaviour of xg at low x . An early α_s analysis [46], in the absence of detailed information about the low x behaviour of xg , assumed $b_g = 0$. A positive or zero value of b_g , for $Q_0^2 \geq 4 \text{ GeV}^2$, is however incompatible with analyses of the HERA DIS data at low x .

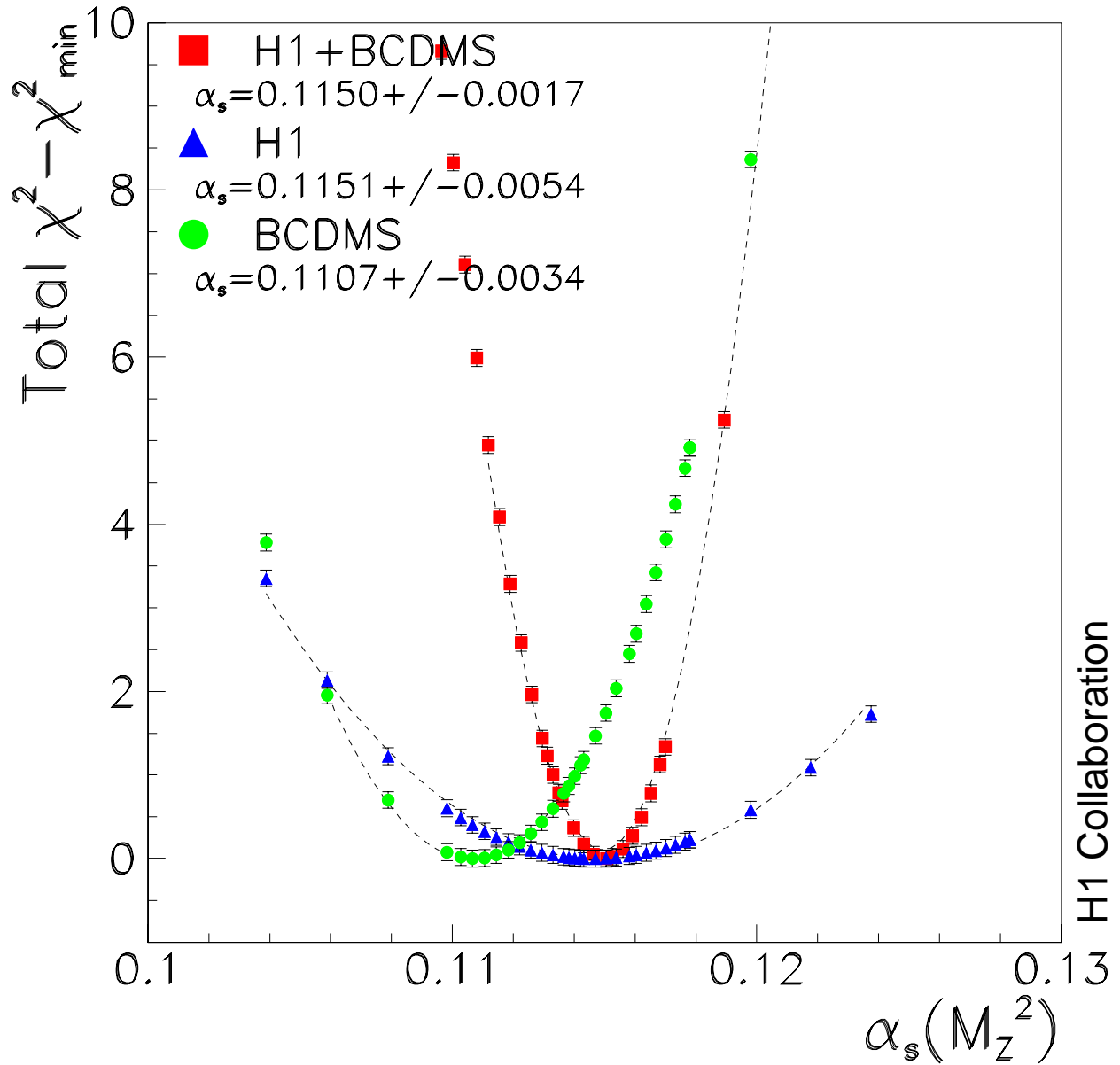


Figure 5.13: Determination of the strong coupling constant $\alpha_s(M_Z^2)$ in NLO DGLAP QCD. Total χ^2 for fits to the H1 ep and BCDMS μp data ($y_\mu > 0.3$) separately and for the fit using data of the two experiments combined.

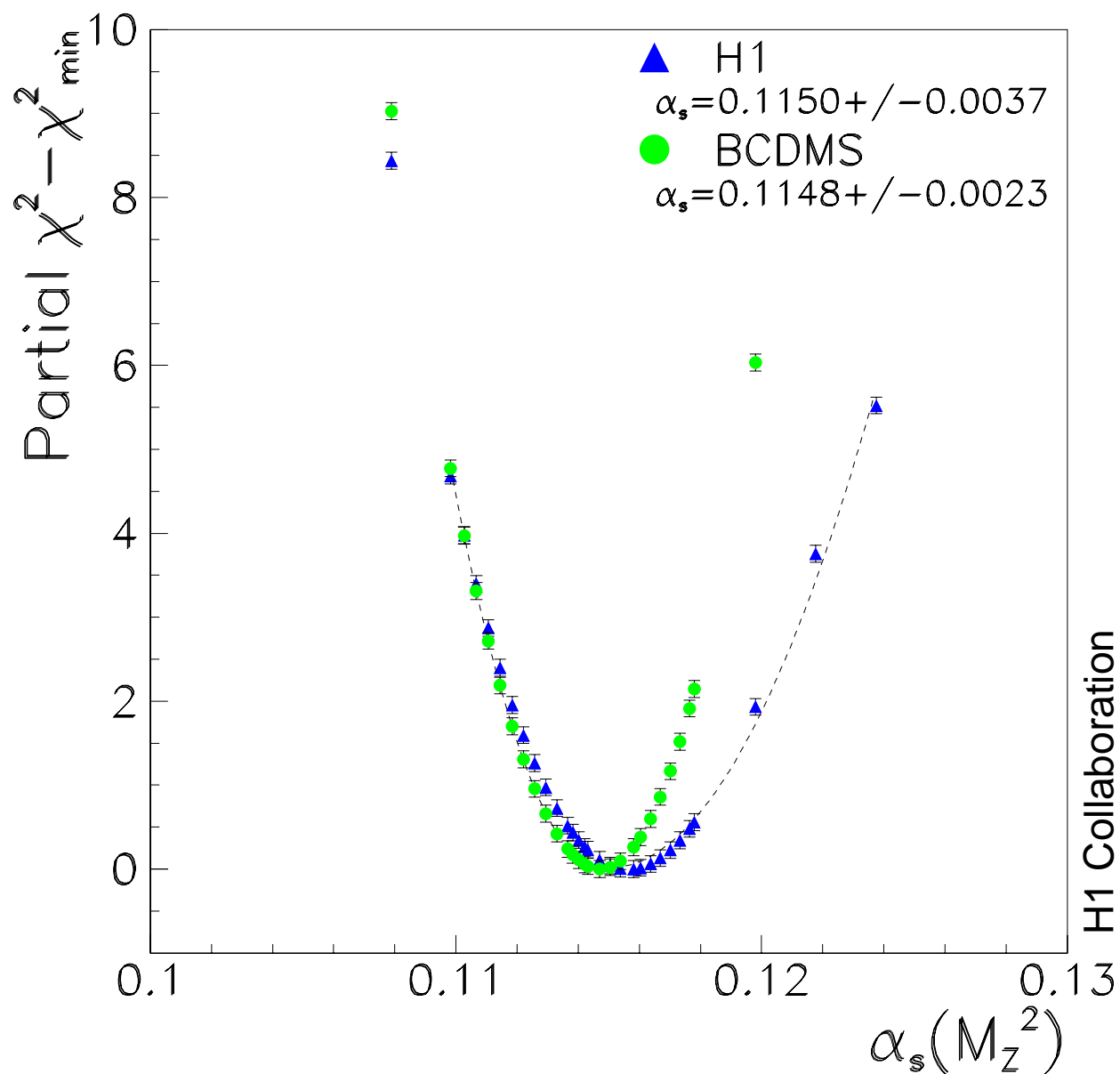


Figure 5.14: Determination of the strong coupling constant $\alpha_s(M_Z^2)$ in NLO DGLAP QCD. Partial χ^2 contributions of the H1 and BCDMS proton data in the fit to determine α_s using both experiments. Both the central values and the experimental errors are of about the same size.

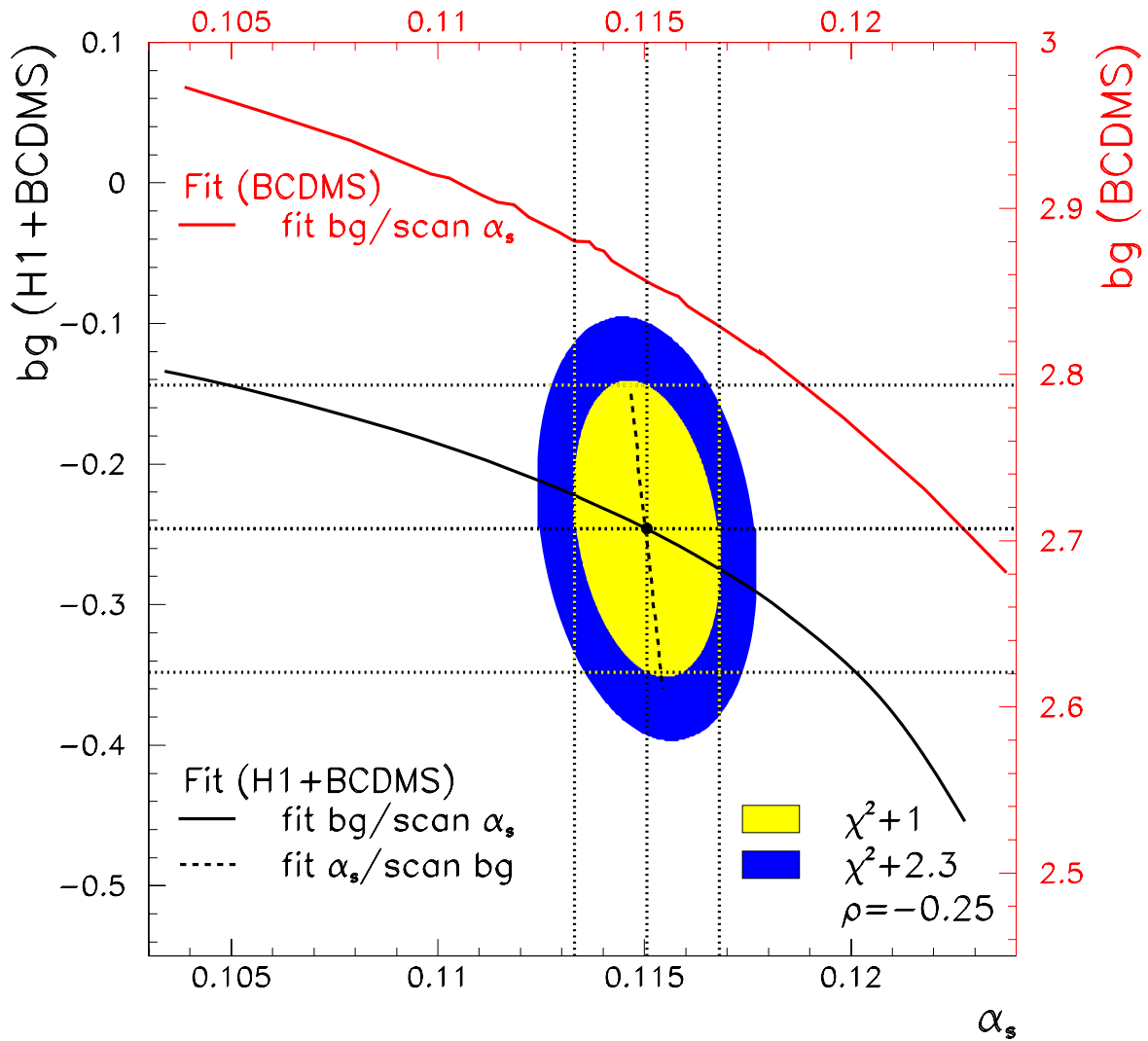


Figure 5.15: Correlation of the parameter b_g governing the low x behaviour of the gluon distribution and of α_s for the fits to H1 and BCDMS data (left scale) and to BCDMS data only (right scale). The solid (dashed) lines depict the line of best χ^2 when α_s (b_g) is scanned, i.e. varied in a series of fits in which all parameters but α_s (b_g) are optimized in the minimisation procedure. The vertical (horizontal) dotted lines denote the one standard deviation for α_s (b_g) in these fits. The $\chi^2 + 1$ ($\chi^2 + 2.3$) contours, are shown for the fit to H1+BCDMS data, denoting the 68.3% confidence level for one (both) parameters to be determined inside the given contour. The correlation coefficient ρ of α_s and b_g is found to be negative. For the fit to BCDMS data alone, $b_g > 0$ is found which is in contradiction to the HERA data.

5.8 Theoretical Scale Uncertainty

The dominant theoretical uncertainty of the NLO analysis results from the choices of the renormalisation scale $\mu_r^2 = m_r \cdot Q^2$ (equation 1.13), and of the factorisation scale $\mu_f^2 = m_f \cdot Q^2$. In the \overline{MS} renormalisation and factorisation scheme both scales are set equal to Q^2 , i.e. $m_r = m_f = 1$. Conventionally, the scales are varied by a factor 4 in order to quantify the effect of the scale uncertainties on α_s . This choice is arbitrary such that the resulting error can hardly be considered as the true error despite the fact that this convention is obeyed for comparing the sensitivity of different processes.

For the combination $m_r = 0.25$, $m_f = 4$, a term $\propto \ln \mu_r^2 / \mu_f^2$ occurs in the splitting function expansion with unequal factorisation and renormalisation scales

$$\alpha_s \cdot [1 + \alpha_s \cdot \beta_0 \cdot \ln(\mu_r^2 / \mu_f^2)] P^{(0)} + \alpha_s^2 \cdot P^{(1)} \quad (5.2)$$

leading to unphysical results [105]. This combination is thus excluded from the estimation. The results are summarized in table 5.4 and figure 5.16.

	$m_r = 0.25$	$m_r = 1$	$m_r = 4$
$m_f = 0.25$	-0.0038	-0.0001	+0.0043
$m_f = 1$	-0.0055	--	+0.0047
$m_f = 4$	--	+0.0005	+0.0063

Table 5.4: Dependence of $\alpha_s(M_Z^2)$ on the renormalisation and factorisation scales m_f and m_r , respectively, expressed as the difference of $\alpha_s(M_Z^2)$ obtained for scales different from one and the central value of $\alpha_s(M_Z^2) = 0.1150$. The combination $m_f = 4$ and $m_r = 0.25$ is abandoned since in the splitting function expansion a term $\propto \ln(m_r/m_f)^2$ becomes negative at low Q^2 which causes a huge increase of χ^2 .

In agreement with previous studies [49] it is found that the renormalisation scale causes a much larger uncertainty on $\alpha_s(M_Z^2)$ than the factorisation scale. Depending on which set of m_r and m_f is chosen, the obtained χ^2 differs by 5-10 units. This suggests that the assumed variation of the scales is indeed too large. The estimated overall uncertainty of about 0.005 on $\alpha_s(M_Z^2)$ is much larger than the experimental error. It is expected to be significantly reduced when next-to-NLO calculations become available [19, 106]. Recently an α_s analysis of moments of structure functions, measured in charged lepton-nucleon scattering, was presented extending to NNLO QCD [104]. The effect of the third order correction is to diminish $\alpha_s(M_Z^2)$ by about 0.001.

5.9 Further Cross Checks

The stability of the fit results is checked further with respect to possible changes in the analysis procedure:

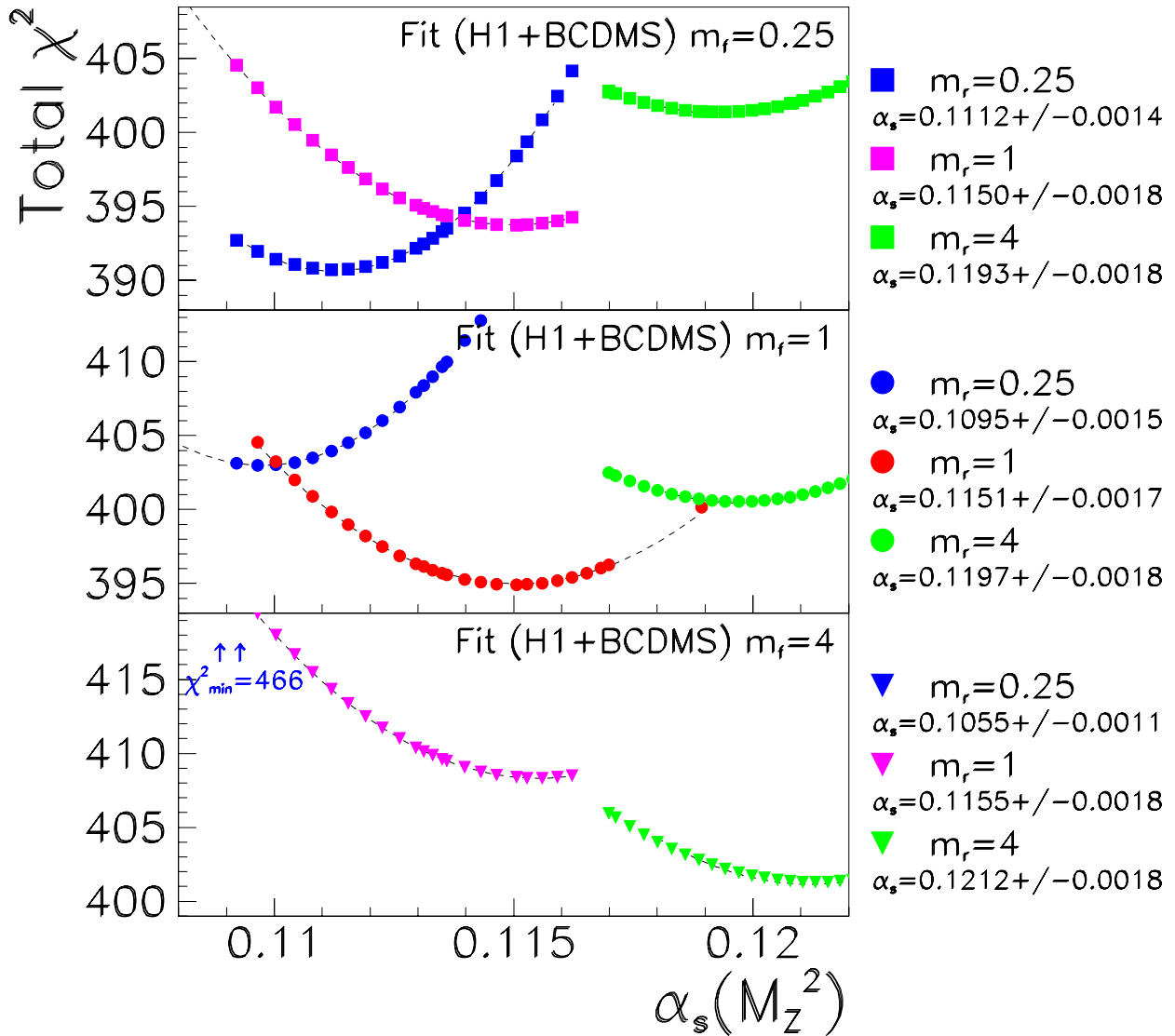


Figure 5.16: χ^2 minimisation curves for variation of the factorisation scale $\mu_f^2 = m_f \cdot Q^2$, top to bottom. For fixed factorisation scale, the renormalisation scale $\mu_r = m_r \cdot Q^2$ is varied similarly. The combination of $m_f = 4, m_r = 0.25$ leads to a negative factor in front of the leading splitting function $P^{(0)}$ of equation 5.8 and thus to an unphysical evolution.

- If the correlation due to systematic errors is neglected, i.e. if the correlated systematic error parameters are not part of the minimisation, the value of $\alpha_s(M_Z^2)$ increases by 0.0005. The χ^2 is significantly worsened by 13 units.
- In the present analysis, the relative normalisations of the data sets are left free. The change imposed by the fit to the BCDMS data is about -1.5% within a total normalisation uncertainty of 3%. The H1 data are moved by about 1% within the experimental error of 1.7%. Thus the selected H1 and BCDMS data are compatible with each other. If the fit is repeated with all normalisations fixed then χ^2 increases by 25, and $\alpha_s(M_Z^2)$ increases by 0.0005, with the error diminishing from 0.0017 to 0.0014.

These results are illustrated in Figure 5.17.

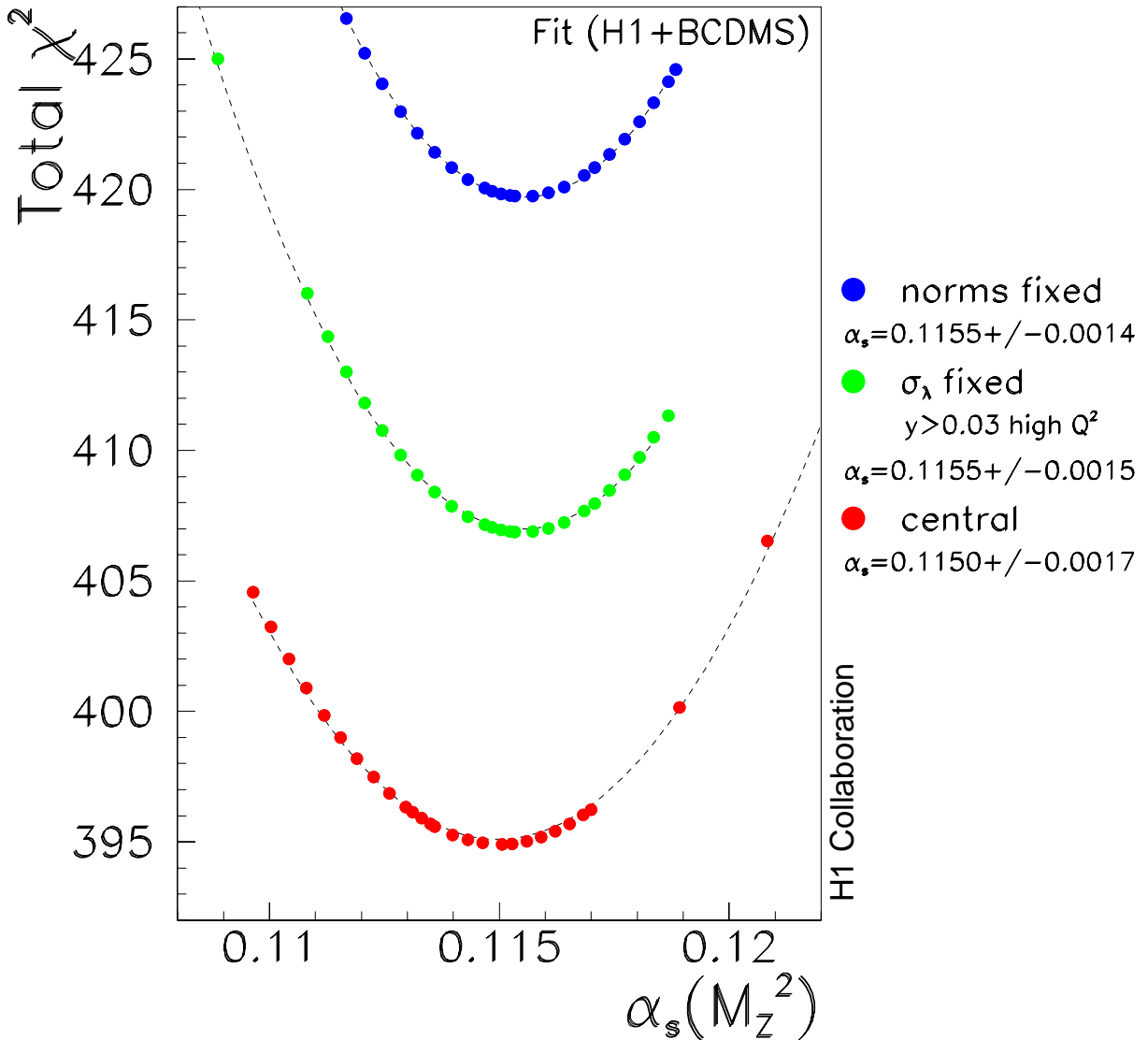


Figure 5.17: Dependence of $\alpha_s(M_Z^2)$ on the systematic error scale parameter treatment. χ^2 gets significantly worse when the systematic errors or the normalisations are not part of the minimisation while α_s is changed by only a small amount.

Further theoretical analysis assumptions are:

- If the heavy flavour treatment is changed and a massless, four flavour fit performed, $\alpha_s(M_Z^2)$ is enlarged by +0.0003. The χ^2 in such an analysis is much worse, i.e. enlarged by 15 units.
- The strong coupling constant is defined here by the solution of the renormalisation group equation to order α_s^3 by means of an iterative method. In the double logarithmic approxi-

mation the value for $\alpha_s(M_Z^2)$ is calculated to be lower by 0.0003. The double logarithmic approximation is the convention of [11].

- If F_L is computed to $\mathcal{O}(\alpha_s)$, $\alpha_s(M_Z^2)$ is enlarged by +0.0005. The χ^2 improves by 2 units reflecting the observation discussed in chapter 4 that the data prefer F_L to be somewhat larger than the values obtained in NLO QCD.

These results are summarized in Figure 5.18.

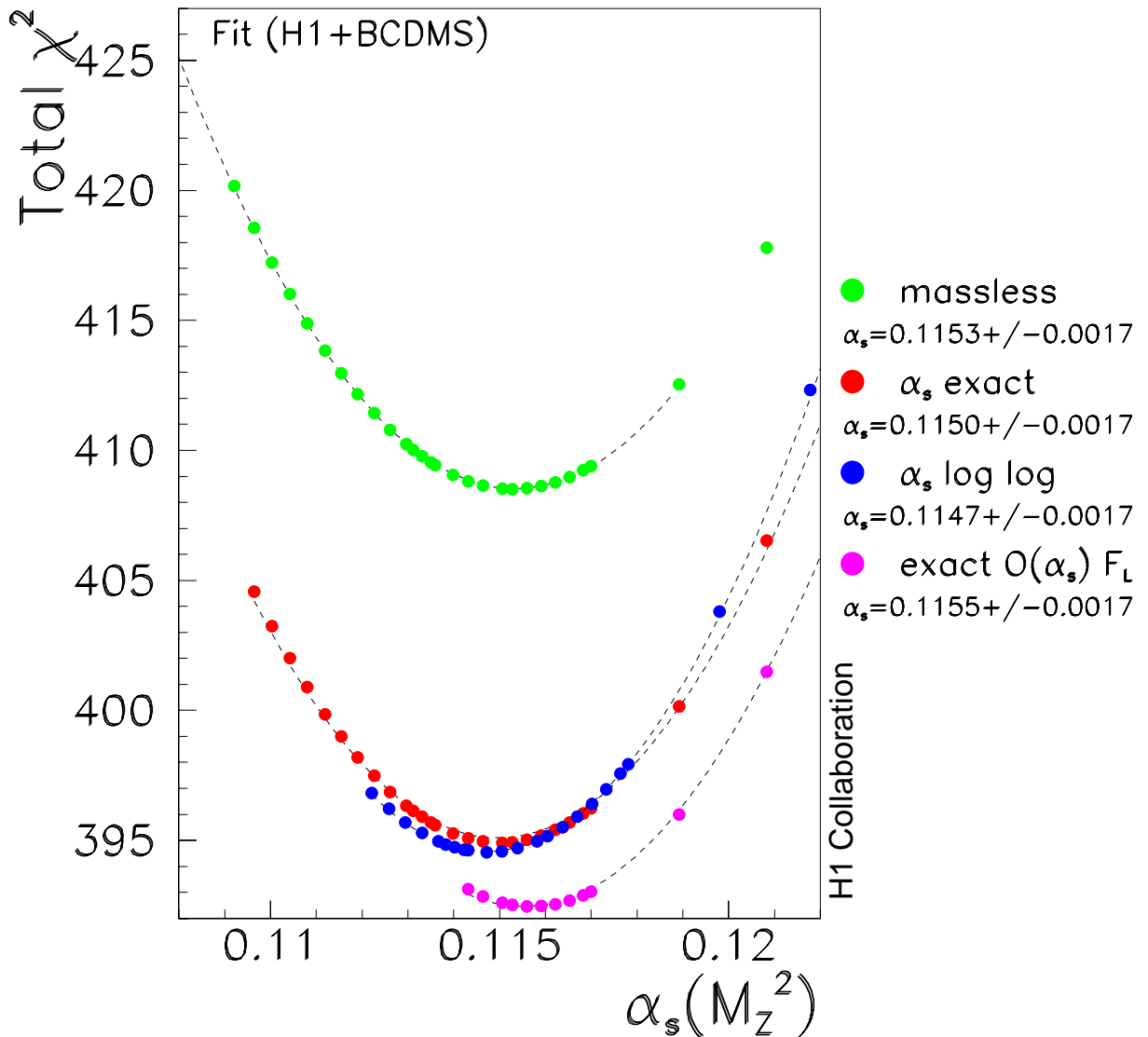


Figure 5.18: Sensitivity of $\alpha_s(M_Z^2)$ with respect to changing the theoretical prescription for the heavy quark treatment and to its theoretical definition and to what order in α_s the longitudinal structure function F_L is computed.

The central result can also be compared to variations of the data sets:

- If the H1 data at high and low Q^2 taken in 1996/97 are replaced by the previously published datasets taken in 1994, $\alpha_s(M_Z^2)$ comes out lower by 0.0008 with an enlarged experimental error.
- If the BCDMS data is replaced by data of the NMC collaboration [107], imposing the low Q^2 limit of the BCDMS data, a consistent value of $\alpha_s(M_Z^2) = 0.1158 \pm 0.003$ (*exp*) is obtained. From the size of the experimental error it can be deduced that the NMC data may be neglected once the BCDMS data is used.
- The addition of the BCDMS deuteron target data, with $y_\mu > 0.3$, to the H1 and BCDMS proton data yields $\alpha_s(M_Z^2) = 0.1158 \pm 0.0016$ (*exp*), i.e. $\alpha_s(M_Z^2)$ increases by 0.0008, while the experimental error only marginally improves. In this analysis nuclear corrections are applied using the integral relations of [50], and the conventional flavour decomposition into valence and sea quarks is used.

These results are summarized in Figure 5.19.

To summarise these cross checks, one observes a remarkable stability of the α_s result against quite significant variations in the analysis procedure and choice of datasets. The usage of H1 ep and BCDMS μp provides a most accurate and clean result and remains to be preferred over analyses which employ many datasets of hardly controllable systematic errors.

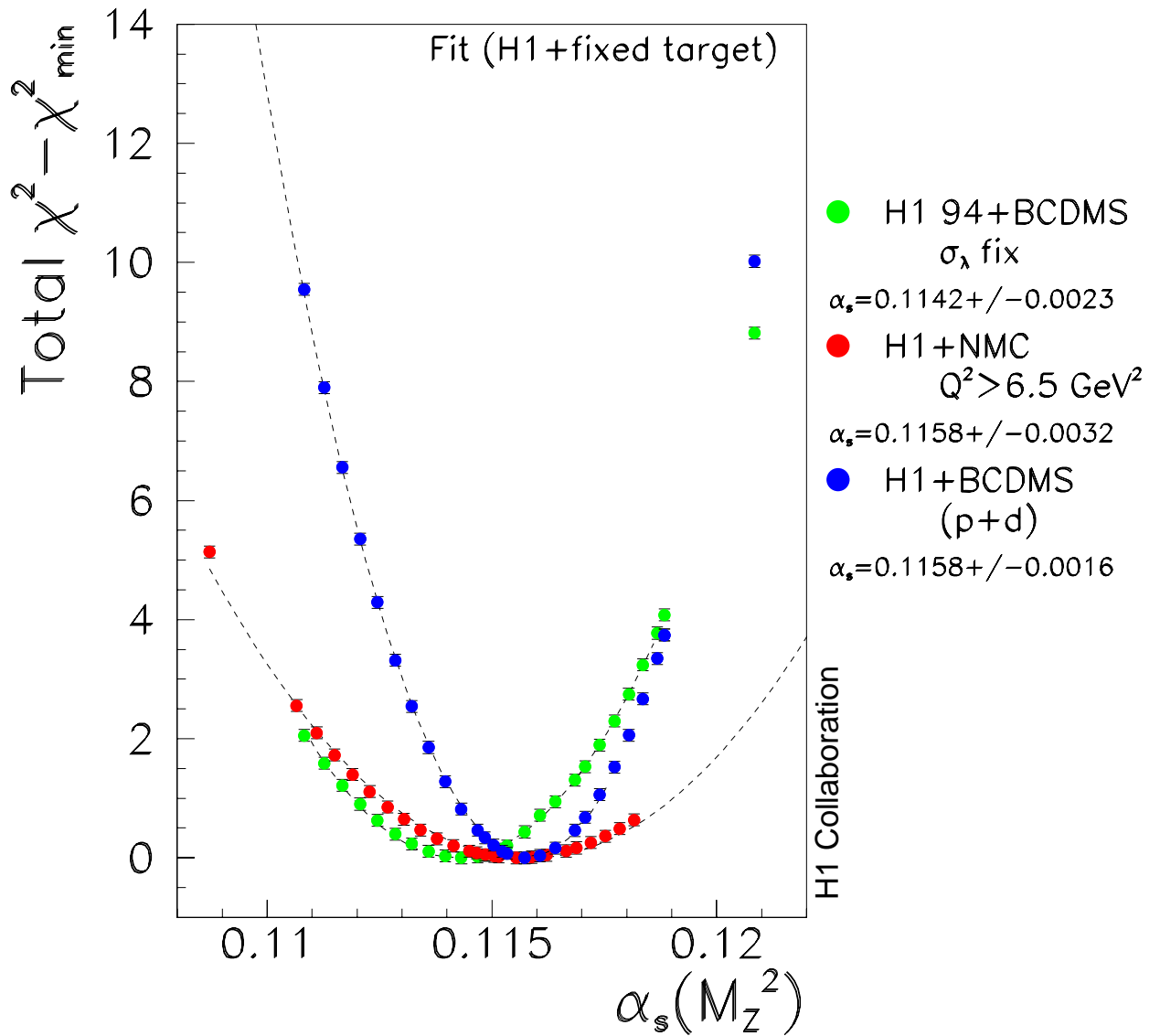


Figure 5.19: Variation of $\alpha_s(M_Z^2)$ on exchanging fit data with similar data sets. Shown are the H1 94 dataset replacing the H1 low and high Q^2 data taken in 96 and 97, the NMC data for $Q_{\min}^2 > 6.5 \text{ GeV}^2$ and a fit to H1+BCDMS proton and deuteron target data, allowing to use a conventional flavour decomposition.

5.10 $\alpha_s(M_Z^2)$ and the Gluon Distribution at High x

The gluon distribution is obtained from the scaling violations of F_2 . At low x , quark-antiquark pair production from gluons is the dominant process, and the gluon density is thus strongly correlated with α_s . At high x the scaling violations are due to gluon bremsstrahlung from quark lines, and the gluon distribution becomes very small, see figure 5.20.

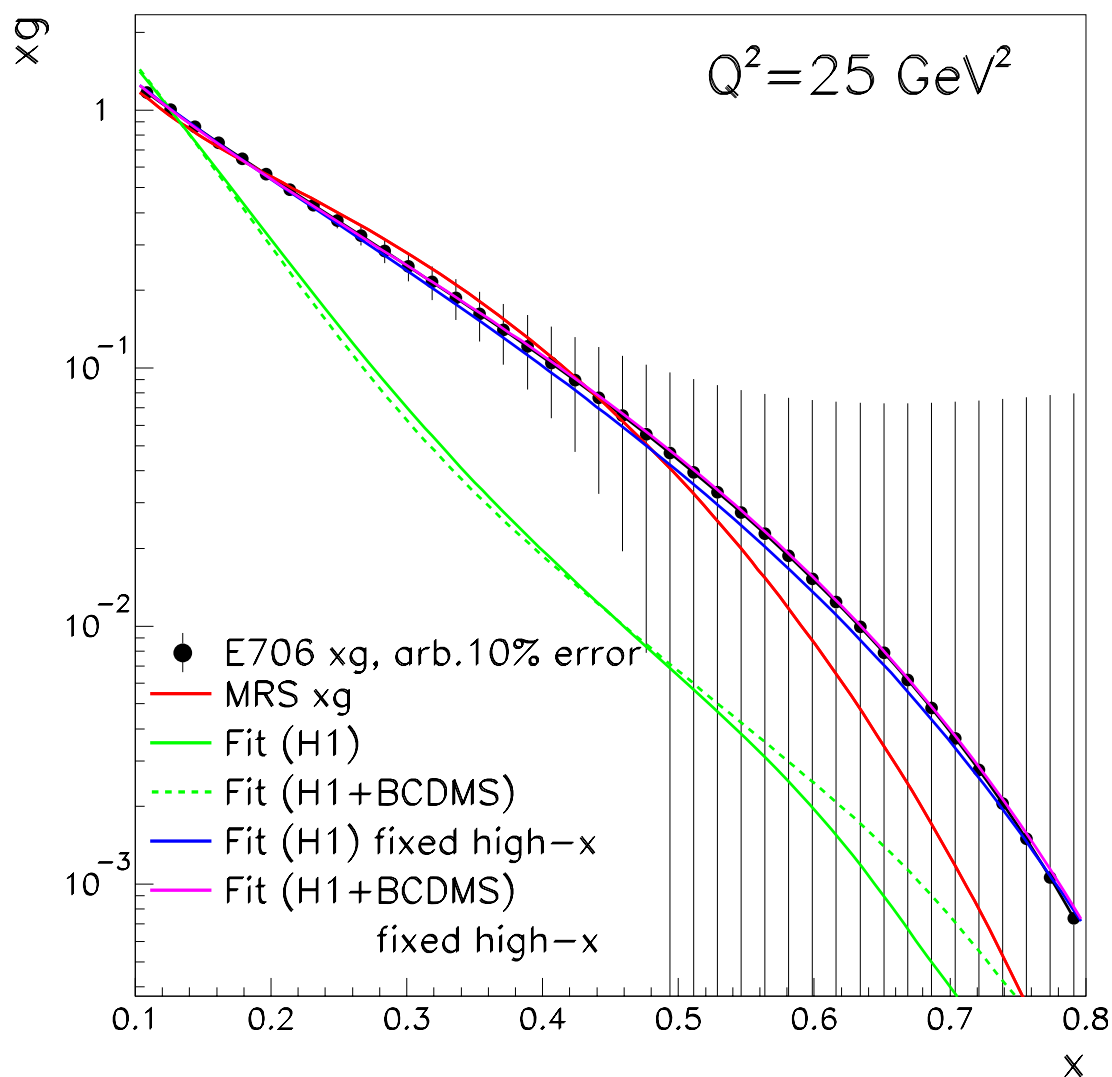


Figure 5.20: The gluon distribution at high $x > 0.1$ as obtained by a QCD analysis by [38] and [108] which use high E_t jet data to constrain the high x gluon distribution. Fits to H1 and H1+BCDMS are shown where the high x behaviour of the gluon was fixed to the E706 result in the region $0.1 < x < 0.8$

However, the high $x > 0.2$ domain of the gluon distribution does not completely decouple from

the low x domain by virtue of the momentum sum rule. As can be seen in figure 3.11, around 10% of the proton's momentum is carried by gluons at high $x > 0.1$.

In order to measure the gluon distribution at high x , processes other than inclusive lepton proton scattering are considered. One is inclusive jet production, measured at HERA see figure 5.21 or at hadron-hadron colliders. Another process sensitive to the gluon distribution at high x is direct photon production. These processes are often included in the global fits to 'pin down' the gluon at high x . However, these processes are plagued with theoretical uncertainties which limit

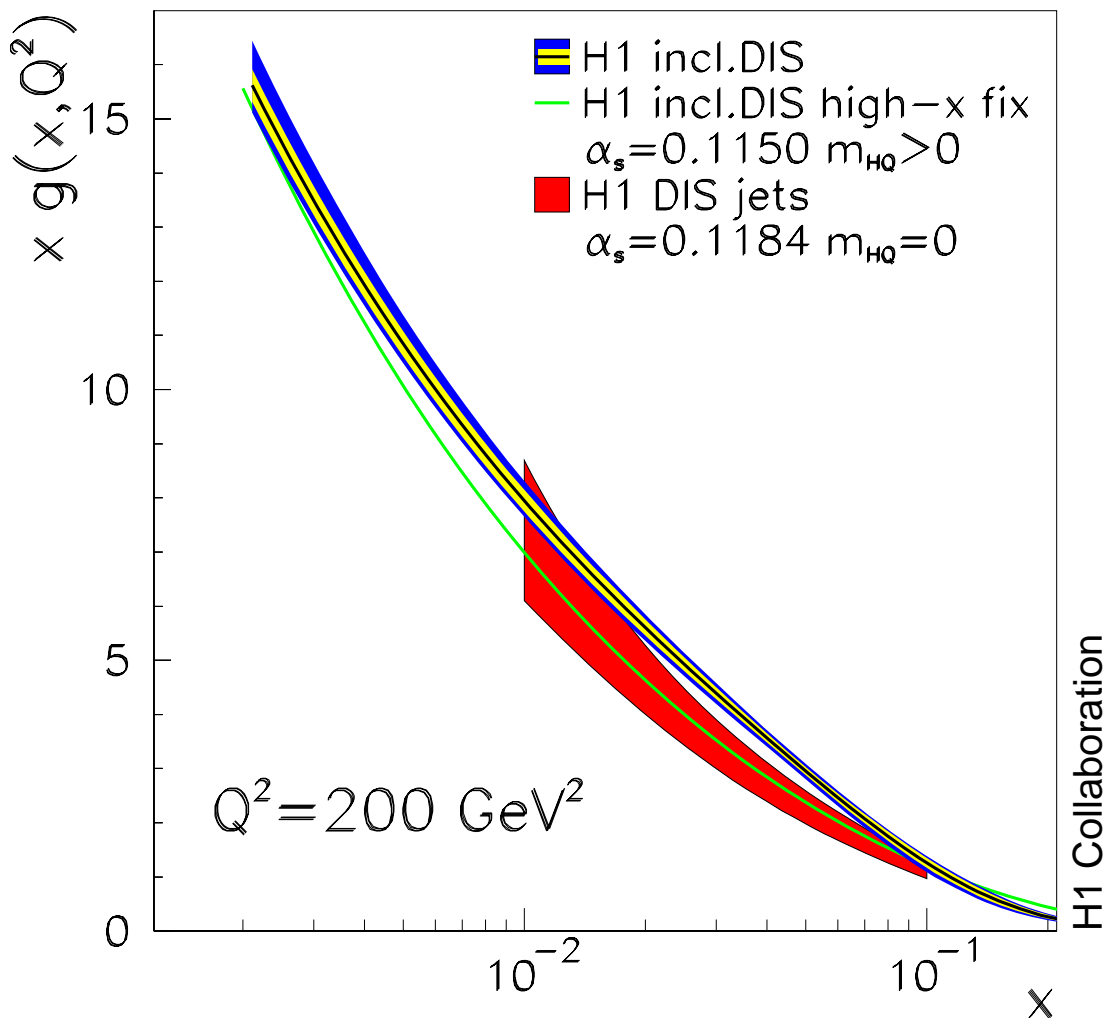


Figure 5.21: Comparison of gluon distributions from scaling violations at $Q^2 = 200 \text{ GeV}^2$ with results from inclusive dijet production [76]. Note that xg in the inclusive analysis is obtained within the fixed flavour scheme. At high $Q^2 \gg m_c^2$ the light flavour scheme produces gluon distributions which are consistently higher by about 10%, see figure 4.25. The single line represents a fit where the high x gluon distribution was fixed to the E706 result.

their practical usefulness. The interpretation of jet measurements is limited by hadronisation corrections and poorly constrained quark distribution functions.

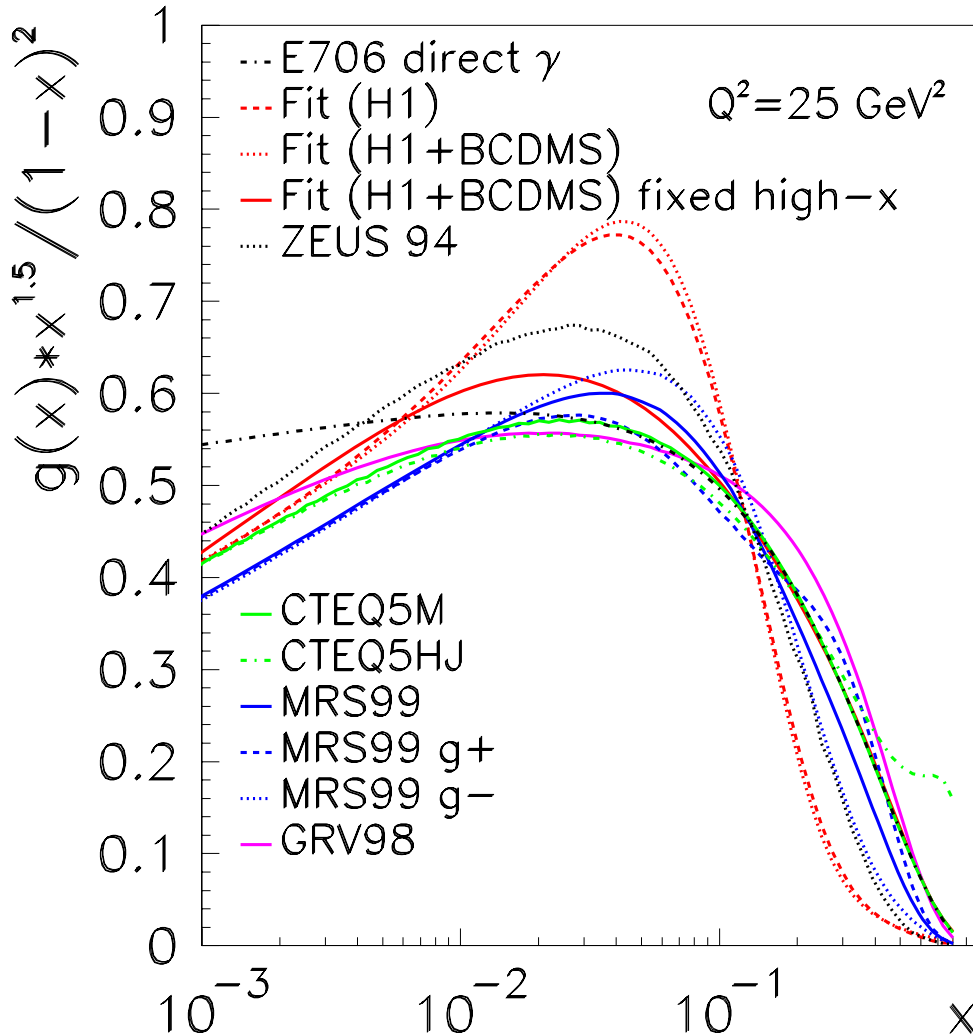


Figure 5.22: Gluon distributions at intermediate x for global fit results, direct photon production and fits to inclusive F_2 data. For the fits where the high $x > 0.1$ behaviour was fixed in the H1+BCDMS fit, the gluon distribution is seen to be lowered in the intermediate $10^{-2} < x < 10^{-1}$ range compared to a fit with an unconstrained gluon distribution.

Direct photon production at NLO requires large non-perturbative correction factors which limit the perturbative QCD interpretation of the data [109]. There is a theoretical debate as to whether intrinsic k_t effects resolve some of the difference observed between measurements and NLO QCD.

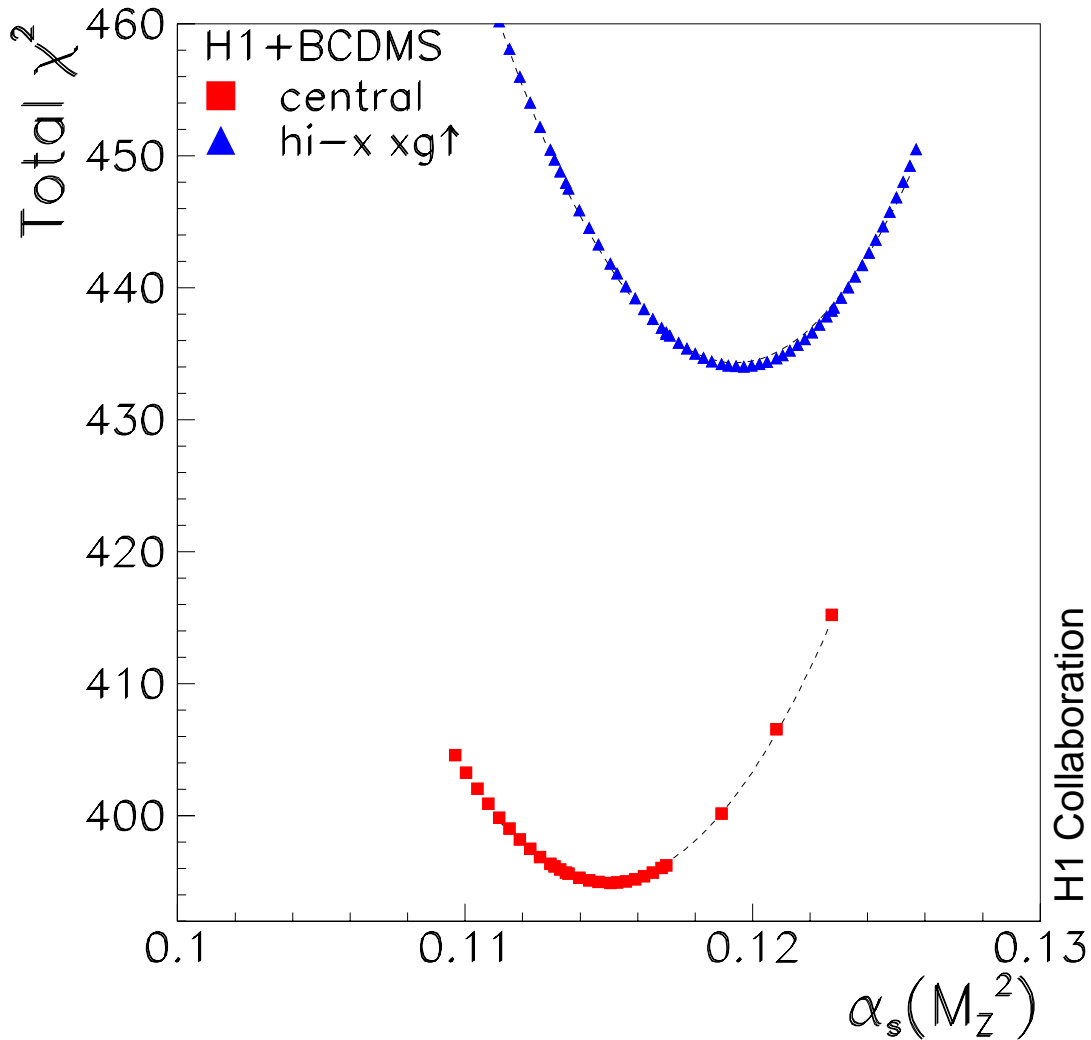


Figure 5.23: χ^2 minimisation curves for fits to H1+BCDMS with and without an enhanced gluon distribution at high $x > 0.1$. The enhanced gluon solution is disfavoured by about 40 units in χ^2 .

A recent extraction of the gluon distribution at high x from direct photon production [108] is shown in figure 5.20 together with the result of a global analysis [38]. Compared to these processes, the gluon distribution from scaling violations comes out quite low, both for the fit to the H1 data alone and to the H1+fixed target data. The uncertainty of xg determined at high x from the structure function data is so large that there is no real discrepancy. However, this striking effect is reproducible in different fit assumptions and programs and thus may not be an artefact of the parameterisation.

To assess the impact of the essentially unconstrained gluon distribution at high x in the NLO DGLAP fits, the gluon distribution was artificially constrained to the E706 determination by adding simulated gluon ‘data’ in the fit with an arbitrarily assigned 10% error. The resulting

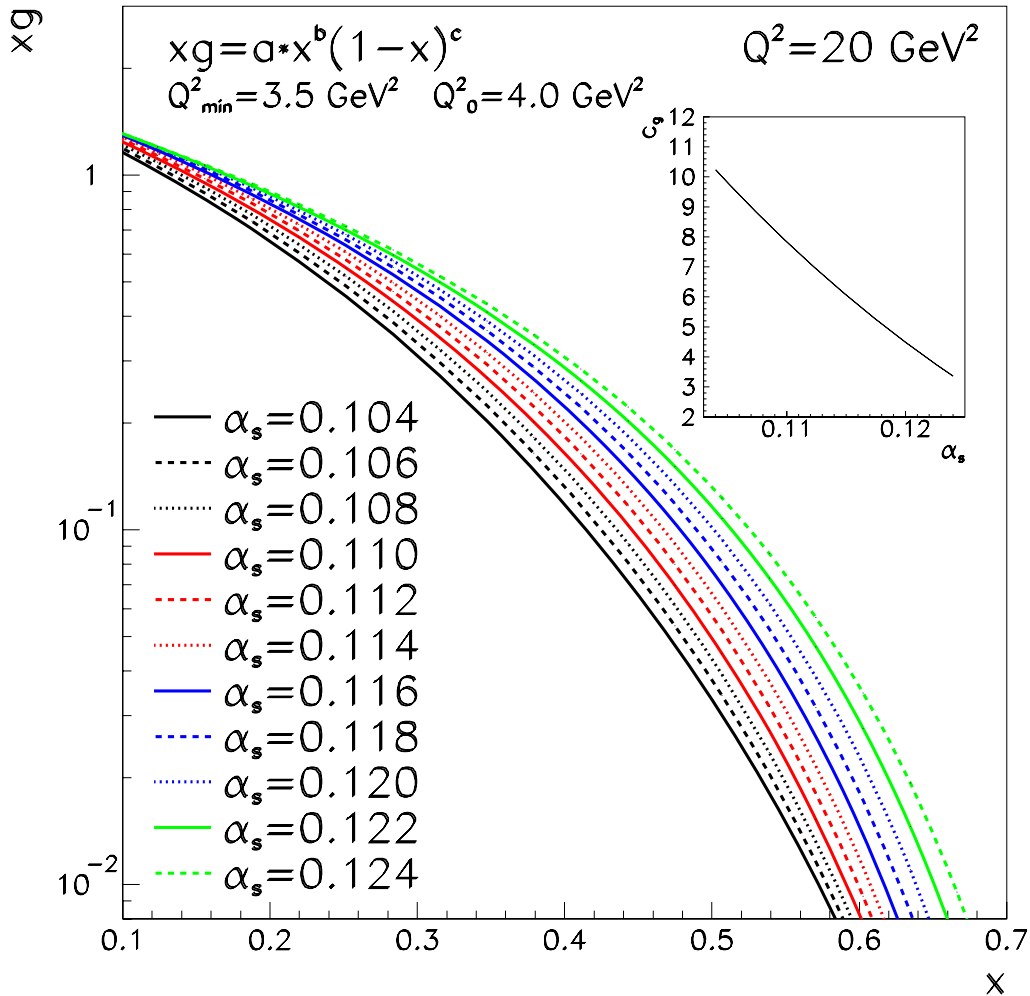


Figure 5.24: Gluon distributions at high $x > 0.1$ for varying α_s . The gluon distributions are parameterised with three parameters. The parameter c_g , governing the high x behaviour of a three parameter ansatz, is correlated to α_s , as can be seen in the insert. Such a behaviour was predicted by [110]

gluon distributions for the H1 and the H1+BCDMS fit are brought to the E706 result as can be seen in figure 5.20. Naively, one would expect no big impact since the gluon is very small at high x , but via the momentum sum rule the effect feeds down to lower x . This can be seen in figures 5.21 and 5.22. Here the gluon distribution obtained from scaling violations of F_2 is compared to a global analysis emphasising the intermediate x region. The constraint at $x > 0.1$ modifies the gluon distribution in the range $10^{-2} < x < 0.1$, rendering it more compatible with the global fit results. It also moves the gluon distribution from inclusive DIS downwards in this range such that a better compatibility with the HERA dijet data is observed, see figure 5.21. At low $x < 10^{-2}$, the scaling violation gluons with and without high x constraint are seen to overlap again, underlining the strong constraint from the low x H1 data imposed in this kinematic region.

Naturally, the question arises which of the possible gluon distribution shapes maybe the correct one. If the low x H1 data had no constraint on the high x behaviour, then one would not expect a significant change in the extracted physics quantities. However, as can be seen in figure 5.23, the extracted $\alpha_s(M_Z^2)$ from fits where the high x gluon was fixed to the E706 data differs from the free fits by about +0.005. Yet, the fit does disfavour such a constrained high x gluon with around 40 units in χ^2 , of which 25 units are contributed by the H1 data and 15 units by the BCDMS data, with the 'fake' gluon data contributing only 2 units to the total χ^2 .

Such a correlation of the high x behaviour of the gluon distribution and $\alpha_s(M_Z^2)$ has been predicted by [110]. Figure 5.24 shows the movement of the gluon distribution at high x with the variation of α_s . The insert displays the correlation of the c_g parameter of a three parameter gluon ansatz with α_s . In a fit with a such a three parameter gluon ansatz, c_g is directly controlling the high x behaviour of the gluon distribution. In this analysis, such a parameterisation of the gluon distribution is ruled out by an increase of 30 units in χ^2 , see figure 5.25, and is thus considered here as a technical study¹.

As is illustrated in figure 5.24 based on fits to H1+BCDMS data, a strongly falling gluon distribution at high x is related to a small value of α_s . If future precision measurements confirm a difference in the high x behaviour of xg and in the values of α_s between jet data and inclusive DIS, this might be an indication of new physics [99], an indication which will be averaged out by too global fits.

¹A recent, preliminary analysis performed by the ZEUS collaboration [63] based on ZEUS data collected in 1996 and 1997, on neutrino nucleon and on proton and deuteron fixed target data prefers a three parameter gluon ansatz and determines a value of $\alpha_s(M_Z^2) = 0.1172 \pm 0.0055(stat \oplus syst)$. If the same model assumptions are imposed in the H1 fit to H1 and BCDMS proton target data, the strong coupling is determined to be $\alpha_s(M_Z^2) = 0.1165 \pm 0.0019(exp)$.

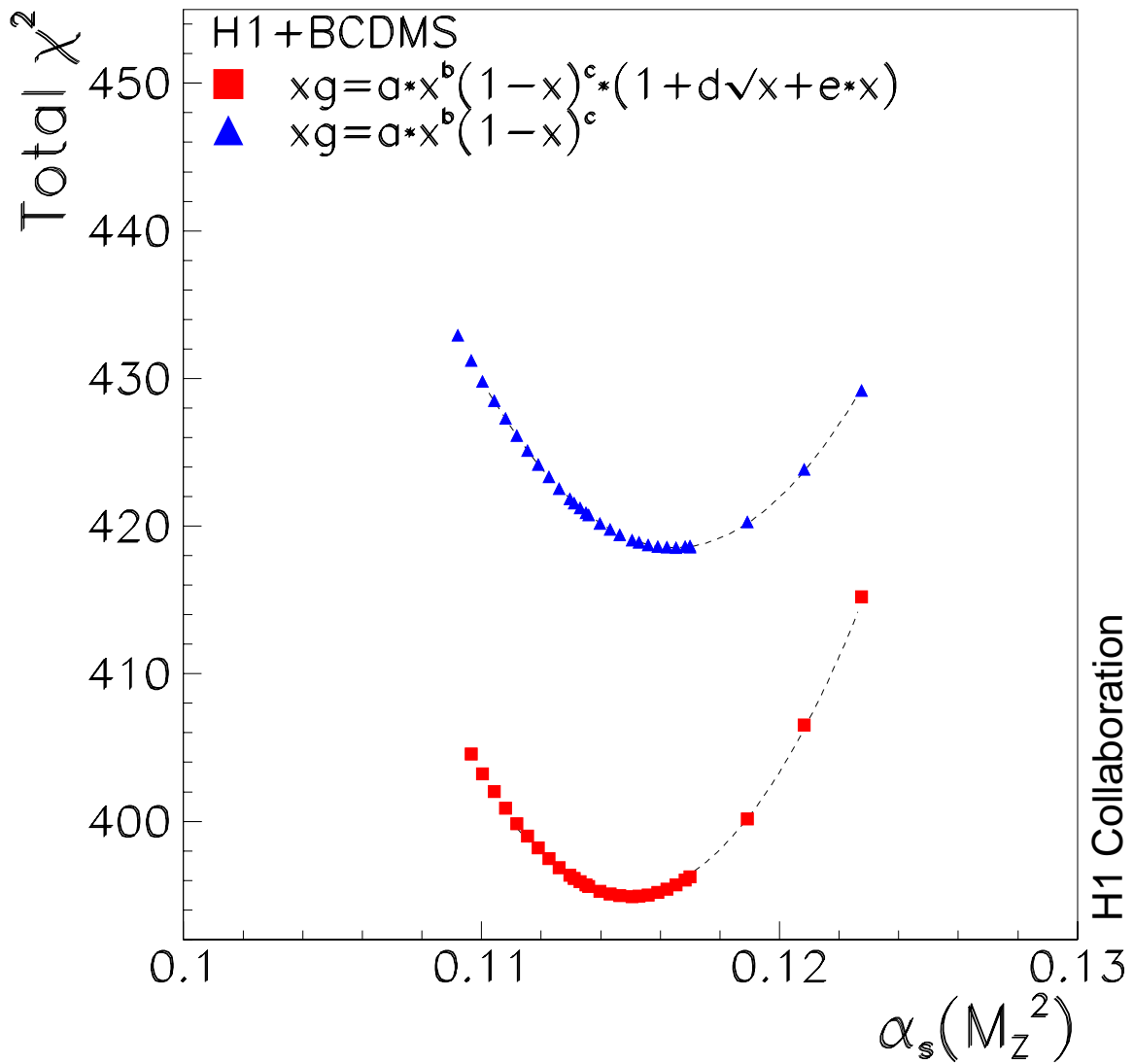


Figure 5.25: χ^2 minimisation curves for a three parameter gluon distribution and a 5 parameter ansatz as used for the analyses to H1 and BCDMS data.

Summary

Deep inelastic scattering has been the most suitable process to test the theory of the strong interaction. By means of a well defined electroweak probe, quark-gluon interactions can be studied in a kinematic regime where QCD is asymptotically free and allows calculations to higher order perturbation theory.

This work discussed the so far most precise measurement of the DIS scattering cross section in the kinematic range of low x accessed by the HERA accelerator. The low x region is accessed at lower Q^2 between 1 and 150 GeV² where the secondary positron is scattered in the backward H1 apparatus, notably the SPACAL calorimeter and the preceding track devices, the BDC and the BST.

With the upgraded H1 backward apparatus and a luminosity of about 20 pb⁻¹ the inclusive DIS scattering cross section was measured with typically 3% precision using data taken in 1996 and 1997. Part of the published data was provided by the author and a complete analysis was performed for cross checks.

The high accuracy of the data allowed a precision QCD analysis to be performed with the goals to

- verify the validity of the description of the measurement within the conventional perturbative QCD approach, the DGLAP equations;
- measure the gluon momentum distribution $xg(x, Q^2)$ in the proton;
- determine the strong coupling constant α_s .

In a novel approach this analysis was performed using proton target data alone.

- No departure was observed of the measured cross section from the QCD calculation, which, however, requires initial parton distributions to be fixed by the data. The QCD calculations, fixed by the scaling violations of F_2 , allow accurate predictions to be made for the longitudinal structure function F_L and for the charm structure function F_2^{cc} which in further analyses by H1 are shown to be well described.
- The gluon distribution $xg(x, Q^2)$ is determined at $Q^2 = 20 \text{ GeV}^2$ to an experimental accuracy of about 3% in the kinematic range $3 \cdot 10^{-4} \leq x \leq 0.1$. The gluon density rises towards low x and no sign for saturation is observed in the DIS region.

- Based on the H1 ep and the BCDMS μp data the strong coupling constant is determined to NLO in the $\overline{\text{MS}}$ renormalisation and factorisation scheme:

$$\alpha_s^{\text{NLO},\overline{\text{MS}}}(M_Z^2) = 0.1150 \pm 0.0017 \text{ (exp)} \pm_{-0.0005}^{+0.0009} \text{ (model)}$$

The result is consistent with the world average value but tends to be lower and has an experimental and model uncertainty of size comparable to the average of all previous data on $\alpha_s(M_Z^2)$.

- The largest uncertainty of the order of ± 0.005 is connected with the uncertainty of the renormalisation scale which requires this data to be re-analysed when the exact NNLO formulae become available.

This result was cross checked with quite a number of analyses using different data sets and varying nearly all assumptions in the fit. For example, a conventional analysis using the standard flavour decomposition and deuteron data leads to a value of 0.1158 ± 0.0016 (exp).

Interesting observations were made on the correlation of α_s with the behaviour of the gluon distribution both at low x and at high x . These deserve further attention when still improved HERA data become available, in particular at high x .

“... und ging nicht alles aus, so ging doch wenigstens was vor.” (P. Hacks)

Bibliography

- [1] M. Bloom et al., M. Breidenbach et al., *Phys. Rev. Lett.* **23** (1969) 935.
- [2] R.Frisch, O. Stern, *Z. Physik* **85** (1933) 4.
- [3] R. Hofstadter, *Rev. Mod. Phys.* **28** (1956) 214.
- [4] R.P. Feynman, *Phys. Rev. Lett.* **23** (1969) 1415.
- [5] M. Gell-Mann, *Phys. Lett.* **8** (1964), 214.
- [6] C. Zweig, CERN Report Nos. TH 401,402 (1964).
- [7] C.G. Callan, D.J. Gross, *Phys. Rev. Lett.* **22** (1969) 156.
- [8] D.J. Fox et al., *Phys. Rev. Lett.* **33** (1974) 1504.
- [9] BEBC Collaboration, *Nucl. Phys.* **B 203** (1982) 362.
- [10] S.Bethke, hep-ph/0004021 (2000).
- [11] Particle Data Group Report, D.E. Groom et al., *Eur. Phys. J. C* **15** (2000) 1.
- [12] J.C. Collins, D.E. Soper, *Ann. Rev. Nucl. Part. Sci.* **37** (1978) 383.
- [13] W. Furmanski and R. Petronzio, *Z. Physik C* **11** (1982) 293.
- [14] W. J. Marciano *Phys. Rev.* **D 29** (1984) 580.
- [15] G.'t Hooft, M.Veltman, *Nucl. Phys.* **B 44** (1972) 189.
- [16] G. Altarelli and G. Martinelli, *Phys. Lett.* **B 76** (1978) 89;
M. Glück and E. Reya, *Nucl. Phys.* **B 145** (1978) 24.
- [17] E. B. Zijlstra and W. van Neerven, *Nucl. Phys.* **B 383** (1992) 525.
- [18] Yu. L. Dokshitzer, *Sov. Phys. JETP* **46** (1977) 641;
V. N. Gribov and L. N. Lipatov, *Sov. J. Nucl. Phys.* **15** (1972) 438 and 675;
G. Altarelli and G. Parisi, *Nucl. Phys.* **B 126** (1977) 298.
- [19] W.L. van Neerven and A. Vogt, *Nucl. Phys.* **B 588** (2000) 345.

-
- [20] F. Lehner, Ph.D. Thesis, University of Hamburg (1998).
- [21] H1 Collaboration, I. Abt et al., *Nucl. Instrum. Meth.* **A386** (1997) 310 and 348.
- [22] M. Klein, *On the Q^2 , x Range at HERA*, Proceedings of the Workshop Physics at HERA, vol. 1, eds. W. Buchmüller, G. Ingelman, DESY (1992).
- [23] A. Blondel and F. Jacquet, Proc. *ep* Facility for Europe, Amsterdam 1979, DESY 79/48 (1979) 391.
- [24] U. Bassler and G. Bernardi, *Nucl. Instrum. Meth.* **A361** (1995) 197.
- [25] S. Bentvelsen, J. Engelen and P. Kooijman, Proc. Workshop on HERA Physics, Vol 1, eds. W. Buchmüller and G. Ingelman, Hamburg, DESY (1992) 25; K. C. Höger, *ibid* 43.
- [26] D. Eckstein, Ph.D. Thesis, Humboldt-University Berlin (2001).
- [27] H1 Collaboration, C. Adloff et al., *Eur. Phys. J. C* **21** (2001) 33-61, DESY-00-181, hep-ex/0012053.
- [28] E. Tzamariudaki, Proceedings of VII calorimeter conference CALOR 97, World Scientific (1998).
- [29] R. Wallny, Diploma Thesis, University Heidelberg (1996).
- [30] A. Meyer, Ph.D. Thesis, University of Hamburg (1997).
- [31] A. A. Glazov, Ph.D. Thesis, Humboldt-University Berlin (1998).
- [32] R. Stamen, Diploma Thesis, University of Dortmund (1998).
- [33] R. Maracek, Ph.D. Thesis, Inst. of Exp. Physics Kosice (1999).
- [34] P. Sievers, Diploma Thesis, University Heidelberg (1999).
- [35] R. Engel and J. Ranft, *Phys. Rev. D* **54** (1996) 4244.
- [36] V.V. Arkadov, Ph.D. Thesis, Humboldt-University Berlin (2000).
- [37] H1 Collaboration, C. Adloff et al., *Eur. Phys. J. C* **13** (2000) 609.
- [38] A.D. Martin et al., *Eur. Phys. J. C* **4** (1998) 463.
- [39] CTEQ Collaboration, H.L. Lai et al., *Phys. Rev. D* **55** (1997) 1280 and hep-ph/9903282 (1999).
- [40] M. Glück, E. Reya and A. Vogt, *Eur. Phys. J. C* **5** (1998) 461.
- [41] W. T. Giele, S. A. Keller and D. A. Kosower, hep-ph/0104052 (2001).
- [42] J. Pumplin et al., hep-ph/0101032 (2001).

-
- [43] D. Stump et al., hep-ph/0101051 (2001).
- [44] A.J. Buras, *Rev. Mod. Phys.* **52** (1980) 199.
- [45] NMC Collaboration, M. Arneodo et al., *Phys. Rev.* **B 309** (1993) 222.
- [46] A. Milsztajn and M. Virchaux, *Phys. Lett.* **B 274** (1992) 221.
- [47] M. Botje, QCDNUM, ZEUS internal notes 98-062 (1998) and 99-027 (1999);
Phys. Lett. **B 472** (2000) 175.
- [48] A. Alekhin, IHEP-2000-39 and hep-ph/0011002 (2000).
- [49] A. Vogt, Proc. DIS'99, *Nucl. Phys.* **B79** Proc. Suppl. (1999) 102, ed. by J. Blümlein and T. Riemann.
- [50] Melnitchouk and A.W. Thomas, *Phys. Rev.* **C 52** (1995) 3373.
- [51] L.Frankfurt, M.Strikman, *Eur. Phys. J.* **A 5** (1999) 293-306.
- [52] E. Laenen et al., *Nucl. Phys.* **B 392** (1993) 162;
S. Riemersma, J. Smith and W. van Neerven, *Phys. Lett.* **B 347** (1995) 143.
- [53] CCFR Collaboration, A.O. Bazarko et al., *Z. Physik* **C 65** (1995) 189.
- [54] E866/NuSea Collaboration, E.A. Hawker et al., *Phys. Rev. Lett.* **80** (1998) 3715.
- [55] NMC Collaboration, P. Amaudruz et al., *Phys. Rev. Lett.* **66** (1991) 2712 and M. Arneodo et al., *Phys. Rev.* **D 50** (1994) R1.
- [56] NuTeV Collaboration, T. Adams et al., hep-ex/9906038 (1999).
- [57] R.D. Ball and S. Forte, *Phys. Lett.* **B 335** (1994) 77-86, and *Phys. Lett.* **B 336** (1994) 77-79.
- [58] A.D. Martin, Proc. of XXI International Meeting on Fundamental Physics, World Scientific (1993).
- [59] V.Lemaitre, Proc. HEP97, Jerusalem, Israel (1997).
- [60] ZEUS Collaboration, J. Breitweg et al., *Eur. Phys. J.* **C 7** (1999) 609-630.
- [61] M. Glück, E. Reya, *Phys. Lett.* **B 83** (1979) 9.
- [62] M. Glück, E. Reya, A. Vogt, *Z. Physik* **C 53** (1992) 127.
- [63] K.Nagano, Proc. DIS2001, Bologna, Italy (2000).
- [64] CTEQ Collaboration, H.L. Lai et al., *Eur. Phys. J.* **C 12** (2000) 375-392.
- [65] CTEQ Collaboration, H.L. Lai et al., *Phys. Rev.* **D 55** (1997) 1280.
- [66] C. Pascaud and F. Zomer, LAL preprint, LAL/95-05 (1995).

-
- [67] R.J.Barlow, Statistics, John Wiley & Sons (1989).
- [68] F.James, MINUIT, CERN Program Library Long Writeup D506.
- [69] C. Pascaud and F. Zomer, QCDFIT manual, unpublished.
- [70] K. Prytz, *Phys. Lett.* **B 311** (1993) 286.
- [71] A. Dubak, Proc. DIS2001, Bologna, Italy (2001).
- [72] S.J. Brodsky and G. Farrar, *Phys. Rev. Lett.* **31** (1973) 1153.
- [73] M. Klein, P. Newman, R. Wallny, H1-Internal Note h1-0600-585.
- [74] R.Roberts, Proc. DIS2000, Liverpool, United Kingdom (2000).
- [75] H1 Collaboration, I. Abt et al., *Nucl. Phys.* **B 545** (1999) 21.
- [76] H1 Collaboration, C. Adloff et al., *Eur. Phys. J.* **C 19** (2001) 289-311.
- [77] R. Thorne, R.G. Roberts *Eur. Phys. J.* **C 19** (2001) 339-349.
- [78] E.Witten, *Nucl. Phys.* **B 104** (1996) 445.
- [79] M. Shifman et al., *Nucl. Phys.* **B 136** (1978) 157.
- [80] H1 Collaboration, C. Adloff et al., submitted to *Phys. Lett.***B**, DESY-01-100, hep-ex/0108039 (2001).
- [81] ZEUS Collaboration, J. Breitweg et al., *Eur. Phys. J.* **C 12** (2000) 35-52.
- [82] D. Müller, Ph. D. Thesis, University of Zürich (1998).
- [83] M. Nedden, Ph. D. Thesis, University of Zürich (1998).
- [84] H1 Collaboration, C. Adloff et al., *Nucl. Phys.* **B 545** (1999) 21-44.
- [85] E. Laenen, S. Riemersma, J. Smith, W. van Neerven *Nucl. Phys.* **B 392** (1993) 162 and 229.
- [86] B. Harris and J. Smith, *Nucl. Phys.* **B 452** (1995) 109.
- [87] S. Riemersma, *Nucl. Phys.* **B 392** (1993) 162.
- [88] W. L. van Neerven, *Acta Phys. Polon.* **B28**(1997) 2715.
- [89] A. Vogt Proc. DIS'96 (1996).
- [90] M. Aivazis, J. Collins, F. Olness, W. Tung, *Phys. Rev.* **D 50** (1994) 3102.
- [91] M. Buza et al. *Eur. Phys. J.* **C 1** (1998) 301-320, hep-ph/9612398 (1996).
- [92] A.D. Martin et al., *Eur. Phys. J.* **C 4** (1998) 463 and hep-ph/9907231 1999.

-
- [93] T. Hadig, Ph.D. Thesis, RWTH Aachen, preprint PITHA 99/41 (1999).
The program is based on J. Blümlein and A. Vogt, *Phys. Rev. D* **58** (1998) 014020.
- [94] M. Cooper-Sarkar et al. Proc. Workshop on HERA Physics, Vol 1, ed. R.Peccei, Hamburg, DESY (1987) 231.
- [95] L.A.T. Bauerdick, A.Glazov, M.Klein, Workshop on Future Physics at HERA, Hamburg, DESY (1996) 77.
- [96] L.Favart et al., DESY grey report FH1K-96-01 (1996).
- [97] BCDMS Collaboration, A.C. Benvenuti et al., *Phys. Lett. B* **B223** (1989) 485;
CERN preprint CERN-EP/89-06.
- [98] L. Clavelli, hep-ph/9908342 (1999).
- [99] J. Blumlein and J. Botts, *Phys. Lett. B* **325** (1994) 190; [Erratum-*ibid.* **B331** (1994) 450]
hep-ph/9401291.
- [100] L. W. Whitlow et al., *Phys. Lett. B* **282** (1992) 475.
- [101] A. Milsztajn et al., *Z. Physik C* **49** (1991) 527.
- [102] J. Bartels, K. Charchula and J. Feltesse, Proc. Workshop on HERA Physics, Vol 1, eds.
W. Buchmüller and G. Ingelman, Hamburg, DESY (1992) 193.
- [103] C. Pascaud and F. Zomer, DESY 96-266 (1996).
- [104] J. Santiago and F.J. Yndurain, *Nucl. Phys. B* **563** (1999) 45 and *Nucl. Phys. Proc. Suppl.*
86 (2000) 69.
- [105] C.Pascaud, private communication.
- [106] A. Vogt, private communication.
- [107] NMC Collaboration, M. Arneodo et al., *Phys. Lett. B* **309** (1993) 222.
- [108] E706 Collaboration, L. Apanasevich et al., *Phys. Rev. Lett.* **81** (1998) 2642-2645.
- [109] P. Aurenche et al., *Eur. Phys. J. C* **39** (1999) 107-119.
- [110] 'Georgi Plot' M.Klein, private communication.

Acknowledgments

I wish to express my sincere gratitude to Prof. Ulrich Straumann for offering me the opportunity to work as a Ph.D. student for the H1 experiment. He gave me a large degree of freedom and trust while I was pursuing my scientific goals. I thank him for his support and patience.

Heartfelt thanks go to Max Klein who has been the driving force behind this work. Maybe too driving at times, he shared all the ups and downs of this work, and without him this analysis certainly would not have succeeded. I could always count on his advice and continuous support, including the difficult last months of writing up this work. I much appreciated his good sense of humour and our discussions on topics outside physics as well.

I also wish to thank Christian Pascaud, who provided and maintained the QCD evolution program, and who also was a steady stronghold of knowledge and advice even in Le Bourge. It was a distinct pleasure to see, with these two gentlemen, the first inclusive measurement of α_s from HERA emerge from the countless numbers and plots.

I also wish to express my gratitude to Doris Eckstein, Sasha Glazov, Thorsten Kleinwort, Frank Lehner and Fabian Zomer. Doris and I survived the data analysis together and cheered each other's spirit up at the Zeuthen lake and elsewhere. Thorsten did an extremely fine job in maintaining the Linux cluster which we tortured with countless analysis and QCD fit jobs. Sasha openly shared his wisdom concerning data analysis with me and Fabian and Frank provided their knowledge concerning QCD fitting for which I am very grateful.

I am indebted to my ELAN colleagues Vladimir Arkadov, Andreas Meyer, Philipp Sievers, Vladimir Shekelyan, and Sasha Zhokin. Their knowledge and co-operation in the data analysis is, albeit not documented in this thesis, distinctly felt throughout my time as a Ph.D. student and hereby acknowledged. I also would like to thank Andreas Vogt whose help in computing the renormalisation and factorisation scale uncertainties was much appreciated.

Much of this work has already found its way to the conferences during the spokespersonship of Prof. John Dainton. I hope he did not take it as a hideous attack on his good health when we shipped the preliminary data to the Stanford Lepton-Photon Conference 1999 the way we did. Many thanks are also due to his successor Eckhard Elsen who continued supporting and encouraging this analysis.

The hospitality of the DESY Directorate (Hamburg and Zeuthen) is gratefully acknowledged, as is the hospitality of quite a different kind of David Müller und Renate Nussberger in Zürich. Frank Lehner and Phil Geissbuehler went through the pain of proof-reading on short notice, for which I owe them a lot. I extend my gratitude to all the colleagues at Heidelberg, Hamburg, Zürich and Zeuthen; physicists, engineers and technicians, who are too numerous to mention but enriched my life while I was in their midst. Thank you all.

The last words of gratitude belong to my family, especially to my mother. Her example of bearing adversity with perseverance spurred me to prove that we are akin indeed.

This work has been supported by the German Bundesministerium für Bildung und Forschung and the Swiss National Science Foundation.

Curriculum Vitae

Personalien:

Name: Rainer Wallny
Staatsangehörigkeit: deutsch
Geboren: 12. August 1969 in Esslingen am Neckar, Deutschland

Bildungsgang:

1976 - 1980 Grundschole in Reutlingen Rommelsbach
1980 - 1989 Albert-Einstein-Gymnasium Reutlingen
1989 Abitur
1989 - 1992 Studium der Physik an der Universität Tübingen
1991 Vordiplom
1992 - 1994 Studium der Physik an der University of Washington, Seattle, WA, U.S.A.
1994 *Master of Science* Abschluss
1994 - 1996 Studium der Physik an der Universität Heidelberg
1995 - 1996 Diplomarbeit in Experimentalphysik unter der Leitung von Prof. Dr. U. Straumann
1996 Diplom in Experimentalphysik
1995 - 1997 Forschungsaufenthalt DESY Hamburg
1997 - 1999 Wissenschaftliche Mitarbeit beim H1 Experiment am Physikalischen Institut der Universität Heidelberg,
1997 - 2000 Forschungsaufenthalt DESY Zeuthen
1999 - 2001 Wissenschaftliche Mitarbeit beim H1 Experiment am Physikinstitut der Universität Zürich, Dissertation bei Prof. Dr. U. Straumann.

Dozentenverzeichnis:

Universität Zürich:

U. Straumann P. Truöl

Universität Heidelberg:

H.-G.Bock	F.Eisele	D.Habs	W.Hoffmann	S.Hunklinger
E.-E.Kluge	K.T.Knöpfle	J.v.Krogh	K.-H.Meyer	H.-W.Siebert
I.Stamatescu	K.Tittel	H.-A.Weidenmüller	F.Wegner	

University of Washington:

D.G.Boulware	L.S.Brown	V. Chaloupka	S.D.Ellis	L.G.Jaffe
G.A.Miller	P.C.Peters	J.E.Rothberg	S.R.Sharpe	

Universität Tübingen:

M.Baumann
R.Hübener
H.Müther
G.Staudt

A.Fässler
H.Kaul
H.Pfister
G.Wagner

H.Fischer
B.Kümmerer
H.Reinhard

F.Gönnenwein
F.Lenz
H.Ruder

W.-D. Hartmann
E.Lindner
A.Schwenk